Strong Field Studies of Cesium Using Intense Mid-infrared Light

A Dissertation Presented

by

Anne Marie March

to

The Graduate School

in Partial Fulfillment of the Requirements

for the Degree of

Doctor of Philosophy

in

Physics

Stony Brook University

May 2009

Stony Brook University

The Graduate School

Anne Marie March

We, the dissertation committee for the above candidate for the Doctor of Philosophy degree, hereby recommend acceptance of this dissertation.

Louis DiMauro – Dissertation Advisor
Adjunct Professor, Department of Physics and Astronomy
and Professor, The Ohio State University

Peter Koch – Chairperson of Defense
Professor, Department of Physics and Astronomy

Konstantin Likharev
Professor, Department of Physics and Astronomy

Michael White
Senior Chemist, Brookhaven National Laboratory

This dissertation is accepted by the Graduate School.

Lawrence Martin
Dean of the Graduate School

Abstract of the Dissertation

Strong Field Studies of Cesium Using Intense Mid-infrared Light

by

Anne Marie March

Doctor of Philosophy

in

Physics

Stony Brook University

2009

In the interaction of a short laser pulse with an atom or molecule, the strong field regime is realized when the strength of the laser's electric field is comparable to that of the Coulomb binding field. For several years now, these laser field strengths have been achievable using neodymium-based (1 μm) and titanium:sapphire-based (0.8 μm) laser technologies. This has led to the discovery of surprising phenomena such as above-threshold ionization (ATI) and high-harmonic generation (HHG). HHG has subsequently been used to generate light pulses with durations on the order of tens of attoseconds (1 as = 10^{-18} s), opening up the exploration of dynamics in atoms and molecules on the time scale of the electronic motion.

Numerous studies have detailed the role of the intensity of the laser field, but the range of laser wavelengths over which the strong field interaction has been explored has been limited by the availability of sources. In addition, this wavelength constraint has imposed a restriction on the type of neutral atoms that have been explored. In order for an atom to experience the peak intensity of the laser pulse, it must not completely ionize during the intensity increase on the pulse's rising edge. In practice, this has restricted laser strong field exploration to atoms with high ionization potentials, specifically the noble gases.

In this dissertation, strong field studies of the weakly bound neutral cesium atom, utilizing a unique, intense, 100 fs, mid-infrared laser (3.6 μm), are presented. Photoelectron energy spectra are shown which exhibit very high order ATI peaks, and electron energies many times the cesium ionization threshold energy. The 31^{st} harmonic of the 3.6 μm light has been observed. In addition, a cross-correlation frequency-resolved optical-gating (XFROG) technique has been used to measure the complete spectral amplitude and phase of harmonics 5 through 13, as well as their relative phase. The harmonics are found to exhibit negative dispersion, where the higher harmonic orders lead the lower orders in time. The complete temporal reconstruction including harmonics 7-13 consists of a train of pulses with a temporal envelope having a full-width at half-maximum of 40 fs and individual pulse durations $\sim$ 2 fs, which is 1/6 of the driving laser period.

To my parents

Contents

List of Figures viii

List of Tables xiv

Acknowledgements xv

1 Introduction **1**

1.1 The Strong-Field Regime of Intense Laser-Atom Studies . . . 1

2 Strong-Field Models **7**

2.1 Keldysh Tunneling Ionization 7

2.2 Simpleman's Model and Rescattering 11

2.3 Keldysh-Scaled Atom-Laser System 14

3 Mid-infrared Laser System **21**

3.1 Difference Frequency Generation 22

3.2 Pump (0.815 μm Radiation) 23

3.3 Signal (1.053 μm Radiation) 24

3.4 Pulse Synchronization 24

3.5 Idler (3.6 μm Radiation) 25

3.6 Multipass Amplifier 26

3.6.1 Gain Model 27

3.6.2 Layout 31

3.6.3 Beam Models 32

3.6.4 Cooling 35

3.6.5 Performance 37

4 Photoelectron Spectra **41**

4.1 Introduction 41

4.2 Experimental Apparatus 44

4.2.1 Overview of the Time-of-Flight Spectrometer 44
4.2.2 Spectrometer details 46
4.2.3 Measurement of Time-of-Flight Mass Spectra 51
4.2.4 Measurement of photoelectron spectra 53
4.2.5 Cesium Oven 56
4.3 Experimental Results 62
4.3.1 Ion Yield 62
4.3.2 Photoelectron Spectra 63

5 Harmonic Generation 77
5.1 Introduction 77
5.2 Experimental Apparatus 82
5.2.1 Heat Pipe 82
5.2.2 Spectrometers 86
5.3 Experimental Results 89
5.3.1 Harmonic Spectra 89
5.3.2 XFROG Measurement 105

6 Conclusions 136

Bibliography 138

List of Figures

1.1 ATI and HHG spectra. Panel (a): Progression of ATI peaks as the intensity is increased. The behavior is seen to become non-perturbative. The peaks are generated using Xe and a 135 ps Nd:YAG laser at 1.064 μm. In the lowest plot (6.8 mJ) $I \approx 5 \times 10^{12}$ W/cm^2. Reproduced from [18]. Panel (b): Harmonic peak strengths, H3-H33, generated in Ne using a 30 ps, Nd:YAG laser at 1.064 μm. $I \approx 3 \times 10^{13}$ W/cm^2. Reproduced from [19]. 3

1.2 ATI spectra for the noble gases, displaying the high energy plateau. For the He spectrum, $I \approx 3 \times 10^{14}$ W/cm^2. For all others, $I \approx 2 \times 10^{14}$ W/cm^2. Reproduced from [20]. 4

2.1 Depiction of tunnel ionization for a linearly polarized laser field. The potential, a combination of the atomic and laser potentials, is shown at three different times, t_1, t_2, and t_3, during the laser's oscillation. At the maxima of the laser field, at times t_1 and t_3, the potential barrier is reduced, allowing for tunnel ionization. 8

2.2 Keldysh parameter as an indication of tunnel ionization or multiphoton ionization. 9

2.3 Black curve: Electric field amplitude as a function of time for a laser pulse with a wavelength of 3.6 μm, pulse duration of 110 fs FWHM, and peak intensity of 2×10^{12} W/cm^2. Red curve: Ratio of ions to the total number of atoms as a function of time, derived from the ADK formula found in [19]. 10

2.4 Calculated classical trajectories for an electron in a laser field, for three different ionization times during the laser field's period: $\mathbf{t}_1$) Ionization occurs shortly before the peak of the field and the electron subsequently drifts away from the ion core, $\mathbf{t}_2$) Ionization occurs at the peak of the field and the electron revisits the ion core each cycle of the field, but with zero return velocity, $\mathbf{t}_3$) Ionization occurs shortly after the peak of the field and the electron returns to the ion core with a return velocity,v_r. . . . 16

2.5 Possible scenarios upon the electron's return to the core. Figure reproduced from [41]. 17
2.6 Photoelectron spectra at different driving laser field wavelengths, λ. All spectra were taken using argon and an intensity of 8×10^{13} W/cm^2. Solid line: $\lambda = 0.8$ μm ($\gamma = 1.3$), dot-dash: $\lambda = 1.3$ μm ($\gamma = 0.8$), dash: $\lambda = 2.0$ μm ($\gamma = 0.5$), dotted: $\lambda = 3.6$ μm ($\gamma = 0.3$), gray lines: TDSE calculations. Figure reproduced from [24]. 18
2.7 Electron return time versus return energy. 19
2.8 Measurement of the relative delay between harmonic orders, generated in neon using 0.8 μm light at $I \approx 3.8 \times 10^{14}$ W/cm^2. The blue points (with error bars) are measured values, the red points are predictions from the Simpleman rescattering model. The black line is the measured harmonic intensity. Figure reproduced from [44]. 20

3.1 Mid-infrared laser system. 22
3.2 Modeled pump fluence along the length of the ti:sapphire crystal. Black squares and red circles indicate the individual pump arms and the yellow triangles indicates the sum of the two. . . 29
3.3 Modeled energy buildup of the ti:sapphire pulse along the length of the crystal. Purple squares indicate pass 1, blue circles indicate pass 2, and orange triangles indicate pass 3. 30
3.4 Multipass amplifier layout for the mid-infrared (4 μm) laser system. 33
3.5 Multipass amplifier layout for the 2 μm laser system. 34
3.6 Ti:sapphire beam focusing configuration for the 4 μm and 2 μm amplifiers. Although lenses are shown in the figure, all focusing elements used for the ti:sapphire beam were mirrors. 35
3.7 Pump beam focusing configuration for the 4 μm and 2 μm amplifiers. 36
3.8 Measured profiles of the pump beam and ti:sapphire beam, at its first and second pass, at the gain crystal position for the 2 μm system's amplifier. The $1/e^2$ radius widths for the ti:sapphire beam, obtained from a Gaussian fit to the x and y lineouts, as well as the 2^{nd} moment widths for the pump beam are included. 39
3.9 Measured profiles of the pump beam and ti:sapphire beam, at its first and second pass, at the gain crystal position for the 4 μm system's amplifier. The $1/e^2$ radius widths for the ti:sapphire beam, obtained from a Gaussian fit to the x and y lineouts, as well as the 2^{nd} moment widths for the pump beam are included. 40

4.1 Schematic diagram of the time-of-flight spectrometer. The interaction region contains the laser (**L**) which passes through a CaF_2 input window (**IW**) and an output window (**OW**), as well as field plates (**P1**, **P2**, and **P3**). The flight tube is surrounded by mu-metal (**MM**) and a Faraday cage (**FC**) to keep it field free. The detector consists of a grounded grid (**G**), the multichannel plates (**MCP**) and collecting anode (**A**). 45
4.2 Field plate geometry. 46
4.3 Schematic diagram of multichannel plate detector. Voltages supplied to the front MCP plate, back MCP plate and anode for electron (ion) are shown. 48
4.4 Time-of-flight electronics. 49
4.5 Mass spectrum containing Cs^+ and small amounts of Rb^+. . . 52
4.6 ATI spectrum, 800 nm ionizing Xe. 55
4.7 Side view of the cesium oven on the vacuum chamber. 57
4.8 Vapor pressure curve for cesium. This curve uses coefficients from from Taylor and Lanqmuir [85] via Rozwadowski and Lipworth [86] and is valid for pressures less than 1 Torr. 58
4.9 Calculated mean free path for a gas of cesium atoms, assuming a Maxwell distribution. The shaded region highlights oven temperatures for which the mean free path is greater than the oven exit aperture radius (0.015 cm). In this region, the oven can be considered effusive. 59
4.10 Sketch of oven/collimator geometry (not to scale). 60
4.11 Calculated cesium density at the laser focus position. 61
4.12 Cesium Ion Yield Curve. 63
4.13 Cesium Photoelectron Spectra: (a): I = 4.02 TW/cm^2, U_p =4.86 eV (b): I = 1.92 TW/cm^2, U_p =2.32 eV (c): I = 1.80 TW/cm^2, U_p =2.18 eV (d): I = 1.65 TW/cm^2, U_p =2.00 eV (e): I = 1.60 TW/cm^2, U_p =1.93 eV (f): I = 1.57 TW/cm^2, U_p =1.90 eV. . 68
4.14 Cesium Photoelectron Spectra, scaled in units of U_p. (a): I = 4.02 TW/cm^2, U_p =4.86 eV (b): I = 1.92 TW/cm^2, U_p =2.32 eV (c): I = 1.80 TW/cm^2, U_p =2.18 eV (d): I = 1.65 TW/cm^2, U_p =2.00 eV (e): I = 1.60 TW/cm^2, U_p =1.93 eV (f): I = 1.57 TW/cm^2, U_p =1.90 eV. 69
4.15 Cesium Photoelectron Spectrum, linear scale. (a): I = 4.02 TW/cm^2, U_p =4.86 eV (b): I = 1.92 TW/cm^2, U_p =2.32 eV (c): I = 1.80 TW/cm^2, U_p =2.18 eV (d): I = 1.65 TW/cm^2, U_p =2.00 eV (e): I = 1.60 TW/cm^2, U_p =1.93 eV (f): I = 1.57 TW/cm^2, U_p =1.90 eV. 70

4.16 Examples of resonant structures in PES from noble gases and 0.8 μm light. On the left, argon. Reproduced from [90]. On the right, xenon. Reproduced from [77]. 71
4.17 Expected positions in PES of rescattered electrons produced from channel-closing resonances for the interaction between cesium and 3.6 μm light. 71
4.18 Cesium-3.6 μm PES at 1.65 TW/cm^2, plotted in units of photon energy (0.344 eV). The ATI peaks within the 8 eV resonant structure are shown to line up very well with photon number, as would be expected for a channel-closing resonance. 72
4.19 Cesium-3.6 μm PES at 1.65 TW/cm^2, plotted in eV. The energy ranges where 12, 13, and 15 photon channel-closing resonances should appear are indicated in grey. 73
4.20 Cesium Photoelectron Spectrum, low energy portion. (a): $I =$ 4.02 TW/cm^2, U_p =4.86 eV (b): $I =$ 1.92 TW/cm^2, U_p =2.32 eV (c): $I =$ 1.80 TW/cm^2, U_p =2.18 eV (d): $I =$ 1.65 TW/cm^2, U_p =2.00 eV (e): $I =$ 1.60 TW/cm^2, U_p =1.93 eV (f): $I =$ 1.57 TW/cm^2, U_p =1.90 eV. 74
4.21 Cesium Photoelectron Spectrum, low energy portion. (a): $I =$ 4.02 TW/cm^2, U_p =4.86 eV (b): $I =$ 1.92 TW/cm^2, U_p =2.32 eV (c): $I =$ 1.80 TW/cm^2, U_p =2.18 eV (d): $I =$ 1.65 TW/cm^2, U_p =2.00 eV (e): $I =$ 1.60 TW/cm^2, U_p =1.93 eV (f): $I =$ 1.57 TW/cm^2, U_p =1.90 eV. 75
4.22 Cesium-621 nm PES, exhibiting a double peak structure in the ATI peaks. Reproduced from [98]. 76

5.1 Comparison between the energies involved in the 0.8 μm-argon case and and 3.6 μm-cesium case. 79
5.2 Comparison of harmonic spectra from (a) 0.8 μm-argon and (b) 3.6 μm-cesium. 80
5.3 Schematic of heat pipe, cross-sectional view. 83
5.4 Internal, on-axis, heat pipe temperature versus heater voltage for several buffer gas pressures, (a), and versus position, (b). . 86
5.5 Energy per Counts/ms conversion factor for the Triax system with the ICCD gain set to 1.5. 89
5.6 Comparison of harmonic spectra taken with the 110 fs mid-infrared driving pulse (a) and the 2.5 ps mid-infrared driving pulse (b) [108]. 90

5.7 Same spectra as in Figure 5.6, but plotted on a logarithmic scale. (a): spectrum taken with the 110 fs mid-infrared driving pulse. (b): spectrum taken with the 2.5 ps mid-infrared driving pulse [108]. 91
5.8 Nitrogen purged harmonics. 93
5.9 Harmonic spectra versus focus position, 60 μm slit, 77 mW (iris open), $\omega_0 \approx 80$ μm, $I \approx 3.5 \times 10^{12}$ W/cm^2. 96
5.10 Harmonic spectra versus focus position, 2000 μm slit, 77 mW (iris open), $\omega_0 \approx 80$ μm, $I \approx 3.5 \times 10^{12}$ W/cm^2. 97
5.11 Harmonic spectra versus focus position, 2000 μm slit, 67 mW with iris closed to 15.25 mm, $\omega_0 \approx 109$ μm, $I \approx 1.6 \times 10^{12}$ W/cm^2. 98
5.12 Harmonic spectra versus focus position, 2000 μm slit, 67 mW with iris closed to 15.25 mm, $\omega_0 \approx 109$ μm, $I \approx 1.6 \times 10^{12}$ W/cm^2. 99
5.13 Harmonic spectra versus focus position, 2000 μm slit, 67 mW with iris closed to 15.25 mm, $\omega_0 \approx 109$ μm, $I \approx 1.6 \times 10^{12}$ W/cm^2. 100
5.14 Harmonic spectra versus focus position, 2000 μm slit, 67 mW with iris closed to 15.25 mm, $\omega_0 \approx 109$ μm, $I \approx 1.6 \times 10^{12}$ W/cm^2. 101
5.15 Harmonic yield versus laser intensity, 2000 μm slit, iris open, $\omega_0 \approx 80$ μm, 58 Torr, laser focus 10 mm after cesium column center. 102
5.16 Harmonic yield versus laser intensity, 2000 μm slit, iris open, $\omega_0 \approx 80$ μm, 58 Torr, laser focus 10 mm after cesium column center. 103
5.17 Harmonic yield versus laser intensity, 2000 μm slit, iris open, $\omega_0 \approx 80$ μm, 58 Torr, laser focus 10 mm after cesium column center. 104
5.18 Harmonic yield versus laser intensity, 2000 μm slit, iris open, $\omega_0 \approx 80$ μm, 58 Torr, laser focus 10 mm after cesium column center. 105
5.19 Autocorrelation measurement based on second harmonic generation (SHG). 106
5.20 Schematic diagram of a cross-corrleation FROG measurement (XFROG) based on sum-frequency generation (SFG). 109
5.21 Depiction of the generalized projections algorithm as applied to SHG FROG. Figure reproduced from Rick Trebino's website[136]. 110
5.22 Preliminary XFROG trace depicting the group delay separation between the harmonic orders, due primarily to the dispersion of the LiF heat pipe output window. 115
5.23 XFROG experimental layout 117

5.24 XFROG raw data. The intensity scale is in a log scale. Top row: 2 mm + 3 mm LiF window, Middle row: 3 mm LiF window, Bottom row: 2 mm LiF window. 122
5.25 Experimental and Retrieved XFROG Traces, 3 mm LiF window. 124
5.26 Experimental and Retrieved XFROG Traces, 2 mm+3 mm LiF window. 125
5.27 Experimental and Retrieved XFROG Traces, 2 mm LiF window. 126
5.28 Retrieved Second Harmonic. Panel (a): spectral power and phase, $\omega_0 = 1.0558 \pm 0.0001$ rad/fs, $\delta\omega = 0.0248 \pm 0.0001$ rad/fs. Panel (b): time-domain intensity profile, recovered (solid blue), transform limit (dashed black) $\tau = 125.84 \pm 0.92$ fs, $\tau_{TL} = 92.22$ fs. Error bars are represented by the shaded regions. 127
5.29 Retrieved results for H5 through H13. Left column: spectral power (solid blue), phase (dash-dot green), recovered 2mm LiF phase contribution (dotted yellow), phase with LiF contribution removed (dashed red). Right column: time-domain intensity profile (solid blue), transform-limited profile (dashed black). Error bars are represented by the shaded regions. (a) & (b): H5, (c) & (d): H7, (e) & (f): H9, (g) & (h): H11, (i) & (j): H13. . 128
5.30 Retrieved Group Delay values, relative to H5 for the three LiF output window cases. 130
5.31 Group delay between harmonic orders with the contribution from the LiF output window removed. 131
5.32 Total spectral power and phase for harmonics H5-H13. 132
5.33 Time-domain intensity profile, including H5-H13 (solid blue). Transform limit (dashed red). The FWHM duration of the most intense burst is $\tau = 4.39$ fs, with a transform limited value of $\tau = 1.52$ fs. 133
5.34 Time-domain intensity profile, without H5, including H7-H13 (solid blue). Transform limit (dashed red). The FWHM duration of the most intense burst is $\tau = 2.03$ fs, with a transform limited value of $\tau = 1.68$ fs. 134
5.35 Depiction of the long and short trajectory return times. The lines drawn tangent to the electric field indicate the times during the field's period that recombination may occur. For the short trajectories, t_r^{short}, the return occurs when the field is small. For the long trajectories, t_r^{long}, the return occurs when the field is large. 135

List of Tables

1.1 The highest harmonics observed, as of March 2009. 5
1.2 The shortest attosecond pulses created, as of March 2009. . . . 5

2.1 Calculated values for γ for the noble gases ionized by 0.8 μm light at the saturation intensity. The parameters for the work presented here is included for comparison. 15

3.1 Nonlinear crystals suitable for DFG of 3.6 μm light ($\hbar\omega_{0.815} = \hbar\omega_{1.053} + \hbar\omega_{3.6}$). 23
3.2 Gain model predictions. The amplification process is considered to be lossless. Input values: 10 J pump energy for each pump arm, 1.5 mJ ti:sapphire energy, pump and ti:sapphire spot sizes are $\omega_0 = 250$ μm ($1/e^2$ radius). 31
3.3 Output energy and efficiency for the 4 μm and 2 μm amplifiers. The predicted values from the gain model are included for comparison. 38

5.1 Comparison of γ and other parameters for the 3.6 μm-cesium system and those from significant HHG ti:sapphire-noble gas experiments. The over-the-barrier intensity for each atom is given as a reference. 78
5.2 Comparison of energy yields for harmonics generated from a 2.5 ps mid-infrared pulse and a 110 fs mid-infrared pulse. 92
5.3 Set of Type II BBO XFROG crystals and their properties. . . 113
5.4 Retrieved parameters for individual harmonics. 129

Acknowledgements

I have been very fortunate to have had the opportunity to spend time at three different places while doing my Ph.D. work, Stony Brook University, Brookhaven National Lab, and Ohio State University. At each of these places I have met many people who have generously helped me in my work and from whom I have learned a great deal. First and foremost I would like to thank my advisor, Prof. Lou DiMauro, for giving me the opportunity to work in his group and to take part in some very interesting and challenging experimental physics. I have been very fortunate being in the same group as Prof. Pierre Agostini and I have learned a great amount from him. I wish to thank Prof. Peter Koch, for the opportunity to work in his lab during my early graduate school years, for his instruction and guidance, and for serving on my committee. Thanks to Prof. Konstantin Likharev and Prof. Mike White for also serving on my committee.

I greatly enjoyed collaborating with Dr. Erik Power on the XFROG experiment. His ingenuity and determination were admirable and critical to the success of this very difficult experiment. I thank Emily Sistrunk for her help with the XFROG experiment, as well as with the characterization of the heat pipe. I am grateful for Dr. Anthony DiChiara's help in getting the photoelectron spectrometer to work and in data collection of the cesium photoelectron spectra.

I enjoyed several years working along side Dr. Phil Colosimo, building up the 3.6 μm laser system. Phil is very skilled in repairing equipment and making things work and I learned a tremendous amount from him. Dr. Kevin Schultz, Dr. Jennifer Tate, and Dr. Ilya Lachko were very generous sharing their time and expertise. Cosmin Blaga provided much advice and help getting the photoelectron spectrometer working, as well as the alkali oven. I am grateful to all the members of the DiMauro group who have made working in this group so enjoyable, namely Chris Roedig, Jonathan Wheeler, Razvan Chirla, Dr. Fabrice Catoire, Stephen Schoun, Dr. Juana Rudati, Dr. Jan Chaloupka, Dr. Pierre-Marie Paul, Dr. Todd Clatterbuck, and Dr. Claire Lynga.

This work would not have been possible without the support of the techni-

cal staff at Brookhaven National Laboratory Chemistry Department and The Ohio State University Physics Department. In addition, I thank Beth Deinlein for her hard work keeping our group organized and running. Pat Peiliker has been very generous with her time, advice, and encouraging words.

I am tremendously grateful for the support of my family. My mother, Gail March, and my father, Dr. Edward March, have provided encouragement and opportunities throughout my life that I am extremely grateful for. My father introduced me to science when I was very young, encouraged me to excel in mathematics, and was vigilant watching for signs of self-doubt and quickly countered these with encouraging words. I believe it is because of this that I have had the opportunity to follow the path of scientific research and I feel very fortunate for this. My sisters, Christina and Allison, and brother-in-law, Chip, have provided much needed support.

Lastly, I would like to thank those who have been closest to me over these years, Dr. Doug Bennett, Dr. Patrick Truitt, and Dr. Gilles Doumy. Without their encouragement and support I would not have been successful in this endeavor. I am incredibly fortunate to have them as friends.

Chapter 1

Introduction

1.1 The Strong-Field Regime of Intense Laser-Atom Studies

Experimental explorations of the interaction between a strong light field and atoms began shortly after the invention of the laser. Since that time, developments in our understanding of the fundamental physics underlying this interaction have been closely tied to developments in laser technology. The first lasers [1] [2] provided the field strengths necessary to finally observe multiphoton absorption in the optical regime, first in an europium doped calcium fluoride crystal [3], and then in a cesium vapor [4], which had been theoretically predicted by Maria Göppert-Mayer 30 years before [5]. Shortly thereafter, the invention of the Q-switched laser [6] boosted attainable intensities to $\sim 10^{13}$ W/cm^2 by creating pulsed laser radiation with durations $\sim$ 100 nanoseconds. By condensing the laser energy to a short time interval, the field strengths at the peak of the pulse were much higher than those available with CW laser radiation. This technology enabled the observation of multiphoton ionization (MPI), where photoionization occurs by means of the simultaneous absorption of several photons [7] [8], as well as harmonic generation in gases [9]. Subsequent studies of these processes flourished and expanded as new laser sources and higher laser intensities became available.

An understanding of multiphoton ionization developed based primarily on measurements of ion yield curves [10]. In this context, resonant MPI, where m photons of the N photon ionization process are resonant with a bound state of the atom, as well as nonresonant MPI, were modeled successfully using perturbative methods that assumed that the laser field strength was small compared to the field binding the electrons to the nucleus [10]. At the same time, motivated by its potential to be a source of short wavelength coherent light, harmonic generation studies were being carried out. While early studies focused on maximizing the efficiency of the generation of the lowest harmonic order, the third harmonic (H3) [9] [11], later studies demonstrated generation of higher orders. The fifth harmonic (H5) and the seventh harmonic (H7) were demonstrated using a 266 nm frequency-quadrupled Nd:YAG laser with a 30 ps pulse duration and the noble gases [12]. The ninth harmonic (H9) of a picosecond Nd:glass laser was generated in a sodium vapor [13]. The eleventh harmonic (H11) of a 750 ps iodine laser, at 1.315 μm was observed using noble gases [14]. Like the multiphoton ionization studies of the time, these results were interpreted within the context of perturbation theory. The harmonic response was understood as an expansion of the atomic polarizability in terms of the electric field, where the coefficients, $\chi^{(i)}$, indicated the strength of the nonlinear response for harmonic i.

The development of high power, picosecond solid state lasers, based on neodymium doped materials, such as Nd:YAG and Nd:YLF, enabled the observation of two new phenomena that indicated that intense laser-atom studies had entered a new regime. When attention was turned from measuring ion yields to measuring photoelectron energy spectra, above threshold ionization (ATI) was discovered [15]. ATI is a process where more photons are absorbed during ionization than are necessary to overcome the binding energy of the field-free atom. The excess energy is carried off by the freed electrons, making the signature of ATI a series of peaks in the photoelectron energy spectrum that are spaced by one photon energy. When attention turned to looking at the light generated during this intense laser-atom interaction, high harmonic generation (HHG), the production of very high order harmonics of the fundamental driving field's frequency, was discovered [16] [17]. Both of these phenomena were found to exhibit features that indicated the interaction was highly nonlinear and non-perturbative. Figure 1.1 shows examples of ATI and HHG spectra from some of the first experiments. Panel (a) shows a series of ATI spectra at different laser intensities. In the top spectrum, at the lowest intensity, with each increasingly higher order peak the relative height decreases, as would be predicted by a model incorporating perturbation theory since in perturbation theory the contributions from higher order terms decreases with order. However, as is seen in the other ATI spectra, with increasing intensity, higher order peak heights become comparable to or higher than the lower order peaks. This is indicative of a highly nonlinear process, where perturbation theory may no longer be helpful in capturing the dynamics. In panel (b), a harmonic spectrum, containing harmonics 3 (H3) through 33 (H33) is shown. The previous record for highest observed harmonic order had been the eleventh harmonic mentioned above [14], and H33 is dramatically higher.

More importantly, though, is the fact that while the lower harmonic orders, including H3 and H5, drop off with increasing order, H7 and above have comparable heights. This plateau is a feature distinctively different from that of previous harmonic generation experiments. The plateau in the HHG spectrum also indicates that the process underlying the generation is highly non-linear and not described well by perturbation theory. Further investigation of ATI

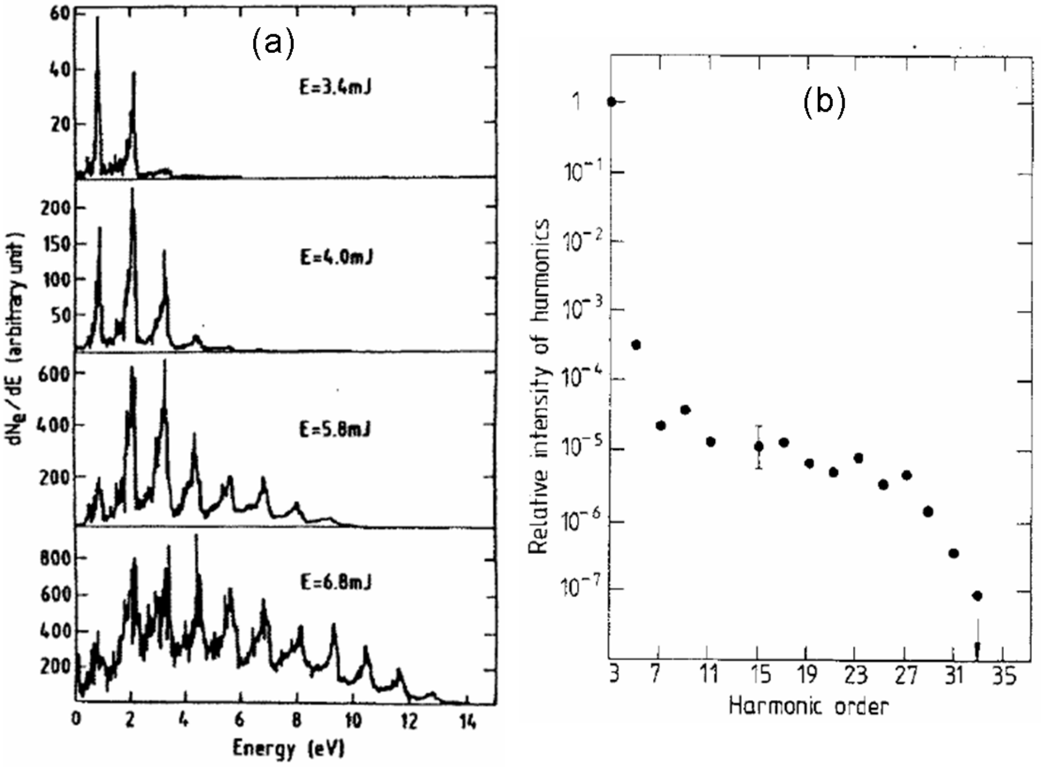

Figure 1.1: ATI and HHG spectra. Panel (a): Progression of ATI peaks as the intensity is increased. The behavior is seen to become non-perturbative. The peaks are generated using Xe and a 135 ps Nd:YAG laser at 1.064 μm. In the lowest plot (6.8 mJ) $I \approx 5 \times 10^{12}$ W/cm^2. Reproduced from [18]. Panel (b): Harmonic peak strengths, H3-H33, generated in Ne using a 30 ps, Nd:YAG laser at 1.064 μm. $I \approx 3 \times 10^{13}$ W/cm^2. Reproduced from [19].

found the order of the process (i.e. number of ATI peaks) could be dramatically extended. Using a high repetition rate, femtosecond laser, a high energy plateau in the ATI spectrum was discovered [20]. Figure 1.2 shows high energy ATI spectra for the noble gas atoms that exhibit the plateau structure. This plateau has played a large role in developing our understanding of the mechanisms involved in ATI and HHG and is a characteristic feature of light-atom interactions within this regime.

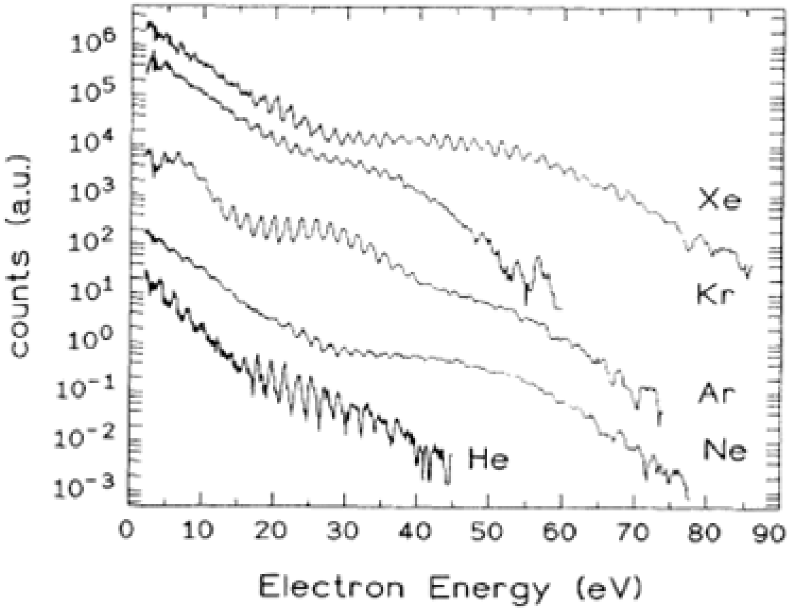

Figure 1.2: ATI spectra for the noble gases, displaying the high energy plateau. For the He spectrum, $I \approx 3 \times 10^{14}$ W/cm^2. For all others, $I \approx 2 \times 10^{14}$ W/cm^2. Reproduced from [20].

Further exploration of HHG found that the order of the process could also be dramatically increased. It became clear that HHG showed great promise as a source of extreme ultraviolet (xuv) and even soft x-ray coherent radiation. In addition, due to the fact that a large bandwidth, at high frequencies, was being produced, it was seen as a possible means of generating light pulses that were unprecedentedly short, on the order of attoseconds (1 as = 10^{-18} s) in duration. The question was whether the phase relationship between the harmonic orders was amenable to such a task, and in 2001 the first measurement of the relative phase between several harmonic orders [21] indicated that the answer was yes. Today, HHG is the only method by which attosecond pulse creation has been demonstrated. Tables 1.1 and 1.2 lists some of the HHG "records" that are standing today.

The regime in which high order ATI and HHG are observed is one where the strength of the laser field is comparable to the strength of the Coulomb

---

[1] Here, a few cycle driving pulse was used, so the harmonic spectrum is continuous and individual harmonic orders are not present. H580 corresponds to the harmonic order that would be at an energy of 1 keV.

Highest Harmonic Observed		
Order	**Laser wavelength, Gas**	**Group**
H155	0.8 μm, Ne	Murnane/Kapteyn [22]
H221	0.8 μm, He	Murnane/Kapteyn [22]
1 keV ($\sim$ H580)[1]	0.72 μm, He	Krausz [23]
H355	2 μm, Ar	DiMauro [24]

Table 1.1: The highest harmonics observed, as of March 2009.

Shortest Attosecond Pulse Created		
Duration	**Laser wavelength, Gas**	**Group**
170 as, train	0.8 μm, Ar	L'Huillier [25]
130 as, train	0.8 μm, Ar	L'Huillier [26]
80 as, isolated	0.72 μm, Ne	Krausz [27]
130 as, isolated	0.75 μm, Ar	Nisoli [28]

Table 1.2: The shortest attosecond pulses created, as of March 2009.

field binding the electrons to the nucleus. It is now commonly referred to as the strong-field regime[2], and it is the regime in which the studies presented in this dissertation are argued to take place. Most of the work that has been done exploring this regime has used neodymium based lasers, which have a center wavelength of 1 μm, or titanium:sapphire based lasers, which have a center wavelength of 0.8 μm, and at these wavelengths, the intensities[3] required to reach the strong-field regime are approximately 10^{14}-10^{15} W/cm^2. Interactions involving intensities below this typically have been in the perturbative regime. Intensities higher than this are easily achievable with today's lasers, and studies of laser-atom interactions at these intensities constitute a very interesting branch where the electrons' motion becomes relativistic and effects due to not just the electric field of the laser, but also the magnetic field become important. At these intensities, however, ATI peaks begin to wash out due to the ionization of multiple electrons and HHG becomes complicated by high intensity macroscopic effects, i.e. propagation, in the gaseous medium [31].

While much work has been done exploring the intensity dependence of ATI and HHG [32] [33], the exploration of the wavelength dependence has

---

[2] Optical studies (i.e. wavelengths in the visible or IR) are not the first to explore this regime of atomic physics. Much work has been done using microwave fields and atoms in highly excited Rydberg states [29, 30].

[3] $I = \frac{1}{2}\epsilon_0 c E^2$ where ϵ_0 is the permittivity of free space and c is the speed of light. When I is expressed in W/cm^2 and E is in V/cm, $I = 1.33 \times 10^{-3} E^2$ or $E = 27.4 I^{1/2}$

been limited due to the small number of intense, short-pulse sources available. This wavelength limitation has imposed an additional constraint on the types of atoms that have been studied in this regime. Of critical importance to the observation of high order ATI and HHG is that the ground state population of the atomic sample not become depleted on the rising edge of the pulse. Otherwise, it will not experience the high intensity at the peak of the pulse. With 0.8 μm and 1 μm light, multiphoton ionization will rapidly deplete the ground state, except in those atoms with the highest of ionization potentials, the noble gases. Therefore, the work studying high order ATI and HHG has primarily been limited to the noble gases. This is evident in Tables 1.1 and 1.2, where all of the work presented is done with titanium:sapphire lasers and the noble gases.

This dissertation presents studies of the weakly-bound cesium atom in the strong-field regime that have been made possible by the development of intense, short pulse lasers in the mid-infrared. Our intense, 100 fs laser, centered at a wavelength of 3.6 μm was used to study ATI and HHG in a cesium vapor. Photoelectron energy spectra have been measured as well as spectra of the harmonic radiation. In addition, using a frequency-resolved optical-gating (FROG) technique, the electric field of harmonic orders H5-H13 was completely characterized allowing for a reconstruction of the full temporal profile for these orders.

This dissertation begins with a brief introduction, in Chapter 2, to the fundamental concepts that have developed to understand the physical mechanisms underlying the strong-field interaction. The mid-infrared laser system is described in Chapter 3. The photoelectron experiments are described in Chapter 4. The harmonics experiments, including the FROG measurement, are described in Chapter 5. Chapter 6 includes conclusions and suggestions for future work.

Chapter 2

Strong-Field Models

While sophisticated theoretical models of the strong field interaction between an atom and laser have been developed, much of the fundamental understanding of the physical mechanisms involved are derived from two simple models: the Simpleman's model and Keldysh tunneling. In this chapter I present the basic ideas behind these models and describe HHG and features of strong-field photoelectron spectra within their context.

2.1 Keldysh Tunneling Ionization

In 1965 [34], Keldysh presented a treatment of the interaction between a strong oscillating electromagnetic field (such as a laser) and an atom that was based not on the absorption of many photons, but on dc tunneling. In this picture, represented in Figure 2.1, the field is seen to severely distort the atomic potential. During a moment within each half cycle of the field, when the electric field is at or near its maximum value, the potential barrier, formed by the combination of atomic and electric field potentials, is suppressed and this creates some non-negligible probability for the bound electron to tunnel through the barrier and become free. An assumption is made that the tunnel ionization takes place quickly, during a small fraction of the laser's half cycle. If this is true, the field can be treated as being quasi-static, and a dc tunneling rate can be applied for each moment during the laser pulse. The applicability of this condition is contained in a parameter presented by Keldysh called the adiabaticity parameter (now often referred to as the Keldysh parameter):

$$\gamma = \frac{\omega}{\omega_t} = \frac{\omega\sqrt{2m_e I_p}}{e\,|E_L|}. \tag{2.1}$$

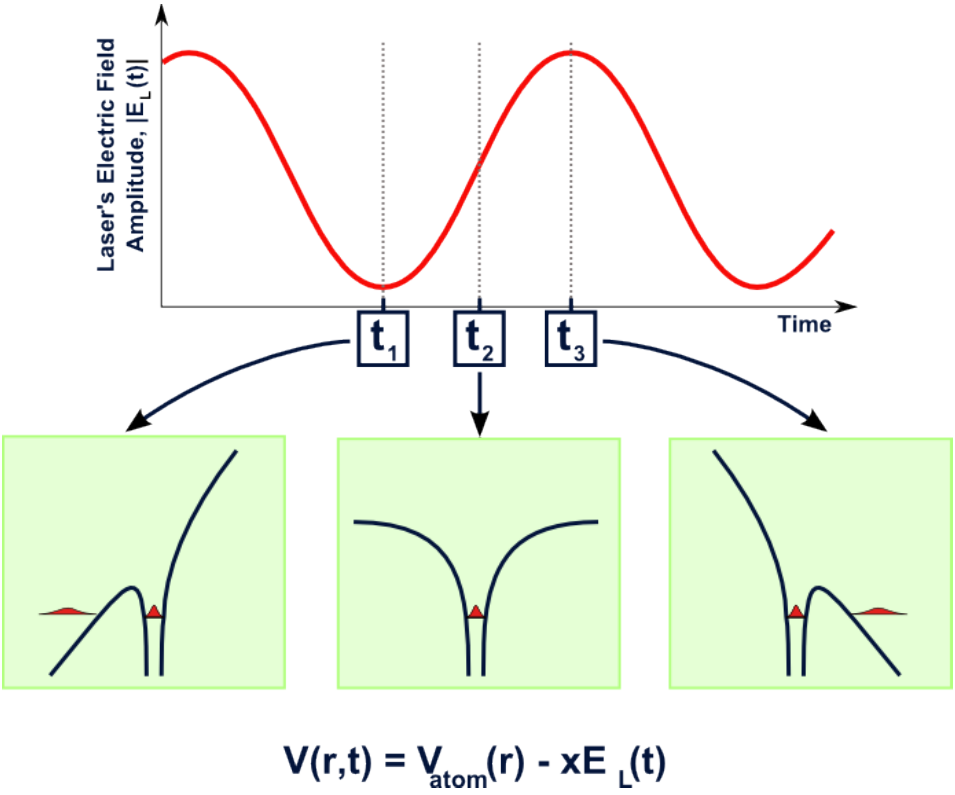

Figure 2.1: Depiction of tunnel ionization for a linearly polarized laser field. The potential, a combination of the atomic and laser potentials, is shown at three different times, t_1, t_2, and t_3, during the laser's oscillation. At the maxima of the laser field, at times t_1 and t_3, the potential barrier is reduced, allowing for tunnel ionization.

It is the ratio between the field frequency, ω, and the tunneling frequency, $\omega_t = \frac{2\pi}{t_t}$. Here $|E_L|$ is the laser field amplitude, I_p is the field-free ionization potential, e is the electron charge, and m_e is the electron mass. The tunneling time, t_t, is estimated to be the time required for the electron to acquire enough kinetic energy from the field to escape an energy barrier of height I_p. In a rough estimation[1] we can set $\frac{m_e v^2}{2} = I_p$ and take $v = at_t$, where a is the acceleration due to the peak field, $a = \frac{e}{m_e}|E_L|$. The tunneling time can then be seen to be given by

$$t_t \cong \frac{\sqrt{2m_e I_p}}{e\,|E_L|}. \tag{2.2}$$

---

[1] In actuality, the kinetic energy under the barrier is negative, which means that either the velocity or the time is imaginary. The rough calculation presented here disregards this important point, but has been commonly used to make an estimate of the tunneling time.

As will be seen in the next section, the cycle averaged kinetic energy of the freed electron in the laser field, known as the ponderomotive energy and denoted U_p, is a useful quantity in the strong-field regime[2]. It is given by

$$U_p = \frac{e^2 E_L^2}{4 m_e \omega_L^2}. \tag{2.3}$$

The Keldysh parameter is often expressed in terms of U_p as

$$\gamma = \sqrt{\frac{I_p}{2U_p}}. \tag{2.4}$$

If the tunneling frequency is large relative to the optical frequency ($\gamma << 1$) then the assumptions for tunnel ionization are valid. If the tunneling frequency is small relative to the optical frequency ($\gamma >> 1$) then the assumptions are not valid and a picture involving multiphoton absorption is more applicable. These two limits are illustrated in Figure 2.2.

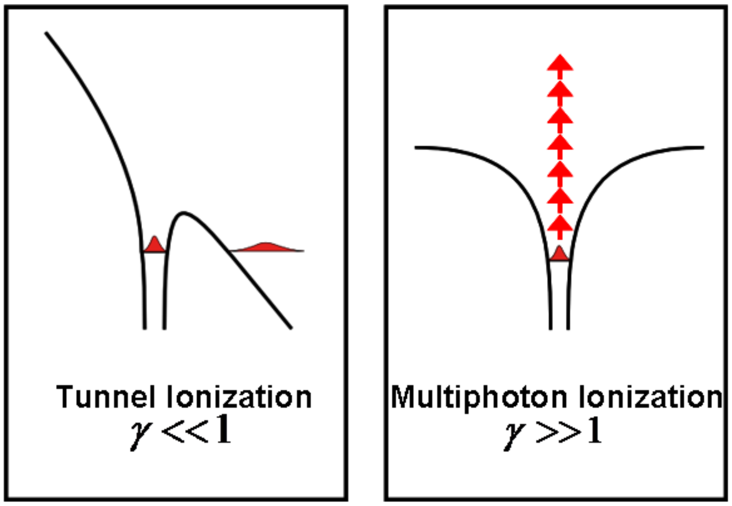

Figure 2.2: Keldysh parameter as an indication of tunnel ionization or multiphoton ionization.

---

[2] In useful units this is: $U_p = 9.33 \times 10^{-14} I\lambda^2$ where U_p is in eV, I is in W/cm^2, and λ is in μm.

The expression for the tunnel ionization rate for hydrogen was developed by Perelomov, Popov, and Terent'ev [35]. Ammosov, Delone, and Krainov extended it to complex atoms (ADK rate) [36]. The ADK formula[3] can be found in [19] and [38]. Figure 2.3 shows the electric field amplitude as a function of time for a laser pulse with parameters that are similar to those of the pulses used in the experiments presented here. In red, the ionization fraction (ratio of ions to total number of atoms) created by the laser field is plotted as a function of time. This curve has been derived using the ADK formula. It can be seen that there is a steep increase in ion production each half cycle of the laser field, during the times when the electric field nears

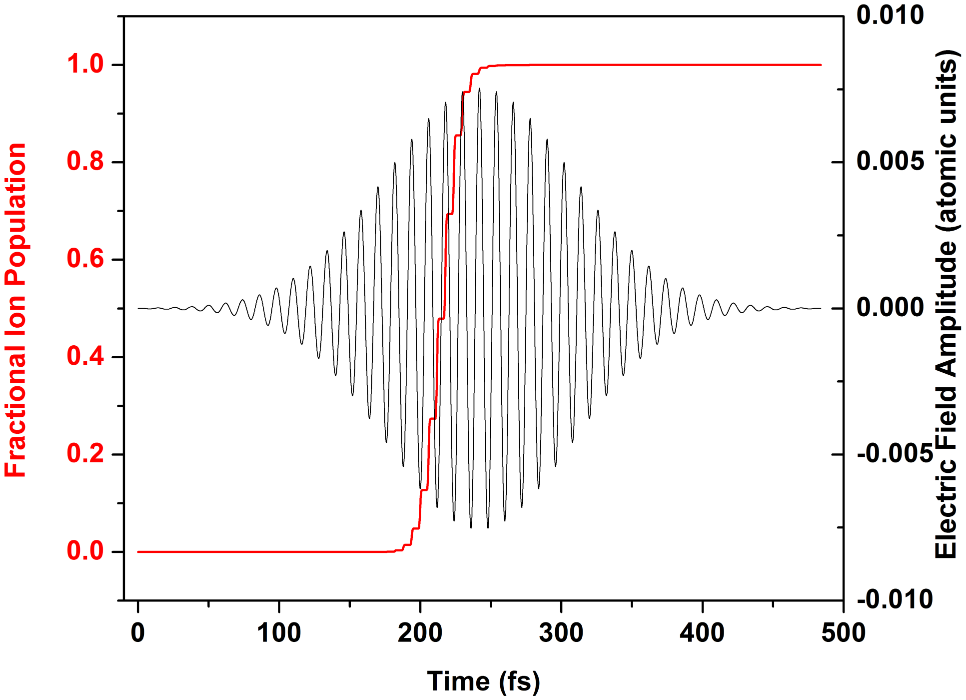

Figure 2.3: Black curve: Electric field amplitude as a function of time for a laser pulse with a wavelength of 3.6 μm, pulse duration of 110 fs FWHM, and peak intensity of 2×10^{12} W/cm^2. Red curve: Ratio of ions to the total number of atoms as a function of time, derived from the ADK formula found in [19].

---

[3] In the case of the strong field interaction of hydrogen Rydberg atoms with microwave fields, the ADK treatment has been shown to be inaccurate [37]. For ground state, or low n, atoms like those used in this work, however, it is a reasonable approximation.

and then reaches its maximum value. Also, it is apparent that this laser pulse saturates the atomic sample. Shortly after the time the laser pulse has reached its peak value, the ionization fraction reaches 1.

Once tunnel ionization has taken place, the electron is assumed to be under the influence of the laser field only. Effects from the Coulomb potential are neglected and the continuum states are treated as Volkov states, the wave functions for a free electron in a classical sinusoidal electric field. (This approximation is known as the strong-field approximation, or the SFA).

More sophisticated formulation of tunneling ionization, using many body S-matrix theory is reviewed in [39].

2.2 Simpleman's Model and Rescattering

In the Simpleman's model [38, 40], after ionization the freed electron is treated classically as a charged particle in an oscillating field. It is assumed that the electron is born into the field with zero initial velocity, $v_0 = 0$, at a time, t_0. It is also assumed that its initial position at the outer side of the potential barrier, x_0, is small compared the distance the electron will travel and so can be treated as $x_0 \approx 0$. The electron's subsequent motion in the field can be solved using classical equations of motion. The effect of the atomic potential during the electron's motion in the field is assumed to be small and is neglected.

Taking the laser field as $E_L = E_0 \cos(\omega t)$ (linearly polarized in the x direction) and the force on the electron to be $eE_L(t)$,

$$\ddot{x} = \frac{eE_0}{m_e} \cos(\omega t) \tag{2.5}$$

$$\dot{x} = v = \frac{eE_0}{m_e \omega} \sin(\omega t) + v_0 \tag{2.6}$$

$$x = -\frac{eE_0}{m_e \omega^2} \cos(\omega t) + v_0 t + x_0 \tag{2.7}$$

Incorporating the assumptions $v_0 = x_0 = 0$, for the electron ionized at time t_0, its velocity and displacement are

$$v = \frac{eE_0}{m_e \omega} \left\{ \sin(\omega t) - \sin(\omega t_0) \right\} \tag{2.8}$$

$$x = -\frac{eE_0}{m_e \omega^2} \left\{ \cos(\omega t) + \omega t \sin(\omega t_0) - \cos(\omega t_0) - \omega t_0 \sin(\omega t_0) \right\}. \tag{2.9}$$

Figure 2.4 shows the electron displacements, or trajectories, for several different ionization times, t_0. It can be seen that shortly after ionization, the electron is swept a fairly large distance away from the core. As the laser field changes sign, the electron slows, turns around and is accelerated in the other direction. For those electrons ionized during the quarter-cycle before the peak of the field, their trajectories cause them to wiggle in the laser field and ultimately drift away from the ion, perhaps to a detector. For those electrons ionized during the quarter-cycle after the peak of the laser field[4], their trajectories take them to revisit the core $x(t = t_r) = 0$ at a return time t_r. Here there are several different scenarios that can take place. Figure 2.5 shows the possibilities. The first (i) is that the electron can elastically backscatter off the core and then gain more energy from the laser field. This is the mechanism by which the high energy electrons in the plateau of the photoelectron energy spectrum are created. The second possibility (ii) is that the electron recombines with the core and radiation is emitted, with an energy equal to that gained by the electron from the field (its return kinetic energy) plus the energy of I_p. This is the mechanism for HHG. The third possibility (iii) is that the collision is inelastic and the electron can free another electron, a process known as non-sequential double ionization. The inelastic collision can also lead to excitation of the bound electrons, which is depicted as possibility (iv). In our particular case (the interaction between cesium atoms and 3.6 μm light), possibilities (iii) and (iv) are not likely to occur with great probability since the energies involved in the interaction, such as the photon energy and U_p, are small relative to the energy required to ionize a second electron from the core, or promote it to an excited state ($\mathrm{I}_p^{Cs^+} \approx 25$ eV, $E^*_{Cs^+} \approx 13$ eV, $h\nu \approx 0.34$ eV, $U_p \approx 3$ eV).

This point leads to a short aside. An assumption often made in modeling the strong-field interaction is that the process involves only one electron. The other electrons are present only by their effect of screening the nucleus and creating an effective nuclear potential. This approximation is called the single active electron (SAE) approximation and it has been shown to work well to describe strong field interactions with noble gas atoms [41]. The only true neutral single electron atom is of course hydrogen, but given that the alkalis have only one electron in the valence shell, they can be seen as the next best thing in terms of this approximation. Discussion of conditions where the SAE begins to breakdown can be found in [41].

The Simpleman's rescattering model has power in not just explaining HHG

---

[4] In the tunnel ionization treatment, given that the ionization rate will be dramatically higher for larger field strengths, most of the electrons are ionized at times near the peak of the field. See Figure 2.3.

and high energy photoelectron production qualitatively, but also quantitatively (at least for some properties). We consider first the predicted energies for photoelectron spectra. Solving the classical equations to find the maximum possible kinetic energy an electron can have if it does not return to the core, but rather drifts away toward the detector, one finds that $KE_{max}^{direct} = 2U_p$ [42]. Taking into account the time dependence of the ionization rates, it becomes clear that most of the electrons that would be ionized will have a kinetic energy at the detector $\leq 2U_p$. Then if we consider the maximum kinetic energy an electron can gain elastically rescattering off the core, we find the classical model predicts $KE_{max}^{rescattered} = 10U_p$ [42]. The number of electrons in the plateau region depends upon the rescattering cross section. These predictions agree well with experimental observation. Figure 2.6 shows photoelectron spectra from argon exposed to an intensity of 8×10^{13} W/cm^2 at four different driving laser field wavelengths. The value for γ for these four cases ranges from 1.3 to 0.3 and it is clear that for those spectra with values of γ that put the interaction deeper within the tunneling regime, there is a clear break in the slope at $2U_p$ and the photoelectrons continue to be present at higher energies until a cutoff at $10U_p$.

Experimental studies of HHG had found an empirical "cutoff" law, where the highest harmonic photon energy was given by $\approx I_p + 3U_p$ [43]. Solving the classical equations to find the maximum possible kinetic energy an electron can have at its return to the core, one finds $KE_{max} = 3.17U_p$, in excellent agreement with observations. Electrons ionized at a moment during the laser's period, such that $\omega t_0 = 17°$, are the ones that gain this maximum kinetic energy. Electrons born at other times within one half of the laser's period either don't recollide, or recollide with less energy. This behavior is often depicted in the plot shown in Figure 2.7. Here the electron's return time, t_r, is plotted on the vertical axis and its return energy is plotted on the horizontal axis. It can be seen that there are two different return times for each return energy. This is due to the fact that there are two different trajectories an electron can have to gain a particular amount of energy from the field. Since one of these trajectories is longer than the other, the respective paths have become known as the short and long trajectories. One way to think about the situation is to consider that there are two electron trajectories that produce a given harmonic order. The slope of the lines in Figure 2.7 then have implications for the relative delay between the harmonic orders. For the short trajectory harmonics, the lower energy harmonics ("redder" harmonics) are generated before the higher energy harmonics ("bluer" harmonics) and for the long trajectory harmonics, it is the opposite. The higher energy harmonics ("bluer" harmonics) are generated first. Considering the harmonic spectrum in the time domain, it can be seen as a short, sub-half cycle (of the driving field) pulse. For the short trajectory harmonic spectrum, the pulse is positively chirped (red leads blue). For the long trajectory harmonic spectrum, the pulse is negatively chirped (blue leads red). Actually, the harmonic spectrum is a mixture of the two, but to generate attosecond pulses, experimental tricks have been developed to remove the contributions from the long trajectory. Experimental confirmation of this picture is shown in Figure 2.8 and discussion of its importance for attosecond pulse creation is found in [44] and [25].

The Simpleman's rescattering model has been incorporated into quantum mechanical models [45–48]. These models formulate the problem in terms of Feynman's path integrals and the classical electron trajectories become "quantum orbits". These models are more complete as they allow for interference and effects such as the spreading of the electron wavepacket as it travels in the laser field. Thinking of the interaction in terms of more quantum mechanical ideas rather than classical, the recombination step in HHG can be thought of as the interference between the continuum electron wavepacket and the portion that remained in the ground state of the atom. Also, ATI peaks can be thought of as interference between electron wavepackets that are produced each half cycle of the laser period.

2.3 Keldysh-Scaled Atom-Laser System

It is interesting to consider the work presented in this dissertation in terms of the Keldysh parameter γ. If we take our laser wavelength, 3.6 μm, and cesium's saturation intensity of 2×10^{12} W/cm^2, as well as cesium's ionization potential, I_p=3.89 eV, we find that $\gamma = 0.9$. If we consider the noble gas atoms interacting with titanium:sapphire light at 0.8 μm and at intensities equal to the saturation intensities, we see that γ takes on values that are very close to 0.9. Table 2.1 summarizes the results. This means that within this picture of Keldysh tunnel ionization, the interaction between cesium and intense 3.6 μm light should be very similar to the interaction between the noble gases and intense 0.8 μm light. Part of the motivation for this work was to test this idea of Keldysh scaling.

Atom	λ_{laser} [μm]	I_{sat} [W/cm^2]	I_p [eV]	U_p [eV]	γ
Xe	0.8	9×10^{13}	12.13	5.37	1.06
Kr	0.8	15×10^{13}	14.00	8.96	0.88
Ar	0.8	25×10^{13}	15.76	14.93	0.73
Ne	0.8	60×10^{13}	21.56	35.83	0.55
He	0.8	80×10^{13}	24.59	47.77	0.51
Cs	3.6	2×10^{12}	3.89	2.42	0.90

Table 2.1: Calculated values for γ for the noble gases ionized by 0.8 μm light at the saturation intensity. The parameters for the work presented here is included for comparison.

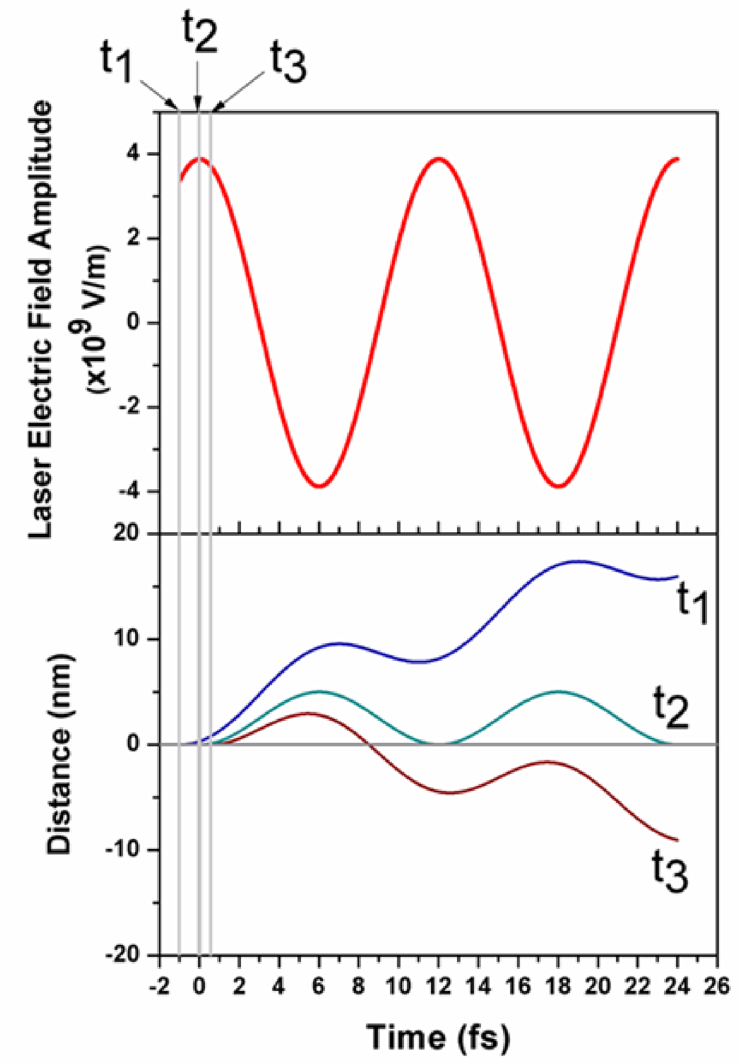

Figure 2.4: Calculated classical trajectories for an electron in a laser field, for three different ionization times during the laser field's period: $\mathbf{t}_1$) Ionization occurs shortly before the peak of the field and the electron subsequently drifts away from the ion core, $\mathbf{t}_2$) Ionization occurs at the peak of the field and the electron revisits the ion core each cycle of the field, but with zero return velocity, $\mathbf{t}_3$) Ionization occurs shortly after the peak of the field and the electron returns to the ion core with a return velocity,v_r.

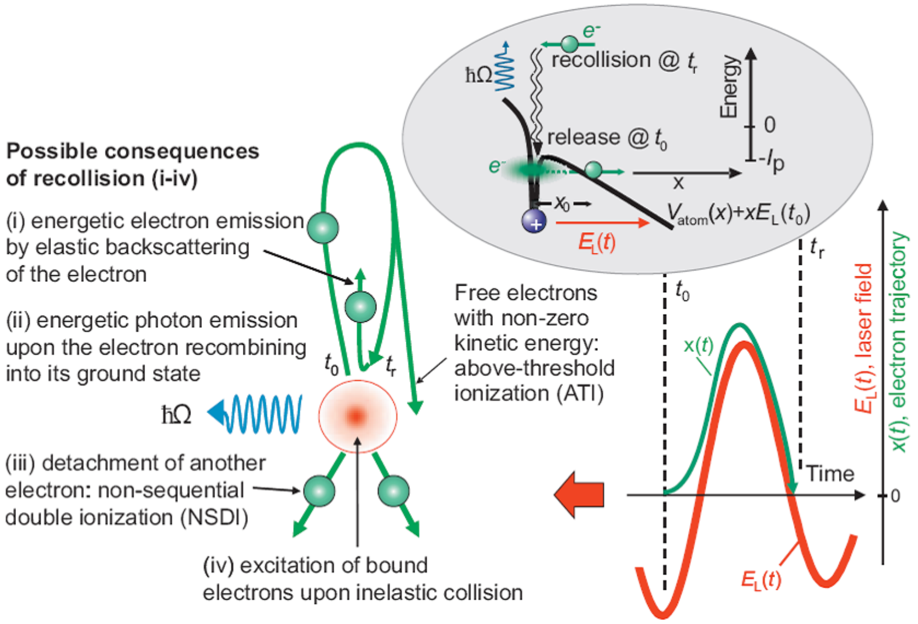

Figure 2.5: Possible scenarios upon the electron's return to the core. Figure reproduced from [41].

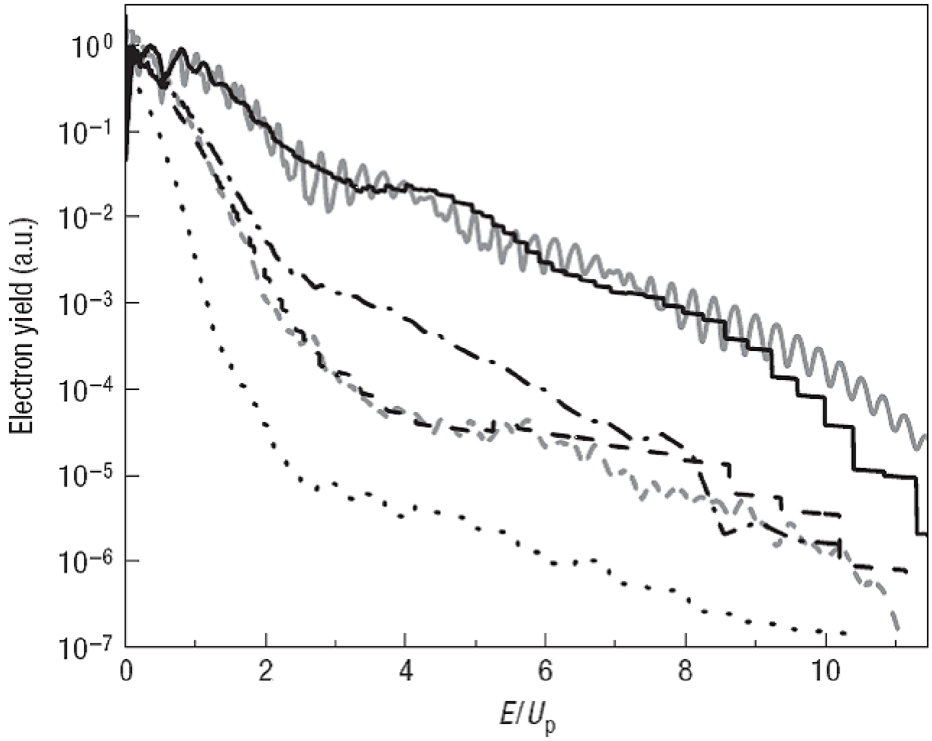

Figure 2.6: Photoelectron spectra at different driving laser field wavelengths, λ. All spectra were taken using argon and an intensity of 8×10^{13} W/cm^2. Solid line: $\lambda = 0.8$ μm ($\gamma = 1.3$), dot-dash: $\lambda = 1.3$ μm ($\gamma = 0.8$), dash: $\lambda = 2.0$ μm ($\gamma = 0.5$), dotted: $\lambda = 3.6$ μm ($\gamma = 0.3$), gray lines: TDSE calculations. Figure reproduced from [24].

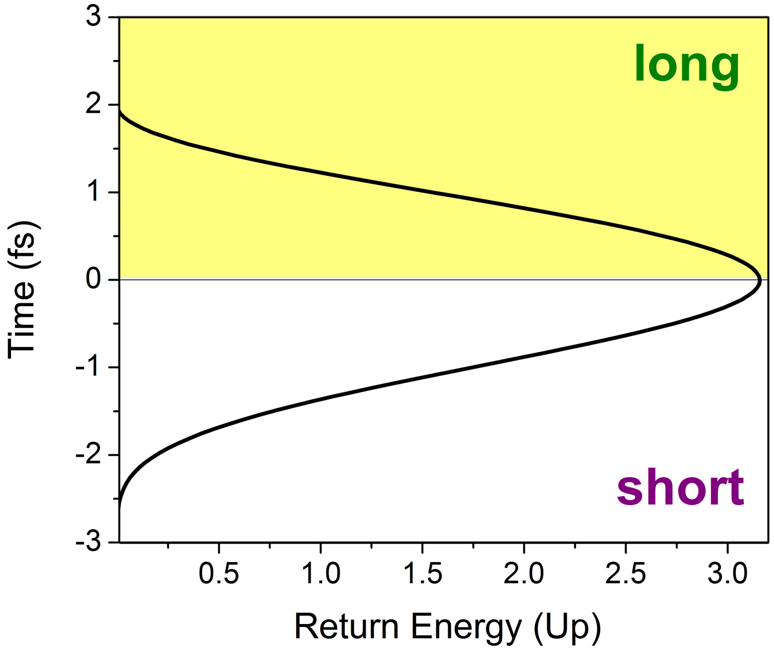

Figure 2.7: Electron return time versus return energy.

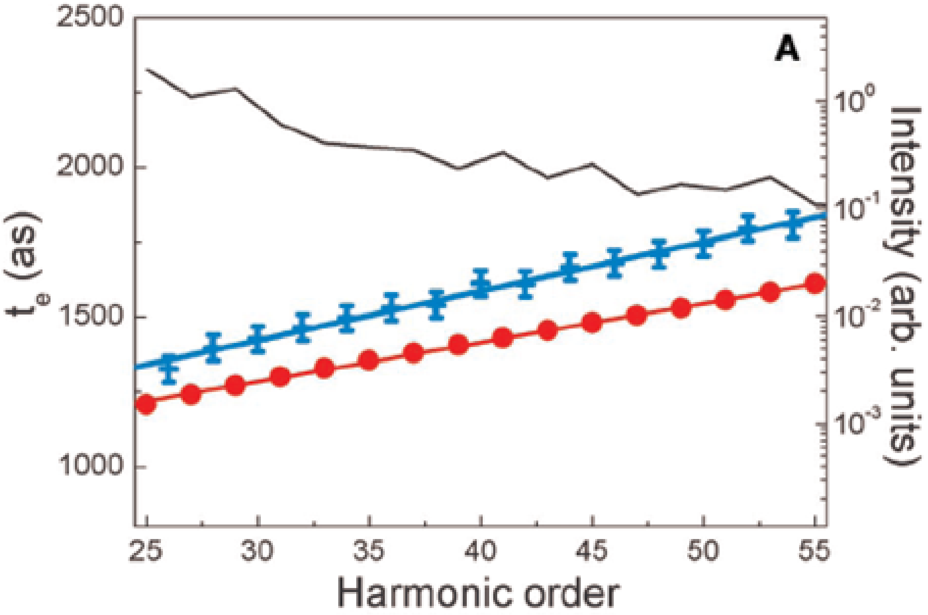

Figure 2.8: Measurement of the relative delay between harmonic orders, generated in neon using 0.8 μm light at $I \approx 3.8 \times 10^{14}$ W/cm^2. The blue points (with error bars) are measured values, the red points are predictions from the Simpleman rescattering model. The black line is the measured harmonic intensity. Figure reproduced from [44].

Chapter 3

Mid-infrared Laser System

While laser gain media for the mid-infrared region of the electromagnetic spectrum do exist, none have proved suitable for the production of short pulses (~ 100 fs) with high pulse energy (>100 μJ). A gain medium with properties similar to those of titanium:sapphire, but that lases in the mid-infrared has yet to be discovered. The best short pulse sources in the mid-infrared have relied upon parametric processes to generate the radiation. Our mid-infrared laser system is based on difference frequency generation (DFG) in a nonlinear crystal.

Since this laser system has been described in detail elsewhere [49], here I will give only a brief overview. However, I will include a more detailed description of the titanium:sapphire based multipass amplifier that is present in the mid-infrared laser system. This laser amplifier was designed and constructed as part of the work of this thesis. This amplifier increased the power and attainable peak intensity of the mid-infrared system, allowing for the studies presented here. A second amplifier, based on the same design, was also constructed on a different laser system, allowing for the production of short-duration, high energy pulses at a center wavelength of 2 μm. Although the work presented in this dissertation did not utilize this 2 μm laser system, it has become an extremely valuable tool and has been used in many other studies in our laboratory.

This chapter begins with a description of the difference frequency generation process and follows with a description of the systems that produce the 0.815 μm and 1.053 μm radiation that is mixed. The method for synchronizing the pulses is presented, which is followed by a description of the mid-infrared pulses that are produced. A detailed description of the multipass amplifier then follows, including a discussion of the theoretical model used, its layout, the crystal cooling method, and finally its performance.

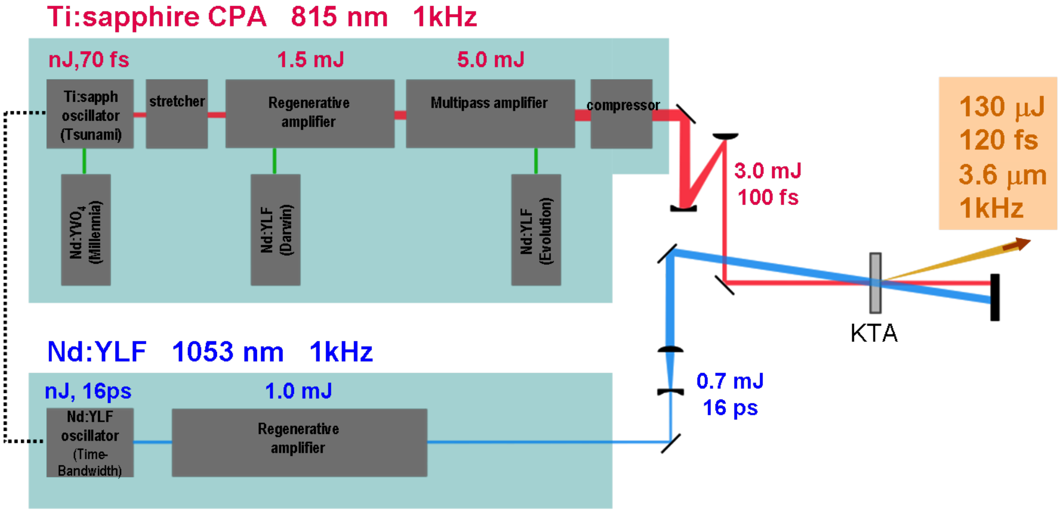

Figure 3.1: Mid-infrared laser system.

3.1 Difference Frequency Generation

Our 3.6 μm light is produced by mixing 0.815 μm light, from a titanium:sapphire based chirped-pulse amplification (CPA) laser chain, with 1.053 μm light, from a Nd:YLF regeneratively amplified laser system, in a nonlinear crystal. In the difference frequency process, energy from the 0.815 μm beam (referred to as the "pump") is converted into energy at 1.053 μm (referred to as the "signal"), and 3.6 μm (referred to as the "idler"). The frequency at 3.6 μm (83.276 THz) is equal to the difference between the frequencies at 0.815 μm (367.844 THz) and 1.053 μm (284.703 THz). The strange terminology used to describe the laser beams involved in this process is historical and probably dates back to the early days of optical parametric amplifier (OPA) sources. The "pump" beam was being used to amplify a "signal" beam, and the third beam was present as a result of energy conservation, otherwise "idle". In our case, the "idler" is the beam that we are interested in generating.

The parametric process can be written in terms of energy conservation as

$$\hbar\omega_p = \hbar\omega_s + \hbar\omega_i \tag{3.1}$$

and in terms of momentum conservation as

$$\hbar\mathbf{k_p} = \hbar\mathbf{k_s} + \hbar\mathbf{k_i} \tag{3.2}$$

Here ω_p, ω_s, and ω_i are the angular frequencies of the pump, signal, and idler and $\mathbf{k_p}$, $\mathbf{k_s}$, and $\mathbf{k_i}$ are the wave vectors for the pump, signal, and idler.

Table 3.1 lists some nonlinear crystals that are suitable for DFG at our wavelengths. (For a nice comparison of the performance of several of these crystals, see [50]). The effective nonlinear coefficient, d_{eff}, is listed as well as the transmission range for the crystal and its damage threshold. To generate the 3.6 μm light used in the work presented here, we used a KTA crystal (Potassium titanyl arsenate, $KTiOAsO_4$). KTA is a positive biaxial crystal, and it was cut to phase match our mixing process with $\theta = 39°$ and $\phi = 0°$. It was 2.5 mm long, with a cross section 10×10 mm^2.

Crystal	Transparency Range [nm]	d$_{eff}$ [pm/V]	Damage threshold [J/cm^2] @1064 nm, 10 ns pulse
KTP	350-4500	-2.21	15
KTA	350-4000	-2.0	15
RTA	350-4500	-2.31	15
$KNbO_3$	400-4500	6.23	1.7
AGS	500-13000	15.7	1

Table 3.1: Nonlinear crystals suitable for DFG of 3.6 μm light ($\hbar\omega_{0.815} = \hbar\omega_{1.053} + \hbar\omega_{3.6}$).

3.2 Pump (0.815 μm Radiation)

The pump radiation for the DFG process is provided by a titanium:sapphire based, chirped-pulse amplification (CPA) laser system. In this system, low energy, short pulses at 0.815 μm are produced in an oscillator and two amplifiers boost the energy to that required for the DFG process. However, if the pulses were amplified directly, the increasing intensity of the pulse as it traveled through the amplifier would soon become problematic and eventually damage the components within the amplifier. Instead, before amplification the pulse is stretched in time, so that its peak intensity while it travels through the amplifier and gains energy, is greatly reduced. The stretching of the pulse is accomplished using a diffraction grating and a telescope in a particular geometry (referred to as the stretcher) and it is undone after the pulse has been amplified by using another diffraction grating in a particular geometry (referred to as the compressor). More details about the stretcher and compressor can be found in [49].

The oscillator for our ti:sapphire laser chain is a commercial laser (Tsunami, Spectra-Physics) that is tunable from 750-850 nm and that produces 100 fs pulses at a repetition rate of 80 MHz and an average power of 700 mW when pumped with 5 W green light. The pump laser for the Tsunami is a frequency-doubled Nd:YVO_4 laser (Millennia, Spectra-Physics). After being sent through the stretcher, where the pulses are stretched to $\sim$ 250 ps, they enter a home-built regenerative amplifier where the repetition rate is dropped to 1 kHz and the pulse energy is increased from $\sim$ nJ to 1.5 mJ. This regenerative amplifier is a replica of one detailed in a former students' thesis [51]. It is pumped by a frequency-doubled Nd:YLF laser (Darwin, Quantronix). The 1.5 mJ pulses are then amplified in a second stage, the multipass amplifier. The details of the multipass are included in Section 3.6. Although referred to as the "multipass" it is better described as a power amplifier. The pulses pass through a pumped ti:sapphire crystal two times and gain 3.7 mJ, making the pulse energy at the output 5.2 mJ per pulse. The pulses then travel through the compressor where they are compressed back to a pulse duration of 100 fs. From there they are sent to the KTA crystal.

3.3 Signal (1.053 μm Radiation)

The signal radiation for the DFG process is provided by a Nd:YLF laser system. A commercial oscillator (GE-100, Time-Bandwidth) produces low energy pulses at 1.053 μm at a repetition rate of 80 MHz. This oscillator is pumped by an internal diode laser and is mode-locked using a semiconductor saturable absorber known as a SESAM. It produces pulses with a duration of 16 ps. Because these pulses are longer in time than the ti:sapphire pulses, they can be directly amplified without problem. They undergo one stage of amplification, in a regenerative amplifier, where their repetition rate is dropped to 1 kHz and their energy per pulse is boosted to 1 mJ. This regenerative amplifier is one of the very first amplifiers developed for radiation at 1 kHz [52]. It has been going strong for 20 years. Details of this amplifier can be found in [49, 53]. Once amplified, these pulses are sent to the KTA crystal.

3.4 Pulse Synchronization

Since we need to overlap the pump and signal pulses in time at the KTA crystal, a method of synchronizing the two laser systems is required. This is accomplished by locking both the Nd:YLF and ti:sapphire oscillator pulse trains to the same master oscillator and deriving all trigger signals for the amplifiers from this same master oscillator.

Each of the oscillators was purchased with optional locking electronics for this purpose. The Tsunami Model 3930 Lok-to-Clock electronics module includes a phase-locked loop to stabilize the repetition rate of the pulse train to either an internal 80 MHz reference signal or an externally supplied signal. In our case, the reference signal from the Nd:YLF is supplied to the 3930 unit to be used as the reference signal. Since the repetition rate of the laser is $\frac{c}{2L}$, where c is the speed of light and L is the cavity optical length, the repetition rate can be adjusted by shortening or lengthening the cavity. An internal photodiode monitors the pulse train and the phase of the train is compared to the phase of the reference signal. Any difference is converted to an error voltage which then drives a piezo-electric transducer (PZT) that is mounted on one of the intracavity mirrors. The cavity length is changed until the phase difference is minimized. In addition, an external knob on the 3930 controls a phase shift that is added to the photodiode signal, allowing an adjustment range of 2 ns. This phase adjustment is critical for achieving the final timing overlap between the ti:sapphire and Nd:YLF pulses at the KTA crystal and optimizing the mid-infrared power. The GE-100's CLX-1100 Timing Stabilizer Feedback System includes a phase-locked loop to stabilize the Nd:YLF pulse train's repetition rate. It's operation is extremely similar to that described for the Tsunami. A previously made measurement of the timing jitter between the two laser systems using a cross-correlation technique indicated that the jitter is < 2 ps [49]. Given the 16 ps pulse length of the Nd:YLF signal pulse, which is long relative to the 100 fs pulse length of the ti:sapphire pump pulse, a 2 ps jitter does not have an appreciable impact on the mid-infrared production.

3.5 Idler (3.6 μm Radiation)

The 0.8 μm pump and 1.053 μm signal beams are brought together at a small angle ($\sim 0.3°$) in the vertical plane, which allows for the separation of the 3.6 μm after the crystal.

The damage threshold for KTA is 15 J/cm^2 for a 10 ns pulse. If we assume the damage threshold scales as $\sqrt{\tau}$, where τ is the pulse duration [54], for a 100 fs pulse the damage threshold will be 0.05 J/cm^2. Given the 2.7 mJ per pulse present in the pump beam at the KTA crystal, this means that for pump spot sizes ≤ 1.3 mm (1/e^2 radius) or 1.54 mm (FWHM) we are at risk for damaging the crystal. To be safe, we kept the pump and signal spot sizes at the KTA crystal to a FWHM value of 2.5 mm.

Mixing the 1 kHz, 2.7 mJ, 0.815 μm and ~ 0.8 μJ, 1.053 μm pulses produced idler pulses with 140 μJ energy centered at a wavelength of 3.6 μm at a 1 kHz repetition rate (140 mW). An interferometric autocorrelation technique was used to measure the mid-infrared pulse duration, which was found to be 110 fs FWHM [49]. A beam block caught the pump and signal beams, while allowing the idler to pass over. To ensure that the mid-infrared beam was not contaminated with radiation at the pump and signal wavelengths, or at wavelengths corresponding to other mixing processes, an AR coated silicon window was introduced into the beam path. This window transmits the 3.6 μm light, but absorbs radiation with wavelengths smaller than ~ 1.1 μm. A reflective telescope expanded and collimated the mid-infrared beam to a spot size of approximately 12 mm FWHM. Using a thermal camera (Electrophysics, PV320), the mode was found to be fairly round and near-Gaussian [49].

3.6 Multipass Amplifier

The multipass amplifier was designed and constructed to increase the energy of the ti:sapphire beam in the mid-infrared laser system and in another system in our lab that produces intense, short-pulse laser light at 2 μm. In the 2 μm system, the ti:sapphire CPA is very similar to the one in the mid-infrared system. The primary differences are the compressed pulse length, which is 50 fs as opposed to 100 fs, and the center wavelength which is 780 nm instead of 815 nm. The regenerative amplifiers in both systems are based on the same design [51], as are the stretcher and compressor [49]. The 2 μm light is generated in a two stage OPA based on superflourescence (HE-TOPAS, Light Conversion) that is pumped by the ti:sapphire beam. The multipass was necessary to boost the ti:sapphire energy to that required by the TOPAS. In the mid-infrared system, the increase in ti:sapphire energy allowed us to generate more mid-infrared energy.

The primary design objective was to achieve high efficiency in the energy extraction. Two pump lasers were available for the amplifiers, the Evolution 30 (Positive Light) for the mid-infrared system, and the Darwin (Quantronix) for the 2 μm system. Both are 20 W frequency-doubled Nd:YLF Q-switched lasers. For the 2 μm laser system, the TOPAS was specified for a pump beam with 5.0 mJ energy. Taking a conservative estimate of a 30% loss in the transport through the compressor, and the 1.5 mJ available at the output of the regenerative amplifier, this required that the multipass boost the ti:sapphire energy by 5.64 mJ to a total of 7.14 mJ. This corresponds to an pump-to-signal efficiency (defined as the energy gained divided by the pump energy) of 30%, an achievable, but not trivial goal. Careful attention was placed on maximizing the energy extraction, by modeling the gain and mode matching the ti:sapphire and pump beams, and on minimizing losses by careful consideration of the beam path geometry.

The ultimate design includes two passes through the ti:sapphire crystal. Two curved mirrors focus each pass into the crystal. They are positioned slightly off confocal positioning to reduce the problem of ASE. The crystal is cooled to liquid nitrogen temperature to remove thermal effects. To avoid condensation on the crystal faces it is contained in a small vacuum chamber. The crystal and the vacuum chamber windows are oriented at Brewster's angle to reduce Fresnel losses. In what follows, the gain model that was used to decide the number of passes to include as well as the ti:sapphire and pump spot sizes at the gain crystal is described. The lens configurations implemented to mode match the ti:sapphire and pump beams are described. Layouts of each of the amplifiers are presented and details of the liquid nitrogen cooling setup are described. Finally, the amplifiers' performance is described.

3.6.1 Gain Model

The amplification process in our case takes place in the following manner. The $\sim$ 150 ns duration green pump pulse enters the gain medium, energy is absorbed, and a population inversion is created. Some time after the pump pulse has passed through, the ti:sapphire input pulse enters the medium and through stimulated emission extracts the stored energy. Because the upper state lifetime of titanium:sapphire, 3.2 μs, is very long relative to our $\sim$ 250 ps stretched out pulse and to the pulse's travel time through the amplifier, the effects of fluorescence can be ignored during the amplification process. The stored energy in the crystal is considered to be already established when the pulse makes its first pass through. Some of this energy is extracted during the first pass. The ti:sapphire pulse is turned around and makes its second trip through the crystal during which it extracts the rest of the energy. One millisecond later, the next pump pulse enters the crystal and the process repeats.

Our 1D gain modeling was done using a model outlined in **Solid-State Laser Engineering** by W. Koechner [55]. It is based on the Frantz-Nodvik model of short pulse amplification [56], where the rate equations for the inverted electron population, n, and the photon flux, ϕ are solved:

$$\frac{\partial n}{\partial t} = -\gamma n c \sigma \phi \tag{3.3}$$

$$\frac{\partial \phi}{\partial t} = c n \sigma \phi - \frac{\partial \phi}{\partial x} c. \tag{3.4}$$

Here x is the distance along the gain medium, where $x = 0$ is at the entrance of the medium, n is assumed to be uniform throughout the gain medium at $t = 0$, γ is the gain coefficient, which for a four level system like ti:sapphire is equal to 1, σ is the stimulated emission cross section, and c is the speed of light. The pulse is treated as a square pulse in time and space and the gain is found to depend on the pulse energy density (as opposed to the power density). The solution can be written in terms of the input and output signal fluences, J_{in} and J_{out}, (where the fluence is the pulse energy per unit area) as

$$J_{out} = J_{sat} \ln \left\{ 1 + \left[\exp(\frac{J_{in}}{J_{sat}}) - 1 \right] G_0 \right\} \tag{3.5}$$

The saturation fluence is

$$J_{sat} = \frac{h\nu}{\gamma\sigma} = \frac{E_{st}}{\gamma g_0}, \tag{3.6}$$

where $E_{st} = h\nu n$ is the stored energy per unit volume, $g_0 = n\sigma$ is the small-signal gain coefficient, and σ is the stimulated emission cross section. G_0 in Equation 3.5 is the small-signal single pass gain,

$$G_0 = \exp(g_0 l). \tag{3.7}$$

Here l is the gain medium length.

In our setup, the pump beam is split in two and one pump "arm" enters the crystal from one side and the other "arm" enters from the other side. This reduces the total fluence on a single crystal face. The resulting pump fluence along the crystal length is presented in Figure 3.2. As is seen in the figure, the pump fluence is not constant along the length of the crystal. Therefore, the inverted electron population is not constant along the length of the crystal. Our gain model took this into account by treating the 1 cm long crystal as 20 segments, each with a length of 0.5 mm. The average absorbed pump fluence in each segment was calculated, which allowed us to calculate the inverted electron population, n, small-signal gain coefficient, g_0, and small-signal single-pass gain, G_0 for each segment. With this information, the fluence of the signal beam at the output of each segment was calculated using Equation 3.5. For subsequent passes through the crystal, g_0 and G_0 were recalculated to take into account the extracted energy from the previous pass. The amplification process was considered to be lossless.

The details of each step in our gain model are as follows. The absorbed fluence in each segment was calculated using the pump absorption coefficient for our crystal[1], $\alpha_{527} = 2.4$ cm^{-1}. The fluence at the end of segment n is

$$J_n^{1+2} = J^1 + J^2 = \frac{E_1}{A_1} \exp -nx\alpha_{527} + \frac{E_2}{A_2} \exp -nx\alpha_{527} \tag{3.8}$$

where 1 and 2 refer to pump arms 1 and 2, $E_{1,2}$ refers to the pump energy in

---

[1] For a 1 cm crystal, this predicts that 91% of the pump light should be absorbed. This is consistent with our measured values.

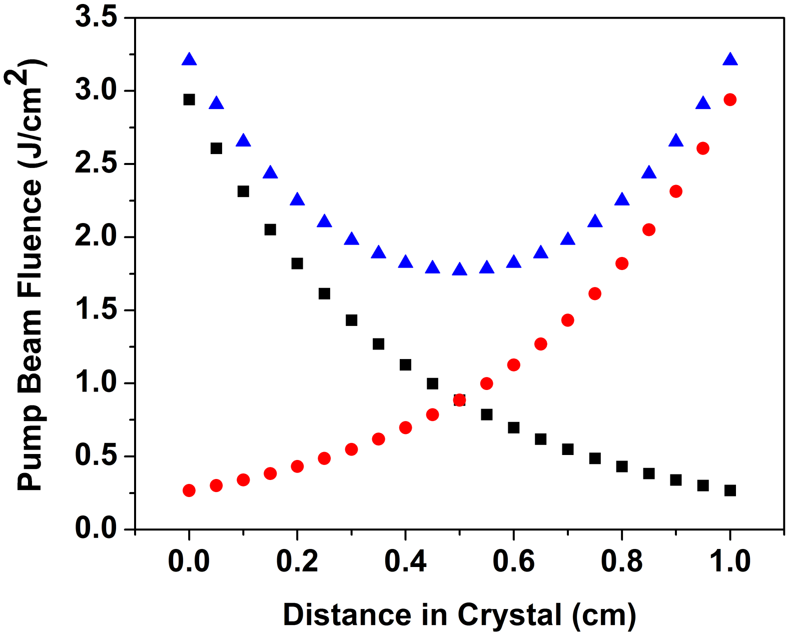

Figure 3.2: Modeled pump fluence along the length of the ti:sapphire crystal. Black squares and red circles indicate the individual pump arms and the yellow triangles indicates the sum of the two.

each arm and $A_{1,2}$ refers to the pump focused spot sizes at the crystal[2] The fluence absorbed is then

$$J_n^{abs} = J_n^{1+2} - J_{n-1}^{1+2} \tag{3.9}$$

This was converted to the stored energy per unit volume E_n^{st} by dividing by the segment length, x, and multiplying by the quantum efficiency, to take into account the energy that is lost as heat.

$$E_n^{st} = J_n^{abs}(h\nu_{ti}/h\nu_{527})/x \tag{3.10}$$

From E_n^{st} the inverted electron population, n_n, the small signal gain coefficient, $g_{0,n}$, and the small signal single pass gain, $G_{0,n}$ were calculated.

$$n_n = \frac{E_n^{st}}{h\nu_{527}} \tag{3.11}$$

---

[2] The spot sizes were taken to be constant across the length of the crystal, since the focused spot sizes were fairly large, $\sim 250\ \mu$m, and therefore the Raleigh lengths were several times the length of the crystal.

$$g_{0,n} = n\sigma \tag{3.12}$$

$$G_{0,n} = \exp g_{0,n}x \tag{3.13}$$

Here σ is the stimulated emission cross section which is 2.0×10^{-19} cm^2 at the peak of ti:sapphire's gain curve [57]. Armed with this information, the fluence of the ti:sapphire signal beam at the output of each segment is calculated using Equation 3.5

$$J_n^{out} = J_{sat} \ln \left\{ 1 + \left[\exp(\frac{J_n^{in}}{J_{sat}}) - 1 \right] G_{0,n} \right\} \tag{3.14}$$

Ti:sapphire's saturation fluence, J_{sat}, is 0.9 J/cm^2 and here J_n^{in}=J_{n-1}^{out}.

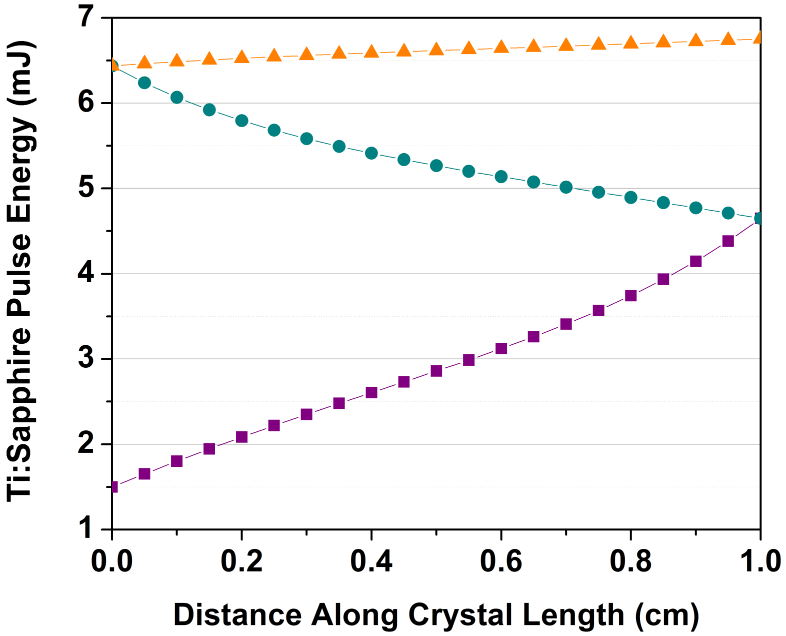

Figure 3.3: Modeled energy buildup of the ti:sapphire pulse along the length of the crystal. Purple squares indicate pass 1, blue circles indicate pass 2, and orange triangles indicate pass 3.

Using this model, and taking into account the feasibility of focusing the pump and ti:sapphire beams to particular spot sizes, it was decided that given 10 J of pump energy in each pump arm and 1.5 mJ ti:sapphire input energy, two passes would be sufficient to extract enough energy with spot sizes at the crystal equal to 250 μm (1/e^2 radius). The results of the model simulation are shown in Figure 3.3 and Table 3.2. While it is shown that a bit more energy can be obtained with a third pass through the crystal, it was decided that the gain was probably not worth the added complexity that would be involved. The amplifier geometry was chosen so that a third pass could be easily added if needed. The efficiency, defined as the energy extracted divided by the stored

Pass	Input Energy mJ	Output Energy mJ	Single Pass Efficiency η
1	1.5	4.65	0.59
2	4.65	6.44	0.83
3	6.44	6.75	0.88

Table 3.2: Gain model predictions. The amplification process is considered to be lossless. Input values: 10 J pump energy for each pump arm, 1.5 mJ ti:sapphire energy, pump and ti:sapphire spot sizes are $\omega_0 = 250$ μm (1/e^2 radius).

energy in the upper laser level at the time of the pulse's arrival

$$\eta = \frac{J_{out} - J_{in}}{g_0 l J_{sat}} \tag{3.15}$$

is calculated in Table 3.2 for each individual pass. According to the model, for a two pass amplifier the total efficiency is $\eta_{2pass} = 0.93$, and for a three pass amplifier the total efficiency is $\eta_{3pass} = 0.99$.

3.6.2 Layout

A simple geometry, using curved mirrors to focus the ti:sapphire beam into the crystal, was chosen. Figures 3.4 and 3.5 show the layouts for the 4 μm system and the 2 μm system respectively. As has been mentioned, the focusing mirrors are positioned slightly off from the confocal distance, to reduce the potential buildup of amplified spontaneous emission (ASE). The mirrors have a radius of curvature of 1.5 m and are separated by a distance of 1.6m. A reflective telescope adjusts the divergence of the ti:sapphire beam before striking the first curved focusing mirror so that it has the appropriate size at the crystal. The first and second passes are slightly offset in the vertical direction so that the second pass can be separated from the input beam and made to exit the amplifier. A periscope steers the beam slightly down after the first pass, but is carefully adjusted so that the beam still passes through the crystal centered on the pump beam to efficiently extract energy on the second pass.

The pump beam is split into two arms, to reduce the total fluence on a single crystal face. Each arm contains a lens which focuses the pump beam to the appropriate spot at the crystal. A telescope is present before the pump beamsplitter to adjust the divergence and spot size of the pump beam so that it focuses to the appropriate size. The second lens of this telescope is mounted on a translation stage, allowing for the divergence of the pump beam to be adjusted while monitoring the power of the amplified ti:sapphire beam to achieve the highest possible gain.

3.6.3 Beam Models

In order to select the optics required to match the modes of the pump and signal at the crystal, the beam propagation was modeled using the software packages Optikwerks® and Laserwerks®. Three laser beams were modeled: that of the Evolution 30, the pump laser for the 4 μm system's amplifier, that of the Darwin, the pump laser for the 2 μm system's amplifier, and the output beam from the ti:sapphire regenerative amplifier. Since both regenerative amplifiers were based on the same design, their output characteristics were very similar, and for the modeling purposes, were assumed to be identical. In order to model the propagation, input parameters for the spot size, divergence, and beam quality factors (M^2 values), were needed. As the regenerative amplifier output is very close to being a lowest order Gaussian mode and leaves the amplifier collimated, only the spot size was unknown and this was easily obtained through a quick FWHM estimation, measuring the diameter of an iris that transmits 1/2 of the power. Since the pump lasers have more complicated mode structure, this spot size measurement technique was inadequate. Instead, the parameters for the pump lasers were obtained by measuring the beam profile, using a CCD camera, as a function of distance as the beam was focused by a lens. Then spot sizes were extracted from the CCD images by calculating the second-moment width of the energy distribution of the beam:

$$d\sigma_x = 4\sqrt{\frac{\sum[(x-x_c)^2 p(x,y)]}{I}} \tag{3.16}$$

$$d\sigma_y = 4\sqrt{\frac{\sum[(y-y_c)^2 p(x,y)]}{I}} \tag{3.17}$$

Here $p(x,y)$ is the intensity at (x,y), I is the total intensity, and x_c and y_c are the centroid locations in the x and y directions. The second-moment widths for both the x and y directions were then plotted as a function of propagation distance and fit using the Gaussian mode propagation formula for a multimode beam:

$$W(z) = \sqrt{W_0^2 + \frac{M^4\lambda^2(z-z_0)^2}{\pi^2 W_0^2}}. \tag{3.18}$$

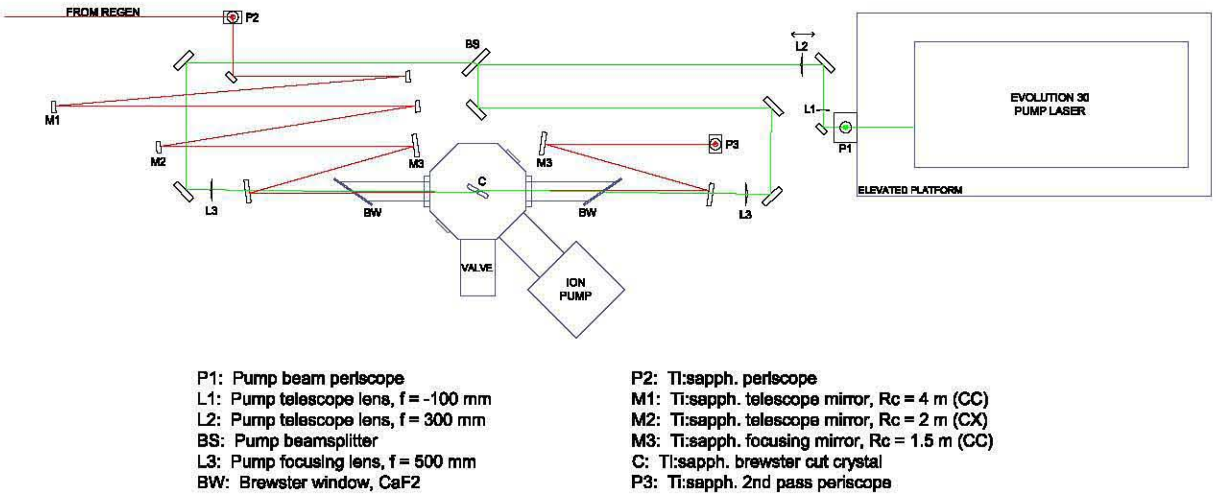

Figure 3.4: Multipass amplifier layout for the mid-infrared (4 μm) laser system.

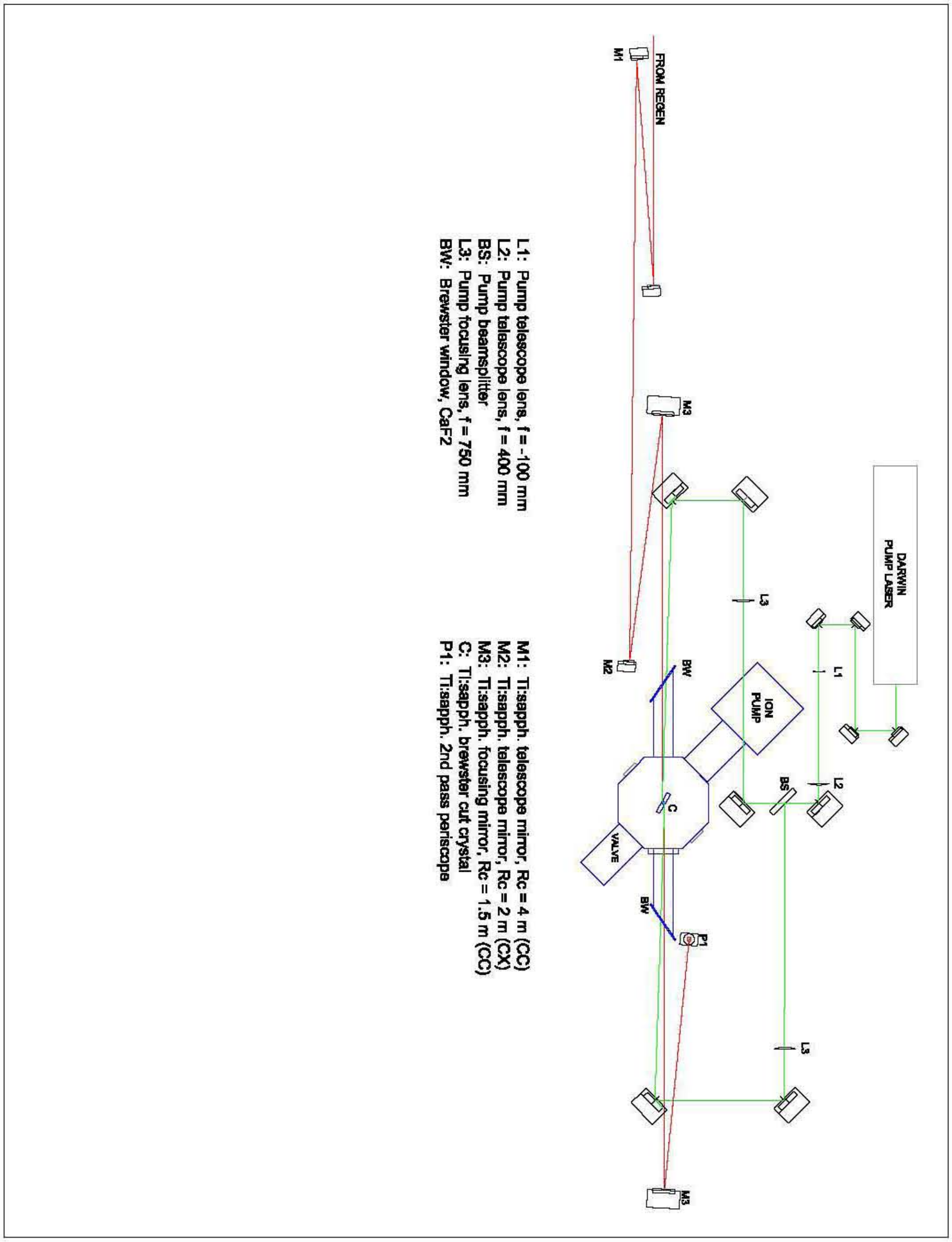

Figure 3.5: Multipass amplifier layout for the 2 μm laser system.

Here W_0 is the second moment radius of the beam at the focus, z_0 is the focus position, and M^2 is the beam quality factor. Using the obtained beam parameters, the lens configurations shown in Figures 3.6 and 3.7 were found to produce spot sizes of ≈ 250 μm at the amplifier crystal. These lens configurations were implemented, and the spot sizes for the pump and ti:sapphire beams at the crystal were measured by picking off a portion of each beam before it entered the crystal vacuum chamber and carefully positioning a CCD camera at a distance equivalent to the crystal position. The measured beam profiles and x and y lineouts for the two amplifiers are shown in Figures 3.8 and 3.9. Here the pump lens translation stage settings are 9 mm and 0.325 inches for the 4 μm and 2 μm amplifiers respectively.

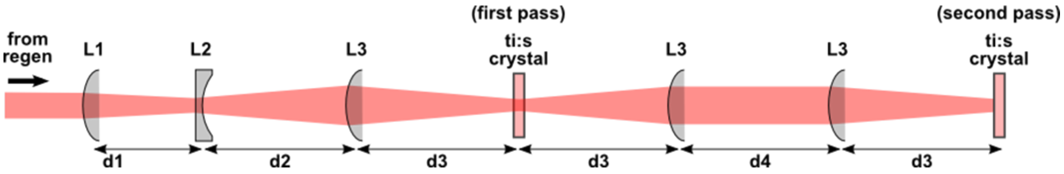

	Amplifier for the 4 µm System	Amplifier for the 2 µm System
L1	f = 2 m	f = 2 m
L2	f = -1 m	f = -1 m
L3	f = 0.75 m	f = 0.75 m
d1	80.0 cm	140.0 cm
d2	50.0 cm	59.0 cm
d3	80.0 cm	89.5 cm
d4	80.0 cm	117.0 cm

Figure 3.6: Ti:sapphire beam focusing configuration for the 4 μm and 2 μm amplifiers. Although lenses are shown in the figure, all focusing elements used for the ti:sapphire beam were mirrors.

3.6.4 Cooling

Even with efficient pumping provided by solid state lasers with wavelengths matched to the excitation energy for ti:sapphire, energy is still lost as heat within the crystal. The spatial profile of the pump creates a radially dependent temperature gradient within the crystal, which, because of the temperature dependence of the index of refraction, sets up an index gradient that can cause the beams passing through the crystal to focus. Techniques have been demonstrated where this thermal

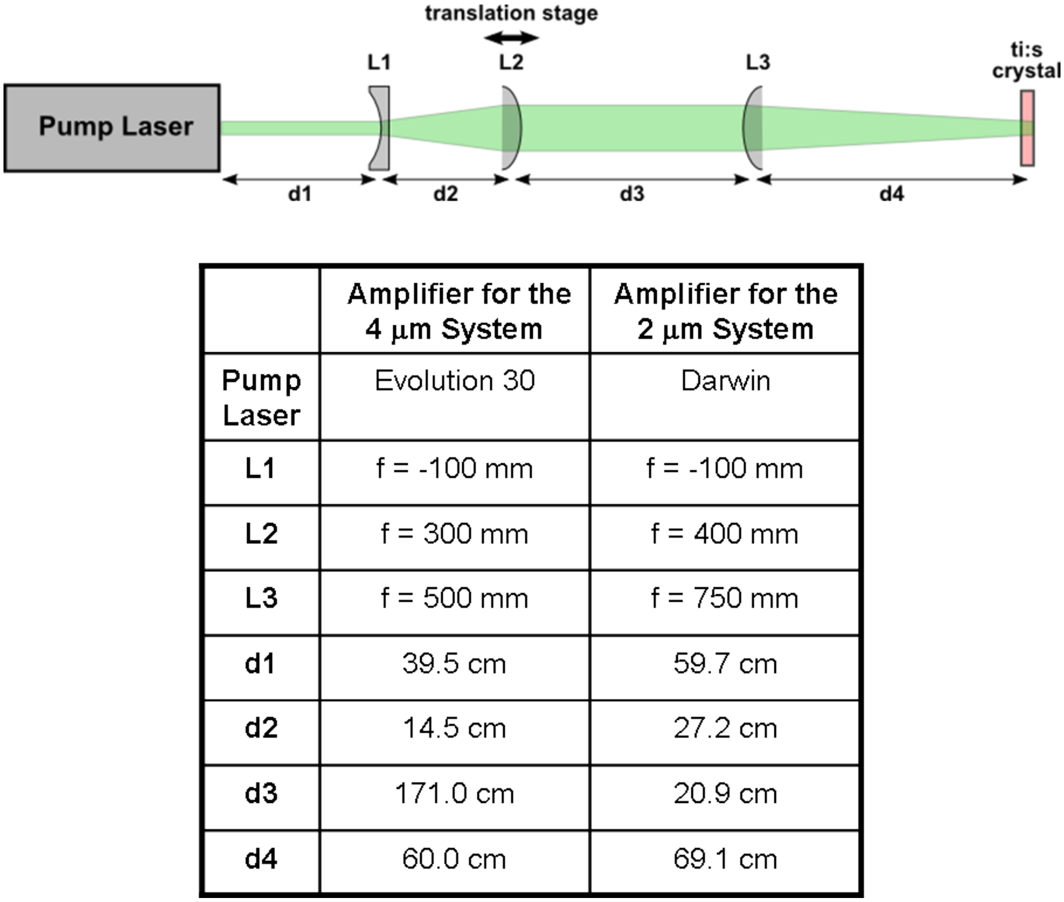

	Amplifier for the 4 μm System	Amplifier for the 2 μm System
Pump Laser	Evolution 30	Darwin
L1	f = -100 mm	f = -100 mm
L2	f = 300 mm	f = 400 mm
L3	f = 500 mm	f = 750 mm
d1	39.5 cm	59.7 cm
d2	14.5 cm	27.2 cm
d3	171.0 cm	20.9 cm
d4	60.0 cm	69.1 cm

Figure 3.7: Pump beam focusing configuration for the 4 μm and 2 μm amplifiers.

lens is incorporated into the optical design of the multipass amplifier [58], [59], however this approach limits the pump powers and repetition rates that can be used in the amplifier and does not remove the distortions and higher-order aberrations that may be present. An alternate approach is to cool the crystal. We decided to adopt the latter, and followed the cryogenic-cooling design of the Murnane-Kapteyn group at JILA [60], [61] where the crystal is cooled using liquid nitrogen. Sapphire's thermal conductivity increases dramatically when it is cooled (from 0.26 W/cm K^{-1} at 300 K to 9.8 W/cm K^{-1} at 77 K [62]), while $\frac{dn}{dT}$ is reduced [63]. This effectively leads to the elimination of the thermal lensing effects at 77 K. Work examining the thermal effects in ti:sapphire amplifiers has determined that thermal lensing and wave-front distortions can be suppressed by keeping the crystal temperature lower than $\sim$ 230 K [64][3].

---

[3] This means we can probably move to a closed-loop chiller, which would be much more convenient than our present setup.

Our setup consists of a stainless steel vacuum can that can hold ≈ 2 L of liquid nitrogen. The can sits upon a small eight-port vacuum chamber that is pumped by a 20 liter/second ion pump (Varian VacIon Plus 20) to a pressure of $\approx 10^{-6}$ Torr. The brewster-cut ti:sapphire crystal is mounted in a copper holder that is bolted to the bottom of the vacuum can, the thickness of which has been kept small so as to enable good thermal conductivity between the copper and liquid nitrogen. Care was taken to ensure the top of the copper block was flush against the liquid nitrogen can. Also, the copper holder, consisting of detachable top and bottom parts so that the crystal could be mounted, was tightened securely so that conductivity to the bottom half was ensured. The crystal was wrapped in soft indium foil before mounting so that it could be held snuggly in the mount, for good thermal contact, but not suffer pressure points which could induce unwanted birefringence and wavefront distortions. To be sure we were not over-tightening the holder, a HeNe, in conjunction with a polarizer, was used to watch for induced birefringence while the block was tightened. A thermocouple was mounted to the bottom of the copper holder. When the full pump power was present, the temperature reading would rise ~ 20 C indicating a temperature of $\sim$ -170 C (103 K).

3.6.5 Performance

To optimize the final performance, the following were adjusted while monitoring the amplified beam's power using a power meter: the temporal delay between the ti:sapphire pulse and the pump pulse, the pump telescope lens position, and the steering of the ti:sapphire beam for each pass. Table 3.3 lists the final output power and efficiency for both amplifiers as well as the gain model's predicted values. The total pump power is the power measured immediately before the input windows of the vacuum chamber. For the measured energy values presented here the pump translation stages were set to 9 mm and 0.325 inches for the 4 μm and 2 μm amplifiers respectively.

	4 μm System Amplifier	*2 μm System Amplifier*	*Gain Model*
Total Pump Power (W)	14.3	20.1	20
Input Energy (mJ)	1.5	1.7	1.5
Energy After 1st Pass (mJ)	3.7	4.6	4.65
Energy After 2nd Pass (mJ)	5.4	6.3	6.44
$\frac{Energy\ Gained}{InputPumpEnergy}$	27 %	23 %	24.7 %

Table 3.3: Output energy and efficiency for the 4 μm and 2 μm amplifiers. The predicted values from the gain model are included for comparison.

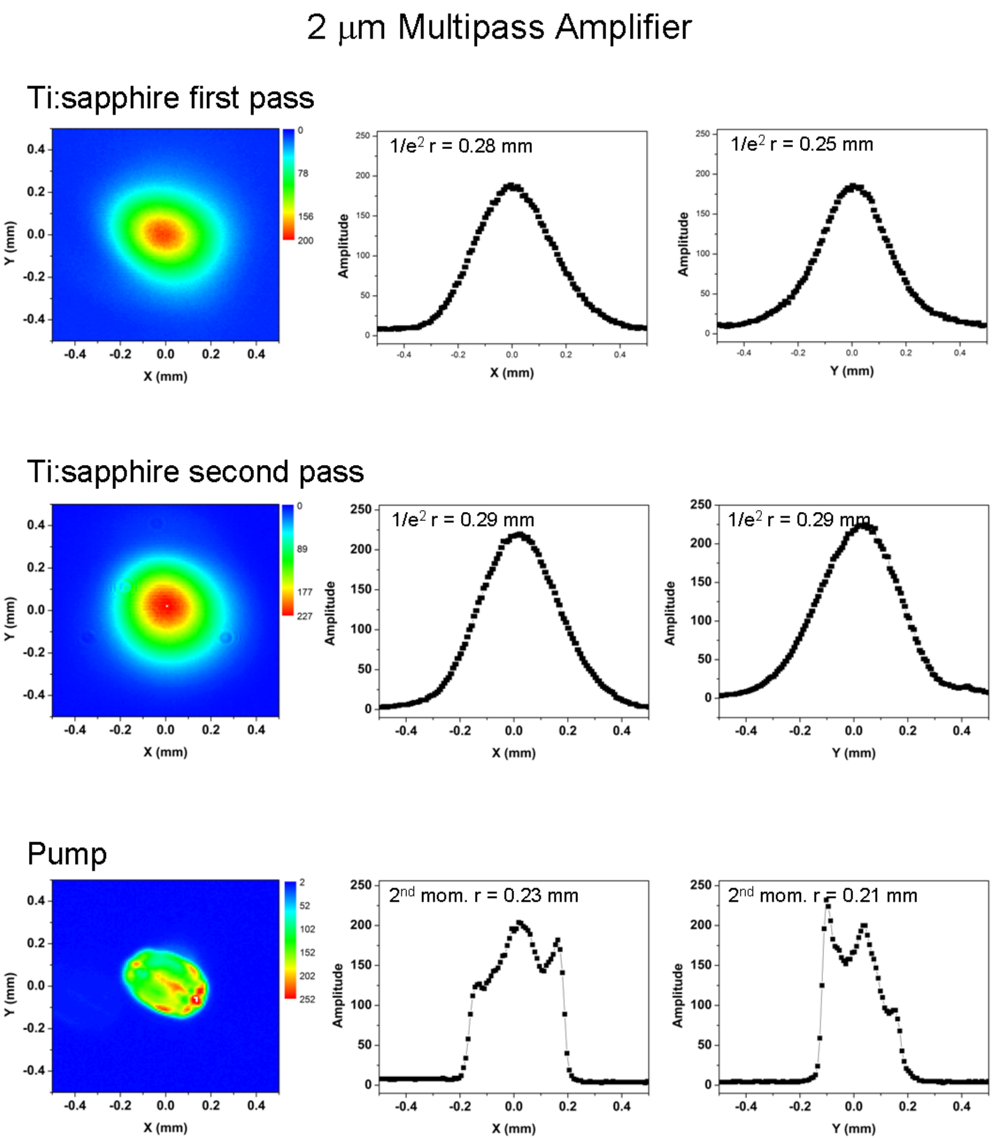

Figure 3.8: Measured profiles of the pump beam and ti:sapphire beam, at its first and second pass, at the gain crystal position for the 2 μm system's amplifier. The $1/e^2$ radius widths for the ti:sapphire beam, obtained from a Gaussian fit to the x and y lineouts, as well as the 2^{nd} moment widths for the pump beam are included.

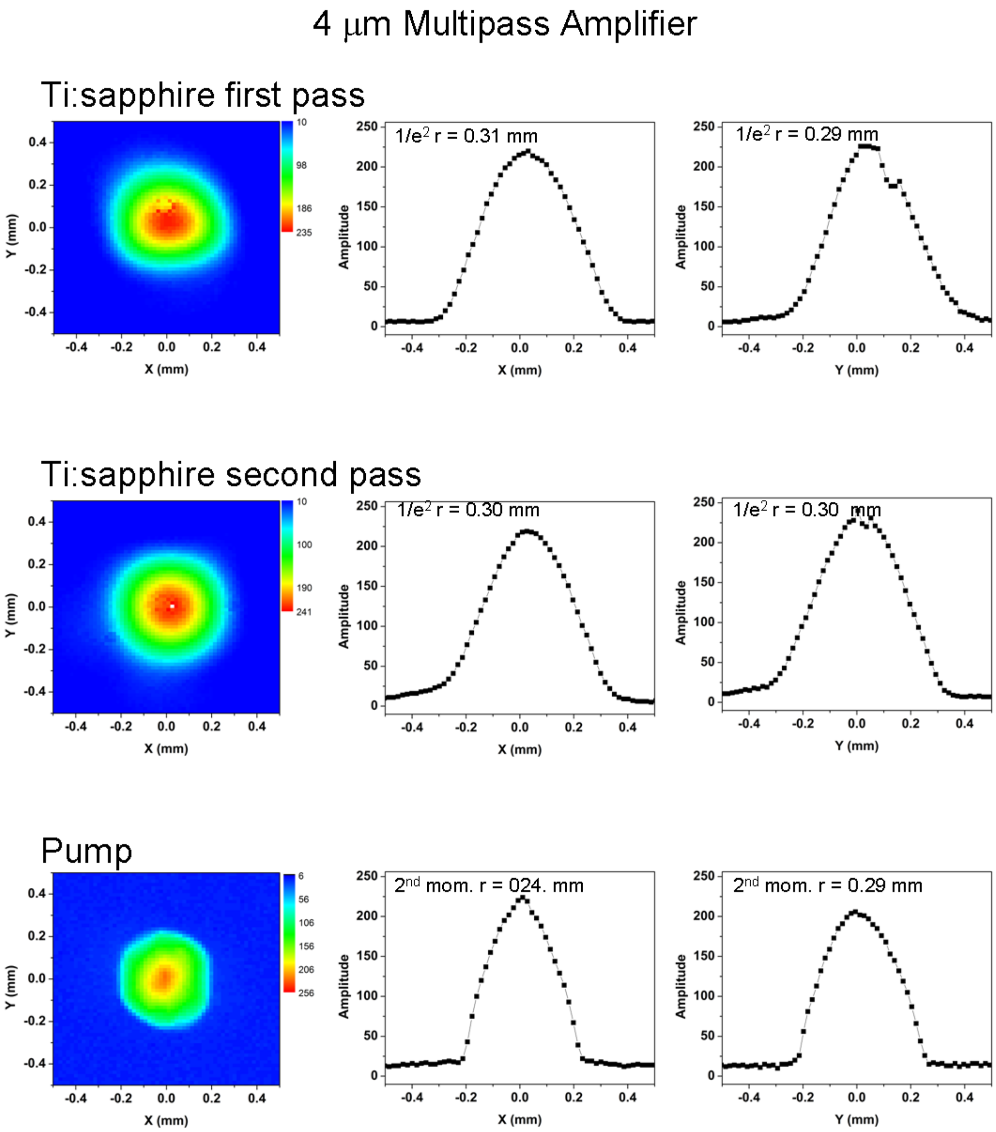

Figure 3.9: Measured profiles of the pump beam and ti:sapphire beam, at its first and second pass, at the gain crystal position for the 4 μm system's amplifier. The $1/e^2$ radius widths for the ti:sapphire beam, obtained from a Gaussian fit to the x and y lineouts, as well as the 2^{nd} moment widths for the pump beam are included.

Chapter 4

Photoelectron Spectra

4.1 Introduction

Experimental studies of the photoelectron energies and ion yields resulting from the ionization of atoms and molecules by short-pulse, intense lasers have been extremely fruitful in progressing our understanding of the strong-field interaction [32]. Ion yield measurements, easily comparable to theoretical ionization rates, have demonstrated the progression from perturbative multiphoton ionization to the nonperturbative regime, and have uncovered surprising phenomena such as nonsequential double ionization [65]. Photoelectron spectra have revealed the existence of above threshold ionization [66] and the plateau of high energy electron production [20] which has led to our present understanding of the rescattering mechanism [38, 40]. Photoelectron spectra from the now well-explored interaction of 0.8 μm light with the noble gases, are used in techniques to measure properties of laser light at unprecedented time resolution, such as the Stereo ATI method to measure the carrier-envelope phase of few cycle pulses [67] and techniques that measure the durations of attosecond pulses, such as RABBITT [68], FROGCRAB [69], and the Atto streak camera [70].

The usefulness of these measurements comes in part from their ability to give us access to the single atom response. While explorations of the light that is produced in these processes (see Chapter refch:HHG) have yielded extremely interesting results, it is often difficult to interpret findings using a fundamental single-atom model since the light consists of contributions from many atoms, and the effects of phase matching need to be taken into account[31]. In addition, effects from the light's propagation through the macroscopic medium can have a strong influence on the light's properties. Modeling these macroscopic effects can be very challenging because it often requires knowledge about the experimental conditions that is difficult to obtain. Measurement of the photoelectron energy, on the other hand, can be carried out quite literally one atom and one laser pulse at a time. By keeping the gas pressure low enough, the ionization probability can be kept to one atom per laser pulse, and the photoelectron spectra can be built up by taking advantage of high repetition rate laser technology and repeating the experiment many times. It should be noted that in these types of measurements the macroscopic size of the laser focus and its Gaussian intensity profiles in space and time play a role in the interpretation of photoelectron spectra. However, the difference is that these effects can be experimentally estimated and theoretical calculations can easily incorporate them by averaging over a range of laser intensities and photoelectron energies.

Cesium, and the alkalis in general, are particularly nice to study because of their similarity to hydrogen, which reduces the uncertainty in theoretical models of the system compared to those that require less striaghtforward approximations. Earlier work using a 54 ps Nd:YAG laser at intensities between 10^9 and 10^{12} W/cm^2 studied the intensity dependence of the ATI spectrum of cesium [71] because it could be compared directly to theoretical calculations. Four and five photon ionization was observed and satisfactory agreement between the experimental results and calculated ionization probabilities was found. At the lower intensities studies, $< 10^9$ W/cm^2, the ionization rates scaled perturbatively, as $P_n \propto \sigma^{(n)} I^n$, where n is the number of absorbed photons and $\sigma^{(n)}$, the generalized cross section, is constant with respect to intensity. At the higher intensities, $\sigma^{(n)}$ becomes intensity dependent, an effect that is interpreted as being due to resonant coupling between excited states.

As is pointed out in the paper regarding cesium, "‘since it ionizes rather easily, compared to Xe or H, high intensity effects can only be observed using ultrashort laser pulses."’ [71] Decreasing the pulse duration, so that there is less time for the ground state to become depleted on the rising edge of the pulse, was the only apparent option at the time, since intense laser systems with wavelengths > 1 μm were not yet developed. Subsequent work continued studies of cesium and other alkalis using newly developed intense femtosecond lasers. A 90 fs mode-locked dye laser at 621 nm (two photons required to ionize) was used to observe 9 ATI peaks from cesium at an intensity of 10^{14} W/cm^2, and found the peaks to have substructure which was interpreted to be from the large Rabi coupling between the ground and first excited states. (This is despite the fact that the photon energy was far from a field free resonance.) A high energy ti:sapphire based laser (150 fs) (777nm) (4 photons required to ionize) was used to study the ionization yields of sodium using a collimated laser beam geometry to reveal subtle effects that would otherwise be obscured by the spatial intensity variation in a focused geometry. Oscillations in the ion yield as a function of intensity were observed and attributed to Ramsey interferences caused by coherent population transfer between bound states at two different times during the laser pulse [72], [73]. An interesting situation was explored in [74], where light with an intensity of 2×10^{12} W/cm^2 and at a wavelength of 266 nm ionized potassium. The photon energy at this wavelength (4.66 eV) is large enough to ionize potassium (I$_p$=4.34 eV) by single photon absorption, but a minimum in the ionization cross section (Cooper minimum [75]) suppresses this ionization channel. The absorption of 3 photons (2 ATI peaks) was observed using both a nanosecond pulse at 2×10^{12} W/cm^2 and a femtosecond pulse at 2×10^{14} W/cm^2.

The studies mentioned here have revealed interesting bound state resonance effects that were distinct from those observed in the noble gases using the same types of lasers at higher intensities. Ionization rates of the noble gases had been found to be described well by the tunneling model [36] and to not be very sensitive to the specific energy level structure of the atom. While bound state resonances have been observed in the noble gases' photoelectron spectra and have been shown to play an important role in ionization, they involved higher lying Rydberg states (Freeman resonances) where the number of photons required to populate the states is large compared to the number required to ionize from the excited state [76], [77]. This is potentially different from the resonance effects involving low lying states in the alkalis, where small numbers of photons populate the excited states and a larger number of photons is required to ionize from these states.

The difference between the observed resonance effects in the alkalis and noble gases can perhaps be attributed to the fact that because of the low ionization potentials of the alkalis, the studies were exploring the multiphoton regime, where it is apparent that bound state resonances could have a dramatic effect. For the experiments described above, $\gamma \approx 6$, which puts the interactions well within the multiphoton regime[1]. Taking the same laser wavelengths (1064 nm, 621 nm, and 777 nm), the higher I_p noble gases could withstand higher intensities, yielding smaller values for γ and the interactions could be understood as being closer to the tunneling regime, where the multiphoton excitation of excited states would appear to play less of a role. The precise role played by bound state resonances in the alkalis when in the strong field regime is not completely clear. Exploration of this regime with the alkalis could provide insight into the strong field interaction that could complement the work that has been done on the noble gases.

To push the interaction of the ground state alkalis into the tunneling regime, we had to wait for the development of intense, short pulse lasers at longer wavelengths. An early study using light at 1.908 μm [78](6 photons required to ionize cesium) (generated by Raman shifting the 1.064 μm output of a Nd:YAG laser) generated 7 ATI peaks ionizing cesium. The pulse durations used were 4 ns and 20 ps, with peak intensity of 3 TW/cm^2 for the ps case, and a saturation intensity for linear polarization found to be 4.4×10^{11} W/cm^2. Here, though, $\gamma \approx 3.5$ and while the interaction is closer to the tunneling regime it is still within the multiphoton regime. It is treated as such in the paper where perturbation theory is used in the theoretical modeling of the experimental results. Work done in our group using picosecond, mid-infrared pulses at wavelengths between 3 and 4 μm, was the first to study ionization of alkalis in the strong field regime [79]. For this work, $\gamma \approx 1.3$. A comparison with theory revealed that the onset and strength of the plateau in the photoelectron spectrum had a more pronounced dependence on the atomic species

---

[1] For the experiment done at 621 nm, the intensity used, 10^{14} W/cm^2, is well above cesium's saturation intensity. To calculate γ for this experiment, the intensity was taken to be $Isat \approx 2 \times 10^{12}$ W/cm^2. The experiment involving the Cooper minimum is not included in this comparison, since the meaning of γ in this specialized case is unclear.

than in the case with noble gases. Subsequent theoretical work explored the effect of 3 and 5 photon resonances between the ground and first excited state of potassium interacting with mid-infrared light [80]. Multiphoton population transfer was found to play a role. This scenario is slightly different from the one we are presently invesitgating, however. At a wavelength of 3.6 μm, we are four photon resonant between the 6s ground state and the 6p excited state, and so due to dipole selection rules [81] this transition is not allowed.

In this chapter, I present our measurements of the photoelectron spectra and ion yields from the interaction between our femtosecond mid-infrared laser and cesium atoms. The organization of the chapter is as follows: I begin by describing our time-of-flight spectrometer and then discuss details related to measuring ion mass spectra and photoelectron energy spectra. The details of the cesium oven are presented. This is followed by experimental results and a short discussion.

4.2 Experimental Apparatus

4.2.1 Overview of the Time-of-Flight Spectrometer

The apparatus we used for these measurements is a linear time-of-flight (TOF) spectrometer. In the most general sense, a TOF spectrometer measures the time required for particles to fly from a source region to a detector by route of a field free region known as the flight tube. The detected flight time is proportional to particular properties of the particles depending on the specific configuration. Our TOF spectrometer is configured to be able to measure either the energy spectra of photoelectrons or the mass spectra of ions generated during photoionization.

Figure 4.1 contains a schematic drawing of the main components of the spectrometer which include: the interaction region that is surrounded by field plates, a long field-free flight tube, and a microchannel plate detector. The details of the components are described shortly in Section 4.2.2. I begin here with a description of the basic operation. The laser enters the spectrometer and focuses at a position along the laser propagation direction which is carefully aligned with the flight tube and detector axis. Atoms which are within the laser focus are ionized and the released electrons fly off in directions governed by momentum conservation. The resulting ions also receive a momentum kick, but given their larger mass relative to the released electron (factor of ≈ 2000), their movement relative to the ion-electron center of mass is negligible. To measure the electron energy spectrum, the field plates around the interaction region are grounded and the MCP detector is configured to detect negatively charged particles. Electrons with trajectories that carry them to the MCP are detected and their arrival time at the detector is recorded. Because the interaction region and flight tube of the spectrometer are made to be as field free as possible, the velocity of the electron is determined predominantly by the energy it gained through the laser interaction and so its arrival time can be used to determine its kinetic energy. To measure the ion mass spectrum, the MCP is configured to detect positively charged particles, and voltages are applied to the field plates surrounding the interaction region to create an electric field to accelerate the ions towards the detector. The final velocity obtained by the ions, with which they enter the flight tube, depends on the ratio of the ions' charge state to their mass. Therefore, from the arrival time at the detector, we get a mass spectrum, which allows us to identify the species that have been ionized as well as the charge states (singly ionized, doubly ionized, etc.)[2] Our spectrometer is easily switched between electron and ion detection modes by swapping the cables providing high voltage to the MCP to different voltage divider circuits, and turning on (or off) the power supply that provides voltages to the field plates.

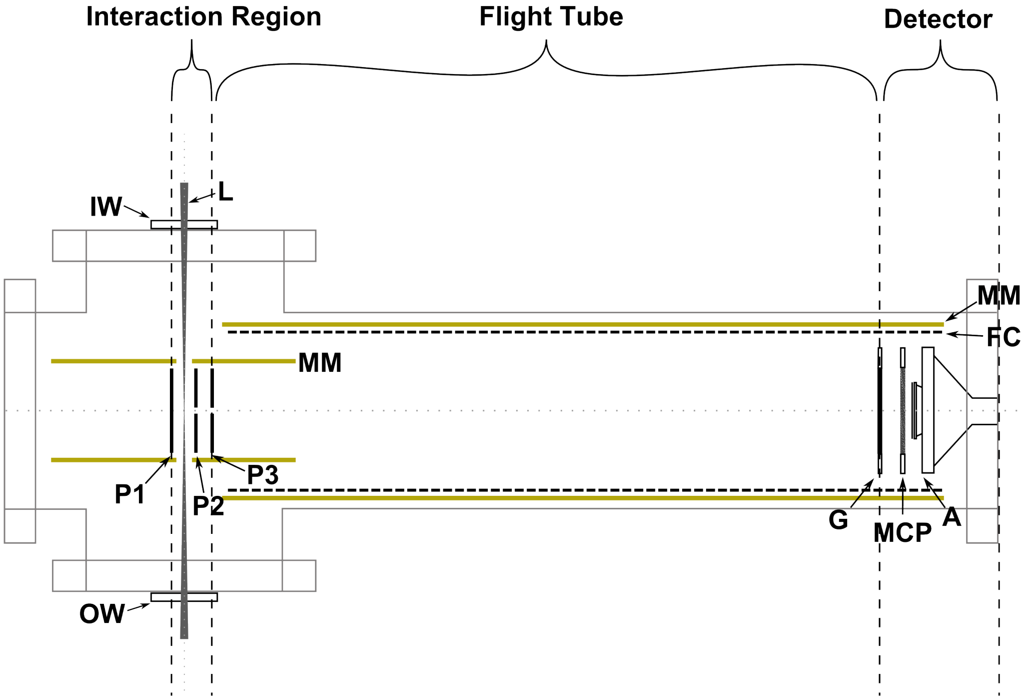

Figure 4.1: Schematic diagram of the time-of-flight spectrometer. The interaction region contains the laser (**L**) which passes through a CaF_2 input window (**IW**) and an output window (**OW**), as well as field plates (**P1**, **P2**, and **P3**). The flight tube is surrounded by mu-metal (**MM**) and a Faraday cage (**FC**) to keep it field free. The detector consists of a grounded grid (**G**), the multichannel plates (**MCP**) and collecting anode (**A**).

---

[2] Different species with equivalent charge to mass ratios will of course be overlapped in time and therefore not identifiable.

4.2.2 Spectrometer details

The time-of-flight spectrometer is housed in an ultra high vacuum chamber that contains, in addition to the required feedthroughs for the detector and field plates, a CaF_2 input window, an exit window, a cesium oven, a liquid nitrogen trap to freeze out the atoms from the cesium beam after they pass through the interaction region, and a variable leak valve. The chamber is pumped by two turbo pumps, a Leybold TurboVac, model TMP 361, and a Pfeiffer Balzer, model TPU110. The pumps have pumping speeds of 300 l/s and 110 l/s, respectively. The base pressure of the chamber, as measured by an ionization gauge, is 2×10^{-8} torr, and when the liquid nitrogen trap is filled the pressure drops to 4×10^{-9} torr. We believe that the base pressure of the chamber is limited primarily by the presence of the cesium oven which is outgassing water, since it cannot be baked, and which is continually effusing cesium atoms even when not heated[3]. For the relatively low intensities used for our cesium measurements, this base pressure is sufficient to keep the counts from the background very low. The laser interaction region is surrounded by field plates that are 2.5 inches in diameter, 0.5 mm thick, and made of molybdenum. As is shown in Figure 4.1, the laser passes between plates P1 and P2; holes at the centers of plates P2 and P3 allow the generated ions, or electrons, to pass through to the flight tube. The geometry of the field plates, along with the detector diameter and flight tube length, restricts the volume of the laser focus over which particles can be detected. Figure 4.2 shows a sketch of the geometry, where it is shown that the distance along the laser propagation axis over which particles are detected is 0.414 cm. For comparison, the confocal parameter for our laser focusing geometry, which includes a 250 mm focal length lens and a laser spot size at the lens ($1/e^2$ diameter) of 10.2 mm, is $b = 2z_R = 0.528$ cm. Generally, ionization is considered to occur throughout the volume of the laser focus, defined by the confocal parameter. In our case, we sample a region slightly smaller than that.

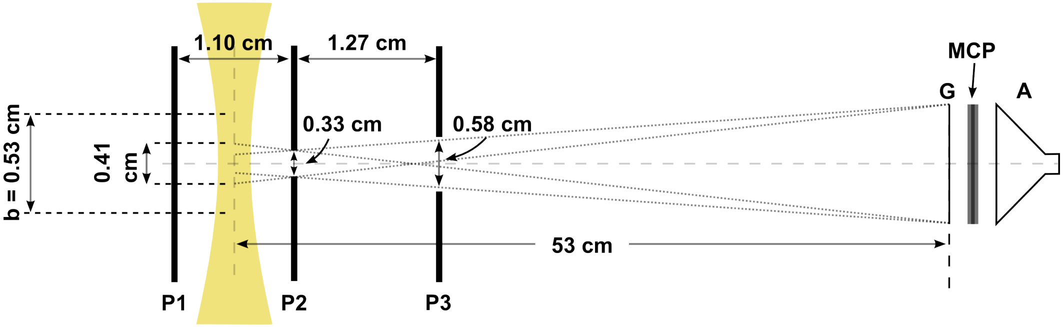

Figure 4.2: Field plate geometry.

---

[3] See the vapor pressure curve in Figure 4.8 and the cesium beam density as a function of temperature in Figure 4.11

For time-of-flight measurements it is critical that the flight tube remain field free. This is achieved by surrounding the flight tube by MuMetal shielding to eliminate unwanted magnetic fields, and within the MuMetal shield by a stainless steel faraday cage to eliminate stray electric fields. In addition, all components with surfaces facing the interior of the flight tube are coated with Aerodag®. Aerodag® is a colloid of graphite and isopropyl alcohol that can be sprayed on to a surface by means of an aerosol dispenser. The disordered orientation of the graphite particles reduces the impact of regions of localized electric fields, or patch effects, on the particle trajectories through the flight tube. The components that were Aerodagged include the field plates, the Faraday cage, the MuMetal surrounding the interaction region and the flight tube, and the grid before the MCP detector.

Our electron/ion particle detector is a multichannel plate (MCP) detector. In its simplest form, this kind of detector consists of a lead-glass plate containing an array of 10^5 to 10^6 parallel channels that are coated on the interior walls with a SiO_2 emissive layer. The front and back faces of the plates are coated with a metal layer acting as an electrode to electrically connect the channels in parallel. A voltage is applied across the plate so that when an incident particle enters a channel and strikes an interior wall, causing secondary emission, these secondary electrons are accelerated through the channel, increasing the energy of subsequent collisions and the number of secondary emissions, leading to an overall amplification of the incident electronic signal by more than 10^4. In addition to amplifying an individual charged particle to an easily detectable signal, the MCP detector provides a very fast time response, an important characteristic for our application. The output pulses of our MCP detector have a rise time less than 1 ns.

The details of our MCP detector are shown in Figure 4.3. The detector assembly was made by R. M. Jordon company and contains two MCP plates. The plates are 1.970 inches in diameter, 0.040 inches thick, and contain channels that are 25 μm in diameter, giving a length to diameter aspect ratio of 40:1. The channels are oriented at 8 degrees from the normal to the plate face to increase the probability that a given particle will enter and strike the wall, as opposed to flying straight through and not being amplified. The two plates are oriented in a Chevron configuration, where one plate is rotated so that the axis of its channels is on the other side of the plate normal relative to the other plate's channels. This configuration suppresses the unwanted phenomenon of ion feedback, where ions are generated by electron collisions with residual gas molecules within a channel and then accelerated back towards the front face of the plate by the MCP bias voltage where they can initiate another electron avalanche, creating false pulses or ultimately damage to the plate. The Chevron configuration removes the straight path from the back of the detector to the front. A stainless steel grid is located before the first MCP plate and is kept grounded to keep fields from the MCP plates from penetrating the flight tube. The grid has an input aperture of 1.750 inches.

The voltages that are applied to the plates, for both electron detection mode and ion detection mode, are included in Figure 4.3. In both modes, 2 kV is applied

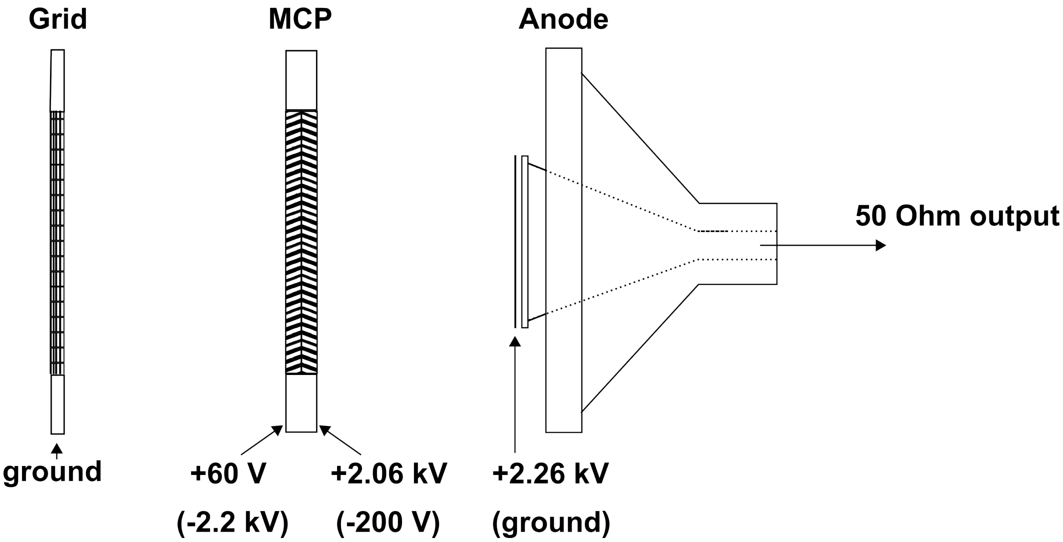

Figure 4.3: Schematic diagram of multichannel plate detector. Voltages supplied to the front MCP plate, back MCP plate and anode for electron (ion) are shown.

across the two MCP plates. Impedance matched plates were purchased so that the voltage drop across each plate would be equivalent. With this bias, the gain is approximately 10^5. In electron mode, there is a 60 V potential difference between the grounded grid and the first MCP plate in order to draw the electrons into the detector and increase their detection efficiency. In ion mode, the ions have already been accelerated by the field plates and so have sufficient energy to be efficiently detected. The amplified electronic signal at the back face of the second plate is accelerated by a 200 V potential difference to the collecting anode. Gold coated Kapton foil is glued to the face of the anode to capactively decouple the high voltage from the signal pulse and the conical shape of the anode reduces the impedance of the signal to 50 Ω, allowing the pulse to be read out and analyzed by standard NIM electronics. In order to eliminate reflections along the high voltage lines, we installed three low pass RC filters in vacuum between the voltage source and each of the leads to the front of the plates, the back of the plates, and the anode. Two separate Bertan power supplies provided the voltages to the detector through two separate voltage divider circuits, one for electron mode, the other for ion mode. In order to supply the voltages indicated in Figure 4.3, the electron mode power supply was set to 2.259 kV and the ion mode power supply was set to 2.174 kV.

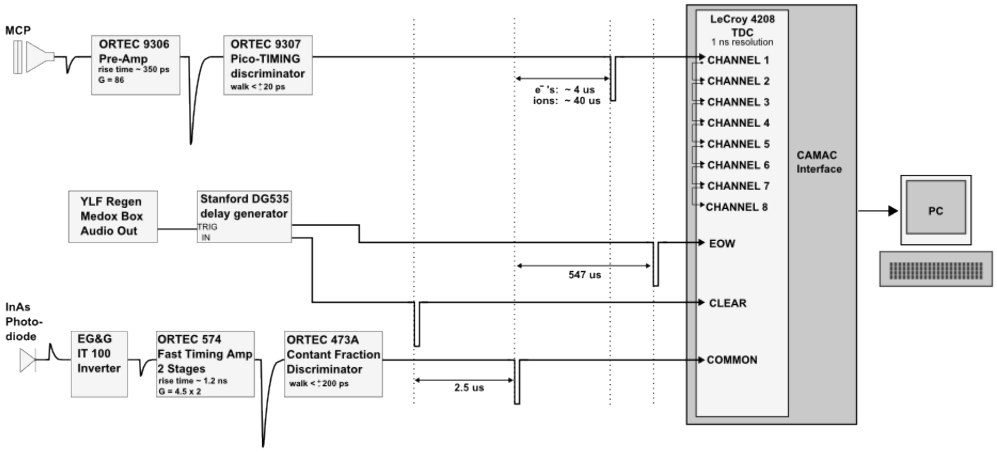

Figure 4.4: Time-of-flight electronics.

Our main objective is to measure the arrival time of electrons or ions at the detector. This is achieved using the chain of electronics that is depicted in Figure 4.4. The MCP pulses are amplified by a fast timing amplifier, sent to a discriminator to reduce false counts due to noise and convert the pulse to a logic pulse, and then sent to the input channel of a time-to-digital converter (TDC). The TDC (LeCroy, model 4208) outputs a digitized measure of the time between the input signal pulse and a common pulse. Our common pulse is provided by an unbiased InAs photodiode[4], positioned 2 meters before the interaction region of the spectrometer, which detects the arrival of the laser pulse. An EG&G IT-100 inverting transformer flips the photodiode signal to a negative going pulse and the pulse is then amplified by two fast timing amplification stages. The amplified pulse is discriminated by a constant fraction discriminator before being sent to the common input of the TDC. Clear and End of Window input pulses put the TDC in ready to operate and ready to readout modes respectively and are supplied by a Stanford DG535 timing delay generator which is synchronized to the laser repetition rate by a trigger from an output of the YLF regen Medox Pockels cell controller. The relative time delays between the four input pulses to the TDC are depicted in Figure 4.4. Although the dynamic range of the TDC is 8.3 msec, the time interval over which particles generated from a given laser pulse arrive is about 4 μs for electrons and 40 μs for ions. Data is collected from the TDC over these shorter time ranges. The TDC has eight channels that are cascaded so that a hit in one channel enables the next, and multiple hits, up to eight, can be recorded. For our experiments, in order to avoid space charge effects, the gas pressure was controlled so that the average count rate would be less than one hit per laser shot. Eight hits in one laser shot were rarely recorded. Readout of the data from the TDC is done via a CAMAC computer interface. A LabView program records and saves the data.

The time resolution of the TDC is 1 ns, and to take full advantage of this resolution it is necessary that all other components in the signal processing chain be equally as fast. The MCP pulse itself has a rise time of less than 1 ns (and a FWHM of 1.5 ns). As can be seen in Figure 4.4, the amplifier and discriminator used for the MCP pulse have sufficient rise time responses (bandwidth) to preserve the time resolution of the MCP. Also, the jitter due to discriminator walk from the Pico-TIMING discriminator is very small, less than 20 ps. The output of the InAs photodiode is also short and has a rise time of ~ 1 ns. The photodiode is operated in a slightly saturated mode, to reduce the effects of amplitude fluctuations in the laser, but not so saturated as to distort the shape of the pulse in time. Unfortunately, the output of the InAs photodiode is small, about 20-30 mV in amplitude, so multiple amplification stages are necessary to bring the pulse height up to the range required by the constant fraction discriminator, which adds some noise. Also shown in Figure 4.4 are the rise time and walk specifications for the amplifier and constant fraction discriminator used for the photodiode pulse, which preserve the fast time resolution of the photodiode pulse.

---

[4] InAs is sensitive to radiation at 3.6 μm.

An estimate of our actual timing resolution can be made by splitting the photodiode pulse and sending it down both its usual electronics chain and that of the MCP pulse. This is the method we use to determine t_0 (see Section 4.2.4). In this case, the counts fell into four time bins, although the majority of counts were limited to just two bins. A Gaussian fit to these four points indicates a FWHM of 1.5 ns.

4.2.3 Measurement of Time-of-Flight Mass Spectra

As was mentioned before, an ion's detected flight time is proportional to the square root of the ion's mass-to-charge ratio, $\sqrt{m/q}$. This is straightforward to understand by considering that the force experienced by an ion within the plates is $F = qE$ and so the total kinetic energy gained by the ion after it has moved through the accelerating region is $KE = qxE$, where x is the distance traveled within the accelerating region and q is the ion's charge state. Knowing that $KE = \frac{1}{2}mv^2$, it follows that the ion's final velocity at the exit of the accelerating region is $v = \sqrt{2qxE/m}$, and that ions with larger q/m ratios will arrive at the detector sooner than those with smaller q/m ratios. Given a flight tube of sufficient length, as the ions fly through the flight tube they will separate into bunches that are well spaced in time (and space) so that their arrival at the detector produces a time-of-flight spectrum consiting of a series of well resolved peaks, one for each q/m state present[5].

The sharpness of the peaks, and therefore the degree by which different species can be resolved, depends upon, among other things, the spatial distribution of the ions within the volume of the laser focus. This is evident from the expression for the velocity, which depends not only on q/m, but also on x. Considering just one q/m state, ions that are generated farther away from the detector fly through the flight tube faster, and although they first lag the other ions, having entered the flight tube later, at a particular point they catch up to the slower ions and then overtake them. Therefore, the spatial (and temporal) extent of a given q/m bunch changes in size as it moves through the flight tube. To obtain the narrowest peaks, and therefore best resolution in the mass spectrum, it is necessary for the particular point where the bunch is the tightest to be the position of the detector.

Our spectrometer is configured in a Wiley-McLaren configuration[82], which allows for easy control of the bunch focusing position. In this configuration, two accelerating regions are used instead of just one, and this provides additional parameters one can tune in order to focus the ion bunches at the detector. Specifically, in our setup the ratio of the electric field in the two regions can be easily adjusted by means of a voltage divider with variable resistors. Empirically, we found that the following voltage values produced the sharpest cesium ion peak: P1 = 222 V, P2 = 145 V, P3 = 0V[6], where the labeling of the plates is indicated in Figure 4.2. These are very close to our calculated values of P1=222V, P2=176V, and P3=0V.

---

[5] During data collection there is ≈ 1 ion flying down the flight tube at a time, but the bunch picture helps convey the main idea.

[6] This plate is kept at 0V as it is the beginning of the flight tube.

Figure 4.5 shows a time-of-flight spectrum for cesium ionized by our 3.6 μm laser at the highest intensity we used, 2.6×10^{12} W/cm^2. The FWHM of the cesium ion peak is 35 ns, giving a resolution of 0.1%.

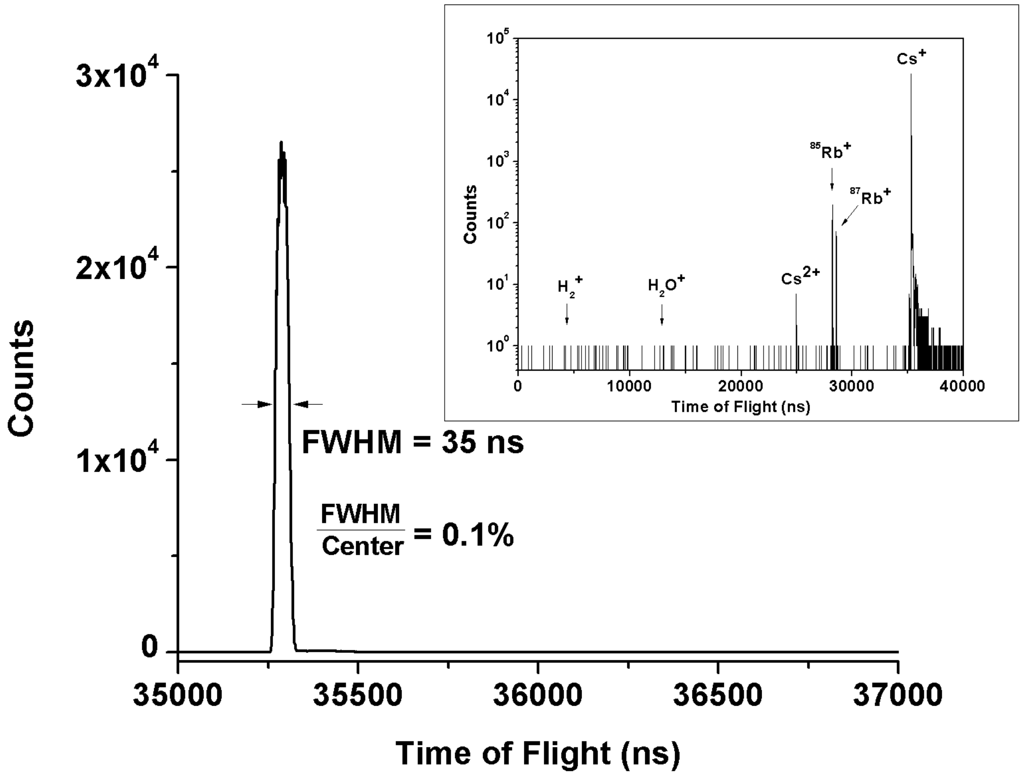

Figure 4.5: Mass spectrum containing Cs^+ and small amounts of Rb^+.

In order to calibrate the time axis for our mass spectra, we used the distinctive spectrum of xenon with its 9 isotope peaks. Xenon's fairly low I_p of 12.1 eV allowed us to collect a spectrum using the focusing geometry for our cesium measurements (f/20 lens). The 3.6 μm laser intensity was too low to produce enough ionization, but the higher power ti:sapphire beam produced a nice xenon ion spectrum. Since cesium has a mass of 133, the singly ionized Cs peak sits right between the $^{132}Xe^+$ and $^{134}Xe^+$ isotope peaks, which was quite convenient when originally searching for the cesium signal.

Examination of the mass spectra gives us an idea of the contamination counts that may be present in the photoelectron spectra. The inset of Figure 4.5 shows the same cesium mass spectrum, zoomed out and on a logarithmic scale. It is clear that even at our highest intensity, 2.6×10^{12} W/cm^2, our background counts are very low. There are no discernable counts from H_2O or H_2, only from Rb, which is most likely a contaminant in the cesium source. Even here, the cesium/rubidium ratio is high, 200:1. Interestingly, in this spectrum of 10^6 Cs^+ counts, there are 8 Cs^{2+} counts. It is a bit surprising to have any given the very high binding energy of 23.2 eV for Cs^{2+}, our meager photon energy of 0.34 eV, and estimated ponderomotive energy, U_p, of 3.14 eV. There were no appreciable Cs^{2+} counts at lower intensities, however, and this issue was not explored further.

4.2.4 Measurement of photoelectron spectra

The photoelectron kinetic energy can be obtained from the measured flight time through the simple relationship

$$KE = \frac{1}{2}mv^2 = \frac{md^2}{2(t+t_0)^2}$$

where d is the distance from the electron's generation point to the detector and t_0 is the time at which the electron was generated. In order to convert the measured time to energy, it is necessary to have precise knowledge of both t_0 and d. This is acquired through two measurements.

The t_0 measurement is done utilizing the photodiode signal produced by the arrival of the laser pulse shortly before the chamber. This photodiode pulse ultimately becomes the Common pulse for the TDC, from which the timing of the MCP signal pulses are measured. If the delay along the electronic chain from the photodiode to the TDC were equal to the delay along the electronic chain from the MCP output to the TDC, then the beginning of the first bin in our time-of-flight spectra would be t_0. In general this is not the case, however, and we are left with the task of measuring the difference in delay. Fortunately, this can be easily carried out by connecting a teed-off portion of the photodiode signal, which is usually connected to a pulse monitor, to the MCP preamplifier and allowing the photodiode pulse to travel along the chain of electronics usually traversed by the signal MCP pulse. Data acquisition is run as usual and the time bin in which the pulse through the MCP signal chain arrives, plus 6.67 ns to account for the fact that the photodiode is located 2 meters before the interaction region, is the value for t_0. We measured $t_0 = 10.17ns$ for the cesium measurements and $t_0 = 15ns$ for the spectrometer length calibration measurement described next. The two situations are not the same because they required different photodiodes.

The measurement of d is carried out by taking advantage of the well studied phenomenon of above threshold ionization by a long-pulse laser. In above-threshold ionization (ATI), which was first observed in 1979 [66], the ionizing electron absorbs more photons than necessary to escape the binding potential of the atom. The photoelectron energy spectrum for this process consists of a comb of peaks, with a peak separation of one photon energy. Given the right experimental conditions, which are explained below, the peaks are narrow and their absolute positions in energy can be easily predicted. To obtain the value for d, we measure an ATI spectrum under the appropriate conditions and use d as a fitting parameter in the time-to-energy conversion to force the peaks to fall in the predicted locations.

To understand the experimental conditions which yield an ATI spectrum with easily predictable peaks, we begin by considering that in order for above-threshold ionization to become appreciable, the atom is required to experience a moderately high laser intensity[7]. At such intensities, the laser field distorts the field free atomic system by ac-Stark shifting the Rydberg energy levels and continuum boundary up in energy by an amount equal to U$_p$, the ponderomotove energy, which is proportional to the laser intensity ($U_p \propto I\lambda^2$). The energy of an outgoing ionized electron is then given by

$$KE = (n+s)h\nu - (I_p + U_p)$$

where n is the minimally required number of photons to ionize, s is a positive integer representing the excess number of photons absorbed, and I_p is the field free ionization potential of the atom. Prediction of the peak locations then depends upon knowledge of U_p, which requires knowledge of the precise value of the laser intensity at the moment the electron was generated, which is difficult to obtain. Fortunately, all is not lost since a serendipitous result eliminates the problem. In an actual experiment, one must consider that the finite volume of the laser focus plays a role and that the measured electron energy reflects not only the energy gained in the ionization process, but also the energy gained through the freed electron's interaction with the laser field as the electron leaves its parent ion and traverses through the spatial extent of the laser focus. It can be shown [83], by treating the problem as a moving point charged particle in a laser focus, that no matter the initial position within the laser focus, the energy the electron will have gained after it has moves through the intensity gradient and left the laser focus is equal to U_p. This exactly cancels the energy loss due to the ac-Shift of the ionization potential and the electron energy is given simply by

$$KE = (n+s)h\nu - (I_p + U_p) + U_p = (n+s)h\nu - I_p.$$

The only condition is that the laser pulse be long enough for the electron to move completely out of the focus before the pulse leaves the interaction region.

To measure our ATI spectrum, we used our ti:sapphire, 0.8 μm laser, but bypassed the compressor so that the pulse was stretched out to approximately 200 ps. A $f = 100$ mm lens was used to focus the light into the spectrometer, producing an estimated spot size of approximately 5 μm. Considering the slowest of the expected electrons, with an energy of 1.5 eV, the time required to move out of the focus is approximately 2 ps, which is shorter than the 200 ps laser pulse and the long-pulse condition is satisfied. Xenon was used for the ionizing atom since its ionization potential is large enough to experience a laser intensity at 0.8 μm that is high enough to produce many ATI peaks before saturating, but not so large as to require a very high laser intensity to ionize. Since our pulse was stretched out in time, the peak

---

[7] Not too high, or the interaction moves from the multiphoton to the tunneling regime.

intensity we could reach was limited. We estimate that our intensity was 4.5×10^{12} W/cm^2, giving $U_p = 0.27$eV. Given this and that $I_p = 12.1eV$ for Xe, the value for the Keldysh parameter is $\gamma = 4.7$, consistent with a multiphoton ionization picture.

Figure 4.6 shows the energy-converted spectrum for the best fit of d. It is broken into two graphs for better visibility. Ten ATI peaks are present, with the first three displaying a double peak structure that is due to the fine structure splitting of the Xe$^+$ core. An ionized electron leaves the xenon ion in a p state. The splitting of the ion's ground state is imprinted in the electron's energy, where electrons that have left the ion in a $^2P_{3/2}$ state will have lower energy than those that left the ion in a $^2P_{1/2}$ state. In Figure 4.6, the solid lines in the data plots mark the expected positions of the $^2P_{3/2}$ and $^2P_{1/2}$ ATI peaks, plus a small offset of -0.365 eV. The peaks fall very nicely along the predicted points. The best fit value for d is 54.7 cm. The width of the ATI peaks give an upper estimate of the spectrometer resolution

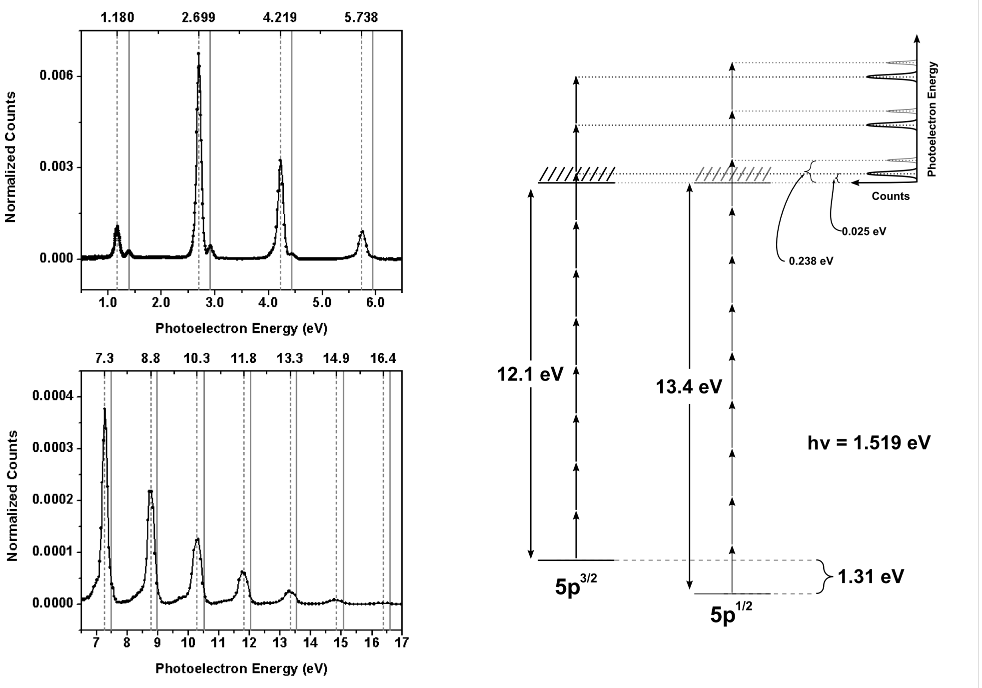

Figure 4.6: ATI spectrum, 800 nm ionizing Xe.

in electron mode. The FWHM widths of the first two ATI peaks is 0.1 eV. Over the full range of the spectrum (excluding the first peak), the fractional resolution is 3%.

Care must be taken when converting the TOF data sets into energy spectra because of the non-linear relationship between the two variables, t and E. The objective is to conserve the number of counts integrated over all the time bins, during the conversion to energy bins. The straightforward mathematical procedure consists of weighting the number of counts in an energy bin, that corresponds to a particular time bin, by a factor proportional to dt/dE, which in our case is $\propto E^{-3/2}$. In practice, this method comes with two problems which require subsequent treatment. First, for low energy electrons, the arrival times are distributed over a larger number of time bins, so that an individual time bin receives very few shots and its signal-to-noise ratio is lower. This makes the energy converted spectrum look very noisy on the low energy end. The solution here is to aggregate several time bins to produce a larger energy bin. Second, for much faster, high energy electrons, one time bin contains counts from a relatively wide range of energy values. The solution retained here tries to statistically redistribute the counts over smaller fixed energy bins. Both these data treatments are integrated in a Labview virtual instrument (vi) program, which allows selection of the energy bin that best suits the data conditions.

4.2.5 Cesium Oven

Atoms are introduced into the vacuum chamber by two means, a variable leak valve and an effusive oven. The variable leak valve (made by Varian) provides a controlled flow to fill the entire chamber with a gas and maintain a given pressure. This valve was used to introduce xenon into the chamber for diagnostic purposes and to calibrate the spectrometer length. The cesium studies were performed using the effusive oven, which produces a defined atomic beam. The details of the oven are presented in the following discussion.

The oven consists of three main parts: the inner-most chamber, containing the cesium and heating element; a collimator; and a cooling jacket. Figure 4.7 contains a diagram of the elements. The inner chamber consists of two parts which are joined together by a 1.33 inch conflat flange. The cesium is contained in the bottom part. A resistive heating element (Thermocoax, part number SEI 10/100-20/2 CFP10) is wound around the top portion of the oven. Its leads are connected through feedthrough vacuum connectors to a 30 V regulated power supply (Lambda, model LK342). A thermocouple (Thermocoax, part number LKA 10/50) is attached to the bottom of the oven and provides a measurement of the oven temperature. A 0.3 mm diameter aperture is present at the top of the oven allowing cesium to effuse out from the oven. The oven is bolted to the interior of a MuMetal cylinder which acts as a collimator, producing the well defined atomic beam. The collimator's aperture is 1 mm in diameter and is positioned 8 mm above the oven aperture. The collimator-oven assembly sits snuggly inside a water cooled (processed chilled water kept at 17° C) metal jacket which is connected to an 8 inch vacuum flange assembly that contains a bellows and tip-tilt positioning mount to provide adjustment of the oven and therefore cesium beam pointing. To load the oven, the bottom portion of the oven is loaded with 5 grams of cesium in a glove bag filled with clean nitrogen.

Care is taken when transferring the oven from the glove bag to the vacuum chamber to expose the oven to as little air as possible to avoid contamination of the cesium.

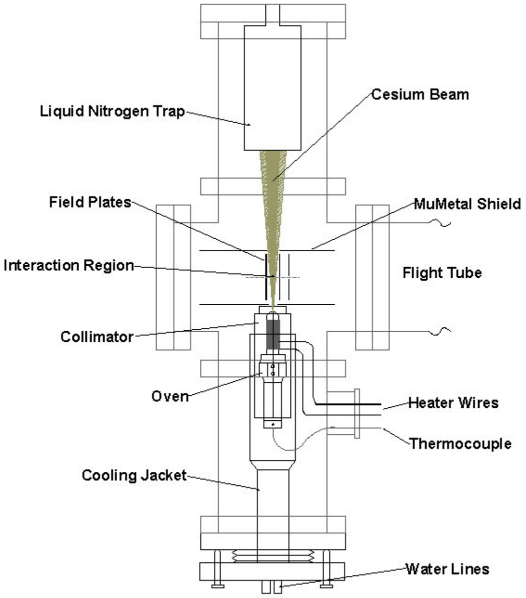

Figure 4.7: Side view of the cesium oven on the vacuum chamber.

To determine the properties of the cesium beam, results from kinetic theory can be applied provided the flow out of the oven is effusive. This is the case if the following assumptions are valid. First, it is necessary that the effusion of atoms from the oven does not alter the spatial or velocity distributions of the atoms within the oven source. This is valid as long as the radius of the oven aperture is small relative to the mean free path of the atoms in the source. Second, scattering of atoms as they exit through the oven aperture should be negligible. For an infinitely thin exit aperture, there is no scattering. For the real world case where the exit aperture has some thickness, scattering can still be ignored as long as the aperture thickness is small relative to the mean free path of the atoms.

It is easy to see that our oven behaves as an effusive source for the temperatures used in this work. Figure 4.9 shows the calculated mean free path for a gas of cesium atoms as a function of temperature. A Maxwell distribution was assumed within the oven source so that the mean free path is given by

$$\lambda = \frac{1}{n\sigma\sqrt{2}}. \tag{4.1}$$

Here n is the number density obtained from the ideal gas law and the vapor pressure curve shown in Figure 4.8. The atomic cross section, σ, is taken from Estermann, Foner, and Stern [84] to be 2.35×10^{-13} cm^2 for cesium-cesium collisions. Given that the radius of the exit aperture of our oven is $r_{aperture} = 0.015$ cm, it is seen from Figure 4.9 that $\lambda \geq r_{aperture}$ for oven temperatures less than 150° C. The highest temperature used in the work presented here was 115° C so we can be confident in the first assumption. The estimated aperture thickness is $\sim$ 1 mm, and it can be seen from Figure 4.9 that for the temperature range over which we operated, this thickness is not large compared to the mean free path, so we can assume scattering will not detrimentally affect our estimations.

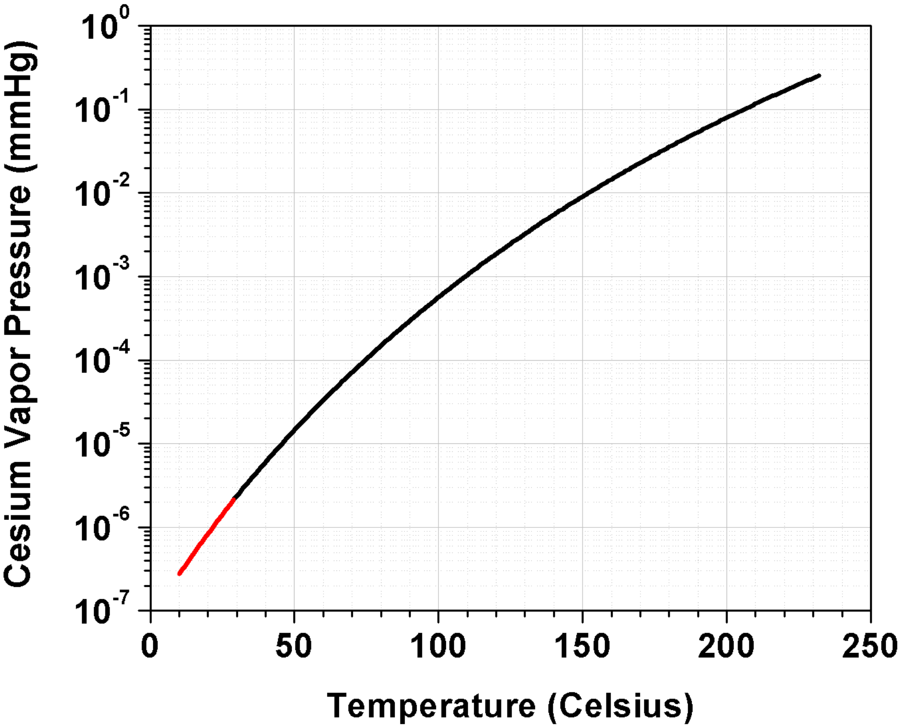

Figure 4.8: Vapor pressure curve for cesium. This curve uses coefficients from from Taylor and Lanqmuir [85] via Rozwadowski and Lipworth [86] and is valid for pressures less than 1 Torr.

The two main characteristics of interest for our oven are the beam size and density at the interaction region. The discussion here follows that presented in the first chapter of Norman F. Ramsey's book **Molecular Beams** [87].

The shape of the atomic beam is determined primarily by the geometry of the oven and collimator. Figure 4.10 displays the specific geometry for our oven and the resulting profile of the beam as it leaves the collimator. In the region where

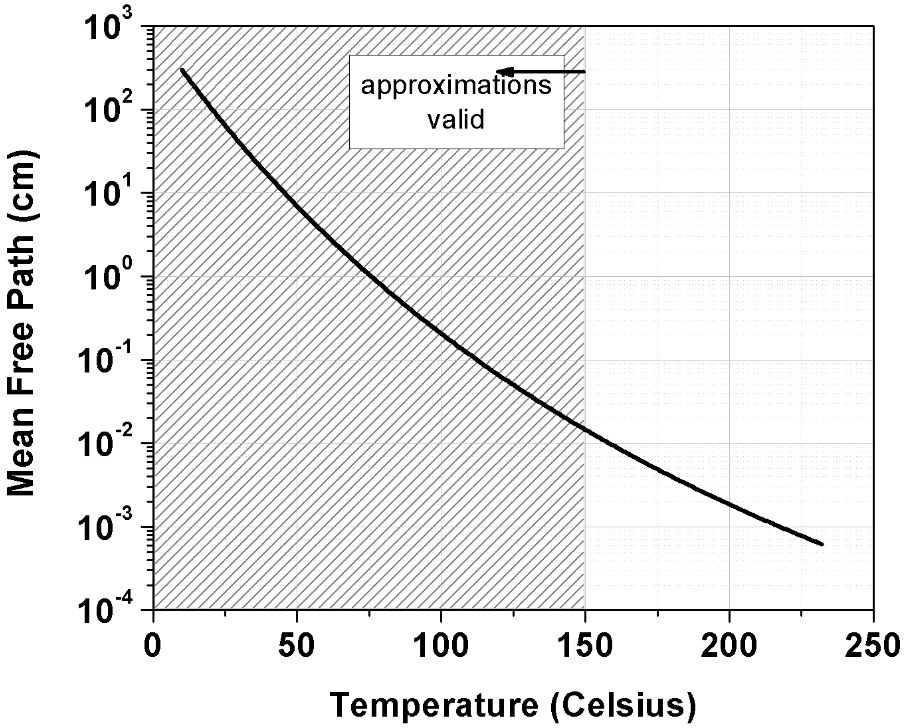

Figure 4.9: Calculated mean free path for a gas of cesium atoms, assuming a Maxwell distribution. The shaded region highlights oven temperatures for which the mean free path is greater than the oven exit aperture radius (0.015 cm). In this region, the oven can be considered effusive.

there is a direct line of sight through both apertures, the beam intensity can be considered constant. In those regions where a part of one aperture is obscured, the beam intensity drops off linearly. Shown in the figure is the position above the oven where the laser focuses, 41 mm above the collimator aperture. The constant intensity portion of the cesium beam at this plane is 4.59 mm in diameter. This is very large relative to the diameter of the laser focus, which is on the order of 100 μm. Also, this can be compared to the length, along the laser propagation, of the interaction region that we can detect (discussed in Section 4.2.2), which is 0.414 cm. The constant intensity portion of the cesium beam is comparable to this length. Based on these comparisons it is valid to assume a constant density within the interaction region.

With the value for the beam size at the interaction region, the density of cesium atoms can be estimated if the number of atoms passing through the interaction region plane per second, or intensity, is known. To determine the intensity of the

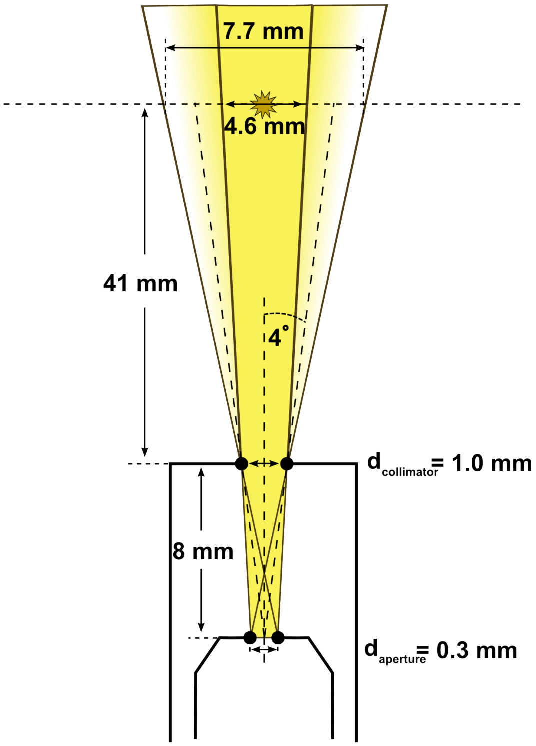

Figure 4.10: Sketch of oven/collimator geometry (not to scale).

cesium beam, it is necessary to first consider the number of atoms leaving the oven per second as a function of angle. For an effusive oven, with an infinitely thin exit aperture, this is given by

$$dQ = (\frac{d\omega}{4\pi}) n\bar{v} cos\theta A_s \tag{4.2}$$

where $n = \frac{p}{kT}$ from the ideal gas law, $\bar{v}$ is the mean molecular velocity in the source (given by $\frac{2}{\sqrt{\pi}}\sqrt{\frac{2kT}{m}}$ for a Maxwell distribution), A_s is the area of the source aperture, and θ is defined in the plane perpendicular to the plane of the aperture and from the normal to the plane of the aperture. Figure 4.10 shows that our collimator selects the atoms exiting at angles between -4° and +4°. So, to determine the number of atoms passing through the collimator per second we integrate 4.2 over these angles and find

$$Q = \frac{1}{2} n\bar{v} \sin^2 4^\circ. \tag{4.3}$$

The density at the interaction region is found by dividing Q by the beam area and the velocity of the atoms in the beam. The area is simply $\pi(4.6mm/2)^2$, using the beam size given in Figure 4.10. For the velocity, we take the most probable atomic velocity in the beam, which is modified from the most probable velocity in the source by $v_{beam} = \sqrt{\frac{3}{2}}v_{beam} = 1.22\sqrt{\frac{2kT}{m}}$ to take into account the fact that the velocity distribution in the beam is not a Maxwell distribution as in the source [87]. This is the case because the probablity for an atom to effuse from the source depends upon its velocity, as can be seen in Equation 4.2. Figure 4.11 shows the calculated cesium density at the interaction region as a function of oven temperature. Throughout this calculation, it has been assumed that there is no attenuation of the beam by scattering, within the channels of the oven and collimator apertures or within the beam itself. This is a valid assumption given a sufficiently low pressure. To check whether the calculated density values are reasonable estimates of the actual cesium density, a comparison was made between the expected ion count rates based on the calculated density and the actual detected ion count rates. Estimating the volume over which ions are detected as the area of the laser focus, with $\omega_0 \approx 55$ μm, times the length along z which is visible to the detector, 4 mm, (see Section 4.2.2), and taking a cesium density of 2.2×10^6 atoms/cm^3 corresponding to an oven temperature of 44 Celsius, we find there are 90 atoms within the interaction region. Measured ion count rates at this oven temperature and at intensities around the saturation intensity are $\sim$ 1 hit/shot. We do not know the precise detection efficiency for our

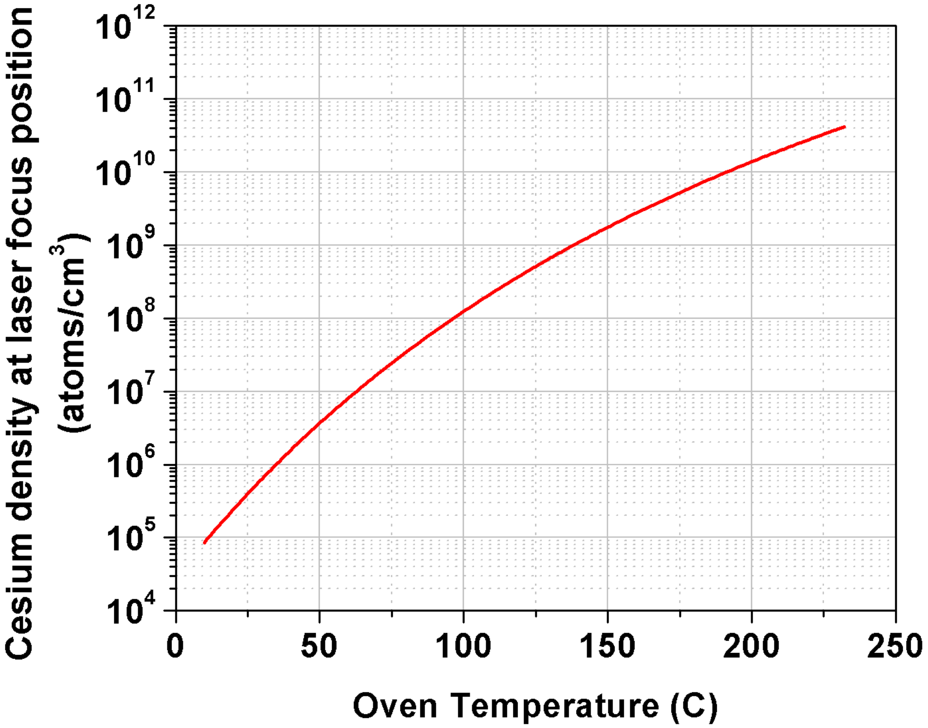

Figure 4.11: Calculated cesium density at the laser focus position.

MCP detector, but taking reported typical ion detection efficiencies for MCP's of 5-85% [88], we can see that our estimate is in the right ball park. Further evidence for the validity of our estimates can be seen in the ion yield curve, presented later in Figure 4.12, where different data sets taken at different oven temperatures have been scaled using the density estimate and the sets are found to overlap well.

4.3 Experimental Results

For the results presented here, a one inch diameter, $f = 250$ mm focal length, uncoated CaF_2 lens focused the mid-infrared laser light into the spectrometer chamber. The beam size at the lens was measured to be approximately 10 mm in diameter ($1/e^2$) using the FWHM estimation technique of closing an iris to reduce the transmitted power by a factor of 2, and measuring the diameter of the iris.

The power of the mid-infrared beam was controlled by two means: an attenuator comprised of a polarizer (II-VI Inc., part number PAZ-25-AC-2) and $\lambda/2$ waveplate (CVI, part number QWPO-3600-10-2-R15), and a set of three neutral density filters. The extinction ratio for the polarizer is not very good. It is specified to be 13:1 and we measured only $\sim$ 10:1. We found that the setting of the waveplate angle affected the shape of the photoelectron spectra, an effect we attributed to a rotation of the linear polarization of the laser field. This meant that our measurements at some waveplate settings were not sampling the same portion of the angular distribution as other settings. Therefore, only the photoelectron data that was collected at the waveplate setting corresponding to maximum transmission is presented here. A rotation of the linear polarization should not affect the ion yields, as the detection of the ions is dictated by the accelerating fields between the field plates. Since this data has been taken, a larger set of ND filters has been purchased and a longer focal length lens has been installed to reduce the intensity of the mid-infrared beam without the need for the attenuator.

The average power and power fluctuations were recorded for each data set using an InAs photodiode monitor at the output window of the chamber. The photodiode signal was amplified and then sent to the LeCroy 9362 1.5 GHz scope, where the histogram feature was used to get average pulse height values and widths. Typical fluctuations were 4-5 %. The photodiode amplitude was calibrated to power using a set of ND filters and a power meter (Coherent Lasermate, LD3 sensor).

4.3.1 Ion Yield

The ion yield curve is comprised of four different data sets taken at three different cesium oven temperatures, 44 C, 67 C, and 86 C, which according to our cesium beam modeling correspond to 2.2×10^6, 1.4×10^7, and 5.2×10^7 atoms/cm^3 respectively. The number of ion counts has been scaled by these cesium density values. In Figure 4.12, red lines mark the intensities at which the presented photoelectron spectra were taken. The intensity is obtained from the power measurements by assuming a

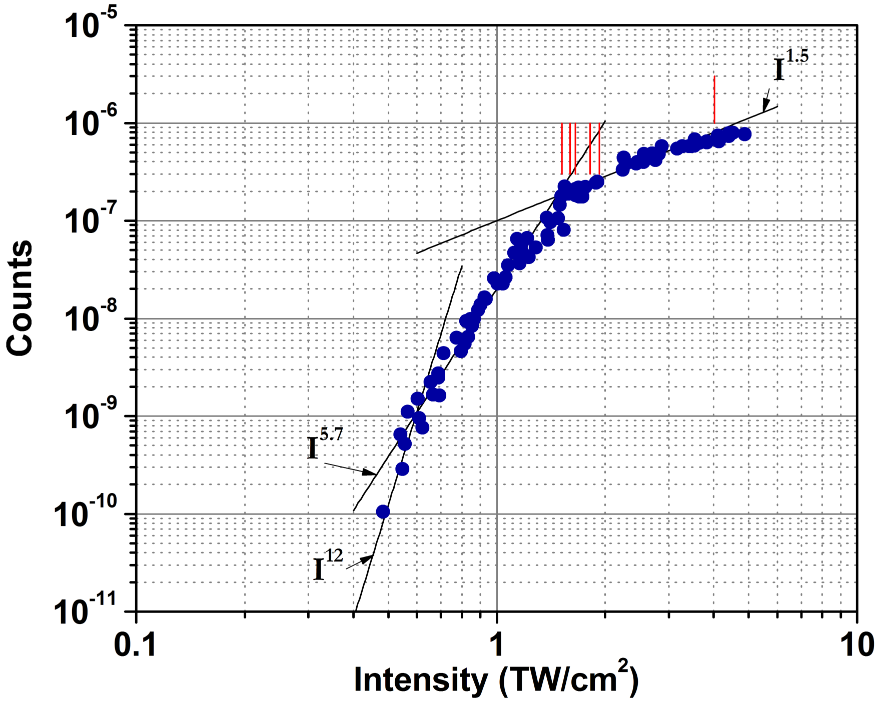

Figure 4.12: Cesium Ion Yield Curve.

focal spot size of $\omega_0 = 70\ \mu$m (1/e^2 radius) and a pulse duration of 110 fs. Saturation is seen to occur at 1.5×10^{12} W/cm^2. Above saturation, the yield scales as $I^{3/2}$ as is expected from the increase in focal volume [89]. Below saturation, the rate is $I^{5.2 \pm 0.15}$. Shown for comparison is the rate predicted by perturbation theory for a 12 photon process, I^{12}.

4.3.2 Photoelectron Spectra

Six spectra are presented at laser powers of 73, 35, 33, 30, 29, and 28.5 mW corresponding to intensities of 4.02, 1.92, 1.80, 1.65, 1.60, and 1.57 TW/cm^2 respectively. The spectra shown here have been converted to energy using the LabView vi described in Section 4.2.4. The spectra were taken at different cesium densities and count rates, but the number of counts in each spectrum is the same, ≈ 200,000 counts. Figure 4.13 shows the spectra plotted on log scales, from highest intensity, in the upper left hand corner, to lowest intensity, in the lower right hand corner. There are three main features present in the spectra. First is the high energy plateau. Second are the three "bumps", possible resonant structures, at ≈ 8 eV, ≈ 4.5 eV, ≈

2 eV. Third is the double peak structure of the individual ATI peaks in the lower energy portion. Each of these features is discussed in more detail below.

High energy plateau

In Figure 4.13 it is clear that a high energy plateau, similar to the plateau due to rescattering observed in noble gas atoms, is present. At the lowest intensity of 1.57 TW/cm^2, shown in panel (f), the plateau extends out to $\approx$ 20 eV. Taking the 3.6 μm photon energy of 0.34 eV and considering a multiphoton picture, this energy corresponds to a 71^{st} order process. As is seen from the other spectra, as the intensity increases, so does the cutoff position. Figure 4.14 shows the same spectra plotted in scaled energy units of U_p. The cutoff positions of all the spectra fall at the same point, 10 U_p[8]. While a 2 U_p break may be apparent at the highest intensity of 4.02 TW/cm^2 (panel (a)), it is somewhat questionable. In the lower intensity spectra, the "'bumps"' present around 2 U_p obscure any possible change in slope.

Resonant structures

Three "bumps" are evident in the spectra at $\approx$ 8 eV, $\approx$ 4.5 eV, $\approx$ 2 eV. For an alternate view, the spectra are shown in Figure 4.15 on a linear scale. In these plots, the grid lines indicate a spacing of one photon energy, 0.344 eV. The first grid line is positioned at 0.2389 eV, the expected excess energy carried by an electron assuming an absorption of the minimally required 12 photons and the field free value for the ionization potential. The 8 eV structure, which is clearly within the plateau of the spectrum, is most prominent in the 1.65 TW/cm^2 and 1.8 TW/cm^2 spectra. The ATI peaks within this structure are better resolved than other peaks in the spectrum, and have a more regular spacing that is closer to being exactly one photon energy.

The 8 eV structure appears to be similar to structures that have been observed in the noble gases with visible or near infrared light, most notably in argon and xenon (see Fig. 4.16). Numerous studies, both experimental and theoretical [77, 90, 91], have tried to shed light on the mechanism that causes this type of structure. A consensus [77, 90, 91] has developed over the majors steps, but there still exist two possible explanations for the basic origin of these enhancements in the plateau.

---

[8] A slight adjustment to the estimated focus spot size was made ($\approx$ 30%) so that this cutoff point would fall at 10 U_p. Given the large uncertainty in the estimated intensity, (±50%) this adjustment seems reasonable. The intensities shown in the ion yield curve (Figure 4.12) also include this adjustment, as do all the quoted intensities for the results. In experiments such as this, it is difficult to know precisely the absolute value of the laser intensity in the vacuum chamber. The large uncertainty (±50%) in the absolute value of the intensities quoted in this work should be kept in mind. However, the relative uncertainty between intensities is much better known. By monintoring the fluctuations in the laser power during the measurements, the relative intensities are known to be within ±5%.

Before discussing the different explanations, I'll first mention the common points that have been established.

First it is accepted that these enhancements can be explained in the single active electron approximation. This became apparent after very precise TDSE calculations, using the SAE, were able to reproduce the experimental results with astonishing precision [77]. This eliminated explanations involving electron correlations. Both experiments and calculation then established that the enhancements are due to very sharp resonant effects in the ionization, happening over a very short range of intensities. It is also clear that these resonant enhancements are the result of quantum effects. This is because they have to be the result of rescattering, since their final energy is in the plateau, but they are completely absent from the Simpleman description of rescattering.

With these points established, both TDSE [91] and quantum paths calculations [90, 92, 93] in the strong field approximation demonstrated that these enhancements are due to electrons whose trajectories cause them to return to the nucleus many times. It's been experimentally verified that these structures become more pronounced using longer pulses (with more cycles for the electrons to return) and it is not observed for few cycle pulses. Another feature exposed by these simulations is that the electrons that are born at a specific resonance (i.e. a specific intensity) appear more prominently in the plateau at energies corresponding to an interval of 5-8 U_p^r (where U_p^r is the value of U_p for the intensity that creates the resonance)[93]. An explanation based on classical trajectories has been proposed to explain this characteristic in [94]. In their calculations, the authors consider electrons born into the continuum at these resonances and the fact that they may have initial excess energy. The electrons whose trajectories allow multiple returns and that ultimately rescatter from the core are then shown to have a final energy between 5 and 8 U_p^r.

The last piece of the puzzle, then, is to explain what resonant effect is at play, producing the excess electrons at specific values of the intensity. As hinted at before, two main candidates have been studied: channel-closing resonances and multiphoton resonances with dressed excited states. A channel closing resonance occurs when the ponderomotive shift of the continuum in the laser field is such that it takes one more photon to ionize the atom. The other mechanism is similar in that it involves excited states (Rydberg states) that are also shifted ponderomotively so that a multiphoton resonant excitation can occur [94, 95], and from this state the electron is easily ionized. This mechanism is the same as that responsible for the so-called Freeman resonances that are visible in the low-order ATI peaks [96, 97].

Coming back to experiments, the important point is that the resonances can still be visible if they are not drowned in the much more numerous direct electrons. Often though, multiple resonances can be at play in a single photoelectron spectrum. Looking then at the results in cesium, it is impossible right now to test the dressed excited states option for lack of knowledge of their behavior, but we can see whether the channel-closing resonances could be invoked. In Fig. 4.17, the channel closing situations are indicated, as well as the expected energy range where the corresponding enhancements would appear. Comparing then to the 1.65 TW/cm^2 spectrum (Fig. 4.15 (d)), shown again in Figure 4.19, it is tempting to conclude that the three bumps observed are very close to being in the expected range of channel closings for 12, 13 and 15 photons. Figure 4.18 shows that the bump that would correspond to the 15 photon resonance also presents peaks at exact multiples of the photon energy, which is what is expected for a channel closing resonance [92].

Low energy structure

In Figure 4.20 a low energy portion of the spectra, from 0 to 6 eV, is plotted and in Figure 4.21 an even narrower low energy portion from 0 3 eV is plotted. Here we can make a few observations. First, we can see that the relative strength of the lowest order ATI peaks and the structure at 2 eV evolves as the intensity is increased. In the 1.57 TW/cm^2 and 1.60 TW/cm^2 spectra (panels (f) and (e)) the 2 eV structure is distinct from the first two lowest energy ATI peaks. As the intensity increases, this distinction becomes less apparent.

A second observation involves the energies of the ATI peaks in this energy range. By comparing the peak positions with the grid line positions it is easy to see that the energy of the peaks shift to lower energies as the intensity increases. This behavior is expected for nonresonant above threshold ionization. At higher intensities, the ponderomotive shift of the Rydberg and contiuum levels is larger which makes the effective ionization barrier larger and the excess energy carried by the electrons smaller.

A third observation regards the structure within each ATI peak. Each peak is split into two, with an energy separation of ≈ 0.1 eV. This separation appears to be constant regardless of the ATI peak's energy.

It is not clear at this point what is causing this splitting. It may be due to a complex Freeman resonance structure [96, 97]. Since the value of U_p in our case is a considerable fraction of I_p, and our photon energy is rather small, many resonances are produced in a small energy region, which may not be resolvable with our spectrometer, and which together could conceivably appear as broader structures within an ATI peak. It is also worth pointing out that the double peak structure in our ATI peaks is very similar to the structure observed in an older ATI experiment (one that was mentioned in the introduction to this chapter) performed with cesium and 621 nm light [98]. Figure 4.22 shows their ATI spectrum, compared with a calculation. The peaks labeled (1) and (2), comprising the double peak structure, are attributed as being due to the 6s-6p ac Stark doublet. It would be interesting if the structures in our peaks were due to a coupling between bound states. However, the conditions in the 621 nm experiment are drastically different from ours. As was stated in the introduction, for this experiment γ=5.2 (taking cesium's saturation intensity to be 2×10^{12} W/cm^2), clearly within the multiphoton regime. Also, in this experiment the ATI peaks' energy was observed to increase with increasing intensity, which is in direct contrast to our observation of the energy dependence of our ATI peaks.

It seems unlikely that such disparate experiments would share a similar underlying mechanism. To determine the cause of our peak splitting, a comparison with a theoretical model is required.

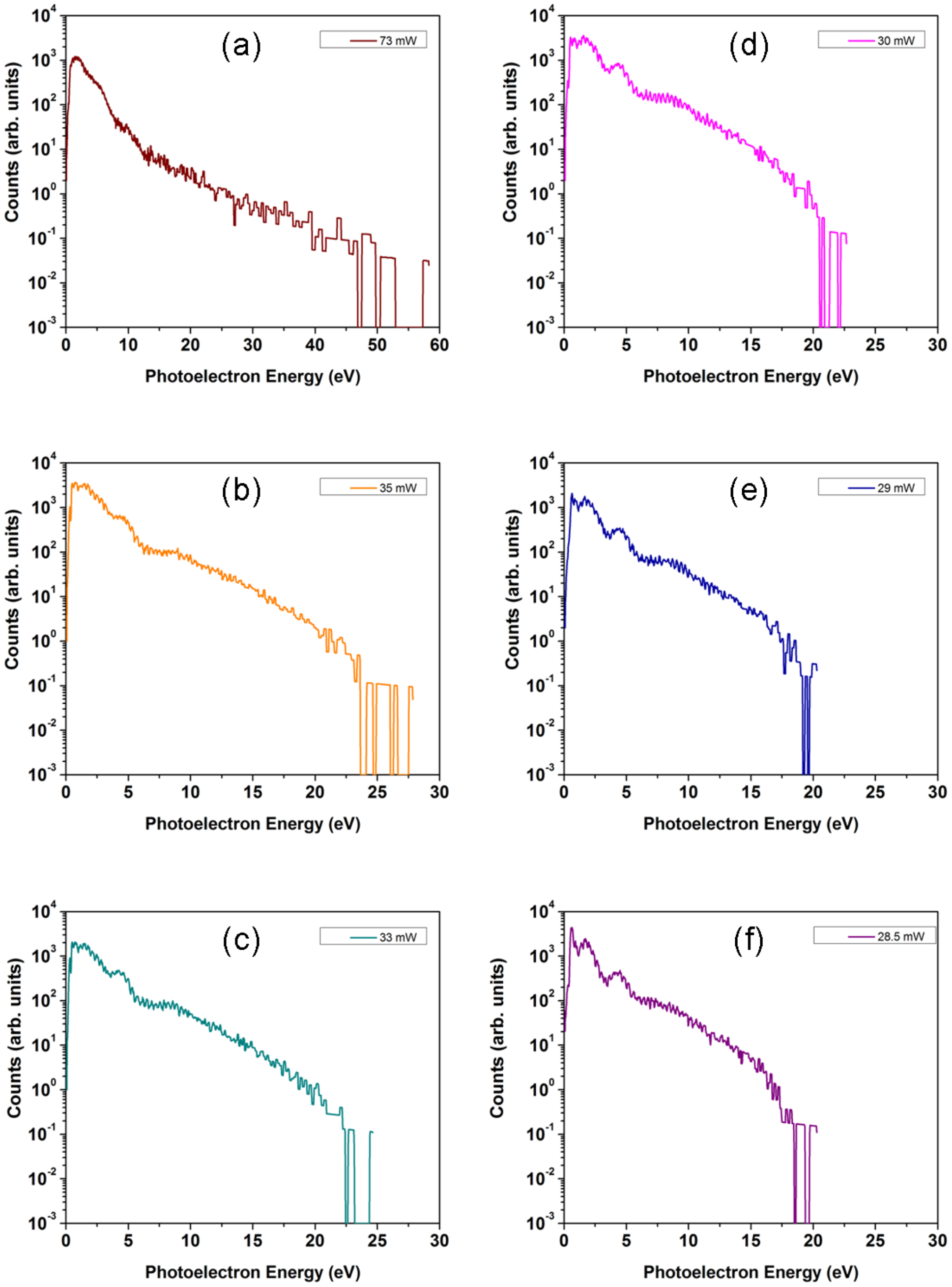

Figure 4.13: Cesium Photoelectron Spectra: (a): $I = 4.02$ TW/cm^2, $U_p = 4.86$ eV (b): $I = 1.92$ TW/cm^2, $U_p = 2.32$ eV (c): $I = 1.80$ TW/cm^2, $U_p = 2.18$ eV (d): $I = 1.65$ TW/cm^2, $U_p = 2.00$ eV (e): $I = 1.60$ TW/cm^2, $U_p = 1.93$ eV (f): $I = 1.57$ TW/cm^2, $U_p = 1.90$ eV.

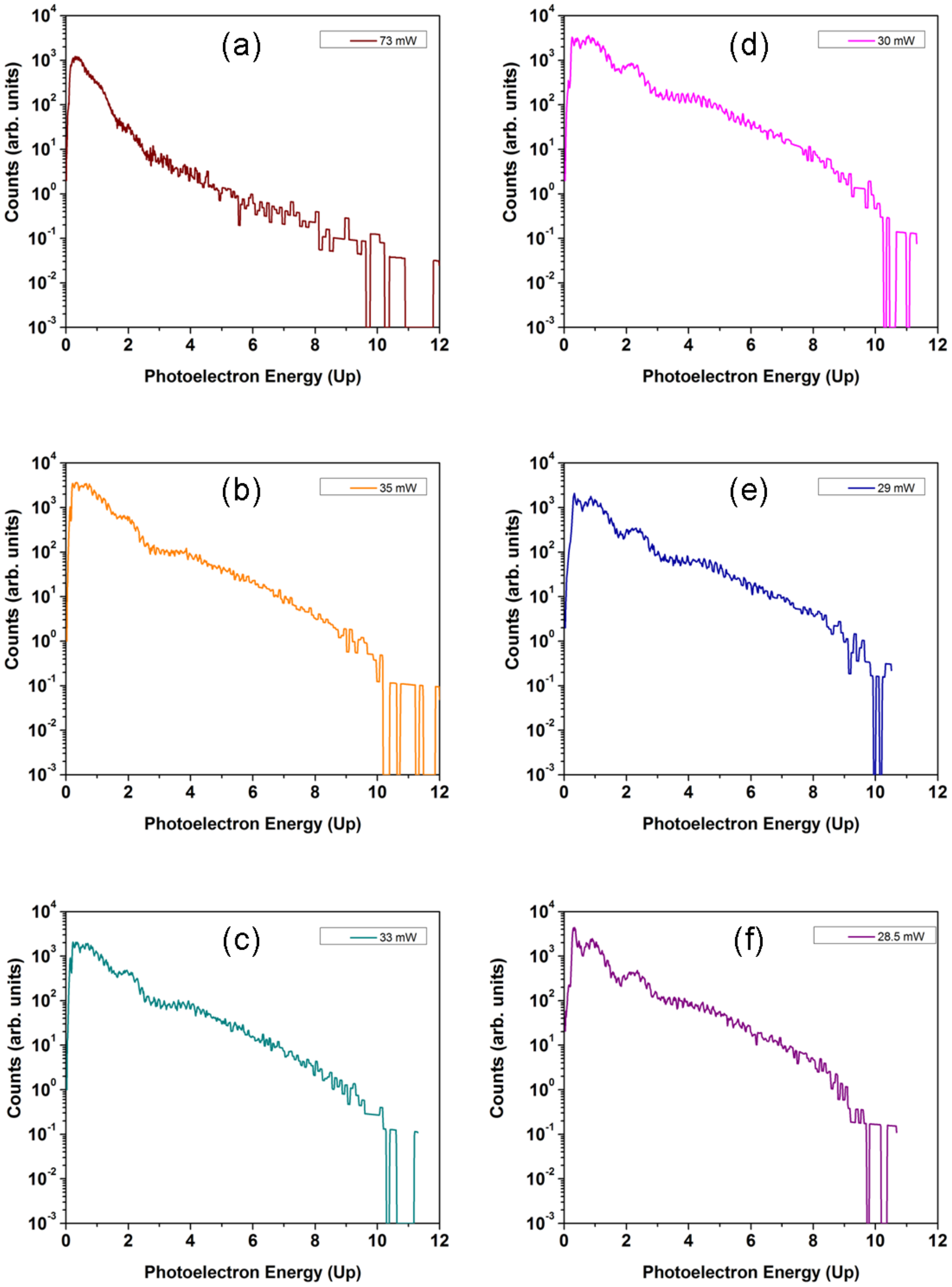

Figure 4.14: Cesium Photoelectron Spectra, scaled in units of U_p. (a): I = 4.02 TW/cm^2, U_p =4.86 eV (b): I = 1.92 TW/cm^2, U_p =2.32 eV (c): I = 1.80 TW/cm^2, U_p =2.18 eV (d): I = 1.65 TW/cm^2, U_p =2.00 eV (e): I = 1.60 TW/cm^2, U_p =1.93 eV (f): I = 1.57 TW/cm^2, U_p =1.90 eV.

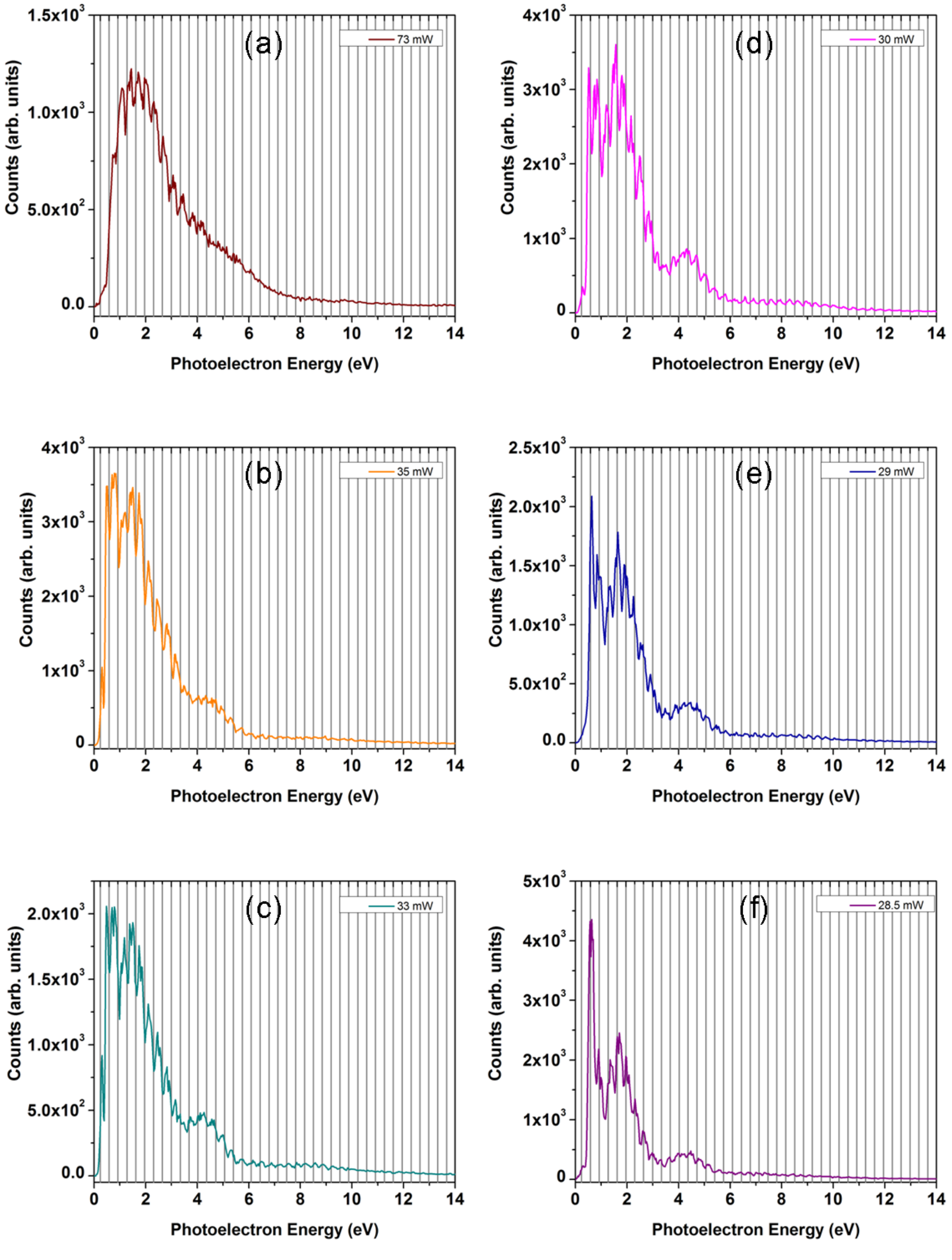

Figure 4.15: Cesium Photoelectron Spectrum, linear scale. (a): I = 4.02 TW/cm^2, U_p =4.86 eV (b): I = 1.92 TW/cm^2, U_p =2.32 eV (c): I = 1.80 TW/cm^2, U_p =2.18 eV (d): I = 1.65 TW/cm^2, U_p =2.00 eV (e): I = 1.60 TW/cm^2, U_p =1.93 eV (f): I = 1.57 TW/cm^2, U_p =1.90 eV.

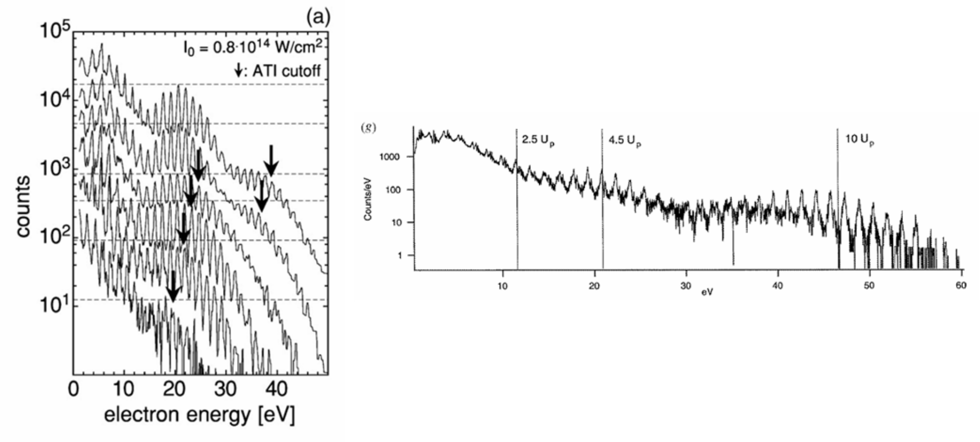

Figure 4.16: Examples of resonant structures in PES from noble gases and 0.8 μm light. On the left, argon. Reproduced from [90]. On the right, xenon. Reproduced from [77].

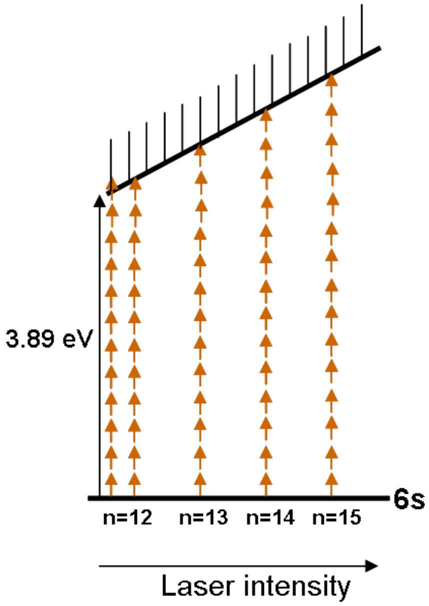

Cesium (I_p = 3.89 eV) **3.6 μm (hν = 0.344 eV)**				
n	12	13	14	15
U_p^r [eV]	0.25	0.6	0.95	1.3
5 U_p^r [eV]	1.25	3	4.75	6.5
8 U_p^r [eV]	2	4.8	7.5	10.4

Figure 4.17: Expected positions in PES of rescattered electrons produced from channel-closing resonances for the interaction between cesium and 3.6 μm light.

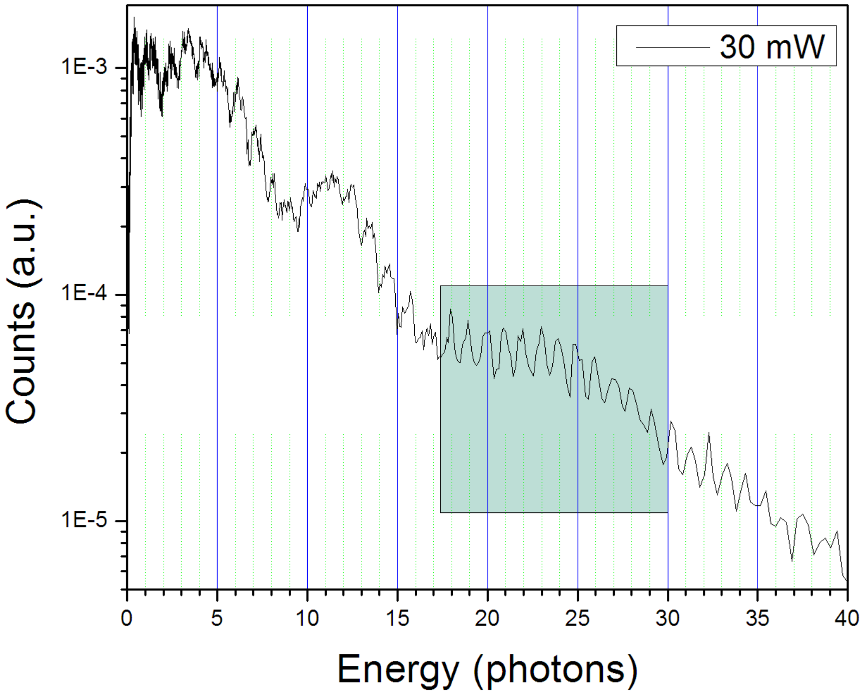

Figure 4.18: Cesium-3.6 μm PES at 1.65 TW/cm^2, plotted in units of photon energy (0.344 eV). The ATI peaks within the 8 eV resonant structure are shown to line up very well with photon number, as would be expected for a channel-closing resonance.

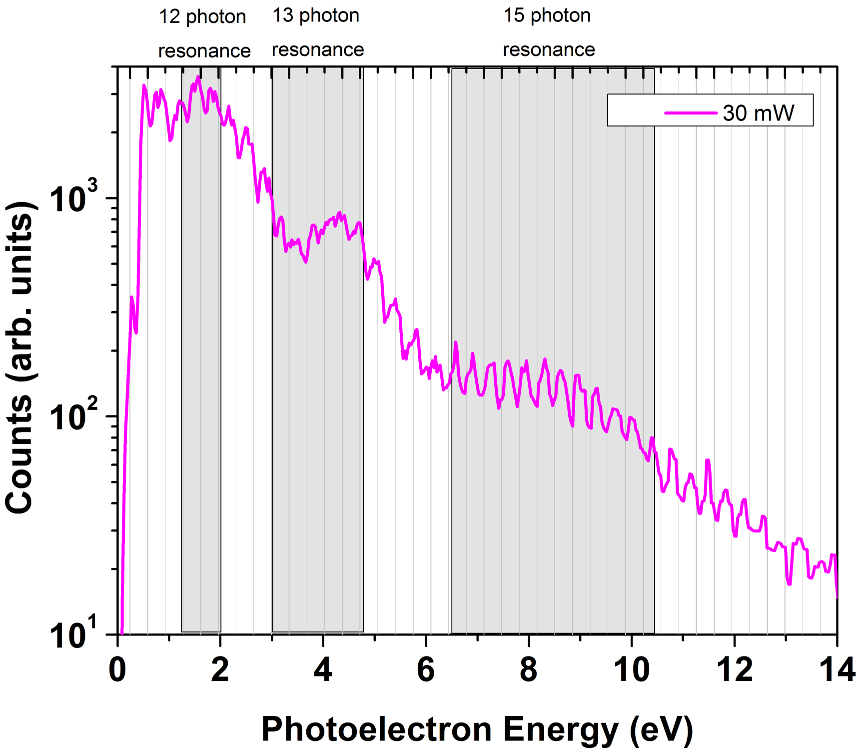

Figure 4.19: Cesium-3.6 μm PES at 1.65 TW/cm^2, plotted in eV. The energy ranges where 12, 13, and 15 photon channel-closing resonances should appear are indicated in grey.

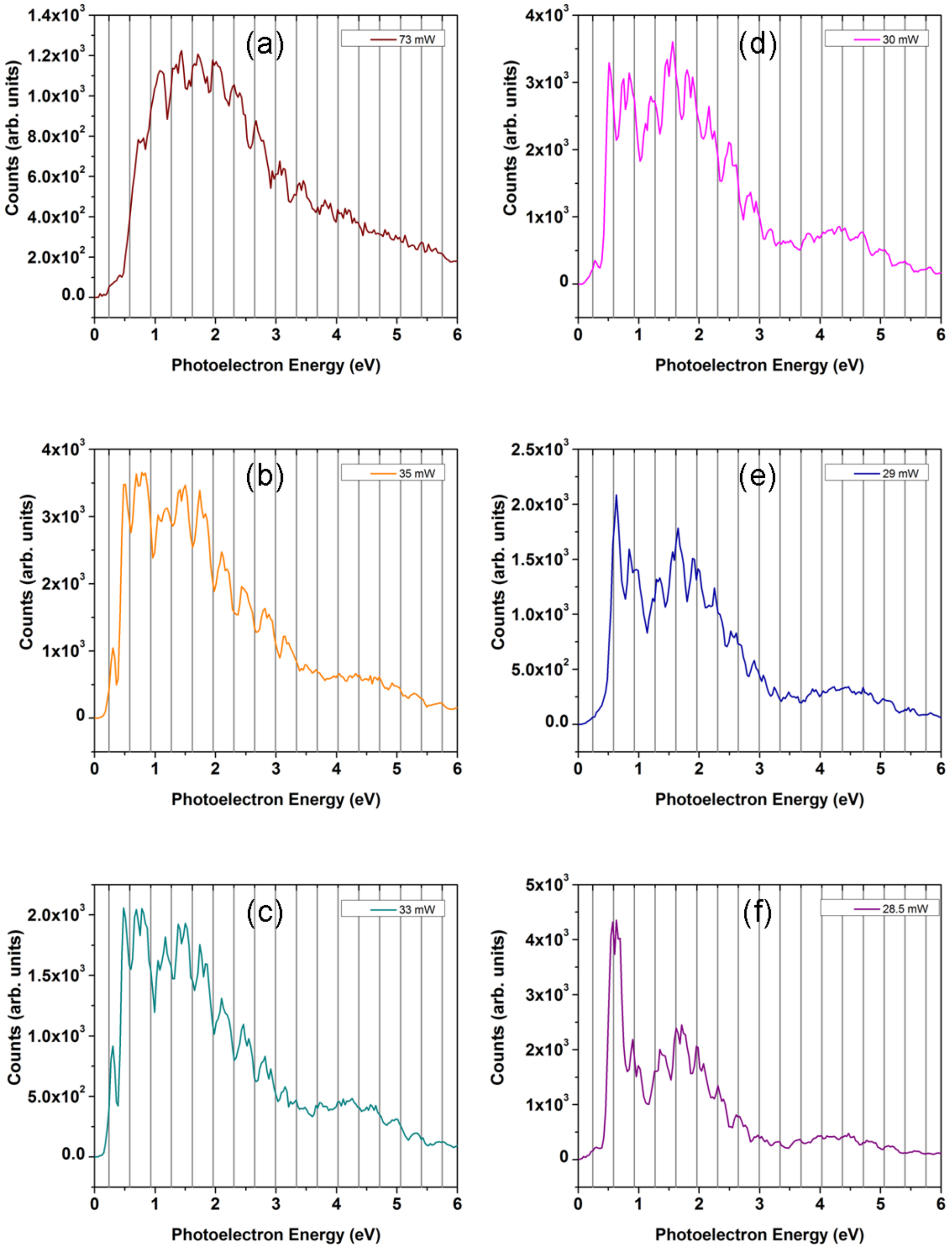

Figure 4.20: Cesium Photoelectron Spectrum, low energy portion. (a): I = 4.02 TW/cm^2, U_p =4.86 eV (b): I = 1.92 TW/cm^2, U_p =2.32 eV (c): I = 1.80 TW/cm^2, U_p =2.18 eV (d): I = 1.65 TW/cm^2, U_p =2.00 eV (e): I = 1.60 TW/cm^2, U_p =1.93 eV (f): I = 1.57 TW/cm^2, U_p =1.90 eV.

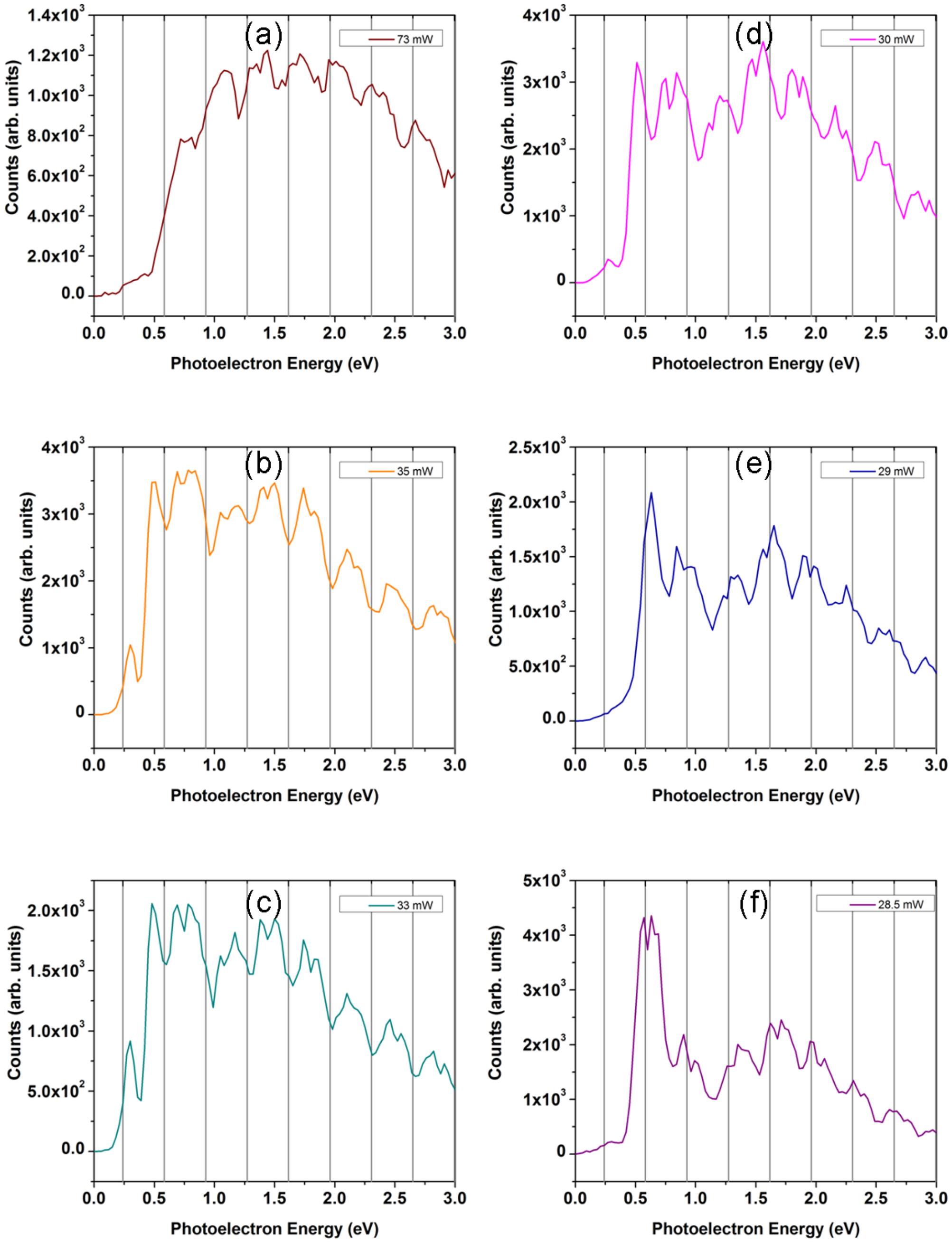

Figure 4.21: Cesium Photoelectron Spectrum, low energy portion. (a): I = 4.02 TW/cm^2, U_p =4.86 eV (b): I = 1.92 TW/cm^2, U_p =2.32 eV (c): I = 1.80 TW/cm^2, U_p =2.18 eV (d): I = 1.65 TW/cm^2, U_p =2.00 eV (e): I = 1.60 TW/cm^2, U_p =1.93 eV (f): I = 1.57 TW/cm^2, U_p =1.90 eV.

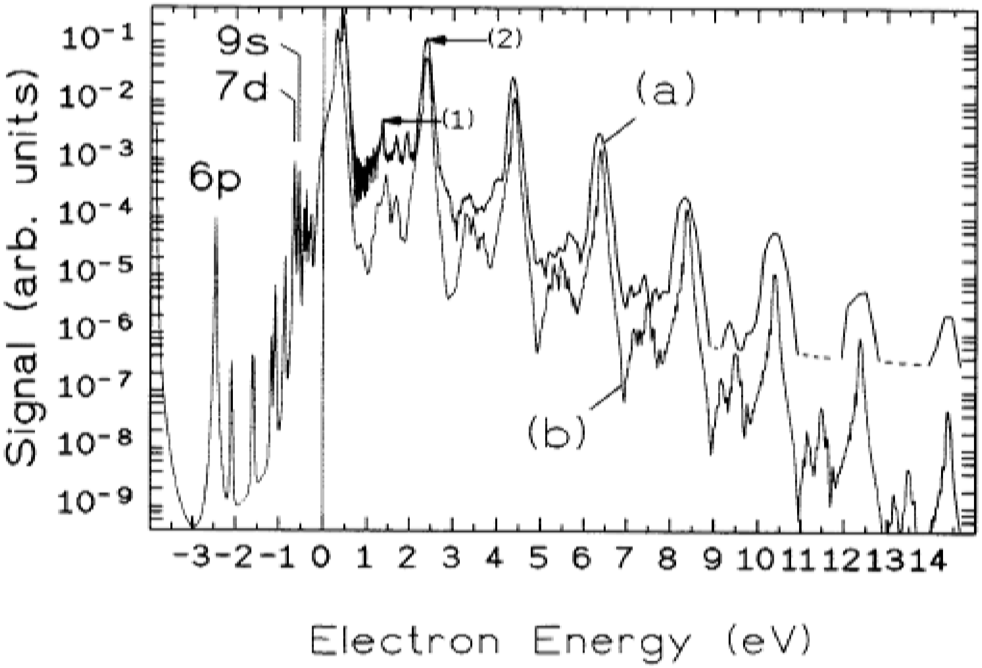

Figure 4.22: Cesium-621 nm PES, exhibiting a double peak structure in the ATI peaks. Reproduced from [98].

Chapter 5

Harmonic Generation

5.1 Introduction

One of the most spectacular phenomena resulting from the strong field interaction between an intense, short pulse laser and an atomic (or molecular) system is high harmonic generation (HHG). As was described in Chapter 1, HHG is the production of coherent radiation that has a distinctive broad-bandwidth spectrum consisting of a comb of peaks centered at odd order[1] harmonic frequencies of the fundamental driving laser frequency. The comb can extend up to very high orders and it has been demonstrated that the radiation can be phase-locked, allowing for the creation of extremely short pulses in time, on the order of 100 attoseconds. In this chapter I present our studies of the harmonic radiation generated in the strong field interaction between our 3.6 μm laser and cesium atoms.

Because our 3.6 μm-cesium laser-atom system can be described as a Keldysh-scaled system, we believe that our harmonics are related to the high harmonics that have been generated with ti:sapphire many cycle pulses and noble gases. Taking a moment to examine the parameters relevant to our harmonic generation experiments, we see that the focused intensity took values around the saturation intensity, $I_{sat} = 2 \times 10^{12}\ W/cm^2$, and that this intensity, along with our 3.6 μm laser wavelength, corresponds to a ponderomotive energy of $U_p = 2.4\ eV$. Taking this value for U_p along with $I_p = 3.89\ eV$ for the ionization potential of cesium we find the Keldysh parameter to have a value $\gamma = \sqrt{\frac{I_p}{2U_p}} = 0.9$. Table 5.1 shows a comparison between these values and those for several ti:sapphire-noble gas systems that have been used in particularly significant HHG experiments. In the first column are

---

[1] The presence of only the odd orders in the harmonic spectrum can be understood by considering the symmetry in the problem. Based on the Simpleman's model (2.2), the harmonic radiation is generated every half cycle of the driving laser field. The Fourier composition of this temporally periodic signal consists of odd orders in the spectral domain. If the radiation were generated once each cycle instead, the spectrum would contain both even and odd orders.

	Paul et al. (Saclay)	Mairesse et al. (Saclay)		Lopez-Martens et al. (Lund)	Our work (Ohio State)
	0.8 μm Ar	0.8 μm Ar	0.8 μm Ne	0.8 μm Ar	3.6 μm Cs
I_p	15.76 $[eV]$	15.76 $[eV]$	21.56 $[eV]$	15.76 $[eV]$	3.89 $[eV]$
I	1.0×10^{14} $[W/cm^2]$	1.2×10^{14} $[W/cm^2]$	3.8×10^{14} $[W/cm^2]$	1.4×10^{14} $[W/cm^2]$	2.0×10^{12} $[W/cm^2]$
U_p	5.97 $[eV]$	7.17 $[eV]$	22.69 $[eV]$	8.36 $[eV]$	2.42 $[eV]$
γ	1.15	1.05	0.69	0.97	0.90
I_{OTB}	2.5×10^{14} $[W/cm^2]$	2.5×10^{14} $[W/cm^2]$	8.6×10^{14} $[W/cm^2]$	2.5×10^{14} $[W/cm^2]$	9.2×10^{12} $[W/cm^2]$

Table 5.1: Comparison of γ and other parameters for the 3.6 μm-cesium system and those from significant HHG ti:sapphire-noble gas experiments. The over-the-barrier intensity for each atom is given as a reference.

parameters from an experiment done in 2001 at the CEA Saclay in France. Paul et al. [21] presented measurements of the relative phases of H11-H19 and were the first to demonstrate a train of attosecond pulses ($\sim$ 250 as). Presented in the second and third column are experiments done in 2003, also at Saclay. Mairesse et al. [44] presented studies of the relative harmonic phases over a larger harmonic range using both argon and neon and they demonstrated the importance of this phase for attosecond pulse production. In the fourth column are the parameters for an experiment done at the Lund Institute of Technology in Sweden by Lopez-Martens et al. [25] in 2005. They demonstrated a train of almost Fourier-transform-limited pulses of 170 attoseconds in duration. For all of these experiments, the value for γ falls in the range of 0.7 to 1.2. It is clear that our experiment is in the same Keldysh regime.

In Figure 5.1 we take a closer look at the comparison between the 3.6 μm-Cs system and the 0.8 μm-Ar system. Here the ionization potentials of argon and cesium are drawn roughly to scale, along with the photon energies of 0.8 μm and 3.6 μm. We can think about the scaled system as one in which the energies that are involved in the strong field interaction (photon energy, ionization energy, laser field strength, ponderomotive energy), have been scaled down to smaller values. This scaling includes the energy range of the harmonic spectrum. Figure 5.2 shows a comparison of the spectra. While the 0.8 μm harmonic spectrum begins in the ultraviolet (H3 is at 267 nm), H5-H11 of the 3.6 μm spectrum fall within the visible range of 750 nm-300 nm. This makes the scaled system a poor choice if one's intention is to

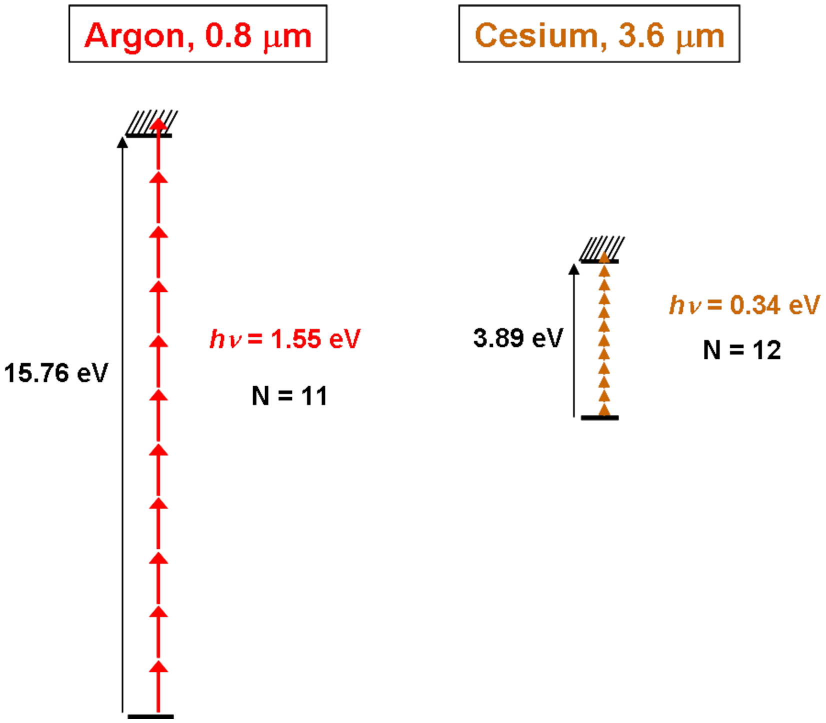

Figure 5.1: Comparison between the energies involved in the 0.8 μm-argon case and and 3.6 μm-cesium case.

generate coherent soft x-ray radiation, or attosecond pulses[2]. However, the scaled system provides a unique opportunity to do studies of strong field harmonic generation using standard, well-tested pulse characterization techniques that have been developed for the visible region.

Having established the hypothesis that our mid-infrared laser gives us access to the strong field regime and enables us to study HHG in the visible, there is an important difference between our experiment and those that have been done with ti:sapphire light and noble gases that should be mentioned. In our experiment the photon energies of many of the harmonics in the visible range are smaller than the ionization potential of cesium. In particular, H11 and those below have photon energies smaller than I_p, while H13 and above have larger photon energies. In the ti:sapphire studies, most of the recent work has focused on harmonics well within the plateau region of the spectrum or within the cutoff, where the harmonic photon energies are well above the ionization potential of the atom. This difference is notable because the Simpleman's rescattering model or its quantum generalization

---

[2] However, using the long wavelength driving lasers with high I_p noble gases is a good choice for these objectives. The HHG cutoff scales as λ^2 [24], [99] and the attochirp, which dictates the minimum achievable pulse width in a pulse train, has been demonstrated to scale as $1/\lambda$ [100]

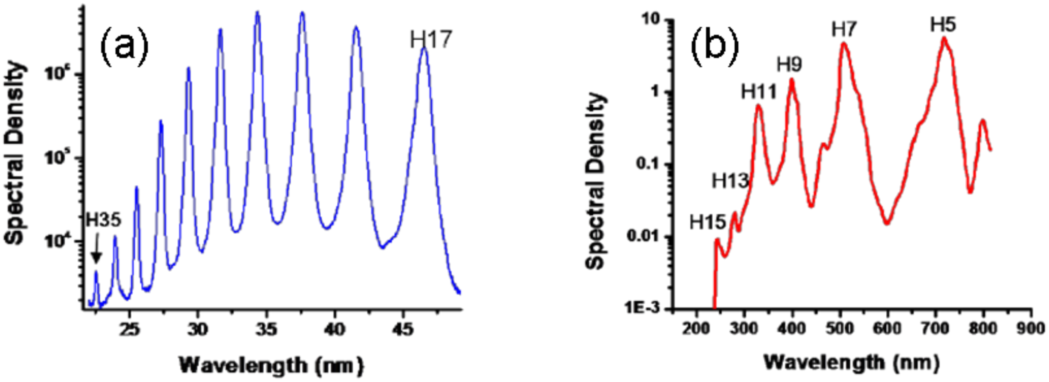

Figure 5.2: Comparison of harmonic spectra from (a) 0.8 μm-argon and (b) 3.6 μm-cesium.

(Lewenstein model), which have allowed for a simple interpretation of many properties of the ti:sapphire harmonics [43], assumes that the final step of the harmonic generation process is recombination of the electron wavepacket from the continuum to the ground state of the atom. The lowest predicted energy, which corresponds to an electron with zero return energy, is then I_p. It is not immediately apparent how the so-called "below threshold" harmonics fit within this simple model. A further investigation is required.

Because much of the recent work has focused primarily on higher order harmonics, it is necessary to look back to the early days of HHG to find work exploring the lower order harmonics. The group at the CEA Saclay in France was one of the first to observe HHG, up to H33 in Ar, H29 in Kr, and H21 in Xe, using a 36 ps Nd:YAG laser at 1.064 μm [16], [101]. Similar to our case, with argon and krypton H3-H11 of 1.064 μm light were below-threshold harmonics, and with xenon H3-H9 were below-threshold. In their spectra, they observed a rapid decrease in the strength of H3, H5, H7 and then a flat plateau beginning with H7 and extending to a high order cutoff. Extensive studies of the harmonics' properties were carried out, properties such as their dependence on laser intensity, on gas density, and focusing geometry [102]. In addition, nonperturbative theoretical calculations were carried out, including a numerical integration of the time-dependent Schrodinger equation (TDSE) with an incorporation of macroscopic propagation effects that was found to match the experimental results very well [103]. This work predates the Simpleman's rescattering model, however, so the results were not interpreted within this context. Subsequent work turned towards optimizing the high harmonic efficiency and cutoff position, and so experimental apparatus were modified to be more effective detecting very short wavelength radiation and less attention was paid to the lower orders. In fact, most HHG experimental setups that are used today are blind to the lowest order harmonics due to the necessity of filters to block the fundamental radiation from sensitive xuv or x-ray cameras.

It is also important to mention the large amount of work that has been done in the regime of more traditional nonlinear optics using alkali vapors. The alkalis were seen as a promising medium for frequency upconversion due to the fact that they possess a very high value for $\chi^{(3)}$ (orders of magnitude larger than that of the noble gases). Harris and collegues at Stanford University used mixtures of noble gases and alkali vapors to enhance the phase matching in third harmonic generation [104]. Using a 30 ps laser at 1.064 μm and a mixture of rubidium and xenon, they generated the third harmonic at 0.3547 μm with an efficiency of 10% [105]. (This is in stark contrast with the efficiencies reported for HHG, where 10^{-5} is considered to be not too bad.) Some of the highest harmonic orders generated in the traditional nonlinear optics regime have been reported using alkali vapors. For instance, the ninth harmonic of a picosecond Nd:glass laser was produced in a sodium vapor [13]. The impact of multiphoton ionization on third harmonic generation was explored using a 28 ps Nd:YAG laser at an intensity of 3×10^{12} W/cm^2 in a sodium vapor [106].

Our work with the scaled atom-laser system is in one sense a bridge between these two bodies of work. Our mid-infrared laser allows us to drive the harmonic generation process beyond the perturbative regime into the strong-field regime. In addition, our scaled-system allows us to study the below-threshold harmonics since they are easily accesible in the visible range. The hope is that by studying these harmonics, we can gain a better understanding of how the ideas that have been developed to describe HHG can be applied to the threshold region, as well as learn how features characteristic to this region, such as bound-bound transitions, can impact the harmonic generation process.

The work presented here is an extension of work that was done in our group at Brookhaven National Lab using a previous version of the mid-infrared laser that produced pulses with a duration of 2 picoseconds [107, 108]. The yield of harmonics H5 through H17, generated in a cesium vapor, was measured and an autocorrelation measurement technique was used to estimate the pulse durations for harmonics H5, H7, and H9.

The organization of the chapter is as follows. The heat pipe oven and spectrometer set-ups are described. Then, measurements of the harmonic spectra are presented, including yield measurements and detection of H31. Following this, the XFROG measurement is presented.

5.2 Experimental Apparatus

5.2.1 Heat Pipe

In order to generate a detectable harmonic signal, it is necessary to use a gas target with a rather high density, typically on the order of 10^{17}-10^{18} atoms/cm^3 (corresponding to $\sim$10-100 Torr). When working with cesium, producing a reasonably dense vapor is a bit trickier than when working with the noble gases. To begin, there is the fact that cesium is a solid at room temperature. Although cesium's melting point is low (28.4° C), and its vapor pressure is relatively high (10 Torr at 370° C), so that heating to very high temperatures is not required, the mere necessity of a heater is a complication not present in noble gas sources. More importantly, though, is the fact that cesium is extremely reactive. It will ignite spontaneously in air at room temperature, and it will react violently with hydrogen, oxygen, and water. With water, cesium reacts creating cesium hydroxide, CsOH, a very strong base that will corrode metals and etch glass. Because of this, care has to be taken not to expose cesium to air and to keep it away from all optical components.[3]

For our experiments, to produce a contained column of dense, cesium vapor we used a conventional spectroscopic heat pipe oven. Spectroscopic heat pipe ovens have long been used as a reliable means of producing a homogeneous column of alkali vapor. The spectroscopic heat pipe oven was first presented in 1969 by Vidal and Cooper [110], as a modification of the heat pipe [111], a device designed to efficiently, and continuously, transport large amounts of heat. In the original heat pipe, continuous heat transfer is achieved through the repetition of the following sequence: a fluid is evaporated at one end of a pipe, the resulting gas diffuses along the length of the pipe, the gas condenses at the other end of the pipe, and the fluid is returned to the evaporation region by means of capillary action in a wick. Due to the nature of the evaporation and condensation processes, heat transfer is achieved from one end of the pipe to the other with very little temperature gradient. As a consequence of this the vapor throughout the pipe remains at a constant temperature (that at which it was evaporated). The heat pipe's isothermal properties, as well as its ability to contain and recycle reactive materials such as alkalis, were recognized by Vidal and Cooper as being useful for a spectroscopic vapor source. Their modification allowed for the heat pipe to operate in an "open-ended fashion", with the vapor contained in the middle section of the pipe and with windows on each end so that light could enter and exit. In this section, I will begin by briefly describing ideal heat pipe operation, which we attempted to achieve for our experiments. I'll then discuss the specific details of our setup and our heat pipe's performance. For further details theoretical treatments that model the

---

[3] Sapphire is one optical material that is fairly inert to cesium's reactants. Because of this, sapphire cells are often used to contain dense cesium vapors. See for example, Reference [109]. Sapphire's transmission properties were not optimal for our experiments, and so we did not use it.

spectroscopic heat pipe's operation can be found in [112] and [113] and an analysis of its limitations in [114].

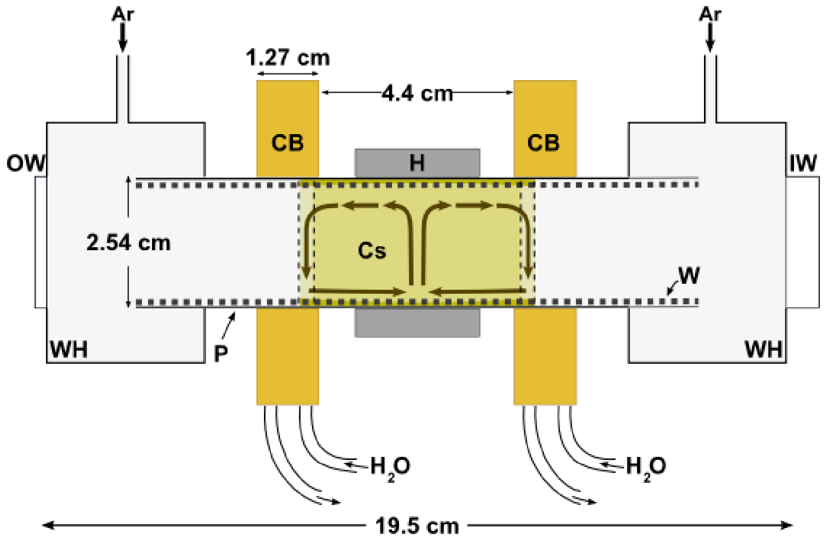

Figure 5.3: Schematic of heat pipe, cross-sectional view.

Figure 5.3 presents a cross-sectional view of the heat pipe and depicts the primary components which include: the stainless steel pipe (P), the band heater around the middle section of the pipe (H), the stainless steel mesh lining the interior of the pipe which acts as the wick (W), the input and output windows (IW,OW), the cooling blocks surrounding the pipe near the windows (CB), and cesium which is loaded onto the wick in the center of the pipe. The details concerning each of the components are given below. To operate the heat pipe, it is first filled with a buffer gas at a fixed pressure and the cooling blocks are chilled to cool the ends of the pipe. The heater is turned on which causes the cesium to melt and then evaporate, creating a saturated vapor. Convective flow, as was described for the original heat pipe, becomes established; The cesium evaporates, moves towards the cooler ends of the pipe, condenses, and then is wicked back to the heater region. Due to the cesium movement in the pipe, the buffer gas is pumped out of the central region and an equilibrium is produced where a well defined vapor column, consisting only of cesium, is present in the middle of the pipe. The regions in the ends of the pipe near the windows contain only the buffer gas, and there is a narrow transition region delineating the cesium and buffer gas regions with a width on the order of the mean free path of cesium in the buffer gas). Once this equilibrium is established, the pressure of the cesium vapor is equal to the pressure of the buffer gas. A further increase in the heater power will not raise the cesium vapor temperature and pressure, but rather will extend the length of the cesium column.

To control the cesium pressure, the buffer gas pressure is changed. For a given buffer gas pressure, there is a range of supplied heater powers that create this ideal heat pipe operation. If the heat supplied is too low, the convective flow cannot be established. If it is too high, the vapor velocity will have reached the limiting sonic velocity, leaving the vapor unable to convect all the input heat.

Our heat pipe was constructed using a stainless steel tube, with length ~ 18 cm, an outer diameter of 1 inch, and a wall thickness of 0.13 inches. Stainless steel mesh, rolled up to be two layers thick, sat along the full length of the interior of the pipe to act as the wick. A 150 W mica band heater (Industrial Heater Corporation) with a width of 1 inch fit around the middle section of the pipe. A Variac voltage supply controlled the heater power. Copper, water-cooled, cooling blocks were positioned 2.2 cm from either side of the center of the pipe. Window holders were attached to each end of the pipe with compression fittings. The input and output windows were sealed to the holders by viton o-rings. Metal rings, bolted very gently into each window holder, held the windows in place when the pipe was at atmosphere. The input window was a 1 inch diameter, 0.25 inch thick uncoated CaF_2 window. The output windows used were 1 inch in diameter and either 0.25 inch thick suprasil or 2mm or 3 mm thick LiF. The suprasil window had the advantage of blocking approximately 40% of the 3.6 μm light. The LiF has better transmission at shorter wavelengths and less dispersion.

The heat pipe was loaded with 2 grams of cesium in a nitrogen purged glove bag. Two grams was sufficient to wet the whole wick and leave a small visible puddle at the bottom. We found that assembling the heat pipe without cesium first and baking to a low temperature helped clean the wick so that the cesium would flow more easily.

A gas manifold controlled the delivery and evacuation of the buffer gas. We used argon for our buffer gas. The manifold connected to ports on the window holders via 1/4 inch diameter vacuum rated flexible tubing. The flexible tubing was long enough to allow the heat pipe some small range ($\sim$10 cm) of movement on the optics table, but was kept short enough to ensure that the gas pressure in the pipe was the same as that in the manifold, where the pressure measurement was done. A low pressure regulator controlled the buffer gas pressure to the manifold and hence heat pipe. The gas source could be valved off and the whole heat-pipe/manifold assembly could be pumped down by a mechanical roughing pump to approximately 30 mTorr, as read by thermocouple pressure gauge. A variable leak valve allowed escape of small amounts of gas to the vacuum pump, which was handy when making adjustments of the gas pressure in the heat pipe. A Baratron pressure transducer (type 222BA), provided the pressure measurement of the buffer gas, and therefore of the cesium vapor.

A thermocouple, mounted to the heater on the exterior of the pipe, provided a monitor of the heater temperature. While this temperature reading did not correspond to the temperature of the cesium vapor, it was useful in determining the stability of the heat pipe operation. An unstable reading or one that slowly crept up to higher values indicated that the heat pipe was no longer performing in an ideal mode.

A graduated rail was fixed on the table, against which the heat pipe could be slid to adjust the cesium column position relative to the fixed laser focus position. In the experimental configuration for the XFROG measurement, the heat pipe was mounted on a translation stage, for finer position control.

To determine the appropriate voltages for heat pipe operation at different buffer gas pressures, we followed the method described in [113] and monitored the internal, on axis, temperature of the heat pipe as it was being operated. To measure the temperature inside the pipe, we used a thermocouple mounted at the end of a stainless steal sheath. This probe could be mounted through one of the window holders and the amount by which it extended into the pipe could be adjusted by sliding the probe through two rubber o-rings. To find the voltage range for a given buffer gas pressure, we positioned the thermocouple at the center of the heat pipe and recorded the temperature for different heater voltage values. Panel (a) of Figure 5.4 shows our measured results for 10, 12, 15, 20, 30, and 50 Torr. The internal temperature can be seen to increase with increasing voltage until a certain point where it levels off. This point marks the "'turn-on"' of ideal heat pipe operation. The additional heat supplied at voltages after this point go into making the column longer. The vapor pressure corresponding to the leveled-off temperature is in good agreement with the buffer gas pressure. Shown in Panel (b) of Figure 5.4 is the on-axis temperature mapped out along the length of the heat pipe. The data shown is with a buffer gas pressure of 12 Torr and a constant voltage of 125 V. The sharp temperature gradient, indicating the transition region between the cesium column and the buffer gas, is evident. From this study we can see the cesium column length is approximately 3 cm.

While the heat pipe performed well enough to complete the experiments presented here, there are a couple of improvements that should be made to make it even better. First, the compression fittings that hold the window holders to the pipe should be replaced with conflat flanges to improve the leak rate of the heat pipe. We found that over the course of a few days, enough air would leak into the pipe to cause the cesium to react. This was evident from the presence of whitish cesium hydroxide. To prevent this, when the heat pipe was not in use it was over pressurized with argon so that it would leak outwards rather than inwards. However, this was not a particularly satisfying solution. Second, warmer water should be used for the cooling blocks. House processed chilled water was used, which we discovered was too cold for our application. The water temperature was 17 C and cesium's melting point is 28.4 C. This caused some of the condensing cesium at the cooling block position to solidify rather than flow back into the wick. When buildup of the cesium started to occur, the heat pipe voltage was stopped and the solid cesium was melted back into the wick with a heat gun. We attempted to slow the rate of water flow through the cooling blocks, but this failed since a very slow rate was necessary and the water ended up completely stopping, causing the cesium to

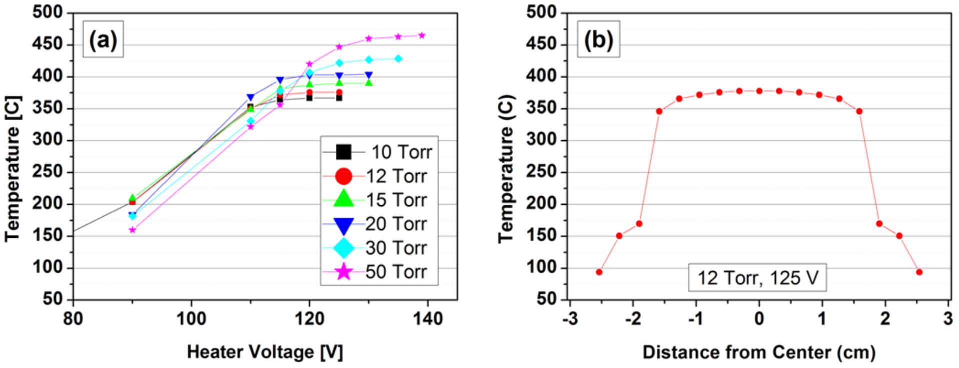

Figure 5.4: Internal, on-axis, heat pipe temperature versus heater voltage for several buffer gas pressures, (a), and versus position, (b).

coat the windows. Instead, the house water should be replaced by a temperature controllable chiller unit.

5.2.2 Spectrometers

Two separate, but similar, spectrometer systems were used to detect our harmonics and will be referred to as the ”Triax” system and the ”SP300” system. The Triax and SP300 systems both have spectrometers that are flat-field Czery-Turner designs and which contain a grating turret that holds three gratings. Both use similar thermoelectrically cooled intensified charge-coupled devices (ICCD) to detect the spectrally resolved light and that can be gated synchronously with the mid-infrared laser pulse.

The ”Triax” system is an Instruments S. A. Inc. 0.18 m spectrometer, model Triax-180, which contains a 1200 g/mm (400nm blaze) grating, a 2400 g/mm (250nm blaze) grating, and a 147 g/mm (300 nm blaze) grating. The ICCD was made by Princeton Instruments Inc., model ICCD1024MS, and contains a CCD chip with 1024 × 768 pixels, 70% of which are active. The Princeton Instruments model ST-130 controls the ICCD. The FG-100 pulse generator provides a gate pulse for the ICCD. The controller was interfaced via RS232 to a PC and Princeton Instruments' software, WinSpec32, was used to set the ICCD temperature (typically -35° C), the collection parameters, and to collect the data. A hand held controller (Handscan) allows for the grating selection and rotation of the grating, as well as adjustment of the width of the entrance slit. Typically, we would operate using the 147 g/mm grating rotated to a center wavelength of 450 nm which allowed us to view wavelengths between 800 and 170 nm, which includes H5 through H19. The entrance slit was set to either 60 μm or 2000 μm.

In order to synchronize the ICCD gate with the arrival of the laser pulse, a Stanford Research DG535 delay generator was included in the electronic triggering chain. It provided an adjustable delay trigger signal for the FG-100 pulse generator and was itself triggered by an audio out signal from the Pockels cell driver for the ylf regen. To achieve the initial overlap, an InAs photodiode was used to detect the mid-infrared laser pulse at the spectrometer, and this signal was observed on a scope along with the monitor signal from the FG-100 pulse generator. The delay from the DG535 was adjusted until the two signals overlapped in time. Then, fine tuning was done while observing the harmonic spectrum, to set the delay so that the gate was centered in time around the harmonics signal. The gate width was kept at 20 ns, the minimum width for this ICCD unit.

To collect a spectrum, the gain setting of the ICCD and exposure time (corresponding to the number of laser shots averaged) were adjusted to maximize the 16 bit dynamic range of the system without saturating. We found the minimum reliable exposure time was 30 ms. Typically, a background spectrum was subtracted from the signal. Many accumulations (usually 60), were summed to get a good signal to noise ratio.

The detectable wavelength range for the Triax spectrometer is 900nm-200nm. This is set primarily by the reflectivity of the coatings used on the gratings and optics in the spectrometer as well as the transmission of the entrance window, made of quartz, on the ICCD.

The spectrometer was set up so that a fixed point, relative to the optics table, in the beam path was imaged onto the entrance plane of the spectrometer. The position of the focusing lens, that would focus the mid-infrared light into the heat pipe, was adjusted so that the mid-infrared focused at this fixed point. To move the focus with respect to the cesium column the heat pipe was moved. A parabolic mirror after the focus position, with f_{eff}=152.4 mm, collected and collimated the light. The light is then reflected by two flat mirrors over to the f_{eff}=152.4 mm parabolic mirror that focuses the light into the spectrometer. All the mirrors used were aluminum, which has good reflectivity out to the UV.

The mid-infrared light was found to be too intense for the entrance aperture of the spectrometer. If left for too long a time on the slit it would ablate the metal. To circumvent this problem, two different strategies were adopted. First, a KG2 Corning filter could be used to block the mid-infrared and transmit many of the harmonics. However, this filter did not transmit below $\sim$ 300 nm, and so did not permit observation of all of the harmonics within the detectable range of the spectrometer. Second, the entrance slit was opened to its maximum width of 2 mm and the reimaged focus spot on the entrance plane was used to define the resolution.

As an additional note, because of the intensity present in the mid-infrared beam, extreme care had to be taken to not damage the ICCD. Precautions taken were: blocking the beam while the grating was changed, and keeping the grating angle centered on long enough wavelengths so that the zero-order reflection did not hit the detector.

The SP300 system is an Acton Research Corporation 0.3 m spectrometer, model Spectra-Pro-300i, which contains a 150 g/mm (300 nm blaze) grating, a 1200 g/mm (150 nm blaze) grating, and a 3600 g/mm (130 nm blaze) grating. Its detector is also a Princeton Instruments ICCD, but a newer model, PI-MAX1024UV, with an input window that is made of MgF_2 rather than quartz so that radiation down to $\sim$ 130 nm can be transmitted to the photocathode. The gratings and optics within the spectrometer are coated to optimize the reflectivity of UV radiation. As in the Triax system, the ICCD is typically cooled to a temperature of -35 C. It too is controlled by an ST-133 unit. It is equipped however, with a pulser for the gating, so the FG-100 is not required. The DG535 is again used to provide the synchronization with the laser pulse. Unlike the Triax system, the SP300 spectrometer, DG535 and the ST-133 are all computer controlled using the WinSpec32 software. The SP300 system has greater sensitivity than the Triax. Direct observation of our lowest order harmonics is not possible without saturating the detector. The spectrometer was set up to collect the light in our XFROG experiment (see Section 5.3.2). An f_{eff}=152.4 mm parabolic mirror focused light, which had been collimated after being focused onto the XFROG crystal, onto the entrance plane of the spectrometer.

For both spectrometers, calibration of the wavelength axis was done using an Oriel Instruments spectral pen lamp (part number 6035). The 253.65nm, 404.66nm, and 546.07nm lines of this Hg lamp were used to convert pixels to nanometers. The linewidths of the calibration peaks also gave an indication of the resolutions. At an entrance slit of 60 μm, the peak FWHM was $\sim$ 5 nm.

In order to determine the absolute energy yield of our harmonics, we calibrated the Triax system. This was done using a calibrated photodiode (Coherent, JS3-10), and the ti:sapphire laser. The laser power was attenuated using a waveplate-polarizer attenuator in addition to several ND filters and the number of counts per millisecond acquisition time was recorded as a function of ICCD gain setting. The energy of the attenuated ti:sapphire light was then measured using the calibrated photodiode, and a conversion factor for pJ to counts/ms was obtained for the ti:sapphire's center wavelength of 815 nm. This factor was extrapolated to the other wavelengths using the response curves for the 150 g/mm grating and the cathode in the ICCD. The conversion factor as a function of wavelength is shown in Figure 5.5 for a gain setting of 1.5, the setting used for most of the results presented here. A later measurement was done using a set of absorption filters to isolate each of the cesium harmonics. Their energy was measured using the calibrated photodiode and its wavelength response curve, and the number of counts was recorded for each. The factors obtained from this method were in agreement with those presented in Figure 5.5.

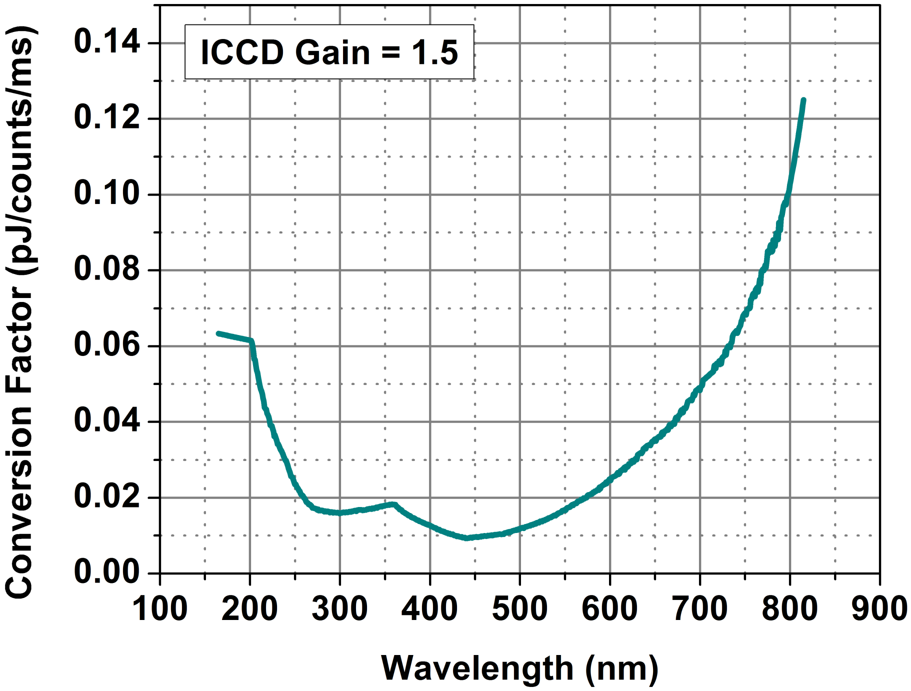

Figure 5.5: Energy per Counts/ms conversion factor for the Triax system with the ICCD gain set to 1.5.

5.3 Experimental Results

5.3.1 Harmonic Spectra

Harmonic Energy Yield

To determine the absolute energy yield for each of our harmonic peaks, we focused the harmonic light onto the entrance plane of the Triax spectrometer with the entrance slit open to its widest width of 2mm, so that we were sure to be collecting all of the generated light. The resulting spectrum was then converted to energy using the calibration factor found by the method described in the Section 5.2.2. Panel (a) in Figure 5.6 shows an energy spectrum generated with our 110 fs, 3.6 μm laser. This spectrum was taken at a cesium pressure of 60 Torr and a 1 inch, f=500 mm focal length lens was used to focus the mid-infrared light at the center of the heat pipe. The maximum available 3.6 μm power before the focusing lens was 75 mW (75 μJ/pulse). However, we found that we could obtain stronger higher order peaks by truncating the 3.6 μm beam using an adjustable iris positioned before the focusing lens. The strongest peaks, shown in the figure, were achieved with the iris closed to a diameter of 15 mm, approximately the $1/e^2$ diameter of the 3.6 μm beam. The measured power passing through the iris was 67 mW. Estimating the focus spot size to be 110 μm, this corresponds to an average intensity at focus of 1.6×10^{12} W/cm^2.

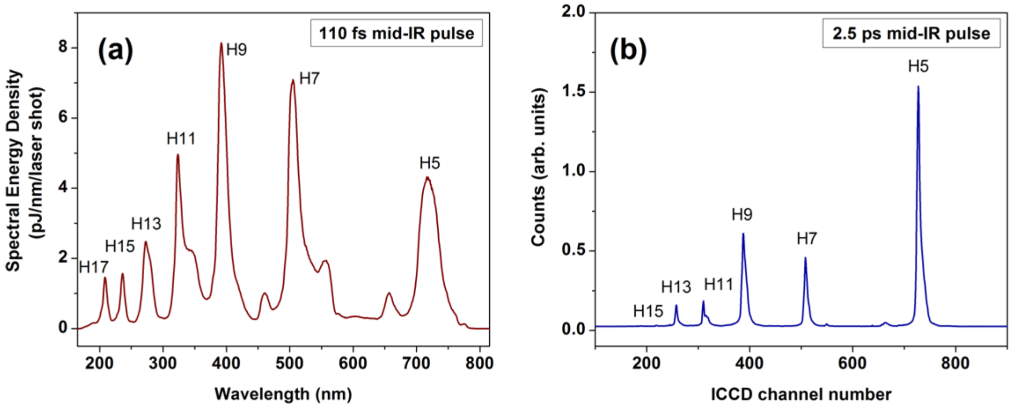

Figure 5.6: Comparison of harmonic spectra taken with the 110 fs mid-infrared driving pulse (a) and the 2.5 ps mid-infrared driving pulse (b) [108].

For comparison, shown in panel (b) of Figure 5.6 is a harmonic spectrum taken previously in our lab with a longer mid-infrared pulse. The mid-infrared had a pulse duration of 2.5 ps FWHM and was centered at 3.4 μm. The spectrum shown was taken with a very similar heat pipe apparatus, but it was not run in an ideal heat pipe mode. The cesium pressure, estimated from a temperature measurement, was approximately 18 Torr, and the N_2 buffer gas had a pressure of 76 Torr. A 1 inch diameter, f=150 mm focal length lens focused 100 mW of mid-infrared light at the center of the heat pipe. Based on these parameters, the average intensity at focus is estimated to be 2.4×10^{12} W/cm^2. The spectrum shown is corrected for the grating and detector response.

In the picosecond case, the energy yield of H5 and H7 were measured using a calibrated photodiode and the energy yields of higher orders were determined relative to H7. These values, as well as values for the yields of the harmonics in the present, femtosecond case, are tabulated in Table 5.2. For the femtosecond case, the yields were found by integrating each harmonic peak. The peak to the left of H5 and the peaks on either side of H7 are diffracted 2^{nd} order peaks and were not included in the integration.

From the comparison, it is clear that the harmonics generated with the shorter

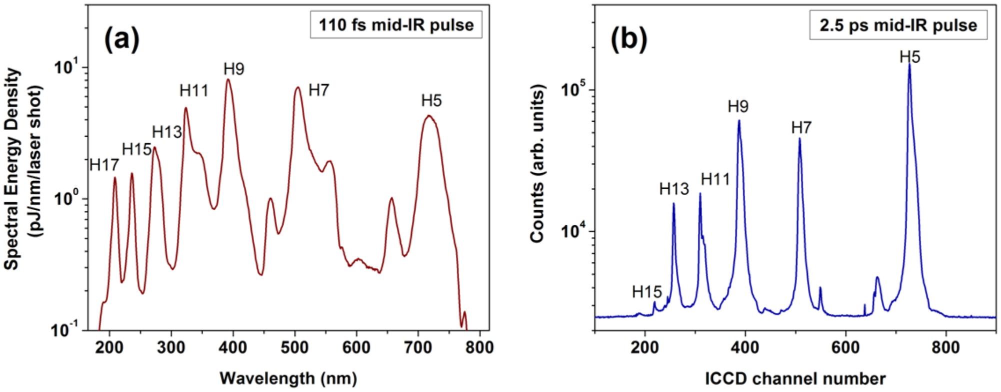

Figure 5.7: Same spectra as in Figure 5.6, but plotted on a logarithmic scale. (a): spectrum taken with the 110 fs mid-infrared driving pulse. (b): spectrum taken with the 2.5 ps mid-infrared driving pulse [108].

mid-infrared pulse have higher pulse energy yields, particularly the higher orders. Part of this increase can be attributed to the difference in focusing geometries. Given that we now have a pulse that is shorter by a factor of 23, we are able to use looser focusing so that the volume over which harmonic can be generated is larger. Given the estimated spot sizes for the two cases of $\omega_{fs} \approx 110$ μm and $\omega_{ps} \approx 23$ μm, if we roughly estimate the generating volume to be equal to the focus area times the confocal parameter ($b_{fs} \approx 21$ mm, $b_{ps} \approx 1$ mm), we find the volume in the femtosecond case is 500 times larger than that of the picosecond case.

The harmonic yield is now greater, which has opened up more possibilities for studying the harmonic properties, for instance, the XFROG measurement that we carried out and which is described in Section 5.3.2. In the present case, given 67 μJ in the mid-infrared driving pulse and a total of 764 pJ in H5-H17, the efficiency of harmonic production is $\sim 10^{-5}$.

Nitrogen purged harmonics

For radiation with wavelengths longer than 200 nm, propagation through air is usually not problematic. (A case where it was found to be problematic can be found in our XFROG measurement, described in Section 5.3.2.) For wavelengths shorter than 200 nm, absorption by oxygen begins to severely limit the transmission. For all of the results presented so far the harmonics have been studied in air and this has limited our visibility to harmonic orders 17 and below (although hints of H19, at 189 nm, would occasionally be present). Here I present my observation of harmonics

	2.5 ps Mid-IR Pulse	**110 fs Mid-IR Pulse**
Harmonic Order	**Energy per pulse [pJ]**	**Energy per pulse [pJ]**
H5	68	171
H7	1.8	198
H9	4.2	185
H11	0.69	127
H13	0.42	49
H15	0.16	18
H17	0.098	16

Table 5.2: Comparison of energy yields for harmonics generated from a 2.5 ps mid-infrared pulse and a 110 fs mid-infrared pulse.

with wavelengths less than 200 nm. Figure 5.8 shows the results.

The data was taken using the SP300i spectrometer and ICCD camera, since this system is optimized to detect shorter wavelength radiation. Its detectable range is from the visible to ≈ 130 nm, the shorter wavelength limit set primarily by the MgF_2 input window on the ICCD camera. The beam path from the output window of the heat pipe to the spectrometer entrance slit was enclosed using plastic bags, paper clips, and tape so that it could be purged with clean nitrogen gas. The built-in gas port on the SP300i spectrometer allowed us to fill the spectrometer with nitrogen as well. The heat pipe was operated at a pressure of 20 Torr. A 1 inch diameter, f=500 mm CaF_2 lens focused the 3.6 μm light into the heat pipe. The position of the heat pipe relative to the focus spot and the diameter of an iris, located ~ 10 cm before the focusing lens, were adjusted to maximize the high-order harmonic signal. The spectra shown were taken with the heat pipe positioned so that the focus is 1 cm before the center of the cesium column. The iris diameter was closed down to 12 mm, which truncated the 15 mm $1/e^2$ diameter beam. Before the iris the laser power was 75 mW; After it was 53 mW.

Shown in Figure 5.8 panel (a) is a spectrum containing H9-H17 (and a fraction of H7 which is not fully on the detector). The inset shows the higher order end zoomed in so that H15 and H17 are visible. This spectrum was taken with the 150 g/mm grating (blazed for 300 nm) where we used a Hg pen lamp to calibrate the wavelength axis. To observe harmonics higher than H17, it was not possible to rotate the 150 g/mm to shorter wavelengths as this would throw the zero-order reflection, containing the mid-infrared beam, onto the detector which would undoubtably cause damage. So instead, we used the 1200 g/mm grating (blazed for 150 nm). We lacked a spectral reference for wavelengths below 200 nm, and so could not calibrate the wavelength axis as we had for the lower order harmonic spectra. Instead, we relied upon the calibration factor of the spectrometer and tuned the grating angle so that a particular harmonic order would fall on the center of the ICCD chip. Starting with H13, the grating was turned and we followed the appearance and progression

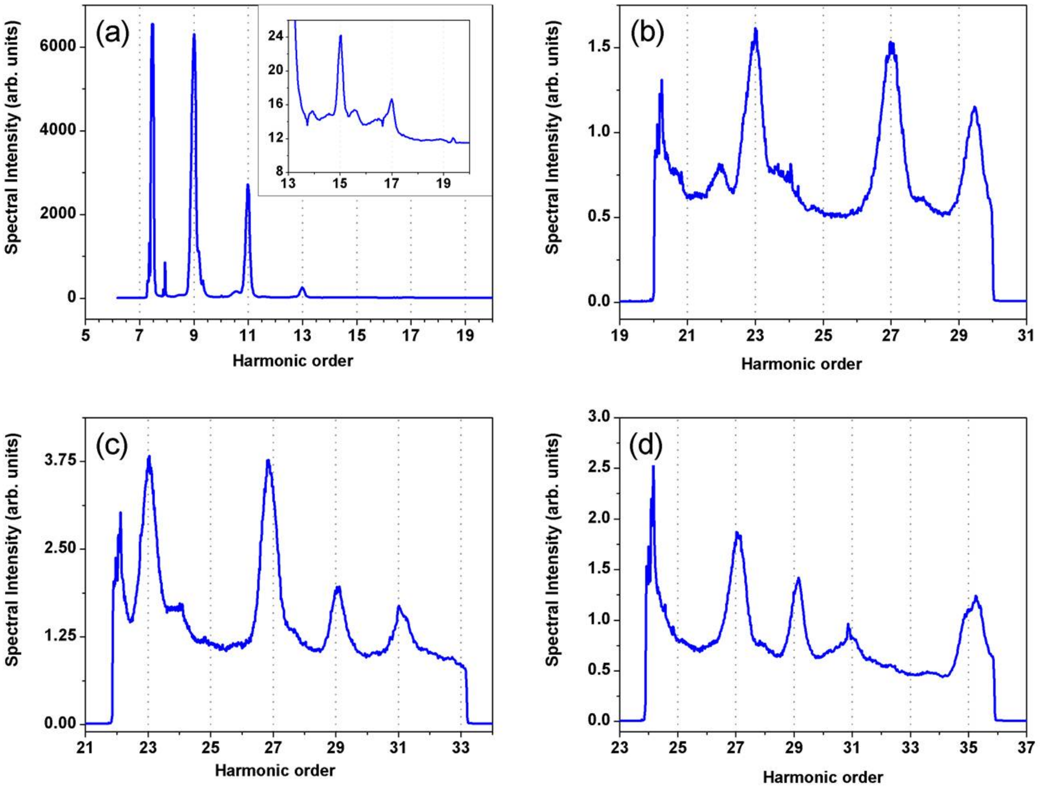

Figure 5.8: Nitrogen purged harmonics.

of the harmonics as they moved across the chip. Scattered light, identified by its unfocused spatial profile on the 2D chip, was a large problem. For grating positions that would allow us to observe H19 and H21, scattered light swamped the harmonic signal. Fortunately, we were able to observe H23, H27, H29, and H31. These harmonics are shown in panels (b), (c), and (d) of Figure 5.8. H31, being centered at 116 nm, is at the very edge of the detection range of our spectrometer, so this was the highest harmonic we were able to detect, not necessarily the highest harmonic present. There is a conspicuous absence of H25 (144 nm).

To maximize the contrast of the harmonics against the background light, it was necessary to close down multiple irises along the path from the heat pipe exit to the focusing parabolic mirror before the spectrometer. Therefore, the spectra presented reflect a very narrow portion of the beam along the propagation axis. Also, the spectrometer's entrance slit was closed to it smallest width, and the steering onto the slit had to be tweaked to maximize the harmonic peak and minimize the background light.

The relative intensity between the spectra in (a) and the others cannot be directly compared since the ICCD gain settings differ between the two. However, a rough estimate was made by comparing H15 captured in both settings. It was found that H23-H31 have intensities on the same order (perhaps within a factor of 2 or 3) as H15, an indication of a plateau in the spectrum. For comparison with the lower orders, H15 is approximately a factor of 10 weaker than H13, and it can be seen in panel (a) that H13 and H11 differ by a factor of 10, and H11 and H9 differ by about a factor of 2. H7 was too strong to be recorded on the ICCD without saturating severely, so the grating was positioned so that only a small portion would be present on the detector. (Remember, the sensitivity of this system is greater than that of the Triax system.) H5 is beyond the detection range of the spectrometer system.

Given the closed iris before the focusing lens, it is difficult to accurately estimate the focused intensity in the cesium. However, if we take a 12 mm pupil diameter and a f=500 mm lens, the diffraction limited spot size is $\omega \approx 132$ μm, 1/e^2 radius. This, along with the 53 μJ present in the mid-infrared beam, corresponds to a peak intensity of 1.76×10^{12} W/cm^2. The expected cutoff, defined by the $I_p + 3.17U_p$ rule, is then 10.6 eV or 116.6 nm, which happens to correspond to the maximum harmonic (H31) observed in our setup.

To study the cutoff, it would be necessary to have a spectrometer system with an extended range into the vuv. LiF, the material of the heat pipe output window for these measurements, has an impressive transmission range that extends all the way to down to 105 nm, but this would transmit only through H35 (103 nm). A windowless heat pipe, where differential pumping was implemented, would probably be necessary to observe higher harmonic orders.

Harmonic Spectral Profiles at Different Laser Focus Positions and Cesium Pressures

In an attempt to get a rough idea of the macroscopic effects at play in the generation of our harmonics, we collected spectra at different focus positions within the cesium column. The progression of spectra as the focus is moved through the cesium column are shown in Figure 5.9, where the spectrometer entrance slit is closed[4] to 60 μm, and in Figure 5.10, where the slit is open to 2000 μm. Each spectrum is broken into three separate windows with different y-axis scales to enable better visibility. The right most column contains H5, the middle contains H7, H9, and H11, and the left most column contains H13, H15, and H17. The numbers in the upper right hand corners of the windows indicate the focus position with respect to the cesium column. The center is indicated as 0 mm, positions before the center are negative values, and positions after are positive. The y-axis is number of counts/ms. By comparing the count rates, the spectrum at 0 mm in Figure 5.9 is roughly half the energy yield of the spectrum presented in the Section 5.3.1.

The Triax spectrometer was used for these measurements. The cesium pressure was 20 Torr and an f=500 mm (f/20) lens focused 77 mW of 3.6 μm light into the

---

[4] For this data, the KG2 filter was not in place. Instead, care was taken to keep the time the mid-infrared was incident on the entrance slit to a minimum.

heat pipe. The iris located before the focusing lens was all the way open, so the beam was not truncated.

One of the most noticeable features in this set of spectra is the disappearance and then re-emergence of H5 as the focus moves from the front of the column to the back. Absorption in the vapor seems suspect, and while H5 is the closest harmonic to the strong D1 (894.6 nm) and D2 (852.3 nm) resonances in cesium, at $\sim$ 720 nm, it is still 130 nm (65 THz) away. A more likely candidate seems to be absorption by cesium dimers in the vapor. It is known that for pressures $\sim$ few Torr, alkali vapors contain from 1 to 10 % diatomic molecules[115][11] and Cs_2 does have a diffuse absorption band in the wavelength range between 700 and 725 nm[116].

Further evidence that absorption is responsible can be found in the harmonic spectra taken at different pressures. Figures 5.11, 5.12, 5.13, and 5.14 show spectra at pressure of 11 Torr, 20 Torr, 40 Torr, and 60 Torr. These spectra were taken with the iris before the focusing lens closed down to a diameter of 15.25 mm, so the intensity is less than for the spectra in Figures 5.9 and 5.10. It is clear that the absorption of H5 is less at lower pressures.

Harmonic Spectral Profiles vs. Laser Intensity

The harmonic yield as a function of laser intensity was investigated. The spectra were measured using the Triax spectrometer. The output window on the heat pipe was a 0.25 inch thick suprisil window. The cesium pressure was 58 Torr and the entrance slit on the spectrometer was set to 2000 μm. The mid-infrared power was reduced using an attenuator made up of a $\lambda/2$ waveplate (CVI, part number) and polarizer (II-VI, part number). When the attenuator was set to transmit the maximum amount of mid-infrared power, the measured power before the heat pipe was 82 mW. The heat pipe was positioned so that the laser focus was 10 mm after the center of the column. Figures 5.15, 5.16, and 5.17 show the measured spectra. Figure 5.18 shows the integrated peak areas as a function of laser intensity. Here, it is clear that the harmonic orders grow with roughly the same rate. The points at which the growth saturates appears to move to higher intensities as the harmonic order increases.

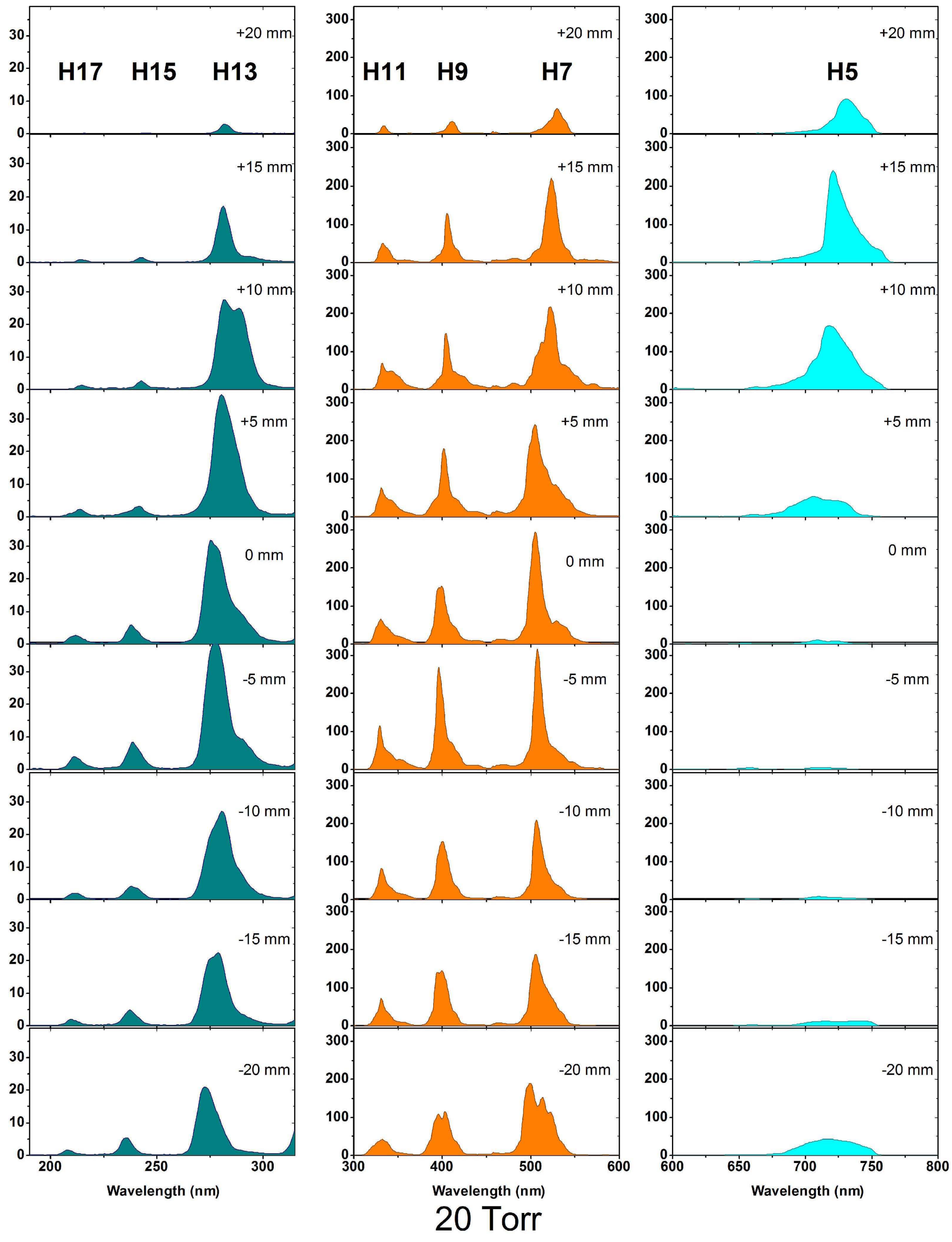

Figure 5.9: Harmonic spectra versus focus position, 60 μm slit, 77 mW (iris open), $\omega_0 \approx 80$ μm, $I \approx 3.5 \times 10^{12}$ W/cm^2.

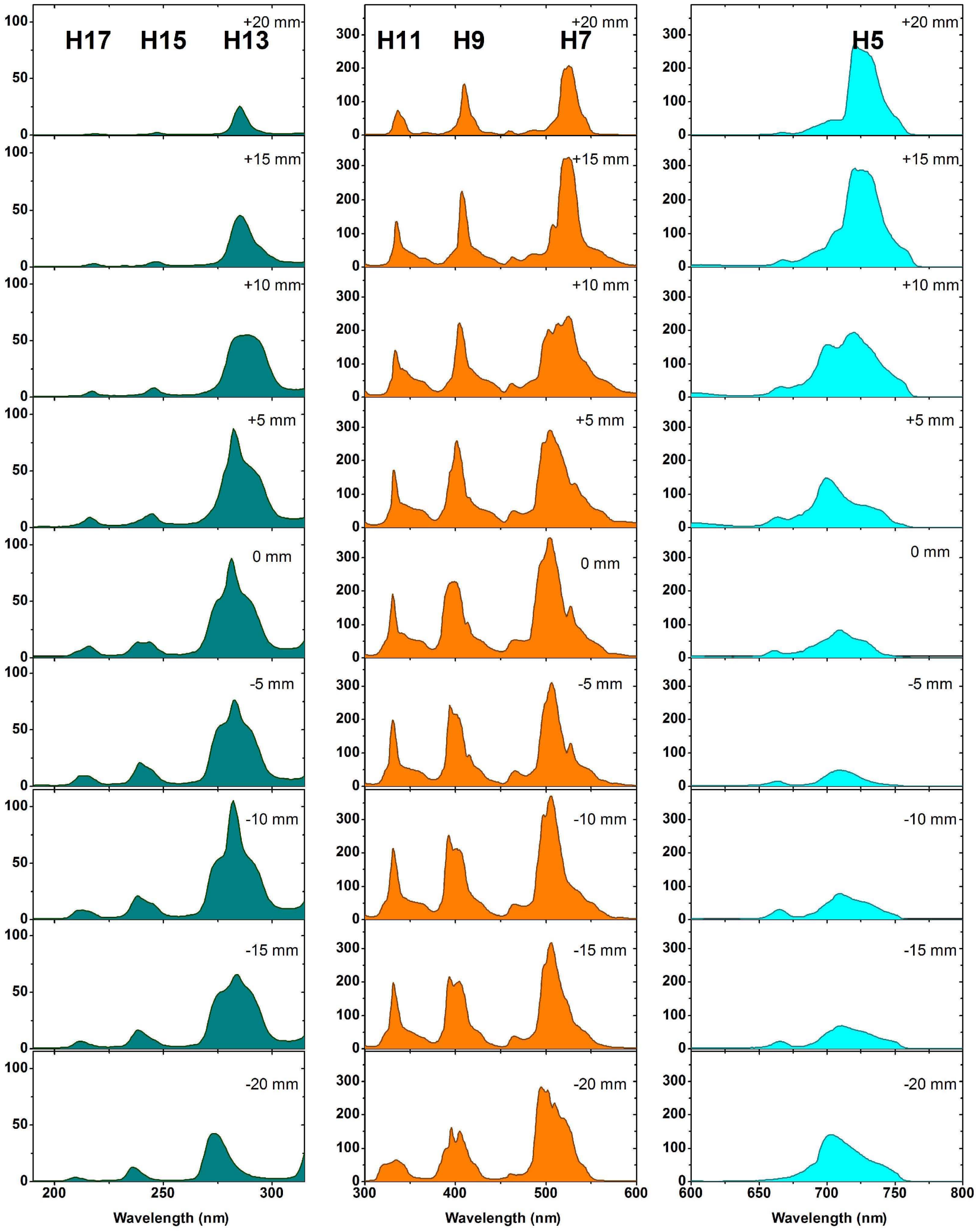

Figure 5.10: Harmonic spectra versus focus position, 2000 μm slit, 77 mW (iris open), $\omega_0 \approx 80$ μm, $I \approx 3.5 \times 10^{12}$ W/cm^2.

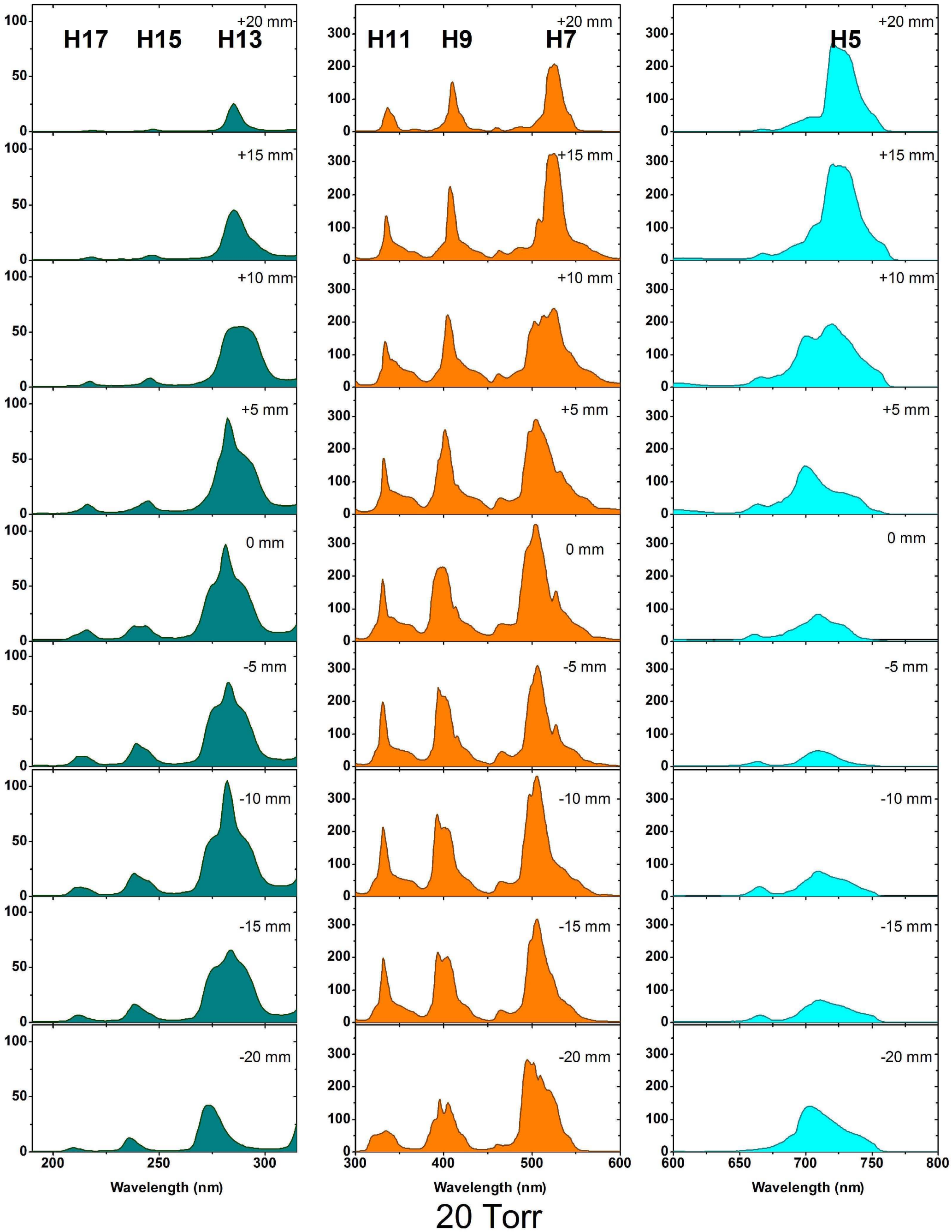

Figure 5.11: Harmonic spectra versus focus position, 2000 μm slit, 67 mW with iris closed to 15.25 mm, $\omega_0 \approx 109$ μm, $I \approx 1.6 \times 10^{12}$ W/cm^2.

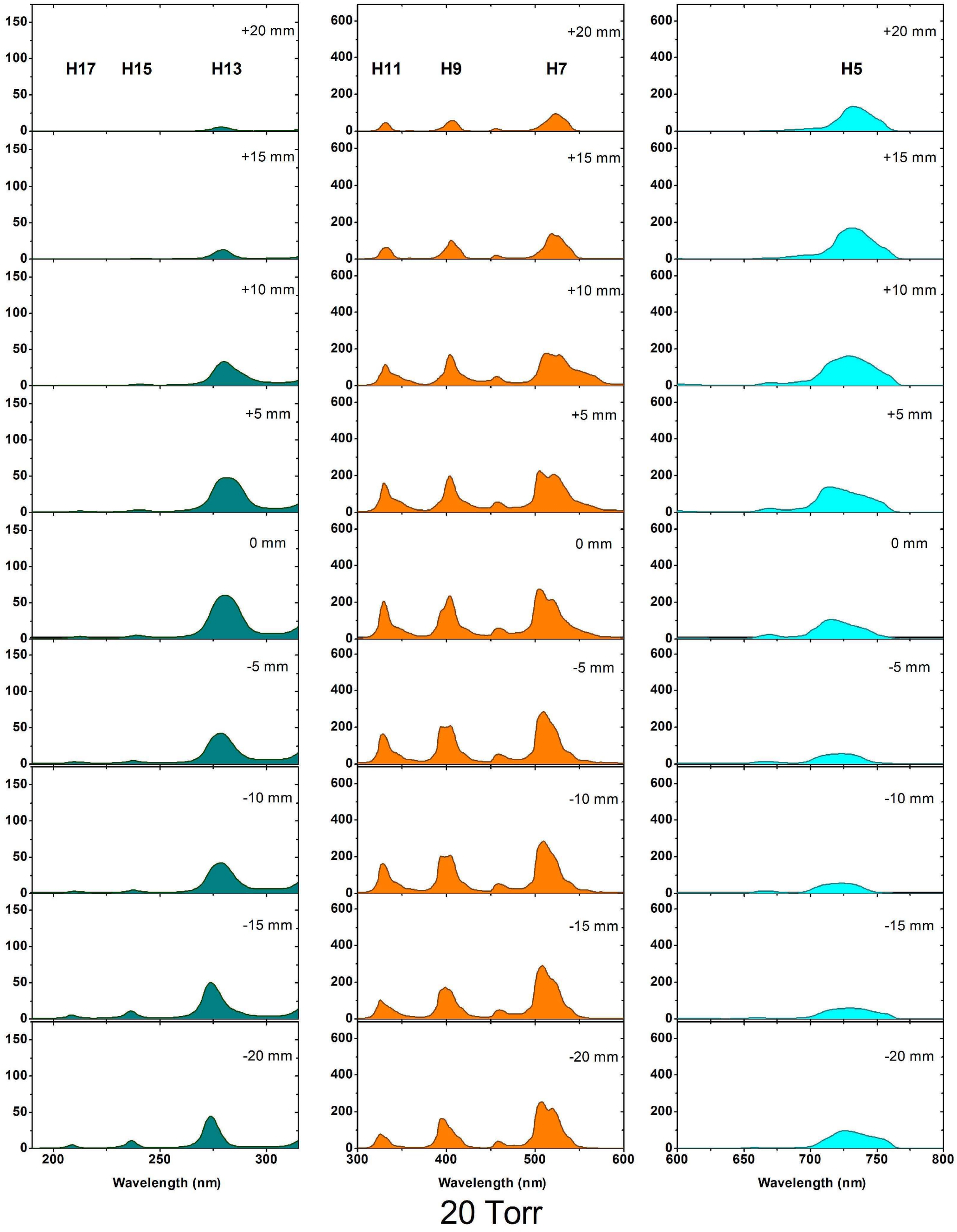

Figure 5.12: Harmonic spectra versus focus position, 2000 μm slit, 67 mW with iris closed to 15.25 mm, $\omega_0 \approx 109$ μm, $I \approx 1.6 \times 10^{12}$ W/cm^2.

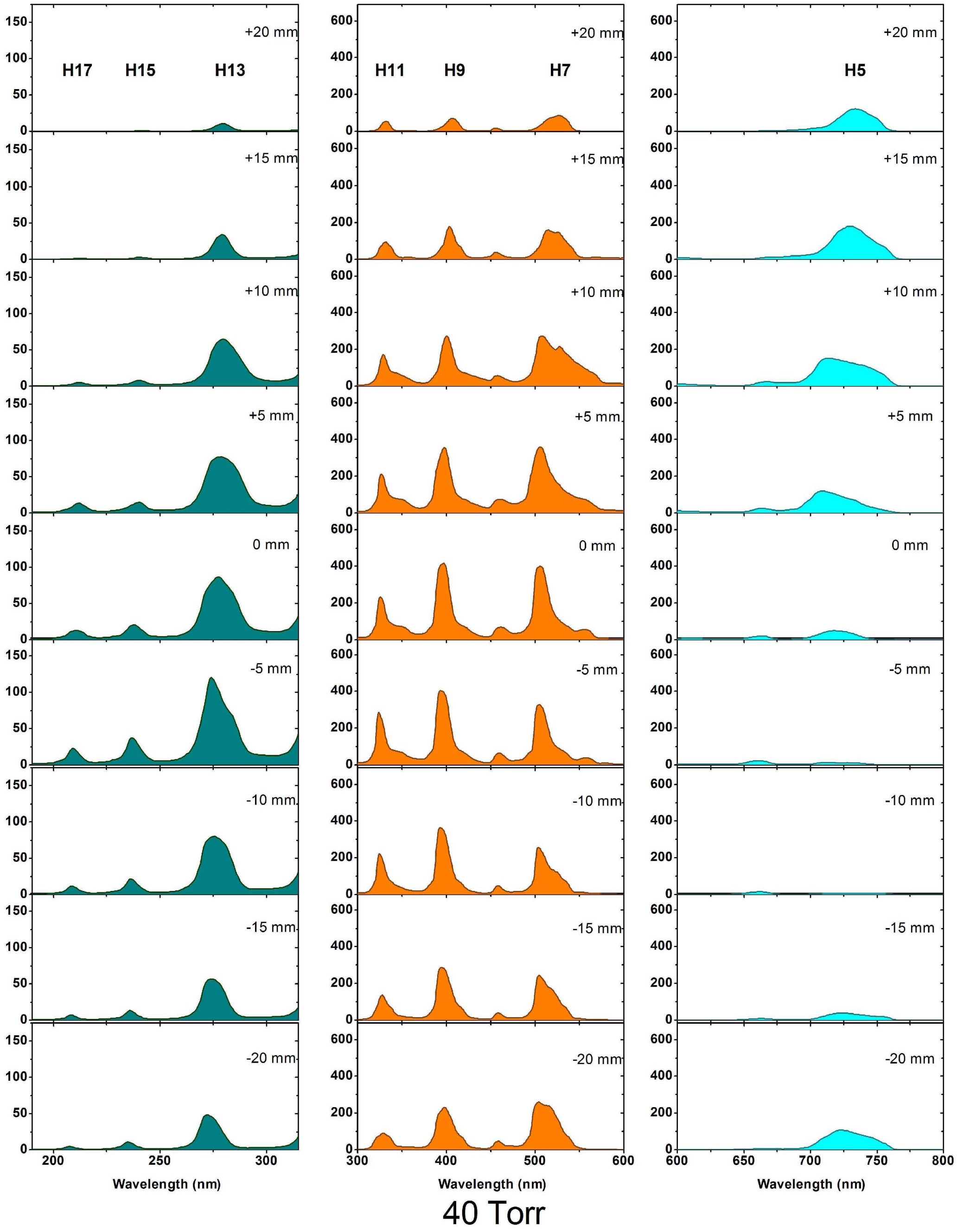

Figure 5.13: Harmonic spectra versus focus position, 2000 μm slit, 67 mW with iris closed to 15.25 mm, $\omega_0 \approx 109$ μm, $I \approx 1.6 \times 10^{12}$ W/cm^2.

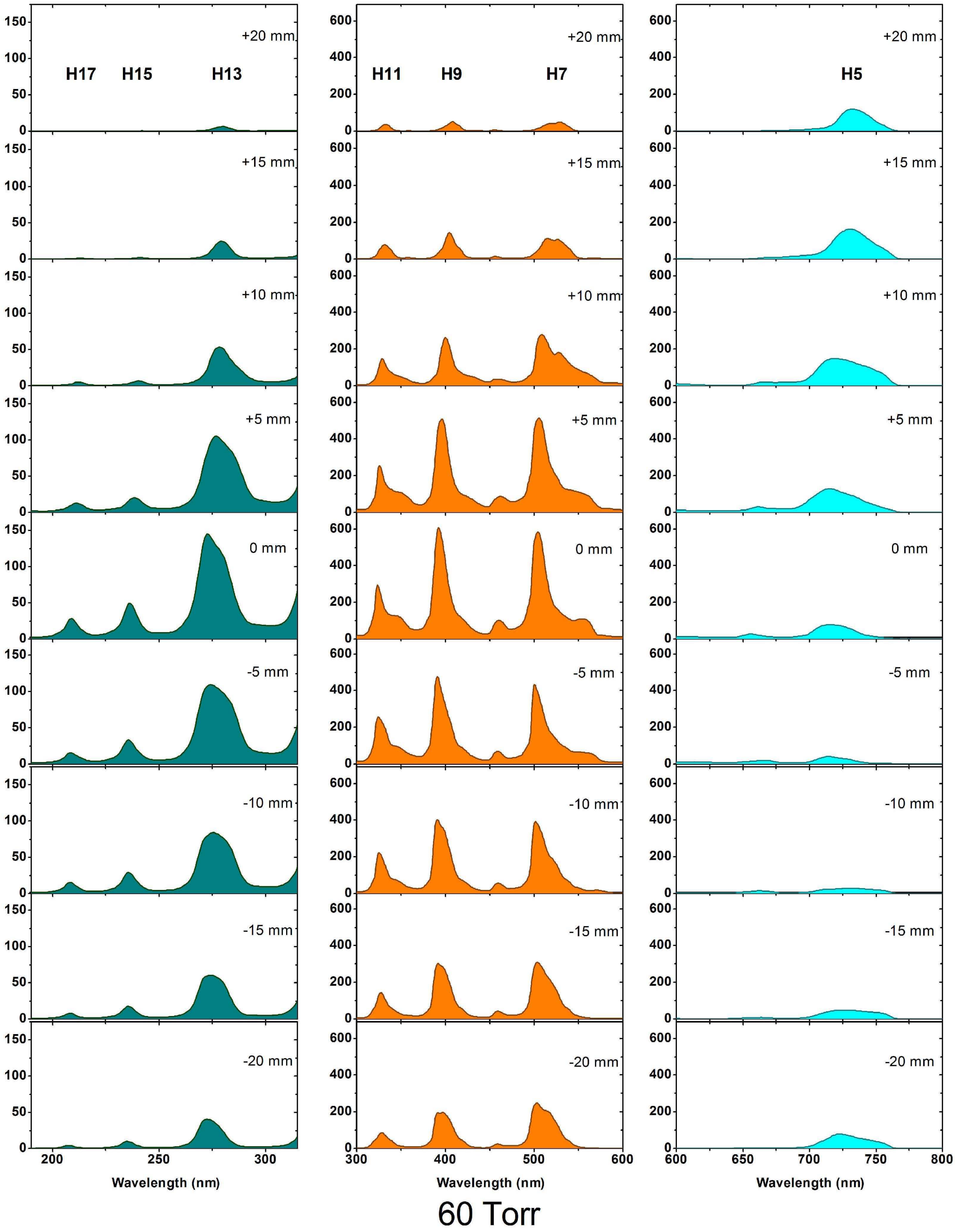

Figure 5.14: Harmonic spectra versus focus position, 2000 μm slit, 67 mW with iris closed to 15.25 mm, $\omega_0 \approx 109$ μm, $I \approx 1.6 \times 10^{12}$ W/cm^2.

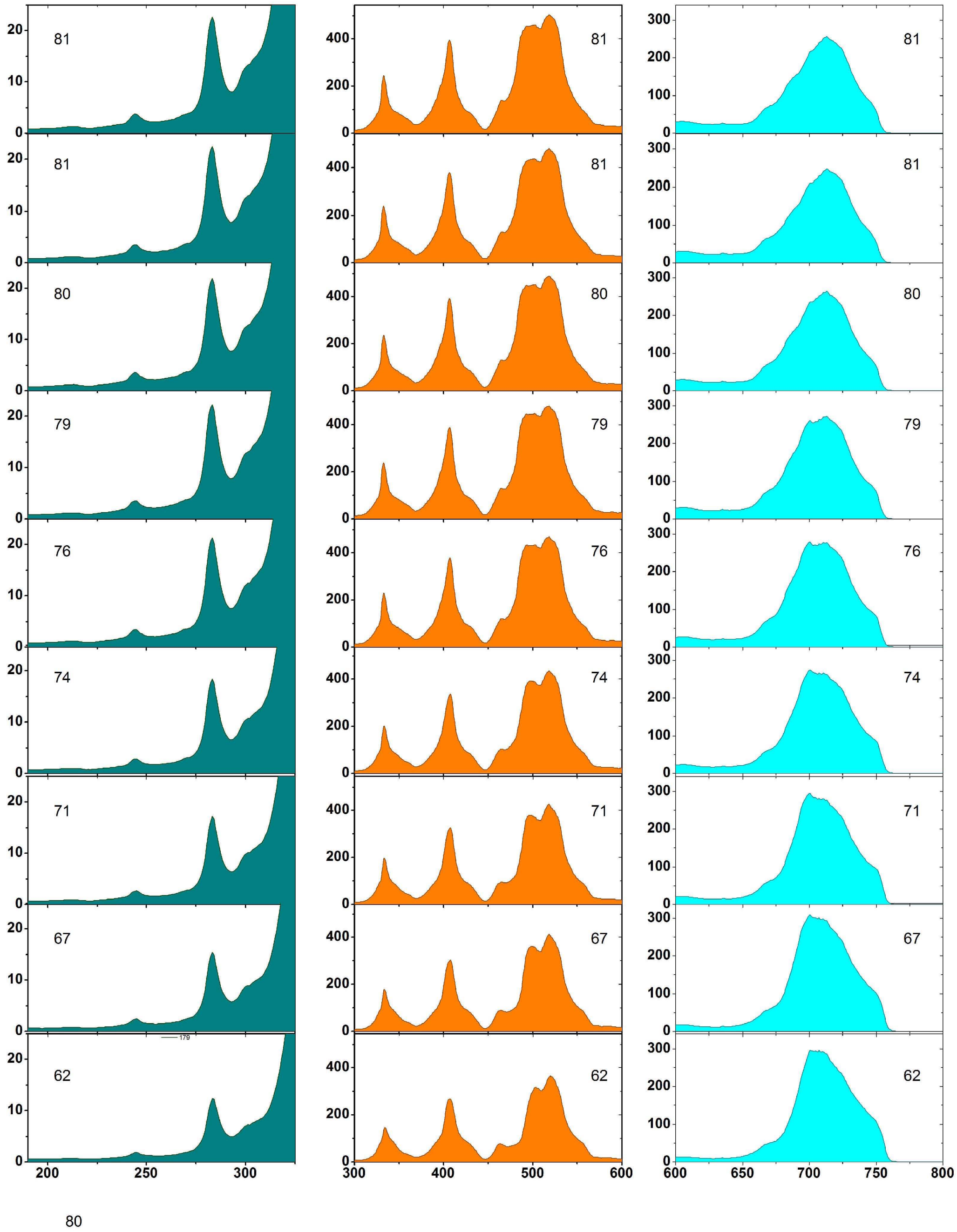

Figure 5.15: Harmonic yield versus laser intensity, 2000 μm slit, iris open, $\omega_0 \approx 80$ μm, 58 Torr, laser focus 10 mm after cesium column center.

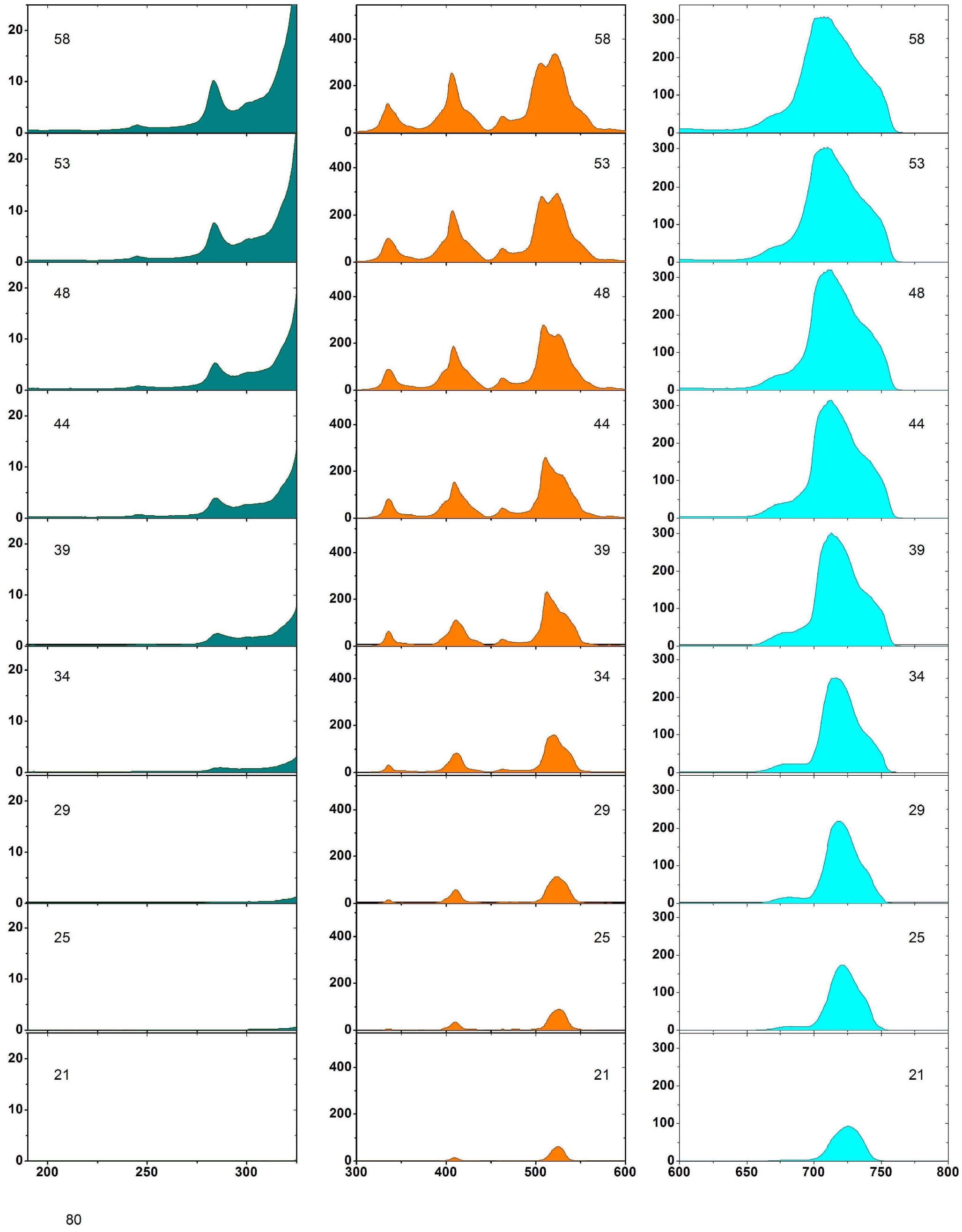

Figure 5.16: Harmonic yield versus laser intensity, 2000 μm slit, iris open, $\omega_0 \approx 80$ μm, 58 Torr, laser focus 10 mm after cesium column center.

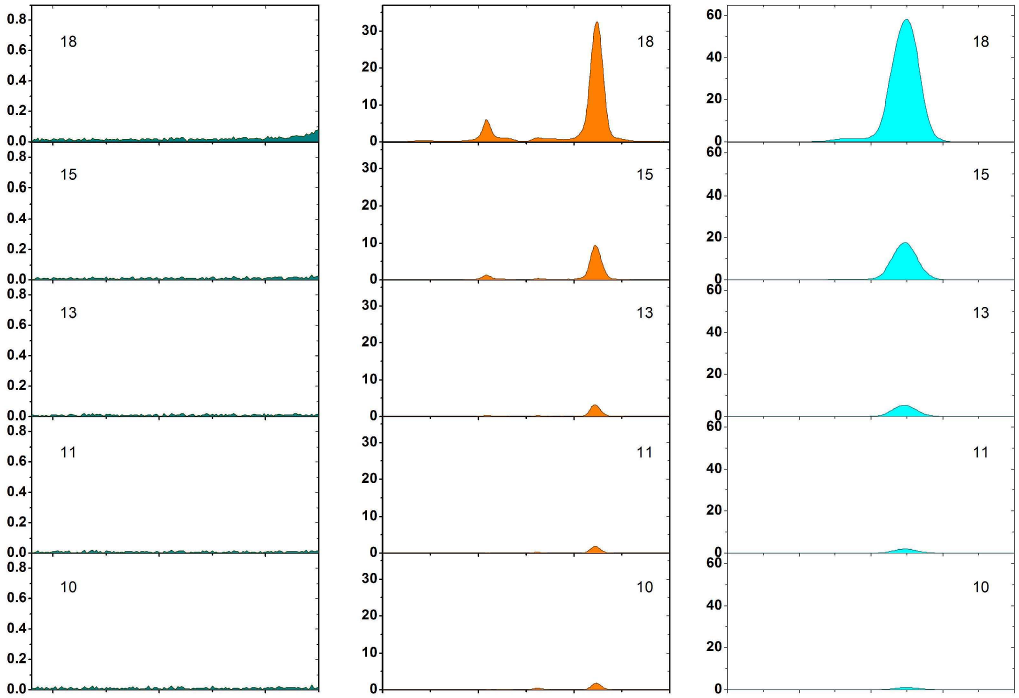

Figure 5.17: Harmonic yield versus laser intensity, 2000 μm slit, iris open, $\omega_0 \approx 80$ μm, 58 Torr, laser focus 10 mm after cesium column center.

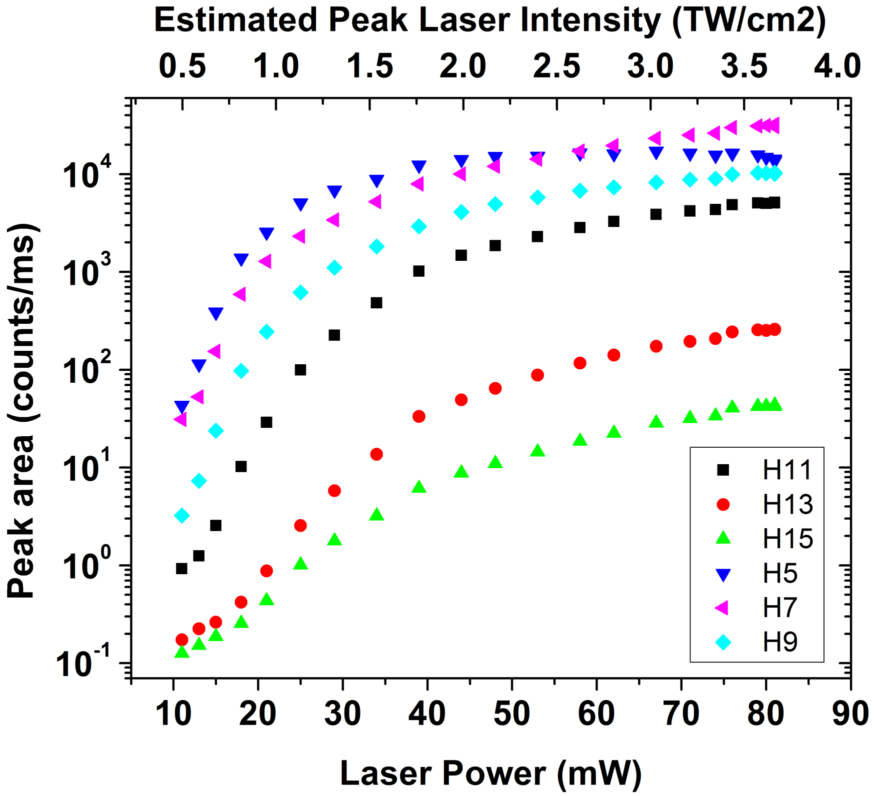

Figure 5.18: Harmonic yield versus laser intensity, 2000 μm slit, iris open, $\omega_0 \approx 80$ μm, 58 Torr, laser focus 10 mm after cesium column center.

5.3.2 XFROG Measurement

Introduction: Temporal Metrology

In this section, I present our measurements of the temporal properties of our harmonic radiation. Previously in our group, autocorrelation measurements were done on harmonics generated with the picosecond mid-infrared laser and cesium. These measurements successfully yielded estimates for the pulse durations of H5, H7, and H9[108]. We wished to push the temporal metrology further and measure the complete temporal profile of our harmonics, which can be described mathematically as

$$I(t) = |E(t)|^2 = |\mathcal{E}(t)\exp[-i\omega t + i\phi(\omega)]|^2 \tag{5.1}$$

where ω is the carrier frequency and $\phi(\omega)$ is the spectral phase.

Measurement of the temporal properties of ultrashort bursts of light with pulse durations on the order of picoseconds or less is challenging due to the fact that there are few controllable events or processes with durations less than the pulse in question that can be used as a metric against which to measure the pulse. All electronic signals are too slow. A means around this problem is to use the pulse as it interacts in a nonlinear medium to measure itself. The first techniques developed to gain access to the pulse duration of short laser pulses [117–121], on which the best methods available today are based, did this in the following manner. First, the laser pulse is split into two identical pulses using a beamsplitter. One pulse travels along a path with variable distance, path 1, the other along a fixed distance, path 2, until they are recombined in a nonlinear medium which produces signal light whose strength is dependent on the amount of overlap between the two replica pulses. By adjusting the distance of the variable path length, the pulses along path 1 are stepped across the pulses of path 2, and the intensity of the nonlinear signal light is recorded as a function of the delay between the pulses. A depiction of this is found in Figure 5.19, for the case where the nonlinear medium is a frequency doubling crystal and the signal light is the second harmonic of the input pulse (SHG). Here, the electric field of the SHG signal can be written

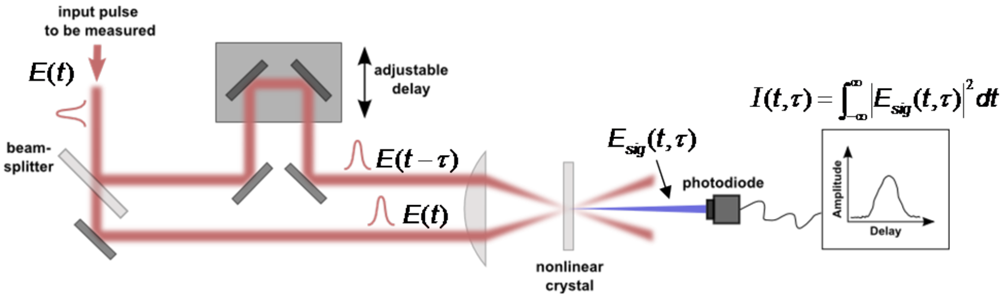

Figure 5.19: Autocorrelation measurement based on second harmonic generation (SHG).

$$E_{sig}(t,\tau) = [E(t) + E(t-\tau)]^2 \tag{5.2}$$

where $E(t)$ is the complex electric field of the unknown pulse and τ is the delay between the pulse and its replica. A detector, typically a photodiode, with a slow response relative to the signal electric field, integrates the intensity of the signal light

$$I_{sig}(t,\tau) = \int_{-\infty}^{+\infty} |E_{sig}(t,\tau)|^2 \, dt. \tag{5.3}$$

Inserting Equation 5.2, expanding, and dropping all but the cross terms, due to the fact that the geometry is noncollinear and therefore the pulses from an individual arm do not hit the detector, we see that the result is mathematically equivalent to an intensity autocorrelation of the two pulses

$$I_{sig}(t,\tau) = A^{(2)}(\tau) = \int_{-\infty}^{+\infty} I(t)I(t-\tau)dt \tag{5.4}$$

where $I(t)$ is the intensity profile of the unknown pulse. An estimate for the actual pulse duration can be extracted from the autocorrelation measurement by assuming a specific temporal profile for the pulse under question ($e^{(-t^2)}$, and $sech^2(t)$ are common laser pulse temporal profiles). The autocorrelation can reveal little more than this, however, because the measurement is not sensitive to the phase of the radiation [122]. Another way of formulating this is that there is no unique solution for the laser pulse, $E(t)$, that produces the autocorrelation $A^{(2)}(\tau) = \int_{-\infty}^{+\infty} I(t)I(t-\tau)dt$.

I will mention here, as somewhat of an aside, that autocorrelation measurements, although limited in their ability to measure temporal properties, are not obsolete. They are still used as invaluable diagnostic tools to continuously monitor the performance and stability of pulsed lasers. On our laser system, we have two autocorrelators to monitor the ti:sapphire oscillator and Nd:YLF oscillator. Also, as is the case with our 3.6 μm laser pulses, there are situations where the components required for more sophisticated temporal measurements are not available or are too expensive and so the traditional autocorrelation is the only practical method available. Many different variants of autocorrelation measurements have been developed [123–125], including the interferrometric autocorrelation technique [126, 127] and autocorrelators that use a nonlinearity in the photodiode detector itself [128, 129].

Measurements that are sensitive to both the amplitude and phase have been developed and two general techniques, known as FROG and SPIDER, have risen in the ranks to be considered the standards within the experimentalist's temporal metrology toolbelt. Our measurement is based on FROG, but for completness, I will briefly describe the basic idea behind the SPIDER technique here. SPIDER (Spectral Phase Interferometry for Direct Electric-field Reconstruction) is a method developed by Ian Walmsley and coworkers[130]. It is based on spectral shearing interferometry [131], and measures the spectrum resulting from the interference between two spectrally sheared replicas of the unknown pulse. From this spectrum, both the amplitude and phase of the pulse can be extracted by means of an algebraic inversion algorithm (as opposed to iterative algorithm used in the FROG measurement which will be described next). To implement this technique, the unknown pulse is split into three replicas. Two are sent through a Michelson interferometer which creates a small temporal delay between the two. The third pulse is chirped by means of a grating, prism, or window. The three pulses are then recombined in a nonlinear crystal and create the spectral shift between the two interferometer pulses by means of frequency up-conversion. The leading pulse mixes with the blue portion of the chirped pulse while the trailing pulse mixes with the red portion. The spectrum of the pulses is then detected. The SPIDER technique has been implemented routinely in numerous labs, including our own, and can be particularly useful on low repetition rate systems when realized as a single shot measurement. However, it was not the technique used in this work, so no further description will be included here. The interested reader can consult these suggested references, and those within, for more on the subject [130, 132–134].

FROG

The FROG (Frequency Resolved Optical Gating) measurement technique was developed by Rick Trebino and coworkers[135–137]. Like SPIDER, it is a modification of the intensity autocorrelation measurement, but its implementation is simpler than that of SPIDER. As a general description, a FROG measurement is a spectrally resolved autocorrelation measurement. The photodiode detector of the autocorrelation measurement is replaced by a spectrometer and the spectrum of the generated signal is recorded as a function of delay between the two pulses. The measured spectra for each time slice are then presented in a 2D plot, called a spectrogram. The spectrogram contains the amplitude and phase information for the electric field of the pulse and this information is extracted through the use of an iterative phase-retrieval algorithm.

Many variants of FROG measurements have been developed, such as polarization-gate FROG (PG FROG) [138–140], transient-grating FROG (TG FROG) [141], third harmonic generation FROG (THG FROG) [142], self-diffraction FROG (SD FROG)[143], second harmonic generation FROG (SHG FROG) [135], GRENOUILLE[5] [144] and cross-correlation FROG (XFROG) [145, 146]. For our application, we chose to use the XFROG method, a close relative of SHG FROG which is a straightforward extension of the SHG autocorrelation described earlier. SHG FROG has the advantage over many other techniques as being simple to implement, since it requires few components. It is also one of the more sensitive methods. XFROG shares these advantages of SHG FROG, but allows for the measurement of very weak pulses, by mixing the unknown pulse not with itself, but with a stronger reference pulse. Figure 5.20 contains a schematic diagram of an XFROG measurement.

The mathematical description of the XFROG spectrogram is straightforward. Remembering that the spectrum of a signal, $E_{sig}(t)$, is defined as the square of the magnitude of the Fourier transform of the signal (Wiener-Khintchine theorem)

$$S(\omega) \equiv \left| \int_{-\infty}^{+\infty} E_{sig}(t,\tau) e^{(-i\omega t)}) dt \right|^2 \tag{5.5}$$

---

[5] GRating-Eliminated No-nonsense Observation of Ultrafast Incident Laser Light E-fields. It means frog in French.

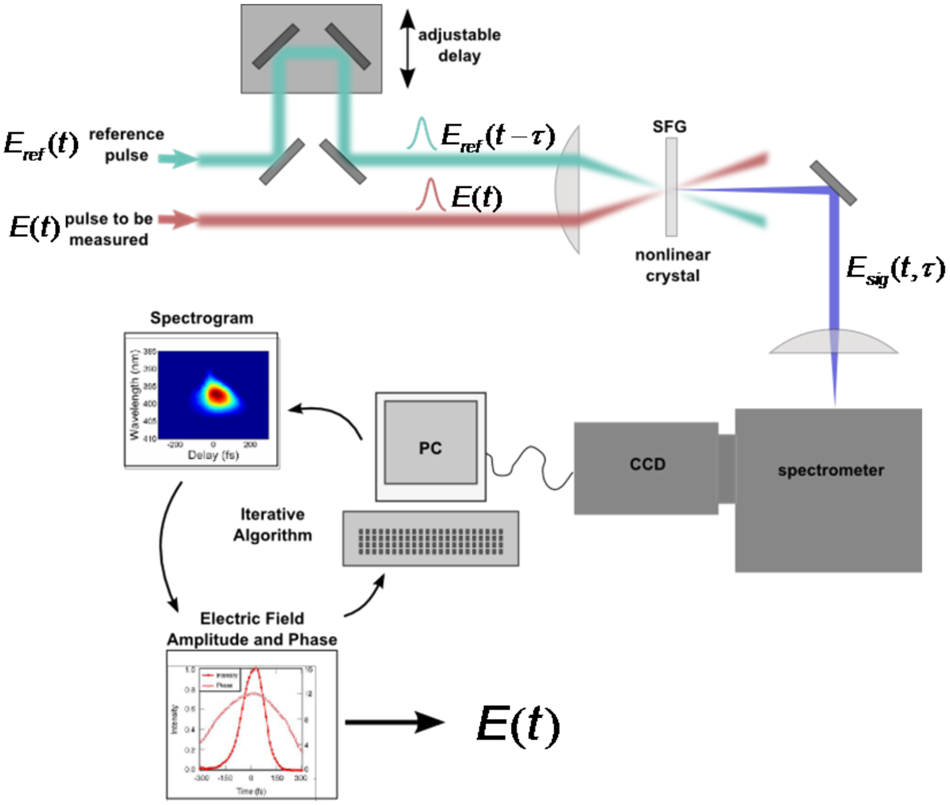

Figure 5.20: Schematic diagram of a cross-corrleation FROG measurement (XFROG) based on sum-frequency generation (SFG).

it is clear that the spectrally resolved autocorrelation can be written

$$I_{FROG}(\omega,\tau) \equiv S(\omega,\tau) = \left| \int_{-\infty}^{+\infty} E_{sig}(t,\tau) e^{(-i\omega t)} dt \right|^2 \tag{5.6}$$

where for a cross-correlation FROG the signal is written as $E_{sig}(t,\tau) = [E(t) + E_{ref}(t-\tau)]^2$, and after dropping all but the cross terms, as in the SHG case

$$E_{sig}(t,\tau) = E(t)E_{ref}(t-\tau) \tag{5.7}$$

with $E(t)$ being the pulse to be measured and $E_{ref}(t)$ the reference pulse.

The spectrogram, I_{FROG}, contains the amplitude and phase information about the measured pulse needed to reconstruct $I(t) = |E(t)|^2$. In order to retrieve the information, an iterative algorithm is used to search the space of complex functions and find the electric field $E(t)$ that produces the measured FROG spectrogram. While there are several different varieties of FROG algorithms [137] the one that is considered to be the most reliable, and which underlies the algorithm used for our measurements, is the generalized projections algorithm[6][148]. This method searches for the complex signal function $E_{sig}(t,\tau)$ that reproduces the FROG spectrogram. Once found, $E(t)$ is obtained through its relationship with $E_{sig}(t,\tau)$, which, again, for XFROG is $E_{sig}(t,\tau) = E(t)E_{ref}(t-\tau)$. There are two constraints imposed to guide the search. First, $E_{sig}(t,\tau)$ needs to be of the set of functions that generates a FROG spectrogram, $I_{FROG}(\omega,\tau) = \left|\int_{-\infty}^{+\infty} E_{sig}(t,\tau)e^{(-i\omega t)}dt\right|^2$, that matches the measured data. Second, $E_{sig}(t,\tau)$ needs to be of the set of functions that are fields that can be generated by a physically realizable electric field through the relationship $E_{sig} = E(t)E_{ref}(t-\tau)$. The means by which the search is undertaken is represented geometrically in Figure 5.21. The algorithm begins with an initial (random) guess for $E_{sig}(t,\tau)$ which is projected onto one of the constraint sets to a point that is closet to the original guess. (The actual means by which the projection is done is described in a moment.) Then the new $E_{sig}(t,\tau)$ is projected onto the other set, to a point that is closest. The iterations continue, projecting from one set to the other, until the point is reached at which $E_{sig}(t,\tau)$ is a member of both sets. This is guaranteed to happen if the constraint set are convex, as shown in Figure 5.21. For FROG, the constraint sets are not convex, and so convergence is not guaranteed, but in practice for pulses encountered in the laboratory it is not a problem and the algorithm will converge[137].

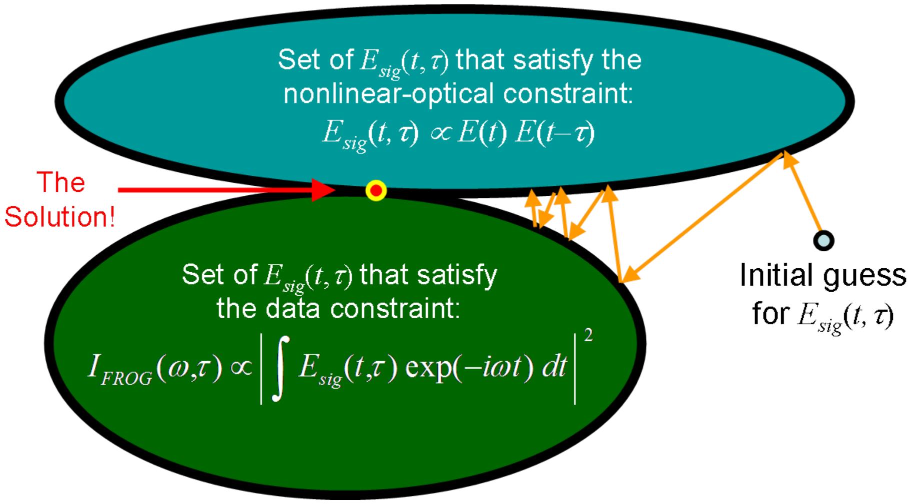

Figure 5.21: Depiction of the generalized projections algorithm as applied to SHG FROG. Figure reproduced from Rick Trebino's website[136].

The projections are carried out in the following manner. To do the generalized projection to the constraint set that produces the measured $I_{FROG}(\omega,\tau)$, the magnitude of the iteration's guess signal in the frequency domain $\widetilde{E}_{sig}(\omega,\tau)$ is replaced

---

[6] This method is often used for phase-retrieval problems, such as image recovery, and it is from such applications that it has been borrowed for FROG[147]

by the magnitude of the experimental FROG spectrogram, while the phase remains unchanged. This can be written

$$\widetilde{E}'_{sig}(\omega,\tau) = \frac{\widetilde{E}_{sig}(\omega,\tau)}{\left|\widetilde{E}_{sig}(\omega,\tau)\right|}[I_{FROG}(\omega,\tau)]^{1/2} \tag{5.8}$$

where $\widetilde{E}'_{sig}(\omega,\tau)$ is the new, projected signal guess and $\widetilde{E}_{sig}(\omega,\tau)$ is the previous guess.

To do the generalized projection to the other constraint set, the functional distance is defined

$$Z = \sum_{i,j=1}^{N} \left|E^{k}_{sig}(t_i,\tau_j) - E^{k+1}_{sig}(t_i,\tau_j)\right|^2 \tag{5.9}$$

where $E^{k}_{sig}(t_i,\tau_j)$ is the current guess for the signal field and $E^{k+1}_{sig}(t_i,\tau_j)$ is a possible new guess. To find the new guess, $E^{k+1}_{sig}(t_i,\tau_j)$, that is closest to the previous guess and which satisfies the constraint of the set, the explicit form for the signal, Equation 5.7 for XFROG, is substituted for $E^{k+1}_{sig}(t_i,\tau_j)$ and a procedure is used to find the function $E^{k+1}_{sig}(t_i,\tau_j)$ that minimizes Z. This function becomes the projected next guess.

A version of the generalized projection algorithm just described is the Principal Components Generalized Projection algorithm (PCGPA)[149], [150]. The PCGPA treats the generalized projection algorithm as an eigenvalue problem, and utilizes ideas from Principle Components Analysis [151], [152]. In doing so it avoids the very time intensive minimization step, making it a much faster alternative. In addition, PCGPA has been shown to work very well for BlindFROG retrieval [148], [153], which, as will be described in the next section, is the type of retrieval used for our case. The PCGPA was the algorithm used to retrieve the amplitude and phase information from our measured spectrograms. The details can be found in [154].

A quantitative measure of the convergence of the FROG algorithm is the FROG error, G [137]. It is defined as

$$G = \sqrt{\frac{1}{N^2}\left|I_{FROG}(\omega_i,\tau_j) - \mu I^{(k)}_{FROG}(\omega_i,\tau_j)\right|^2}. \tag{5.10}$$

It is an rms average across the entire FROG trace, of the difference between the experimental FROG trace, I_{FROG}, and the retrieved FROG trace, $I^{(k)}_{FROG}$. The factor μ is present to take into account the impact of noise in the experimental FROG trace. Since both the experimental and retrieved traces are normalized to a peak of unity, if the highest pixel in the experimental trace is corrupted by noise, its normalization will be skewed and therefore the calculated value for G will be biased. This is dealt with by allowing the normalization of the retrieved trace for each iteration to be varied, and the value for μ that minimizes the error is used to calculate G. The FROG error scales as $N^{-1/2}$ for an $N \times N$ trace. Since for a

128×128 grid size trace, a FROG error of $G = 0.005$ or less is widely accepted as an indication of an accurate retrieval of a low-noise trace, for our 1024×1024 grid size traces, we have a target FROG error of $G = 0.001768$.

XFROG for our application

The XFROG characterization method was chosen to measure the temporal profile of our harmonic radiation. The primary reason for this choice was the low pulse energy present in each of our harmonics (~ 10 pJ, see Section 5.3.1). This low energy made splitting the harmonic beam and then recombining to drive a nonlinear process an unfeasible option. The XFROG alternative was a natural second choice, and also has an added advantage of allowing for the measurement of the relative phases between the harmonic orders. This is a measurement that is extremely important for our main objective of measuring the complete temporal profile of our harmonic radiation, defined by Equation 5.1.

To expound on this, we first consider that for an individual harmonic order, the intensity as a function of time can be written in terms of the electric field amplitude and phase as

$$I_q(t) = |E_q(t)|^2 = |\mathcal{E}_q(t)\exp[-i\omega_q t + i\phi(\omega_q)]|^2 \tag{5.11}$$

where q indicates the q^{th} harmonic order, ω_q is the harmonic frequency, and $\phi(\omega_q)$ is the phase. We wish to know $I_q(t)$ for each of our harmonic orders, which requires a measurement technique that is sensitive to both the amplitude of the electric field and the phase, and we have established that the FROG technique is capable of this. Yet, in addition to measuring individual harmonics, $I_q(t)$, we are interested in knowing the temporal properties of the harmonic spectrum taken as a whole, which is written as

$$I(t) = \left|\sum_N \mathcal{E}_q(t)\exp[-i\omega_q t + i\phi(\omega_q)]\right|^2 \tag{5.12}$$

where N indicates a sum over all the odd-order harmonics of the spectrum. To reconstruct this total temporal profile, $I(t)$, it is necessary to know the relationship between the harmonic phases,

$$\phi_{q+2}(\omega_{q+2}) - \phi_q(\omega_q). \tag{5.13}$$

The form of this phase relationship can have a dramatic influence on the temporal structure of the complete field. For a given number of harmonics, if the individual harmonics were perfectly synchronized with each other, meaning that their phases were given by $\phi(\omega_q) = q\omega_0 k$, where k is a constant, the temporal profile of the full harmonic spectrum would consist of a train of short, transform limited pulses, separated by one half cycle of the fundamental driving field. If, however, the relationship is not constant, but dependent on the harmonic frequency, $\phi(\omega_q) = q\omega_0 f(\omega_q)$, the complete field can suffer a broadening, due to a chirp, of the half cycle peaks, or even the loss of the half cycle peak structure, depending on the magnitude of the phase difference.

Experiments studying HHG using noble gases and many-cycle ti:sapphire laser pulses have found that over portions of the spectrum within the plateau, while the harmonics are not perfectly synchronized, they are close to being so [21], [44], [155], [156], [25]. Instead of a linear relationship between the harmonic phases, there is a quadratic relationship, which means that the frequencies making up a given short pulse of the train are slightly separated in time. This chirp of the attosecond pulses constituting the train has lead to this linear relationship between the phases to be referred to as the "attochirp". A particularly nice description of the experimental implementation required to take advantage of the small attochirp and generate short attosecond pulses can be found in [25].

The relative phase between two pulses cannot ordinarily be measured by FROG, as it requires a phase reference. In the XFROG case, however, by Frogging multiple harmonic orders together on the same spectrogram, the reference pulse can provide the phase reference and the phase relationship between orders can be obtained. Ideally, all of the harmonic orders we were interested in measuring, namely H5-H15, would be collected in one large spectrogram. However, H5-H15 represents a bandwidth of nearly 500 nm, a range far too large for any known nonlinear crystal to be able to phase match at a fixed phase matching angle. The solution we settled upon was to use a set of five nonlinear crystals, each cut to phase match a pair of neighboring harmonics, with the pairs overlapped (i.e. H5+H7, H7+H9, H9+H11, etc.). The spectrograms each then contain 2 harmonics and the relative delay between the two orders can be extracted from a single spectrogram. The delays from the multiple spectrograms could then be concatenated to retrieve the full relationship between all the orders.

Type II sum-frequency generation between a reference pulse centered at 1.8 μm (H2) and H5-H15 was chosen to be the nonlinear interaction for the XFROG measurement.

$$\omega_{H2} + \omega_q = \omega_{q+2} \tag{5.14}$$

BBO (β-BaB$_2$O$_4$ or β-barium borate) was chosen to be the XFROG crystal. Table 5.3 lists the 5 crystals and some of their properties. The crystal lengths were chosen to be long enough to generate sufficient signal, but short enough to phase match the full bandwidth of a given harmonic.

Crystal	**Cut to phase match:**	**Cut angle**	$w \times h \times l$
1	$H2$ and $H5 + H7$	$\theta = 27.5°$	$5 \times 5 \times 0.05\ mm^3$
2	$H2$ and $H7 + H9$	$\theta = 30°$	$5 \times 5 \times 0.05\ mm^3$
3	$H2$ and $H9 + H11$	$\theta = 33°$	$5 \times 5 \times 0.03\ mm^3$
4	$H2$ and $H11 + H13$	$\theta = 36.3°$	$5 \times 5 \times 0.02\ mm^3$
5	$H2$ and $H13 + H15$	$\theta = 40.2°$	$5 \times 5 \times 0.01\ mm^3$

Table 5.3: Set of Type II BBO XFROG crystals and their properties.

The reference pulse was chosen based on the following considerations. The simplest implementation of XFROG would have been to use a replica of the 3.6 μm pulse as the reference pulse. Examination of the phase matching restrictions for nonlinear crystals made clear that this was not possible. Mid-infrared wavelengths do not phase match near UV wavelengths in any of the commonly used nonlinear crystals. The second harmonic of 3.6 μm, 1.8 μm, does however, so we decided to double a 3.6 μm replica pulse in a nonlinear crystal before the XFROG measurement to use as the reference pulse.

Ideally, the 1.8 μm pulse would be completely characterized before the XFROG measurement, so that it's electric field, $E_{ref}(t)$, could be put into the XFROG retrieval algorithm as a constant input. However, we did not have a setup equipped to do such a measurement and so decided to rely upon the XFROG algorithm itself to reconstruct the 1.8 μm reference pulse properties as well as the harmonic properties. This technique is referred to as BlindFROG[7] [153]. While without additional input constraints it is known to have many ambiguities and work poorly, if a constraint, such as the measured spectrum of the reference pulse, is added it can be quite robust. We implemented the 1.8 μm spectrum as a constraint to the XFROG algorithm as well as the constraint of running the algorithm on several spectrograms simultaneously and found that the algorithm converged satisfactorily. This is described in more detail in Section 5.3.2.

An unforeseen problem in the early development of this experiment was related to the large difference between the group velocities of the harmonics as they travel through the heat pipe output window and through air to the XFROG crystal. The ultimate solution added a great amount of complexity to the XFROG measurement. While the harmonics of the scaled atom-laser system are more conveniently located in the visible, instead of the UV, region of the spectrum, making absorption by optical materials and air unproblematic, the dispersion from the heat pipe output window and air was found to have a dramatic influence. During their transit from the cesium column in the heat pipe to the XFROG sum-frequency crystal, the harmonics separated in time by many 10's of fs. This can be seen from preliminary data, shown in Figure 5.22. Here, four harmonics (H5-H11) have been captured on the same XFROG spectrogram. This spectrogram was taken with a 3 mm thick LiF output window on the heat pipe. The expected delay between the orders due to this window, calculated using the Sellmeier coefficients from [158], is shown superimposed on the figure. It is clear that the delay between the orders is due primarily to the LiF. A closer analysis of the situation revealed that dispersion due to air also contributed to the delay between orders, especially for the shorter wavelength harmonics. Given that a main part of our objective was to measure the relative delay, due to the generation process, a solution to remove the LiF/air dispersion was required.

While we briefly considered modeling the dispersion effects, using published

---

[7] This is the so-called 2D blind deconvolution problem. BlindFROG is related to this problem in image science, where both the image and an unknown blurring function can be extracted from a blurred image[157].

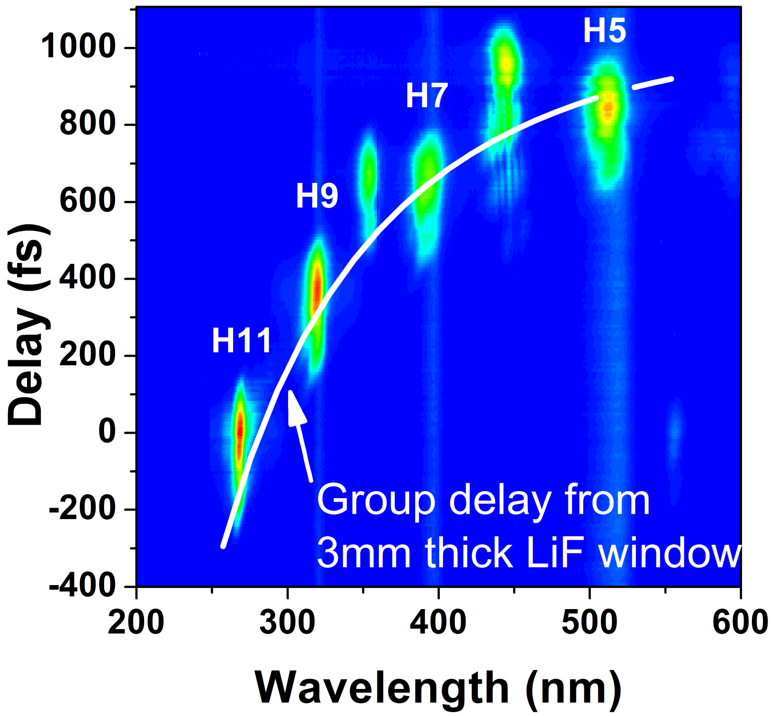

Figure 5.22: Preliminary XFROG trace depicting the group delay separation between the harmonic orders, due primarily to the dispersion of the LiF heat pipe output window.

Sellmeier coefficients for LiF and temperature and humidity dependent models for air, we decided the precision achievable going this route was not sufficient for our main objective. Instead, we decided upon a two-fold solution. First, the air along the harmonic path was removed by enclosing the transport from the heat pipe output to the XFROG crystal in a vacuum chamber. A pressure of $\sim$ 100 mTorr was deemed sufficient to be able to completely neglect the effects of air and this pressure could be easily achievable using mechanical roughing pumps. Second, the effects of the LiF output window were removed through a differential measurement technique. Two different LiF windows were used, a 2 mm thick window, and a 3 mm thick window, and the set of spectrograms was measured three times: once with the 2 mm thick window in place, once with the 3 mm thick window in place, and once with the two windows stacked together. The dispersion effects due to one window, chosen to be the 2 mm window, was determined from the difference between the 3 mm data set and the 2+3 mm data set. This effect was then removed from the data taken with the 2 mm window. This technique proved to be successful and the details are further discussed in Sections 5.3.2 and 5.3.2.

XFROG experimental details

Figure 5.23 shows the experimental layout for the XFROG measurement. 100 μJ of 3.6 μm light was split by a beamsplitter into two beams, referred to as the reference beam and the HHG beam. The beamsplitter was a 0.375 inch thick, uncoated, $\mathrm{CaF_2}$ window, oriented so that the vertical, linear polarization of the incident beam would be s-reflected from the front surface of the window. Given this geometry, it was calculated that 7% of the incident beam should be reflected, which corresponds to 5 μW. Given the fact that the window was uncoated, the back surface of the window produced an additional pulse that trailed the first by 127 ps. For the XFROG measurement this temporal separation was large enough to not cause a problem, but when initially achieving the overlap in time between the reference beam and the harmonics beam care was taken that we were overlapped with the first pulse of the reference beam and not the second.

The reference beam was frequency doubled in a 1 mm thick silver gallium selenide ($\mathrm{AgGaSe_2}$, henceforth referred to as AGSE) crystal. The crystal was supplied by Newlight Photonics, polished only (no AR coating), 5x5x1 mm^3 in size, and cut with a phase matching angle of $\theta = 59.2^\circ$ for type I SHG at 3.6 μm. For accurate convergence of the BlindFROG retrieval, it was important that the reference pulse have a simple temporal and spectral profile, so care was taken to not drive the frequency doubling process too hard causing distortion of the 1.8 μm pulse. SNLO [159] was used to model the mixing process and it was found that for spot sizes between 0.50 mm and 0.75 mm sufficient energy could be obtained in the 1.8 μm beam, but with a temporal profile that was smooth, reflecting the incident beam's (assumed Gaussian) temporal profile. The AGSE crystal was positioned slightly before the focus of a 1 inch diameter, f = 400 mm, $\mathrm{CaF_2}$ lens so that the spot size on the crystal was between the desired 0.50 mm and 0.75 mm values. Fine tuning of the focus size was done by adjusting the lens position relative to the crystal while monitoring the 1.8 μm spectrum on a spectrometer (HR320) fitted with an extended InGaAs photodiode linear array. An optimum position was found that maximized the strength of the signal on the linear array while still producing a smooth spectrum centered at the expected frequency. Another f = 400 mm lens collimated the light.

The 1.8 μm beam was separated from the remaining 3.6 μm beam with a short pass filter (Infrared Optical Products Inc., model SP-2000). Using a power meter we measured 1 mW after the filter, which corresponds to 1 μJ of 1.8 μm energy. Aligning such a low power, long wavelength beam was not trivial. Our most sensitive thermal paper was not sensitive enough to detect the beam. Instead, we had to rely upon a thermal camera (Electrophysics, model PV320) and diffraction rings that we created in the spot with an iris. We also found that by removing the filter, the 3.6 μm could be detected on thermal paper, but only at the focus positions, e.g. at the AGSE crystal and at the XFROG BBO crystal. The reference beam traveled

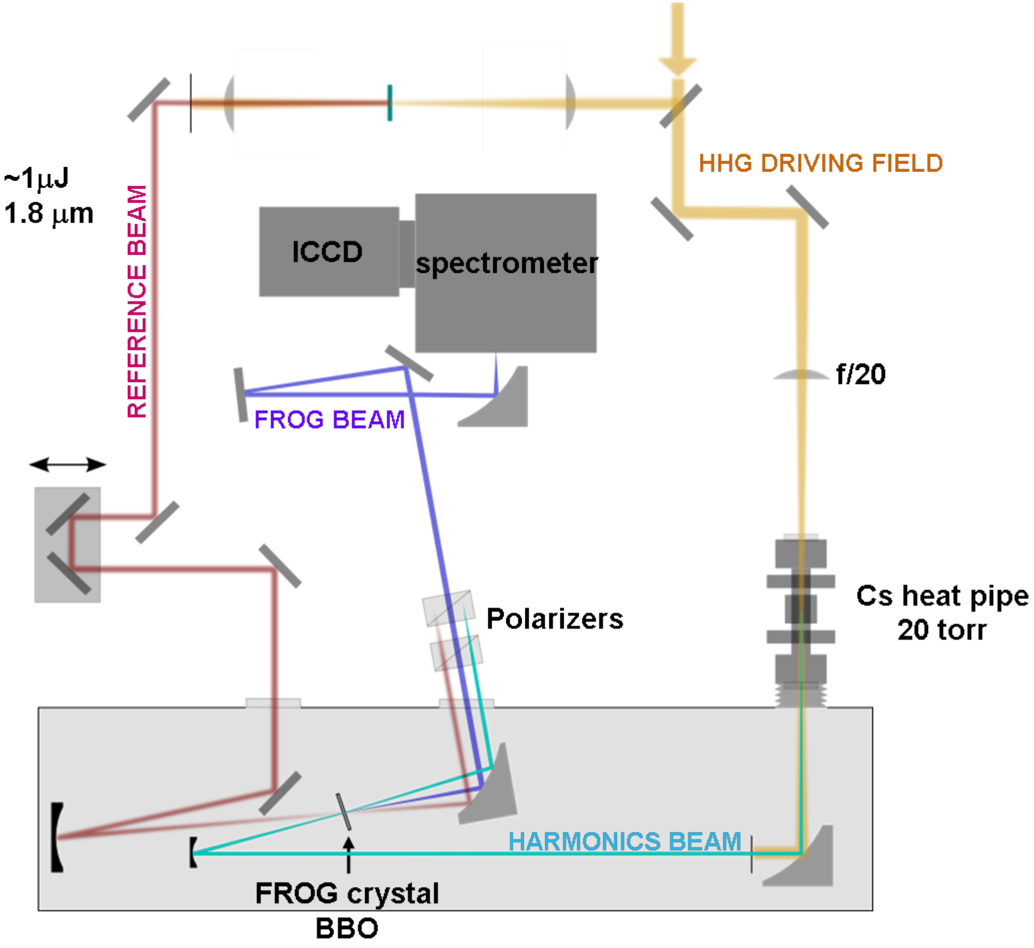

Figure 5.23: XFROG experimental layout

through a delay line consisting of a gold coated hollow retroreflector mounted on a closed-loop piezo stage. The piezo stage had a travel range of 500 μm and 1.5 nm resolution. It was mounted on a manual translation stage, to allow for coarser delay adjustments. After its excursion through the delay line the reference beam then entered the vacuum chamber through a 0.25 inch thick CaF_2 window. It was focused on the XFROG crystal with a 3 inch diameter f = 500 mm mirror.

A graduated micrometer dial was mounted on the mirror proceeding the input window on the vacuum chamber in the reference beam arm. Deflection of the bottom of the vacuum chamber, to which the optics were mounted, when the chamber was pumped down, caused the spatial and temporal overlap between the reference and harmonics beams to be lost. The amount of deflection was repeatable, so the positions of the mirror tilt which brought the temporal and spatial overlap back were found just once and recorded. In addition, due to the difference in optical path through the chamber with and without air present, the manual translation stage had to be adjusted slightly when the chamber was pumped down. (For example, the H7+H2 signal required ~ 200 μm shorter beam path when evacuated.) These values were also found once and recorded.

The transmitted portion of the 3.6 μm beam through the beamsplitter was referred to as the HHG beam. It was focused into the heat pipe by a 1 inch diameter, f = 500 mm lens. Its power after this lens, before the heat pipe was measured to be 77 mW. The heat pipe was positioned so that the laser focus was positioned at the estimated end of the cesium column, 1 mm from the inside edge (closest to the center of the pipe) of the cooling block that was on the exit side. This position produced the largest, smoothest spatial profile for the harmonics beam (as visible by eye on a card), which we believed would focus to the tightest spots on the BBO crystals and therefore create the largest FROG signals (and hence most successful FROG traces). The harmonics and 3.6 μm light passed through the LiF output window (or windows) on the heat pipe and into the vacuum chamber. A f = 327 mm parabolic mirror collimated the light. A 1 inch diameter f = 250 mm protected silver mirror focused the harmonics into the XFROG BBO crystal to a spot size of ~ 10 μm. Due to the fact that the divergence of the harmonic beam decreases with increasing harmonic order, the focused spot size on the BBO increased as a function of the harmonic order. This is opposite to what would have been convenient. Since the energy present in the higher harmonic orders is smaller than in the lower orders we would have liked to focus the higher harmonics tighter at the BBO crystal to drive the sum frequency generation process as efficiently as possible. Added to this was the fact that the BBO crystal lengths for the higher harmonics were shorter. This confluence of conditions caused the higher harmonic XFROG signals to be even more challenging to find than the lower orders.

While we needed to focus the harmonics beam as tightly as possible on the XFROG cyrstal, care had to be taken to not focus the mid-infrared light too tightly on the BBO. Apertures were put in place between the parabolic mirror and the focusing mirror and were closed down around the harmonics beam in an attempt to remove some of the (larger divergence) mid-IR beam. We found that using a shorter focal length lens, f=250 mm, to focus the mid-infrared into the heat pipe was problematic. It produced a spot size on the collimating mirror that was larger, beneficial for tighter focusing of the harmonics on the XFROG crystal, but we were unable to remove enough of the mid-infrared light with apertures before the XFROG crystal to not damage the BBO.

A parabolic mirror (f=152.4 mm, Janos Techonolgy) collected and collimated the XFROG signal light emerging from the BBO, as well as the 1.8 μm and harmonics beams. The light then exited the vacuum chamber through a MgF_2 window. To collect the spectrograms, the XFROG signal needed to be separated from the other light, specifically the harmonic beam since this beam fell in the same positions on the ICCD as the XFROG signal. Although we used a noncollinear geometry (the reference beam and harmonics beam crossed at an angle $\sim 3°$ at the BBO crystal), the XFROG signal was very weak relative to the harmonics and even scattered light from the harmonics beam could dominate the XFROG signal. Fortunately, due to the phase matching in the BBO crystal (chosen to be type II) the XFROG signal and the harmonics had orthogonal linear polarizations. This allowed us to use polarizers to help reduce the harmonics background from the signal.

The first polarizer was a Rochon polarizer, made from αBBO, a form of BBO that has a larger birefringence, over a large range (3500nm - 189 nm) than BBO. Also, its crystal structure has centric symmetry, so $\chi^{(2)}$ is not present. Our Rochon polarizer was purchased from Red Optronics (part number RCP-6010) and had a center aperture of 10 mm. The second polarizer was a Glan-laser polarizer which was also made of αBBO, but was cut for wavelengths < 300 nm. It was found to scatter too much of the light if left in place for the harmonic orders with $\lambda > 300$ nm, so it was only added to collect the XFROG traces for H11 and H13. In addition to the polarizers, a knife edge spatial filter was implemented at the output window of the vacuum chamber. The position of this beam block was adjusted to remove as much of the harmonics beam as possible while still passing a considerable portion of the XFROG signal beam. With the spatial filter and Rochon polarizer in place, the background harmonics level in the XFROG spectrograms was $< 0.3\%$. With the spatial filter, Rochon polarizer and Glan-laser polarizer, the background level was $< 0.1\%$.

The initial temporal overlap between the reference pulse and the harmonics pulse was found using a high speed photodiode (Newport, D-30), with a 30 ps rise time and a linear response from 950-1650 nm. The photodiode was positioned at the XFROG crystal location and the manual stage was slowly translated until the overlap between the 1.8 μm reference pulse and H3 from the harmonics pulse was achieved, as viewed on an analog ocilloscope, which allowed us to get the overlap to within approximately 0.5 ps. The remaining temporal overlap had to be done while looking for the XFROG signal (a very tedious task).

The spatial overlap between both beams was achieved by mounting a 10 μm diameter pinhole into the XFROG crystal holder (crystal having been removed) and then a 1 mm^3 InGaAs photodiode behind the pinhole. The linear response of the photodiode extended from 1.2 μm to 1.8μm and so we were able to detect H3 from the harmonics beam and the 1.8 μm from the reference beam. The crystal holder was positioned on an x-y-z translation stage and its position in each of these directions was tweaked to maximize the throughput of the harmonics beam, effectively positioning the crystal holder at the focus position of the harmonics. Then, the focusing mirror for the reference beam, as well as the z position of the collimating lens, were adjusted to maximize the throughput of the 1.8 μm beam on the photodiode, effectively bringing its focus position to overlap that of the harmonics'. The pinhole and photodiode were then carefully removed and one of the BBO crystals was placed back into the mount.

Once the temporal and spatial overlap where found, the 1.8 μm beam was blocked and the harmonics beam was used to align the optics from the BBO crystal to the SP300 spectrometer. The harmonics beam was also used to carefully set the backreflection from the BBO crystal so that it fell exactly along the beam path, as well as the backreflections from the polarizers. The $f = 152.4$ mm parabolic mirror that focused the light onto the spectrometer slit was tweaked to position the harmonics light just off-center of the slit, so that the XFROG signal would hit center. Then, the 1.8 μm beam was unblocked and the hunt for the XFROG signal began. To find and then optimize the XFROG signal the following were adjusted: the phase matching angle of the BBO crystal, the position of the knife-edge filter, the rotation and tilt of the polarizers, the spatial overlap of the reference and harmonics beams, and the beam pointing into the spectrometer. Needless to say, with so many parameters to tweak, finding the XFROG signal was not trivial.

A data run, to collect one XFROG trace, proceeded in the following manner. Having found and optimized the XFROG signals previously, the XFROG crystal to be used was mounted in the holder, by reaching through a side port on the chamber. This port was then closed and the motorized rotation stage, controllable from the outside of the chamber, that controlled the phase matching angle of the XFROG crystal, was set to the previously found value appropriate for the crystal in use. The values for the reference beam mirror tilt and delay stage position that recover the spatial and temporal overlap after pumping down were set. Then the two roughing pumps were turned on. It took $\sim$ 10-15 minutes for the base pressure in the chamber to reach 100 mtorr. The XFROG acquisition software was then run. Spectra were collected for 2 s (corresponding to 2000 laser shots) at each delay stage position. The camera gain was set to maximize the peak signal in a trace, but not saturate. 10 fs delay steps were taken. Once a trace was completed, it was repeated four times, so that we had five XFROG traces for each crystal/window configuration. Once the five traces were completed, the chamber was brought up to atmosphere, the next crystal was put in place, and the next set of traces were collected. This process was repeated for each window configuration.

Periodically, the data acquisition had to be paused in order to melt back the cesium that had frozen along the cooling block positions. This was a problem due to the fact that the house supplied chilled process water, which we were using for the heat pipe, was too cold (17 C) for our application. Instead of flowing back into the wick as it condensed, some cesium would freeze. A heat gun easily melted it back. This was typically done during a crystal or window change.

XFROG traces were obtained for harmonics 5 through 13 for the three window configurations. Although we had previously managed to get a trace of harmonic 15, during this data run its XFROG's signal was too weak and we were not able to get a trace.

XFROG analysis details

The details of the analysis of the XFROG traces can be found in Erik Power's thesis [154]. Here, I highlight the main points. As was mentioned in Section 5.3.2, the XFROG retrieval algorithm was a double-constraint principle components generalized projection algorithm (PCGPA). Because we did not have a complete characterization of the reference pulse this was a BlindFROG retrieval. The spectral power of the 1.8 μm beam was measured and used as one constraint. The other constraint was to process all the traces in a data set (set for one window configuration) in parallel. After each iteration the 1.8 μm spectral constraint was applied. The next guess for the 1.8 μm spectral phase from all the traces was averaged, and this averaged guess for the gate was used for the next iteration. Parallel processing of all 12 traces was run for 5000 interations, which required 1.5 days to complete.

To obtain error bars on the spectral phase and amplitude, a "bootstrapping" techniqe was used [160]. In this method, the retrieval algorithm is run several times, with randomly selected data points in the experimental traces removed each time. From the resulting retrieved values for the spectral amplitude and phase, error bars can be obtained. To obtain error bars for the harmonics pulses, the 1.8 μm pulse was held constant. 500 sub-sampled XFROG traces were produced for each of the 12 spectrograms. The 6000 traces along with the constant 1.8 μm pulse were submitted to the University of Michigan Center for Advanced Computing Grid for processing. To obtain error bars for the retrieved 1.8 μm pulse, the harmonics pulses were held constant and the sub-sampled XFROG traces were run in parallel with the gate averaging.

XFROG experimental results

Experimental and Retrieved Spectrograms

The raw data from our run is shown in Figure 5.24. Each row contains the averaged XFROG spectrograms for a particular LiF output window configuration. Each column contains spectrograms obtained using a particular BBO crystal.

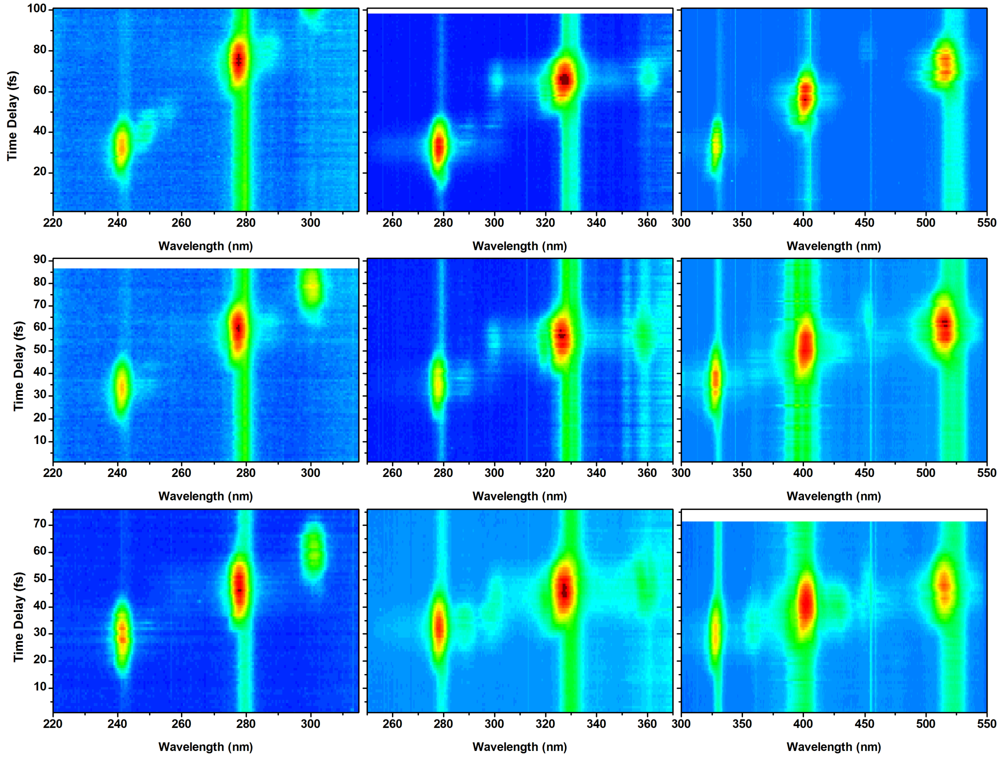

Figure 5.24: XFROG raw data. The intensity scale is in a log scale. Top row: 2 mm + 3 mm LiF window, Middle row: 3 mm LiF window, Bottom row: 2 mm LiF window.

For the raw data, each averaged spectrogram was processed using the following procedure. First, the background harmonic light was subtracted. This was done by taking a portion of the data at the temporal edges of each spectrogram, averaging over the temporal direction, then subtracting this averaged value, a function of wavelength, from the full spectrogram. Then, the spectrogram was filtered using a weak low-pass Fourier filter. The wavelength axis of the filtered spectrogram was then interpolated from wavelength to frequency, while maintaining the appropriate scaling of the spectral amplitude and the time axis was interpolated as well. The final processed spectrogram had a grid size of 1024 x 1024.

Shown in Figures 5.25, 5.26, and 5.27 are the processed experimental spectrograms along side the retrieved spectrograms for the three LiF output window configurations. The retrieved error, G, is included in the figures. As the target error value for our 1024 × 1024 traces was $G = 1.768E - 3$ (see Section 5.3.2), it can be seen that all but three traces met or exceeded the target. The H7/H9 trace with the 2+3 mm window (Figure 5.26), had an error only slightly above the target, $G = 1.784E - 3$, which is close enough to declare a converged result. The other two traces, H5/H7 with the 5 mm window, and H5/H7 with the 3 mm window, are not far off the target value (within a factor of 2). The problem with these traces stems from the stability of the fifth harmonic. Of all the harmonic orders, the fifth was found to be most sensitive to the precise conditions within the heat pipe. This is mostly likely due to the effect from cesium dimers, which was discussed in Section 5.3.1. Close inspection of the experimental XFROG traces for the fifth show that the noise was the greatest here. The fact that the H5 retrieved parameters are the least reliable of the set should be kept in mind when considering the results.

The retreived 1.8 μm pulse is shown in Figure 5.28, both its time-domain intensity profile and its spectral power and phase. Its center wavelength is 1.784 ± 0.0002 μm and its FWHM bandwidth is 41.9 nm. Its FWHM duration was found to be 125.84 ± 0.92 fs, and its transform limit corresponds to 92.22 fs. The retrieved harmonics are shown in Figure 5.29. In the left column the spectral amplitude and phase are shown. In addition, the phase found to be contributed by the 2 mm LiF window is shown, as well as the retrieved phase with the LiF contribution removed. The procedure by which the LiF phase contribution was found is described in the next section. The center frequencies and pulse durations found for the harmonics are summarized in Table 5.4.

Removing Effects of LiF Window

To extract and remove the effects of the LiF output window on the harmonic radiation, two steps were required, treating first the effect on the relative phase between the harmonic orders, and second the effect on the spectral phase of each harmonic order. To tackle the relative phase effect, the first step was to obtain the group delay between successive harmonic orders from the retrieved results. This was done for each spectrogram by Fourier transforming the retrieved time-domain

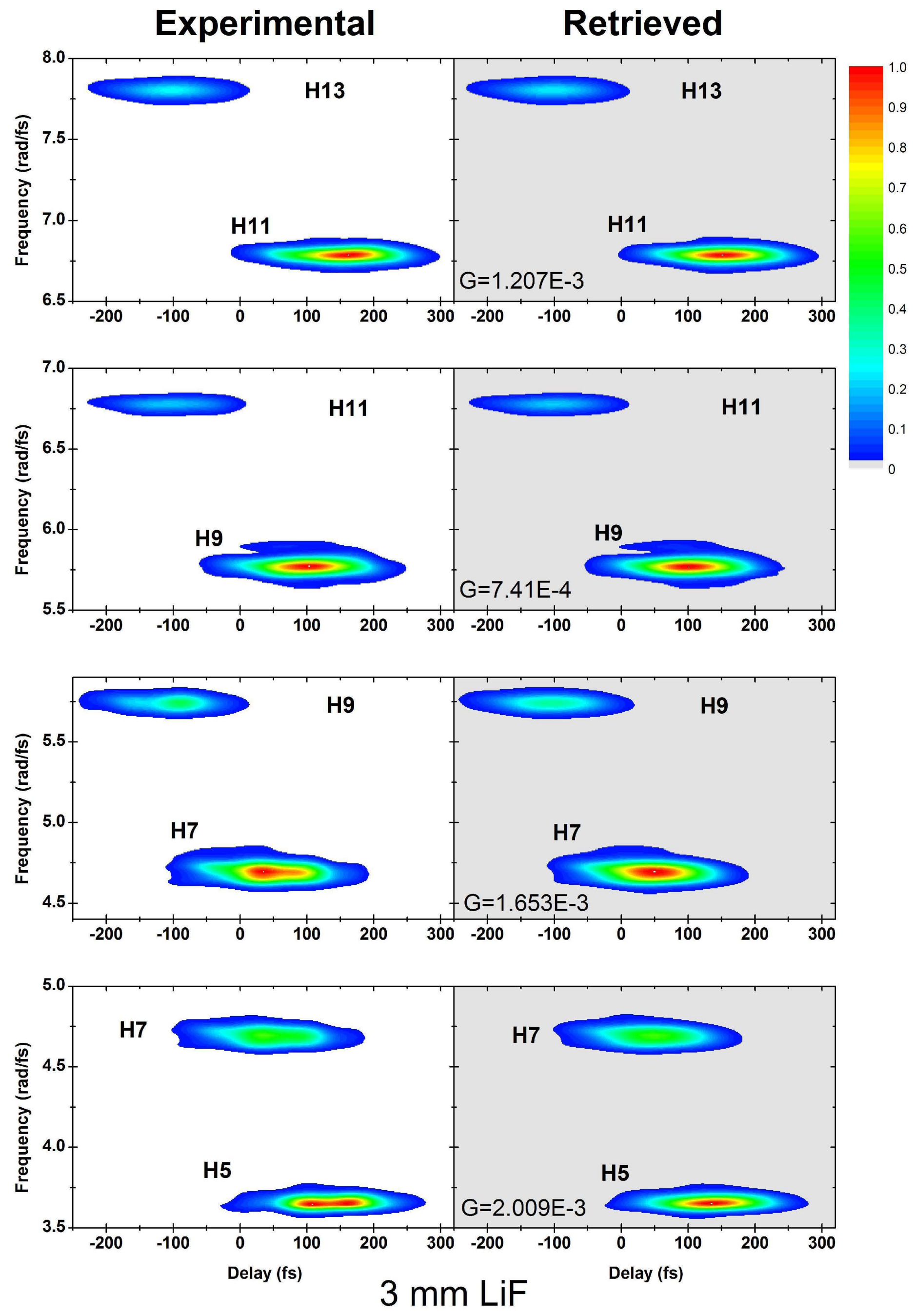

Figure 5.25: Experimental and Retrieved XFROG Traces, 3 mm LiF window.

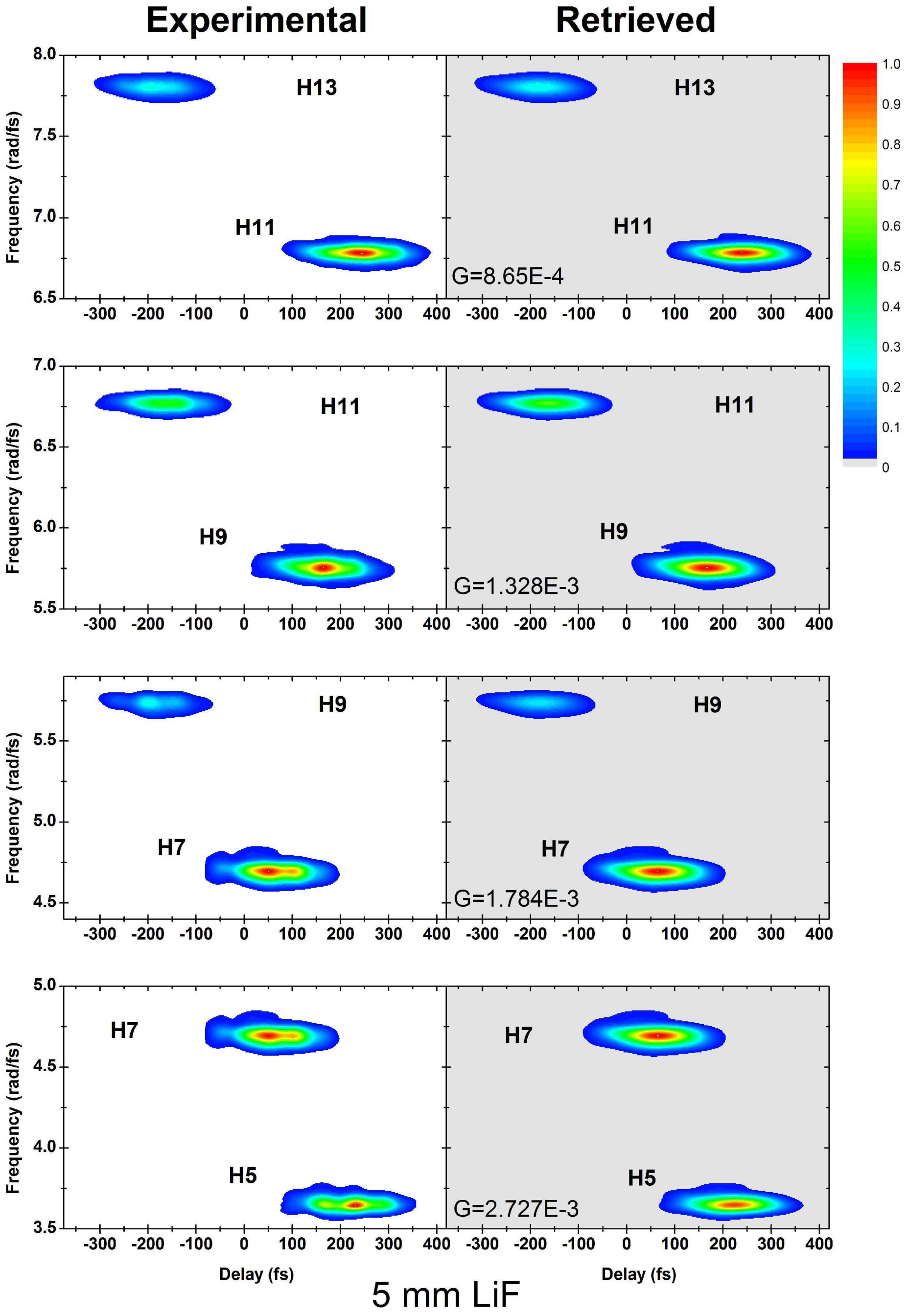

Figure 5.26: Experimental and Retrieved XFROG Traces, 2 mm+3 mm LiF window.

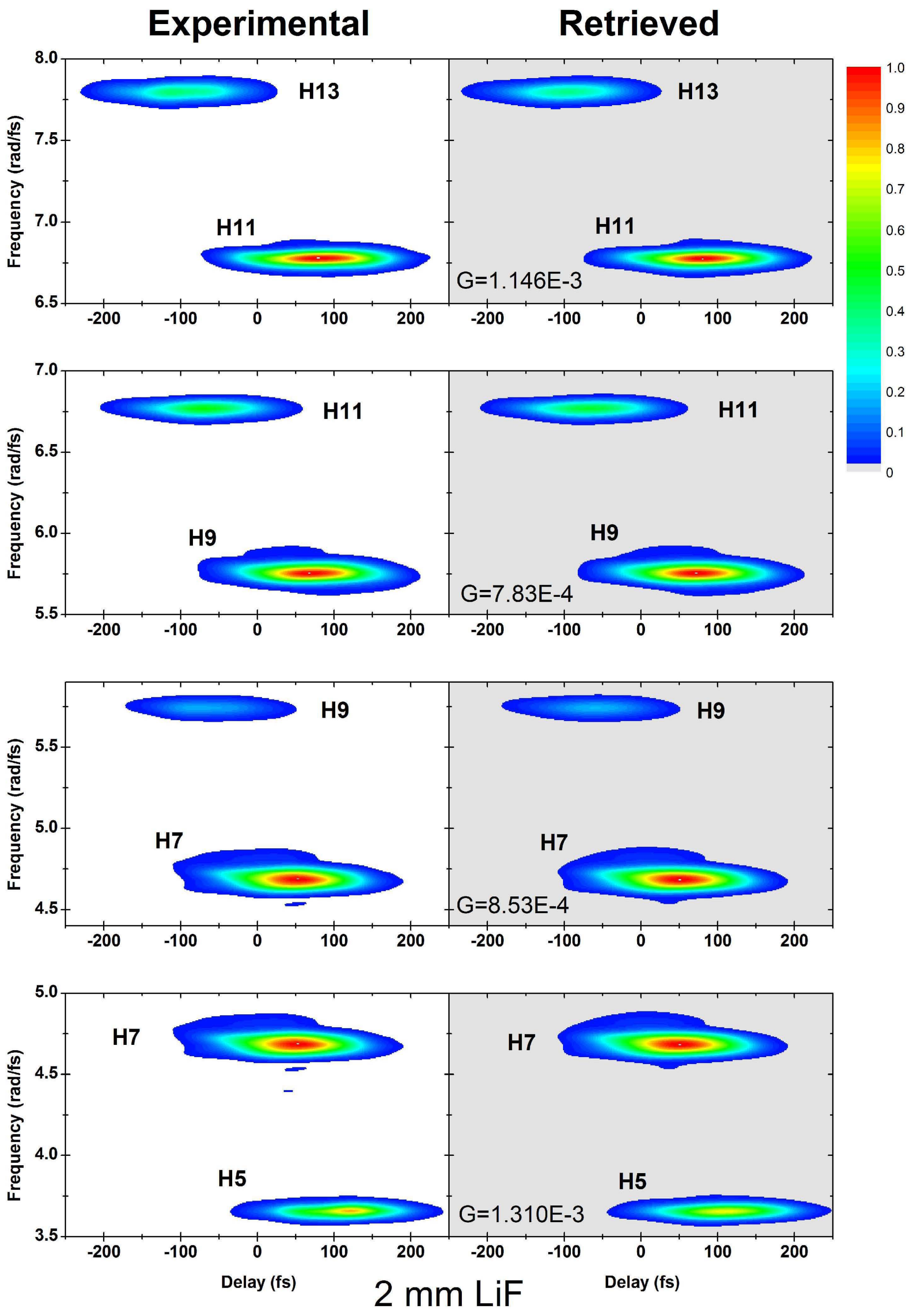

Figure 5.27: Experimental and Retrieved XFROG Traces, 2 mm LiF window.

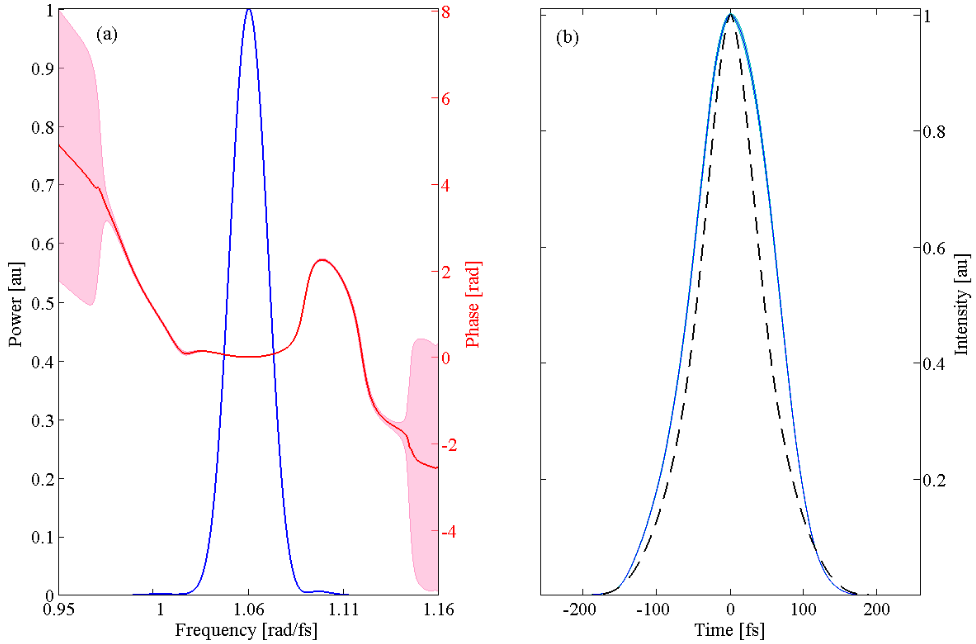

Figure 5.28: Retrieved Second Harmonic. Panel (a): spectral power and phase, $\omega_0 = 1.0558 \pm 0.0001$ rad/fs, $\delta\omega = 0.0248 \pm 0.0001$ rad/fs. Panel (b): time-domain intensity profile, recovered (solid blue), transform limit (dashed black) $\tau = 125.84 \pm 0.92$ fs, $\tau_{TL} = 92.22$ fs. Error bars are represented by the shaded regions.

harmonics, and extracting and unwraping the spectral phase, $\phi(\omega)$. If we write the spectral phase as a polynomial expansion around the center frequency ω_0,

$$\phi(\omega) = \phi(\omega_0) + \left.\frac{d\phi}{d\omega}\right|_{\omega_0} (\omega - \omega_0) + \frac{1}{2} \left.\frac{d^2\phi}{d\omega^2}\right|_{\omega_0} (\omega - \omega_0)^2 + \ldots \tag{5.15}$$

the coefficient of the second term of the expansion represents the group delay. Therefore, we can define the relative group delay between harmonic i and j as

$$\tau^n_{j-i} = \left.\frac{d\phi_x(\omega)}{d\omega}\right|_{\omega_j} - \left.\frac{d\phi_x(\omega)}{d\omega}\right|_{\omega_i} \tag{5.16}$$

where $\phi_x(\omega)$ is the spectral phase retrieved from spectrogram x, and n represents a data set taken with one of the three window configurations (2 mm, 3 mm, or 2 + 3 mm). Figure 5.30 shows the resulting values for τ, where the values from different

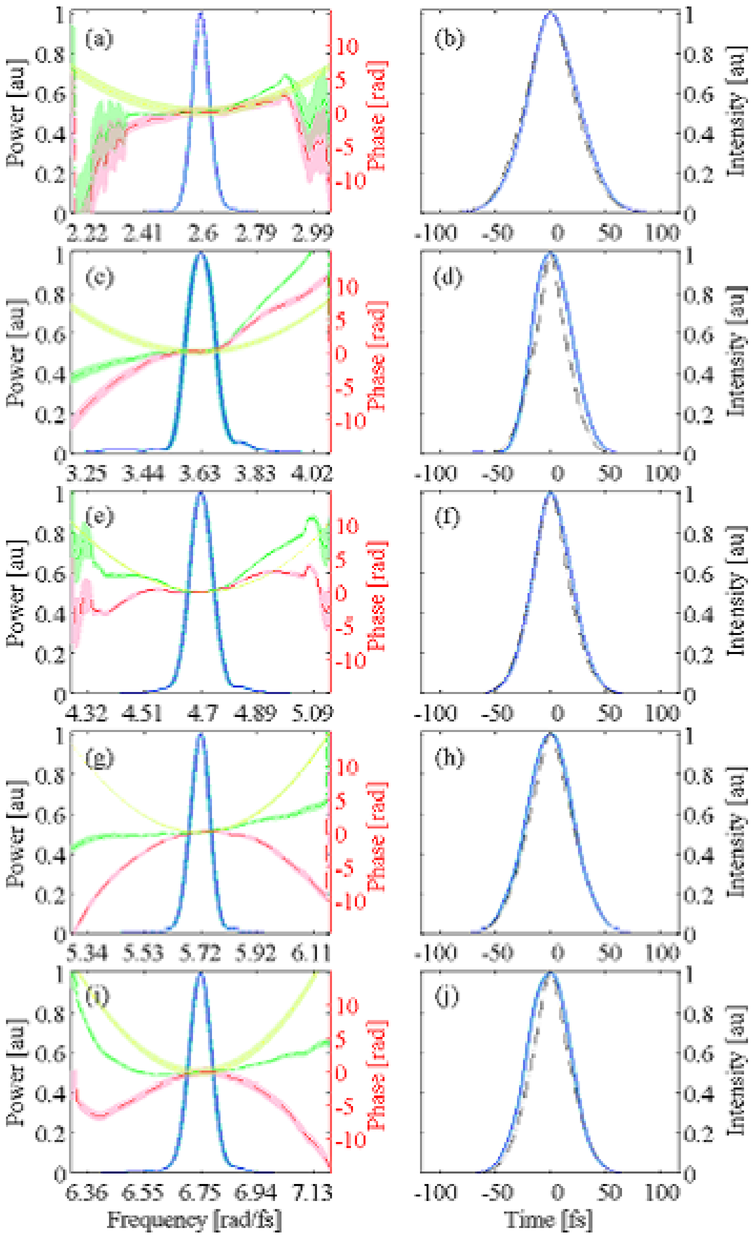

Figure 5.29: Retrieved results for H5 through H13. Left column: spectral power (solid blue), phase (dash-dot green), recovered 2mm LiF phase contribution (dotted yellow), phase with LiF contribution removed (dashed red). Right column: time-domain intensity profile (solid blue), transform-limited profile (dashed black). Error bars are represented by the shaded regions. (a) & (b): H5, (c) & (d): H7, (e) & (f): H9, (g) & (h): H11, (i) & (j): H13.

Harmonic Order	Center Wavelength [nm]	FWHM Pulse Duration [fs]	TL Pulse Duration [fs]
5	723.5 ± 0.4	51.46 ± 0.44	50.46 ± 0.42
7	518.4 ± 0.8	41.75 ± 0.67	32.09 ± 0.29
9	400.5 ± 0.3	40.33 ± 0.37	37.17 ± 0.3
11	329.3 ± 0.2	48.13 ± 0.37	45.01 ± 0.36
13	279.3 ± 0.1	45.97 ± 0.36	38.43 ± 0.3

Table 5.4: Retrieved parameters for individual harmonics.

spectrograms have been referenced to each other and the group delay for H5 has been set to zero. Error bars are present on the data points, but are too small to be seen (∼ 0.1 fs). The relative delay between the harmonic orders before traversing the LiF output window is now easily accesible. Since

$$\tau^{2+3mm} = \tau^{3mm} + \tau^{2mm} \tag{5.17}$$

the delay caused by the 2 mm window is simply

$$\tau = \tau^{2+3mm} - \tau^{3mm}. \tag{5.18}$$

Subtracting this delay from τ^{2mm} leaves the delay due to all things but the LiF window. This delay is shown in Figure 5.31. The error bars shown in the figure are obtained from those of the retrieved group delays through

$$\Delta\tau_q = \sqrt{\Delta\tau_{2mm,q} + \Delta\tau_{3mm,q} + \Delta\tau_{5mm,q}}. \tag{5.19}$$

Having eliminated the contributions to the group delay from the LiF window from the measured harmonics, the remaining task was to remove the LiF contribution from the retrieved spectral phase of each harmonic. The 2 mm LiF window data set was chosen as the set from which to reconstruct the final temporal profile, so this data is the only set considered here. To subtract the contributed phase from the 2 mm LiF window, we need $\phi(\omega)$ that is due to the 2 mm LiF window only. This information is contained in the recovered group delay due to the 2 mm LiF window only, defined as τ in Equation 5.18 and shown in Figure 5.31. Since τ is the group delay, shifted by a constant to make the delay for H5 equal to zero,

$$\tau(\omega) = \frac{d\phi(\omega)}{d\omega} - \left.\frac{d\phi(\omega)}{d\omega}\right|_{\omega_{H5}}. \tag{5.20}$$

Integrating Equation 5.20 then yeilds

$$\int \tau(\omega) = \phi(\omega) - \omega\left.\frac{d\phi(\omega)}{d\omega}\right|_{\omega_{H5}} + b \tag{5.21}$$

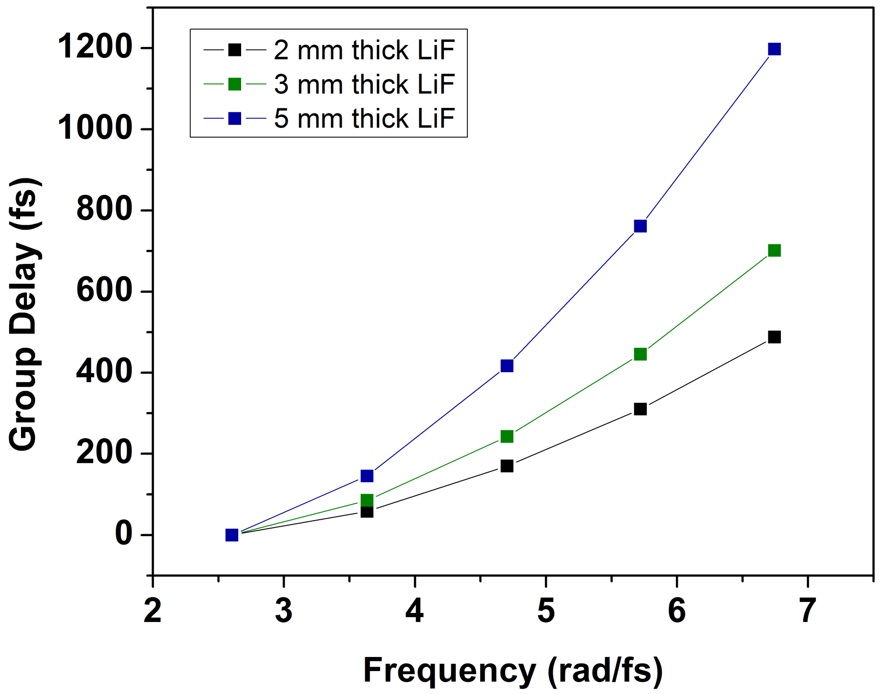

Figure 5.30: Retrieved Group Delay values, relative to H5 for the three LiF output window cases.

where b is a constant. It is clear then that integrating $\tau(\omega)$ yields the desired phase response, $\phi(\omega)$ of the 2 mm thick LiF window. To obtain a full curve from the discrete points of Figure 5.31, the points were fit with a cubic polynomial. This fitted polynomial was then integrated, producing an expression equivalent to that given in Equation 5.21. Although strickly speaking this expression is not simply the spectral phase as a function of frequency due to the 2 mm LiF window, since it contains an extra linear term and a constant term, from the practical point of view of applying the expression to our measured 2 mm LiF results, it is sufficient. This is because we are still referencing our results to H5, and so can still set $\left.\frac{d\phi(\omega)}{d\omega}\right|_{\omega_{H5}}$ to be equal to zero. Also, just as the first term of the polynomial expansion of $\phi(\omega)$ can be ignored since it represents the absolute phase accumulated at the reference frequency, to which we are not sensitive, the constant term can be neglected. To remove the LiF contribution, then, from the measured spectral phases of each harmonic order, the integrated polynomial was evaluated at each center frequency and subtracted from the measured phase. The results of this are shown in Figure 5.29.

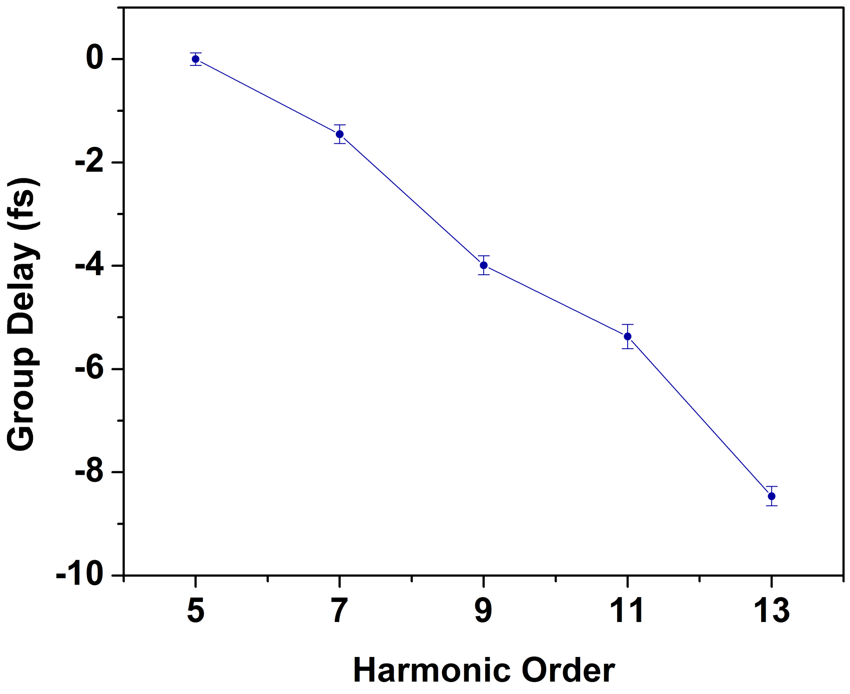

Figure 5.31: Group delay between harmonic orders with the contribution from the LiF output window removed.

Complete Temporal Reconstruction

The spectral phase and power for H5 through H13 are shown together in Figure 5.32. The relative heights of the harmonics' spectral power were scaled using a spectrum measured with the Triax spectrometer, and taking into account the spectrometer and detector wavelength response, as well as the aluminum mirror reflectivity and LiF transmittance. The relative spectral phase between the orders is constructed using the measured group delay values from Figure 5.31. The time-domain reconstruction using H5-H13 is shown in Figure 5.33. Because the results for H5 are somewhat suspect, the complete reconstruction was carried out for just H7-H13. This result is shown in Figure 5.34.

Discussion

To begin, we first consider the meaning of our measurement. First, a clarification of what our measurement was not sensitive to. This measurement is not senstive to the absolute phase of the electric field. (No FROG measurement is). This means that we do not know precisely what the carrier frequency looks like under the tem-

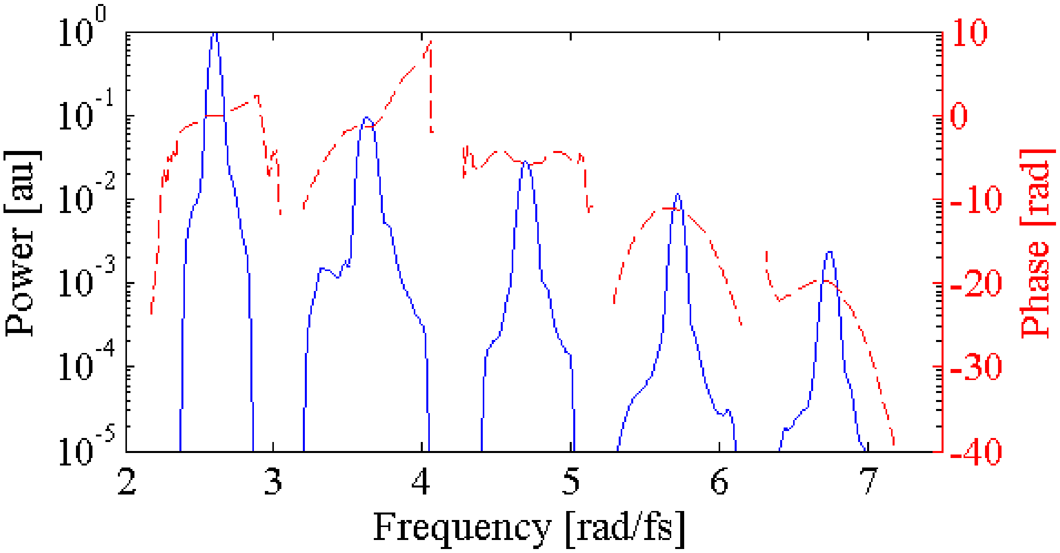

Figure 5.32: Total spectral power and phase for harmonics H5-H13.

poral pulse envelope, e.g. we do not know if the carrier frequency peaks at the same point as the envelope or if there is an offset (known as carrier-envelope offset-CEO). Also, this measurement is an average over the spatial mode of the radiation. Macroscopic effects involving the spatial profile of the focused driving laser field, such as the difference in divergence of the short and long trajectories that has been observed for ti:sapphire driven HHG, are averaged out in our measurement.

For each harmonic order, we have completely reconstructed the intensity profile in the time domain, removing the effects from the dispersion of the LiF window. The dispersion from the window is treated, including up to third order dispersion terms. When taking into account the group delay from the window, we approximate the phase as a fourth order polynomial, but neglect the dc and linear terms. To reconstruct the full temporal profile, we needed to stitch together the results for the individual harmonic orders. In order to do this accurately, the relative heights of the spectral power distributions between the orders need to be known and the relationship between the phases of the individual harmonic orders needs to be known. As was explained, the relationship between the power distributions is accounted for by scaling the results while taking into account the spectrometer and detector responses, as well as mirror reflectivity and LiF transmisivity. The harmonic phases, as shown in Figure 5.29 by the red curves, are added together by using the measured group delay in Figure 5.31. The measured group delay from this curve is multiplied by the difference between the harmonic's frequency and the frequency of H5 (since all our measurements are referenced to H5) and this is added to the spectral phase of Figure 5.29.

Our analysis has revealed that at the output side of the heat pipe, immediately

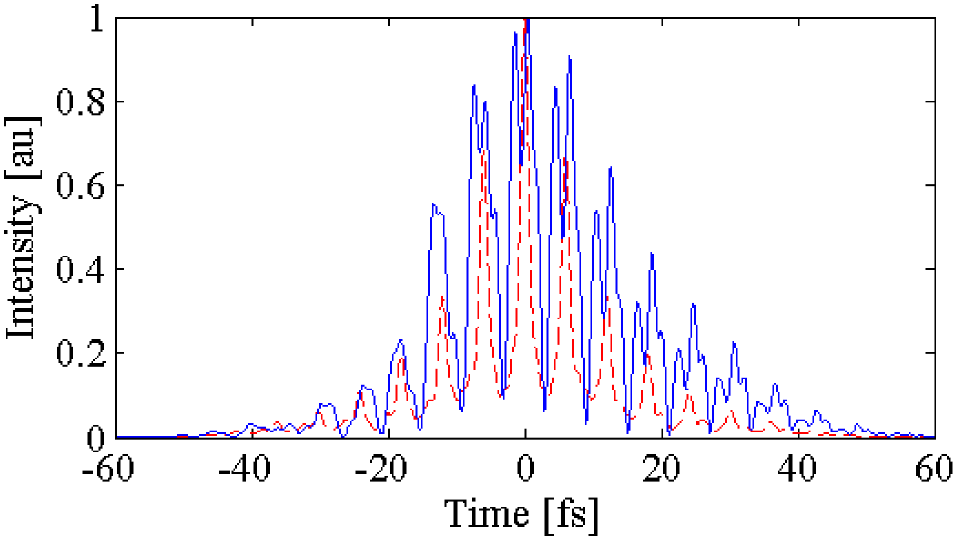

Figure 5.33: Time-domain intensity profile, including H5-H13 (solid blue). Transform limit (dashed red). The FWHM duration of the most intense burst is $\tau = 4.39$ fs, with a transform limited value of $\tau = 1.52$ fs.

before the 2 mm LiF output window, the harmonic spectrum containing H5 through H13 consists of a train of short pulses in the time domain. The pulse separation in the train is ≈ 6 fs, which is equal to 1/2 of the 3.6 μm laser's period. There is considerable structure in the individual pulses, resulting primarily from the negative group delay between the harmonic orders.

At present, the interpretation of the negative group delay is somewhat open. It could be due to the generation process at the single atom level, such as a positive group delay is predicted in the Simpleman's rescattering model for above threshold harmonics with short trajectories and a negative group delay, for long trajectories. Or, the observed group delay could reflect an aspect of the macroscopic production of the harmonic light. To gain insight into this matter, theoretical modeling of the process is required, either of the single atom response, the macroscopic response, or both together. Work is presently underway in our group on a numerical integration of the 1D TDSE to model the single atom response in the 3.6 μm-cesium case.

The present lack of calculational results does not prevent us from speculating on the source of the group delay. As far as the macroscopic response is concerned, the size of the phase matching coherence length and the position of this generating region within the cesium column have important implications for the measured group delay. If the coherence length is short relative to the cesium column length, and is positioned somewhere within the column (not at the end), this means that the generated harmonics will have to travel through some length of cesium before exiting the column and will therefore suffer effects from the dispersion due to the cesium.

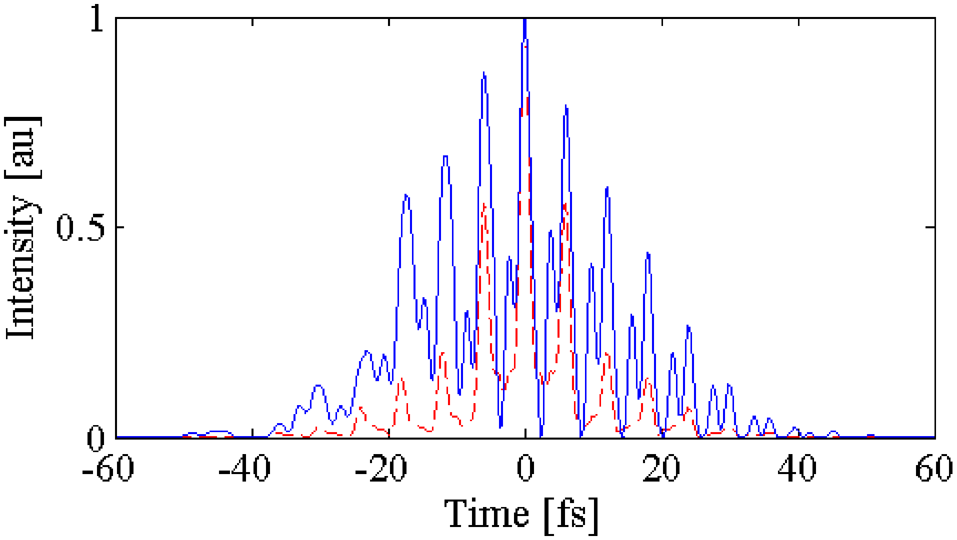

Figure 5.34: Time-domain intensity profile, without H5, including H7-H13 (solid blue). Transform limit (dashed red). The FWHM duration of the most intense burst is $\tau = 2.03$ fs, with a transform limited value of $\tau = 1.68$ fs.

Given that our intensity is high relative to the saturation intensity for cesium at 3.6 μm, this propagation will most likely be through an ionized medium (i.e. a plasma), where the dispersion from free electrons dominates that due to the atoms, and the free electron dispersion is anomolous. This could be the source of our measured negative group delay. In our particular case, it is very difficult to estimate the size and position of the coherence length. Although our laser focus was positioned at the end of the cesium column, the Rayleigh length of the laser focus is of comparable size to the cesium column (see Section 5.3.1). Further complicating the issue is the fact that at such high intensities, free electrons should alter the properties of the 3.6 μm pulse in the cesium column, perhaps leading to a defocusing of the beam.

If we assume that the measured group delay is due to a single atom effect, we can speculate on the involvement of the short and long trajectories from the above-threshold Simpleman's rescattering model. If we consider the return time of the trajectories, depicted in Figure 5.35, we see that within a given half cycle of the fundatmental driving field, the short trajectories return at times when the laser field strength is small and the distortion of the atomic potential is negligible. Recombination at such times would yield harmonics with photon energies of I_p or higher. For the long trajectories, the return occurs when the field is strong, and the distortion of the atomic potential is not negligible. Recombination to the ground state could involve the emission of radiation with photon energies less than I_p, and therefore explain the creation of our below-threshold harmonics. In addition, the group delay between the harmonic orders for the long trajectories, due to the

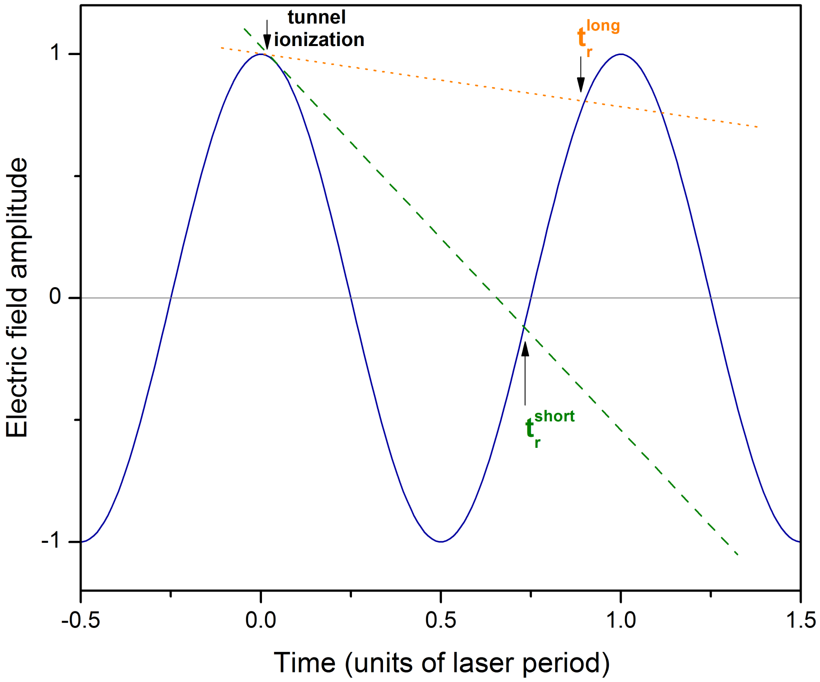

Figure 5.35: Depiction of the long and short trajectory return times. The lines drawn tangent to the electric field indicate the times during the field's period that recombination may occur. For the short trajectories, t_r^{short}, the return occurs when the field is small. For the long trajectories, t_r^{long}, the return occurs when the field is large.

excursion in the laser field away from and then back towards the ion core, is predicted to be negatively chirped, consistent with our observation.

These theories remain speculative until we have further information from the TDSE calculation.

Chapter 6

Conclusions

Our scaled atom-laser system exhibits strong-field behavior. This behavior is evident from features in both the photoelectron energy spectra and the harmonic spectra. The photoelectron spectra contain a high energy plateau that extends to energies that are many times cesium's ionization energy. The cutoff for this plateau is shown to be at $10U_p$, a value consistent with the Simpleman's rescattering model. In addition, structures within the spectrum are found to be similar to those that have been observed in the noble gases using titanium:sapphire laser light. The resemblence to argon spectra is particularly striking. This is consistent with our expectations, since the cesium-3.6 μm scaled system most resembles the argon-0.8 μm system. While at the moment, without theoretical models to which to compare our experimental results, we cannot conclude what the origin of these structures is, we have shown that they may be consistent with the picture of channel-closing resonances. Further investigation into the role of dressed excited states may reveal an interesting connection as well. The double peak structure within the individual ATI peaks of the photoelectron spectra is also intriguing and worthy of future study.

The observation of harmonic 31, at 116 nm, is a clear indication of strong-field behavior. Even within the spectrum of the lower order harmonics, the relative amplitudes of the harmonic peaks exhibit behavior that is more complicated than what is predicted by the traditional nonlinear optics approach using a perturbative treatment. The retrieved pulse durations for the individual harmonic orders also exhibit behavior that is more complicated than predicted by the traditional treatment (where the pulse duration scales with $1/\sqrt{q}$, q being the harmonic order). While the interpretation of our temporal measurement of the below-threshold harmonics awaits results from a TDSE calculation, we can state, for now, that a qualitative interpretation of the group delay between the orders, as well as an explanation for the creation of harmonics "below I_p" can be found in the single-atom response by incorporating the long trajectories and the deformation of the Coulomb potential at the return of the electron to the ion core. To clarify whether our observed group delay is due to the single-atom response or macroscopic effects, we need theoretical models of the single-atom and/or macroscopic response.

Having established that the scaled system does exhibit strong-field behavior, it is interesting to consider how properties of the scaled system that are distinct from properties of noble gas-ti:sapphire systems can be used to possibly expand our understanding of the strong-field interaction. One idea is to take advantage of the low lying first excited state of the alkali atoms and study the strong-field interaction when the atom is initially in an excited state, or even a superposition state. The D transitions of rubidium and cesium are particularly well suited for such a study, since the wavelengths are accessible using standard diode lasers. This idea was first proposed in theoretical papers [161, 162] and preliminary experimental work was done by our group using the picosecond mid-infrared laser [163] and rubidium. In our present set-up, the incorporation of diode lasers to excite the cesium would be feasible in both the photoelectron time-of-flight spectrometer and the harmonic heat pipe. This would be an interesting continuation of the work presented here.

Bibliography

[1] A. L. Schawlow and C. H. Townes. Infrared and optical masers. *Phys. Rev.*, 112(6):1940–1949, 1958.

[2] T. H. Maiman. Stimulated optical radiation in ruby. *Nature*, 187(4736): 493–494, 1960.

[3] W. Kaiser and C. G. B. Garrett. Two-photon excitation in CaF_2:Eu^{2+}. *Phys. Rev. Lett.*, 7(6):229–231, 1961.

[4] I. D. Abella. Optical double-photon absorption in cesium vapor. *Phys. Rev. Lett.*, 9(11):453–455, 1962.

[5] Maria Göppert-Mayer. Über elementarakte mit zwei quantensprüngen. *Annalen der Physik*, 401(3):273–294, 1931.

[6] F. J. McClung and R. W. Hellwarth. Giant optical pulsations from ruby. *Journal of Applied Physics*, 33(3):828–829, 1962.

[7] Voronov and Delone. *Sov. Phys. JETP*, 1:66, 1965.

[8] P. Agostini, G. Barjot, J. Bonnal, G. Mainfray, C. Manus, and J. Morellec. Multiphoton ionization of hydrogen and rare gases. *IEEE Journal of Quantum Electronics*, 4(10):667–669, 1968.

[9] G. H. C. New and J. F. Ward. Optical third-harmonic generation in gases. *Phys. Rev. Lett.*, 19(10):556–559, 1967.

[10] G. Mainfray and G. Manus. Multiphoton ionization of atoms. *Reports on Progress in Physics*, 54(10):1333–1372, 1991.

[11] R. Miles and S. Harris. Optical third-harmonic generation in alkali metal vapors. *IEEE Journal of Quantum Electronics*, 9(4):470–484, 1973.

[12] J. Reintjes, C. Y. She, and R. C. Eckardt. Generation of coherent radiation in xuv by 5^{th}-order and 7^{th}-order frequency-conversion in rare-gases. *IEEE Journal Of Quantum Electronics*, 14(8):581–596, 1978.

[13] M.G. Grozeva, D.I. Metchkov, V.M. Mitev, L.I. Pavlov, and K.V. Stamenov. Direct ninth harmonic conversion of picosecond laser pulses. *Optics Communications*, 23(1):77–79, 1977.

[14] J. Wildenauer. Generation of the ninth, eleventh, and fifteenth harmonics of iodine laser radiation. *Journal of Applied Physics*, 62(1):41–48, 1987.

[15] P. Agostini, F. Fabre, G. Mainfray, G. Petite, and N. K. Rahman. Free-free transitions following six-photon ionization of xenon atoms. *Phys. Rev. Lett.*, 42(17):1127–1130, 1979.

[16] M. Ferray, A. L'Huillier, X. F. Li, L. A. Lompre, G. Mainfray, and C. Manus. Multiple-harmonic conversion of 1064 nm radiation in rare gases. *Journal of Physics B: Atomic, Molecular and Optical Physics*, 21 (3):L31–L35, 1988.

[17] A. McPherson, G. Gibson, H. Jara, U. Johann, T. S. Luk, I. A. McIntyre, K. Boyer, and C. K. Rhodes. Studies of multiphoton production of vacuum-ultraviolet radiation in the rare gases. *Journal of the Optical Society of America B*, 4(4):595–601, 1987.

[18] F. Yergeau, G. Petite, and P. Agostini. Above-threshold ionisation without space charge. *Journal of Physics B: Atomic and Molecular Physics*, 19(19):L663–L669, 1986.

[19] M. Protopapas, C. H. Keitel, and P. L. Knight. Atomic physics with super-high intensity lasers. *Reports on Progress in Physics*, 60(4):389–486, 1997.

[20] G. G. Paulus, W. Nicklich, Huale Xu, P. Lambropoulos, and H. Walther. Plateau in above threshold ionization spectra. *Physical Review Letters*, 72(18):2851, 1994.

[21] P. M. Paul, E. S. Toma, P. Breger, G. Mullot, F. Auge, Ph. Balcou, H. G. Muller, and P. Agostini. Observation of a train of attosecond pulses from high harmonic generation. *Science*, 292(5522):1689–1692, 2001.

[22] Zenghu Chang, Andy Rundquist, Haiwen Wang, Margaret M. Murnane, and Henry C. Kapteyn. Generation of coherent soft x rays at 2.7 nm using high harmonics. *Physical Review Letters*, 79(16):2967, 1997.

[23] J. Seres, E. Seres, A. J. Verhoef, G. Tempea, C. Streli, P. Wobrauschek, V. Yakovlev, A. Scrinzi, C. Spielmann, and F. Krausz. Laser technology: Source of coherent kiloelectronvolt x-rays. *Nature*, 433(7026):596, 2005.

[24] P. Colosimo, G. Doumy, C. I. Blaga, J. Wheeler, C. Hauri, F. Catoire, J. Tate, R. Chirla, A. M. March, G. G. Paulus, H. G. Muller, P. Agostini, and L. F. DiMauro. Scaling strong-field interactions towards the classical limit. *Nat Phys*, 4(5):386–389, 2008.

[25] Rodrigo López-Martens, Katalin Varjú, Per Johnsson, Johan Mauritsson, Yann Mairesse, Pascal Salières, Mette B. Gaarde, Kenneth J. Schafer, Anders Persson, Sune Svanberg, Claes-Göran Wahlström, and Anne L'Huillier. Amplitude and phase control of attosecond light pulses. *Phys. Rev. Lett.*, 94(3):033001, 2005.

[26] E. Gustafsson, T. Ruchon, M. Swoboda, T. Remetter, E. Pourtal, R. Lopez-Martens, Ph. Balcou, and A. L'Huillier. Broadband attosecond pulse shaping. *Opt. Lett.*, 32(11):1353–1355, 2007.

[27] E. Goulielmakis, M. Schultze, M. Hofstetter, V. S. Yakovlev, J. Gagnon, M. Uiberacker, A. L. Aquila, E. M. Gullikson, D. T. Attwood, R. Kienberger, F. Krausz, and U. Kleineberg. Single-cycle nonlinear optics. *Science*, 320(5883):1614–1617, 2008.

[28] G. Sansone, E. Benedetti, F. Calegari, C. Vozzi, L. Avaldi, R. Flammini, L. Poletto, P. Villoresi, C. Altucci, R. Velotta, S. Stagira, S. De Silvestri, and M. Nisoli. Isolated single-cycle attosecond pulses. *Science*, 314 (5798):443–446, 2006.

[29] J. E. Bayfield and P. M. Koch. Multiphoton ionization of highly excited hydrogen atoms. *Phys. Rev. Lett.*, 33(5):258–261, 1974.

[30] T. F. Gallagher. Above-threshold ionization in low-frequency limit. *Phys. Rev. Lett.*, 61(20):2304–2307, 1988.

[31] Mette B. Gaarde, Jennifer L. Tate, and Kenneth J. Schafer. Macroscopic aspects of attosecond pulse generation. *Journal of Physics B: Atomic, Molecular and Optical Physics*, 41(13):132001, 2008.

[32] W. Becker, F. Grasbon, R. Kopold, D.B. Milosevic, G.G. Paulus, and H. Walther. Above-threshold ionization: From classical features to quantum effects. *Advances In Atomic, Molecular, and Optical Physics*, 48:35 – 98, 2002.

[33] Pascal Salieres, Anne L'Huillier, Philippe Antoine, and Maciej Lewenstein. Study of the spatial and temporal coherence of high-order harmonics. *Advances In Atomic, Molecular, and Optical Physics*, 41:83–142, 1999.

[34] L. V. Keldysh. Ionization in the field of a strong electromagnetic wave. *Sov. Phys. JETP*, 20:1307–1314, 1965.

[35] A. M. Perelomov, V. S. Popov, and M. V. Terent'ev. *Sov. Phys. JETP*, 23:924, 1966.

[36] M. V. Ammosov, N. B. Delone, and V. P. Krainov. *Sov. Phys. JETP*, 64:1191, 1986.

[37] B. E. Sauer, S. Yoakum, L. Moorman, P. M. Koch, D. Richards, and P.A. Dando. Dynamic tunneling ionization of excited hydrogen atoms: A precise experiment versus theories. *Phys. Rev. Lett.*, 68(4):468–471, 1992.

[38] P. B. Corkum. Plasma perspective on strong field multiphoton ionization. *Physical Review Letters*, 71(13):1994, 1993.

[39] A. Becker and F. H. M. Faisal. Intense-field many-body S-matrix theory. *Journal of Physics B: Atomic, Molecular and Optical Physics*, 38(3):R1–R56, 2005.

[40] K. J. Schafer, Baorui Yang, L. F. DiMauro, and K. C. Kulander. Above threshold ionization beyond the high harmonic cutoff. *Phys. Rev. Lett.*, 70(11):1599, 1993.

[41] Ferenc Krausz and Misha Ivanov. Attosecond physics. *Reviews of Modern Physics*, 81(1):163–72, 2009.

[42] G. G. Paulus, W. Becker, W. Nicklich, and H. Walther. Rescattering effects in above-threshold ionization: a classical model. *Journal of Physics B: Atomic, Molecular and Optical Physics*, 27(21):L703–L708, 1994.

[43] P. Salires, A. L'Huillier, Ph. Antoine, and M. Lewenstein. Study of the spatial and temporal coherence of high-order harmonics. *Adv. At. Mol. Opt. Phys.*, 41:83, 1999.

[44] Y. Mairesse, A. de Bohan, L. J. Frasinski, H. Merdji, L. C. Dinu, P. Monchicourt, P. Breger, M. Kovacev, R. Taieb, B. Carre, H. G. Muller, P. Agostini, and P. Salieres. Attosecond synchronization of High-Harmonic soft x-rays. *Science*, 302(5650):1540–1543, 2003.

[45] M. Lewenstein, Ph. Balcou, M. Yu. Ivanov, Anne L'Huillier, and P. B. Corkum. Theory of high-harmonic generation by low-frequency laser fields. *Phys. Rev. A*, 49(3):2117–2132, 1994.

[46] W. Becker, S. Long, and J. K. McIver. Modeling harmonic generation by a zero-range potential. *Phys. Rev. A*, 50(2):1540–1560, 1994.

[47] M. Lewenstein, K. C. Kulander, K. J. Schafer, and P. H. Bucksbaum. Rings in above-threshold ionization: A quasiclassical analysis. *Phys. Rev. A*, 51(2):1495–1507, 1995.

[48] W. Becker, A. Lohr, and M. Kleber. Effects of rescattering on above-threshold ionization. *Journal of Physics B: Atomic, Molecular and Optical Physics*, 27(14):L325–L332, 1994.

[49] Philip Colosimo. *A Study of Wavelength Dependence of Strong-Field Optical Ionization*. PhD thesis, Stony Brook University, 2007.

[50] S. Cussat-Blanc, A. Ivanov, D. Lupinski, and E. Freysz. $KTiOPO_4$, $KTiOAsO_4$, and $KNbO_3$ crystals for mid-infrared femtosecond optical parametric amplifiers: analysis and comparison. *Applied Physics B: Lasers & Optics*, 70(7):S247, 2000.

[51] Barry Walker. *One- and Two- Electron Ionization of Atoms by a Strong Laser Field*. PhD thesis, Stony Brook University, 1996.

[52] Muhammad Saeed, Dalwoo Kim, and Louis F. DiMauro. Optimization and characterization of a high repetition rate, high intensity Nd:YLF regenerative amplifier. *Applied Optics*, 29(12):1752–1757, 1990.

[53] Todd Clatterbuck. *High Harmonic Generation From an Intense Mid-Infrared Light Source*. PhD thesis, Stony Brook University, 2003.

[54] B. C. Stuart, M. D. Feit, S. Herman, A. M. Rubenchik, B. W. Shore, and M. D. Perry. Nanosecond-to-femtosecond laser-induced breakdown in dielectrics. *Phys. Rev. B*, 53(4):1749–1761, 1996.

[55] Walter Koechner. *Solid-State Laser Engineering*. Springer-Verlag, New York, 1992.

[56] Lee M. Frantz and John S. Nodvik. Theory of pulse propagation in a laser amplifier. *Journal of Applied Physics*, 34(8):2346–2349, 1963.

[57] P. F. Moulton. Spectroscopic and laser characteristics of $Ti:Al_2O_3$. *Journal of the Optical Society of America B*, 3(1):125–133, 1986.

[58] Francois Salin, Catherine Le Blanc, Jeff Squier, and Chris Barty. Thermal eigenmode amplifiers for diffraction-limited amplification of ultrashort pulses. *Optics Letters*, 23(9):718–720, 1998.

[59] Yasuo Nabekawa, Tadashi Togashi, Taro Sekikawa, Shuntaro Watanabe, Susumu Konno, Tetsuo Kojima, Shuichi Fujikawa, and Koji Yasui. All-solid-state 5-kHz 0.2-TW ti:sapphire laser system. *Optics Express*, 5(13): 318–324, 1999.

[60] Sterling Backus, Randy Bartels, Sarah Thompson, Robert Dollinger, Henry C. Kapteyn, and Margaret M. Murnane. High-efficiency, single-stage 7-kHz high-average-power ultrafast laser system. *Optics Letters*, 26(7):465–467, 2001.

[61] Sterling Backus, Charles G. Durfee III, Gerard Mourou, Henry C. Kapteyn, and Margaret M. Murnane. 0.2-TW laser system at 1kHz. *Optics Letters*, 22(16):1256–1258, 1997.

[62] M. G. Holland. Thermal conductivity of several optical maser materials. *Journal of Applied Physics*, 33(9):2910–2911, 1962.

[63] A. C. DeFranzo and B. G. Pazol. Index of refraction measurement on sapphire at low temperatures and visible wavelengths. *Applied Optics*, 32(13):2224–2234, 1993.

[64] M. Zavelani-Rossi, F. Lindner, C. Le Blanc, G. Chriaux, and J.P. Chambaret. Control of thermal effects for high-intensity ti:sapphire laser chains. *Applied Physics B: Lasers & Optics*, 70(7):S193, 2000.

[65] B. Walker, B. Sheehy, L. F. DiMauro, P. Agostini, K. J. Schafer, and K. C. Kulander. Precision measurement of strong field double ionization of helium. *Physical Review Letters*, 73(9):1227, 1994.

[66] P. Agostini, F. Fabre, G. Mainfray, G. Petite, and N. K. Rahman. Free-free transitions following six-photon ionization of xenon atoms. *Physical Review Letters*, 42(17):1127, 1979.

[67] G. G. Paulus, F. Lindner, H. Walther, A. Baltuka, E. Goulielmakis, M. Lezius, and F. Krausz. Measurement of the phase of Few-Cycle laser pulses. *Physical Review Letters*, 91(25):253004, 2003.

[68] H.G. Muller. Reconstruction of attosecond harmonic beating by interference of two-photon transitions. *Applied Physics B: Lasers and Optics*, 74(0):s17–s21, 2002.

[69] Y. Mairesse and F. Quere. Frequency-resolved optical gating for complete reconstruction of attosecond bursts. *Physical Review A*, 71(1): 011401, 2005.

[70] J. Itatani, F. Quere, G. L. Yudin, M. Yu. Ivanov, F. Krausz, and P. B. Corkum. Attosecond streak camera. *Physical Review Letters*, 88(17): 173903, 2002.

[71] G. Petite, F. Fabre, P. Agostini, M. Crance, and M. Aymar. Nonresonant multiphoton ionization of cesium in strong fields: Angular distributions and above-threshold ionization. *Physical Review A*, 29(5):2677, 1984.

[72] R. R. Jones. Interference effects in the multiphoton ionization of sodium. *Physical Review Letters*, 74(7):1091, 1995.

[73] R. R. Jones. Multiphoton ionization enhancement using two Phase-Coherent laser pulses. *Physical Review Letters*, 75(8):1491, 1995.

[74] D. I. Duncan, J. de Boer, H. G. Muller, and L. D. Noordam. Above-threshold ionization in K via a cooper minimum in the continuum. *Physical Review A*, 56(6):4985, 1997.

[75] John W. Cooper. Photoionization from outer atomic subshells. a model study. *Physical Review*, 128(2):681–693, 1962.

[76] R. Freeman. *Atoms in Intense Laser Fields*. Academic Press, San Diego, 1992.

[77] M. J. Nandor, M. A. Walker, L. D. Van Woerkom, and H. G. Muller. Detailed comparison of above-threshold-ionization spectra from accurate numerical integrations and high-resolution measurements. *Physical Review A*, 60(3):R1771, 1999.

[78] N.J. van Druten, R. Trainham, and H.G. Muller. Above-threshold ionization of cesium by 1.9-μm light. *Physical Review A*, 51(2):R898, 1995.

[79] M. B. Gaarde, K. J. Schafer, K. C. Kulander, B. Sheehy, Dalwoo Kim, and L. F. DiMauro. Strong species dependence of high order photoelectron production in alkali metal atoms. *Physical Review Letters*, 84(13): 2822, 2000.

[80] Mette B. Gaarde and Kenneth J. Schafer. Calculations of resonant multiphoton population transfer in potassium atoms at long wavelengths. *Physical Review A*, 62(5):053411, 2000.

[81] Claude Cohen-Tannoudji, Bernard Diu, and Frank Laloe. *Quantum Mechanics*. Wiley-Interscience, Hoboken, NJ, 2006.

[82] W. C. Wiley and I. H. McLaren. Time-of-Flight mass spectrometer with improved resolution. *Review of Scientific Instruments*, 26(12):1150–1157, 1955.

[83] T. J. McIlrath, P. H. Bucksbaum, R. R. Freeman, and M. Bashkansky. Above-threshold ionization processes in xenon and krypton. *Physical Review A*, 35(11):4611, 1987.

[84] I. Estermann, S. N. Foner, and O. Stern. The mean free paths of cesium atoms in helium, nitrogen, and cesium vapor. *Phys. Rev.*, 71(4):250–257, 1947.

[85] John Bradshaw Taylor and Irving Langmuir. Vapor pressure of caesium by the positive ion method. *Phys. Rev.*, 51(9):753–760, 1937.

[86] M. Rozwadowski and E. Lipworth. Measurement of the density of saturated cesium vapor by an optical method. *The Journal of Chemical Physics*, 43(7):2347–2350, 1965.

[87] Norman Ramsey. *Molecular beams.* Clarendon Press, Gloucestershire, UK, 1956.

[88] J.L. Wiza. Microchannel plate detectors. *Nuclear Instruments and Methods*, 162:587, 1979.

[89] P. Hansch, M. A. Walker, and L. D. Van Woerkom. Spatially dependent multiphoton multiple ionization. *Phys. Rev. A*, 54(4):R2559–R2562, 1996.

[90] G. G. Paulus, F. Grasbon, H. Walther, R. Kopold, and W. Becker. Channel-closing-induced resonances in the above-threshold ionization plateau. *Physical Review A*, 64(2):021401, 2001.

[91] H. G. Muller and F. C. Kooiman. Bunching and focusing of tunneling wave packets in enhancement of high-order above-threshold ionization. *Physical Review Letters*, 81(6):1207, 1998.

[92] D. B. Milosevic, E. Hasovic, M. Busuladzic, A. Gazibegovic-Busuladzic, and W. Becker. Intensity-dependent enhancements in high-order above-threshold ionization. *Physical Review A*, 76(5):053410–16, 2007.

[93] E. Hasovic, M. Busuladzic, A. Gazibegovic-Busuladzic, D. Milosevic, and W. Becker. Simulation of above-threshold ionization experiments using the strong-field approximation. *Laser Physics*, 17(4):376–389, 2007.

[94] Joseph Wassaf, Valérie Véniard, Richard Taïeb, and Alfred Maquet. Roles of resonances and recollisions in strong-field atomic phenomena: Above-threshold ionization. *Phys. Rev. A*, 67(5):053405, 2003.

[95] R. M. Potvliege and Svetlana Vucic. High-order above-threshold ionization of argon: Plateau resonances and the floquet quasienergy spectrum. *Physical Review A*, 74(2):023412–11, 2006.

[96] R. R. Freeman, P. H. Bucksbaum, H. Milchberg, S. Darack, D. Schumacher, and M. E. Geusic. Above-threshold ionization with subpicosecond laser pulses. *Phys. Rev. Lett.*, 59(10):1092–1095, 1987.

[97] R. R. Freeman and P. H. Bucksbaum. Investigations of above-threshold ionization using subpicosecond laser pulses. *Journal of Physics B: Atomic, Molecular and Optical Physics*, 24(2):325–347, 1991.

[98] W. Nicklich, H. Kumpfmüller, H. Walther, X. Tang, Huale Xu, and P. Lambropoulos. Above-threshold ionization of cesium under femtosecond laser pulses: New substructure due to strongly coupled bound states. *Physical Review Letters*, 69(24):3455, 1992.

[99] Bing Shan and Zenghu Chang. Dramatic extension of the high-order harmonic cutoff by using a long-wavelength driving field. *Phys. Rev. A*, 65(1):011804, 2001.

[100] G. Doumy, J. Wheeler, C. Roedig, R. Chirla, P. Agostini, and L. F. DiMauro. Attosecond synchronization of High-Order harmonics from midinfrared drivers. *Physical Review Letters*, 102(9):093002–4, 2009.

[101] X. F. Li, A. L'Huillier, M. Ferray, L. A. Lompré, and G. Mainfray. Multiple-harmonic generation in rare gases at high laser intensity. *Phys. Rev. A*, 39(11):5751–5761, 1989.

[102] L. A. Lompr, A. L'Huillier, M. Ferray, P. Monot, G. Mainfray, and C. Manus. High-order harmonic generation in xenon: intensity and propagation effects. *Journal of the Optical Society of America B*, 7(5): 754–761, 1990.

[103] Anne L'Huillier, Philippe Balcou, Sebastien Candel, Kenneth J. Schafer, and Kenneth C. Kulander. Calculations of high-order harmonic-generation processes in xenon at 1064 nm. *Phys. Rev. A*, 46(5):2778–2790, 1992.

[104] S.E. Harris. Generation of vacuum ultraviolet and soft-x-ray radiation using high-order nonlinear optical polarizabilities. *Physical Review Letters*, 31(6):341–344, 1973.

[105] D.M. Bloom, G.W. Bekkers, J.F. Young, and S.E. Harris. 3^{RD} harmonic-generation in phase-matched alkali-metal vapors. *Applied Physics Letters*, 26(12):687–689, 1975.

[106] K. Miyazaki and H. Kashiwagi. Multi-photon ionization of Na atoms in third-harmonic generation by a mode-locked nd:yag laser. *Physical Review A*, 18(2):635–643, 1978.

[107] T.O. Clatterbuck, C. Lynga, P. Colosimo, J.D.D. Martin, B. Sheehy, L.F. Dimauro, P. Agostini, and K.C. Kulander. Scaled intense laser-atom physics: the long wavelength regime. *Journal of Modern Optics*, 50(3-4):441–450, 2003.

[108] T.O. Clatterbuck, C. Lynga, P.M. Paul, L.F. DiMauro, M.B. Gaarde, K.J. Schafer, P. Agostini, K.C. Kulander, and I. Walmsley. Yield and temporal characterization of high-order harmonics from intense midinfrared excitation of a cesium vapor. *Physical Review A*, 69(3), 2004.

[109] V. O Lorenz, X. Dai, H. Green, T. R Asnicar, and S. T Cundiff. High-density, high-temperature alkali vapor cell. *Review of Scientific Instruments*, 79(12):123104–123104–4, 2008.

[110] C. R. Vidal and J. Cooper. Heat-Pipe oven: A new, Well-Defined metal vapor device for spectroscopic measurements. *Journal of Applied Physics*, 40(8):3370–3374, 1969.

[111] G. M. Grover, T. P. Cotter, and G. F. Erickson. Structures of very high thermal conductance. *Journal of Applied Physics*, 35(6):1990–1991, 1964.

[112] C. R. Vidal. Spectroscopic observations of subsonic and sonic vapor flow inside an open-ended heat pipe. *Journal of Applied Physics*, 44(5): 2225–2232, 1973.

[113] L. A. Melton and P. H. Wine. Operation of near ideal spectroscopic heat pipes. *Journal of Applied Physics*, 51(8):4059–4069, 1980.

[114] Robert W Boyd and Jack G Dodd. Analysis of the pressure, density, and velocity distributions in a spectroscopic heat-pipe oven and the resulting limitations on device performance. *Journal of Applied Physics*, 51(12): 6058–6061, 1980.

[115] A. N. Nesmeyanov. *Vapor Pressures of the Chemical Elements*. Elsevier, New York, 1963.

[116] G. Pichler, S. Milosevic, D. Viza, and R. Beuc. Diffuse bands in the visible absorption spectra of dense alkali vapours. *Journal of Physics B: Atomic and Molecular Physics*, 16(24):4619–4631, 1983.

[117] J. A. Armstrong. Measurement of picosecond laser pulse widths. *Applied Physics Letters*, 10(1):16–18, 1967.

[118] R. K. Jain, J. E. Brown, and W. P. Robinson. Simple distortion-free real-time optical pulse correlator. *Applied Optics*, 21(22):4073–4076, 1982.

[119] K. Sala, G. Kenney-Wallace, and G. Hall. CW autocorrelation measurements of picosecond laser pulses. *IEEE Journal of Quantum Electronics*, 16(9):990–996, 1980.

[120] A. Weiner. Effect of group velocity mismatch on the measurement of ultrashort optical pulses via second harmonic generation. *IEEE Journal of Quantum Electronics*, 19(8):1276–1283, 1983.

[121] Guan Xinan, M. Lambsdorff, J. Kuhl, and Wu Biachang. Fast-scanning autocorrelator with 1-ns scanning range for characterization of mode-locked ion lasers. *Review of Scientific Instruments*, 59(9):2088–2090, 1988.

[122] Jung-Ho Chung and A.M. Weiner. Ambiguity of ultrashort pulse shapes retrieved from the intensity autocorrelation and the power spectrum. *IEEE Journal of Selected Topics in Quantum Electronics*, 7(4):656–666, 2001.

[123] Joshua E. Rothenberg and D. Grischkowsky. Measurement of optical phase with subpicosecond resolution by time-domain interferometry. *Optics Letters*, 12(2):99–101, 1987.

[124] J. W. Nicholson and W. Rudolph. Noise sensitivity and accuracy of femtosecond pulse retrieval by phase and intensity from correlation and spectrum only (PICASO). *Journal of the Optical Society of America B*, 19(2):330–339, 2002.

[125] Erik Power, Joseph Pentland, John Nees, Christoph P. Hauri, Michele Merano, Rodrigo Lopez-Martens, and Grard Mourou. All-reflective high fringe contrast autocorrelator for measurement of ultrabroadband optical pulses. *Optics Letters*, 31(23):3514–3516, 2006.

[126] Toshiyuki Hirayama and Mansoor Sheik-Bahae. Real-time chirp diagnostic for ultrashort laser pulses. *Optics Letters*, 27(10):860–862, 2002.

[127] K. Naganuma, K. Mogi, and H. Yamada. General method for ultrashort light pulse chirp measurement. *IEEE Journal of Quantum Electronics*, 25(6):1225–1233, 1989.

[128] L.P. Barry, P.G. Bollond, J.M. Dudley, J.D. Harvey, and R. Leonhardt. Autocorrelation of ultrashort pulses at 1.5 m based on nonlinear response of silicon photodiodes. *Electronics Letters*, 32(20):1922–1923, 1996.

[129] A. Gutierrez, P. Dorn, J. Zeller, D. King, L. F. Lester, W. Rudolph, and M. Sheik-Bahae. Autocorrelation measurement of femtosecond laser pulses by use of a ZnSe two-photon detector array. *Optics Letters*, 24 (16):1175–1177, 1999.

[130] C. Iaconis and I.A. Walmsley. Spectral phase interferometry for direct electric-field reconstruction of ultrashort optical pulses. *Optics Letters*, 23(10):792–794, 1998.

[131] L. Lepetit, G. Chriaux, and M. Joffre. Linear techniques of phase measurement by femtosecond spectral interferometry for applications in spectroscopy. *Journal of the Optical Society of America B*, 12(12): 2467–2474, 1995.

[132] C. Iaconis and I.A. Walmsley. Self-referencing spectral interferometry for measuring ultrashort optical pulses. *IEEE Journal of Quantum Electronics*, 35(4):501–509, 1999.

[133] C. Dorrer. Implementation of spectral phase interferometry for direct electric-field reconstruction with a simultaneously recorded reference interferogram. *Optics Letters*, 24(21):1532–1534, 1999.

[134] `http://ultrafast.physics.ox.ac.uk/spider/`.

[135] K. W. DeLong, Rick Trebino, J. Hunter, and W. E. White. Frequency-resolved optical gating with the use of second-harmonic generation. *Journal of the Optical Society of America B*, 11(11):2206–2215, 1994.

[136] `http://www.physics.gatech.edu/frog/`.

[137] R. Trebino. *Frequency-Resolved Optical Gating: The Measurement of Ultrashort Laser Pulses.* Kluwer Academic, Boston, 2000.

[138] Daniel J. Kane and Rick Trebino. Single-shot measurement of the intensity and phase of an arbitrary ultrashort pulse by using frequency-resolved optical gating. *Optics Letters*, 18(10):823–825, 1993.

[139] Rick Trebino and Daniel J. Kane. Using phase retrieval to measure the intensity and phase of ultrashort pulses: frequency-resolved optical gating. *Journal of the Optical Society of America A*, 10(5):1101–1111, 1993.

[140] D.J. Kane and R. Trebino. Characterization of arbitrary femtosecond pulses using frequency-resolved optical gating. *Quantum Electronics, IEEE Journal of*, 29(2):571–579, 1993.

[141] John N. Sweetser, David N. Fittinghoff, and Rick Trebino. Transient-grating frequency-resolved optical gating. *Optics Letters*, 22(8):519–521, 1997.

[142] Thomas Tsang, Marco A. Krumbgel, Kenneth W. DeLong, David N. Fittinghoff, and Rick Trebino. Frequency-resolved optical-gating measurements of ultrashort pulses using surface third-harmonic generation. *Optics Letters*, 21(17):1381–1383, 1996.

[143] Tracy Sharp Clement, A. J. Taylor, and Daniel J. Kane. Single-shot measurement of the amplitude and phase of ultrashort laser pulses in the violet. *Optics Letters*, 20(1):70–72, 1995.

[144] Patrick O'Shea, Mark Kimmel, Xun Gu, and Rick Trebino. Highly simplified device for ultrashort-pulse measurement. *Optics Letters*, 26(12): 932–934, 2001.

[145] S. Linden, J. Kuhl, and H. Giessen. Amplitude and phase characterization of weak blue ultrashort pulses by downconversion. *Optics Letters*, 24(8):569–571, 1999.

[146] S. Linden, H. Giessen, and J. Kuhl. XFROG - a new method for amplitude and phase characterization of weak ultrashort pulses. *Physica Status Solidi (b)*, 206(1):119–124, 1998.

[147] H. Stark A. Levi. *Restoration from Phase and Magnitude by Generalized Projections in Image Recovery: Theory and Applications.* Academic, San Diego, 1987.

[148] Kenneth W. DeLong, David N. Fittinghoff, Rick Trebino, Bern Kohler, and Kent Wilson. Pulse retrieval in frequency-resolved optical gating

based on the method of generalized projections. *Optics Letters*, 19(24): 2152–2154, 1994.

[149] D.J. Kane. Recent progress toward real-time measurement of ultrashort laser pulses. *IEEE Journal of Quantum Electronics*, 35(4):421–431, 1999.

[150] D.J. Kane. Real-time measurement of ultrashort laser pulses using principal component generalized projections. *IEEE Journal of Selected Topics in Quantum Electronics*, 4(2):278–284, 1998.

[151] W. H. Press, S. A. Teukolsky, W. T. Vetterling, and B. P. Flannery. *Numerical Recipes in C-The Art of Scientific Computing.* Cambridge University Press, Cambridge, 2nd edition, 1995.

[152] A. K. Jain. *Fundamentals of Digital Image Processing.* Prentice Hall, Englewood Cliffs, 1st edition, 1989.

[153] Kenneth W. DeLong, Rick Trebino, and William E. White. Simultaneous recovery of two ultrashort laser pulses from a single spectrogram. *Journal of the Optical Society of America B*, 12(12):2463–2466, 1995.

[154] Erik Power. *Few-Cycle and Sub-Cycle Metrology for the Characterization of High Harmonics.* PhD thesis, University of Michigan, 2009.

[155] S. A. Aseyev, Y. Ni, L. J. Frasinski, H. G. Muller, and M. J. J. Vrakking. Attosecond angle-resolved photoelectron spectroscopy. *Phys. Rev. Lett.*, 91(22):223902, 2003.

[156] K. Varjú, Y. Mairesse, B. Carre, M.B. Gaarde, P. Johnsson, S. Kazamias, R. López-Martens, J. Mauritsson, K.J. Schafer, P.H. Balcou, A. L'Huillier, and P. Salieres. Frequency chirp of harmonic and attosecond pulses. *Journal of Modern Optics*, 52(2-3):379–394, 2005.

[157] B. C. McCallum and J. M. Rodenburg. Simultaneous reconstruction of object and aperture functions from multiple far-field intensity measurements. *Journal of the Optical Society of America A*, 10(2):231–239, 1993.

[158] H. H. Li. Refractive index of alkali halides and its wavelength and temperature derivatives. *Journal of Physical and Chemical Reference Data*, 5:329–528, 1976.

[159] SNLO version 42. Nonlinear optics code available from A. V. Smith, AS-Photonics, Albuquerque, NM.

[160] Ziyang Wang, Erik Zeek, Rick Trebino, and Paul Kvam. Determining error bars in measurements of ultrashort laser pulses. *Journal of the Optical Society of America B*, 20(11):2400–2405, 2003.

[161] J. B. Watson, A. Sanpera, X. Chen, and K. Burnett. Harmonic generation from a coherent superposition of states. *Phys. Rev. A*, 53(4): R1962–R1965, 1996.

[162] Zhinan Zeng, Ruxin Li, Ya Cheng, Wei Yu, and Zhizhan Xu. Resonance-enhanced high-order harmonic generation and frequency mixing in two-color laser field. *Physica Scripta*, 66(4):321–325, 2002.

[163] P.M. Paul, T.O. Clatterbuck, C. Lynga, P. Colosimo, L.F. DiMauro, P. Agostini, and K.C. Kulander. Enhanced high harmonic generation from an optically prepared excited medium. *Physical Review Letters*, 94 (11):113906, 2005.